MAX-PLANCK-INSTITUT FÜR QUANTENOPTIK

Development of Optical Parametric Chirped-Pulse Amplifiers and Their Applications

Nobuhisa Ishii

MAX-PLANCK-INSTITUT FÜR QUANTENOPTIK

Development of Optical Parametric Chirped-Pulse Amplifiers and

Their Applications

Nobuhisa Ishii

Abstract

In this work, optical pulse amplification by parametric chirped-pulse amplification (OPCPA) has been applied to the generation of high-energy, few-cycle optical pulses in the near-infrared (NIR) and infrared (IR) spectral regions. Amplification of such pulses is ordinarily difficult to achieve by existing techniques of pulse amplification based on standard laser gain media followed by external compression. Potential applications of few-cycle pulses in the IR have also been demonstrated.

The NIR OPCPA system produces 0.5-terawatt (10 fs, 5 mJ) pulses by use of noncollinearly phase-matched optical parametric amplification and a down-chirping stretcher and upchirping compressor pair.

An IR OPCPA system was also developed which produces 20-gigawatt (20 fs, 350 μJ) pulses at 2.1 μm. The IR seed pulse is generated by optical rectification of a broadband pulse and therefore it exhibits a self-stabilized carrier-envelope phase (CEP).

In the IR OPCPA a common laser source is used to generate the pump and seed resulting in an inherent sub-picosecond optical synchronization between the two pulses. This was achieved by use of a custom-built Nd:YLF picosecond pump pulse amplifier that is directly seeded with optical pulses from a custom-built ultrabroadband Ti:sapphire oscillator. Synchronization between the pump and seed pulses is critical for efficient and stable amplification.

Two spectroscopic applications which utilize these unique sources have been demonstrated. First, the visible supercontinuum was generated in a solid-state media by the infrared optical pulses and through which the carrier-envelope phase (CEP) of the driving pulse was measured with an f-to-$3f$ interferometer. This measurement confirms the self-stabilization mechanism of the CEP in a difference frequency generation process and the preservation of the CEP during optical parametric amplification. Second, high-order harmonics with energies extending beyond 200 eV were generated with the few-cycle infrared pulses in an argon target. Because of the longer carrier period, the IR pulses transfer more quiver energy to ionized free electrons compared to conventional NIR pulses. Therefore, higher energy radiation is emitted upon recombination of the accelerated electrons. This result shows the highest photon energy generated by a laser excitation in neutral argon.

Zusammenfassung

Im Mittelpunkt dieser Arbeit steht die Verstärkung von hochenergetischen kurzen Laserpulsen im nahen infraroten- und im infraroten Bereich mit optischer parametrischer Breitbandpulsverstärkung (OPCPA). Mit herkömmlicher Laserverstärkertechnologie ist es mühsam, annähernd ähnliche Verstärkungsparameter zu erreichen. In dieser Arbeit sind weiterhin vielversprechende Applikationen von den kurzen infraroten Laserpulsen demonstriert worden.

Mit dem NIR OPCPA haben wir Laserpulse mit 0.5-terawatt Spitzenleistung (10 fs, 5 mJ) erzeugt. Die Methode beruht auf nichtkollineare phasenangepasste optische parametrische Verstärkung und wir haben einen negativ dispersiven Pulsstrecker verwendet um die positive Dispersion der Glaskompressorblöcke zu kompensieren.

Ein IR OPCPA haben wir zusätzlich entwickelt um 20-gigawatt (20 fs, 350 μJ) Pulse im Wellenlängenbereich von 2.1 μm zu verstärken. Optische Gleichrichtung von den breitbandugen Pulsen wurden eingesetzt um einen "Seed"-Puls mit selbstabilisierende "carrier enevelope"-phase (CEP) zu generieren.

Im IR OPCPA wird eine einzige Laserquelle benutzt um die Pumppulse und die Seedpulse zu erzeugen. Damit wird eine Synchronisation der beiden Pulsen mit sub-pikosekunden Präzision erreicht. Um diese Synchronisationsmethode zu testen haben wir einen Nd:YLF Laserverstärker mit pikosekunden Pulsdauer gebaut und damit direkt die breitbandingen Pulse eines Ti:Sapphir Oszillators verstärkt. Diese Synchronisationstechnik macht die optische parametrische Breitbandpulsverstärkung für verschiedene Einsätze robust und zuverlässig.

Mit diesen einzigartigen Laserquellen haben wir zwei Spektroskopieanwendungen demonstriert. Eine Anwendung ist die Erzeugung eines sichtbaren Supercontinuums im Festkörper. Das Supercontinuum verwendet man für die Detektion von der CE-Phase derselben Pulse mittels eines f-to-$3f$ Schemas. Diese Messung zeigt Selbststabilisierung der CE-Phase und dessen Erhaltung während des optischen parametrischen Verstärkungsprozesses. Die zweite Anwendung ist die Erzeugung von höheren Harmonischen der infraroten Laserpulse über 200 eV in einem Argon-target. Eine höhere "Quiver"-Energie wird bei den ionisierten Elektronen durch die längeren Periode des optischen Trägers im Infrarotbereich angeregt. Die Periode des optischen Trägers im Infrarotbereich ist länger als im sichtbaren Bereich, folglich können damit höherenergetische Harmonische bei Rekombination der beschleunigten Elektronen erzeugt werden. Das ist die höchste experimentell je in neutralem Argon lasererzeugte Photonenergie.

List of publications

Publications included in this thesis are marked with the asterisk.

1 **N. Ishii** and C. Y. Teisset and S. Köhler and E. E. Serebryannikov and T. Fuji and T. Metzger and F. Krausz and A. Baltuška and A. M. Zheltikov, "Widely tunable soliton frequency shifting of few-cycle laser pulses," *Phys. Rev. E*, vol. 74, p. 036617, 2006.

2 E. E. Serebryannikov and A. M. Zheltikov and S. Köhler and **N. Ishii** and C. Y. Teisset and T. Fuji and F. Krausz and A. Baltuška, "Diffraction-arrested soliton self-frequency shift of few-cycle laser pulses in a photonic crystal fiber," *Phys. Rev. E*, vol. 73, p. 066617, 2006.

3* **N. Ishii** and C. Y. Teisset and T. Fuji and S. Köhler and K. Schmid and L. Veisz and A. Baltuška and F. Krausz, "Seeding of an Eleven Femtosecond Optical Parametric Chirped Pulse Amplifier and its Nd^{3+} Picosecond Pump Laser From a Single Broadband Ti:Sapphire Oscillator," *IEEE J. Sel. Top. Quantum Electron.*, vol. 12, pp. 173–180, 2006.

4* T. Fuji and **N. Ishii** and C. Y. Teisset and X. Gu and Th. Metzger and A. Baltuška and N. Forget and D. Kaplan and A. Galvanauskas and F. Krausz, "Parametric amplification of few-cycle carrier-envelope phase-stable pulses at 2.1 μm," *Opt. Lett.*, vol. 31, pp. 1103–1105, 2006.

5 E. E. Serebryannikov and A. M. Zheltikov and **N. Ishii** and C. Y. Teisset and S. Köhler and T. Fuji and T. Metzger and F. Krausz and A. Baltuška, "Nonlinear-optical spectral transformation of few-cycle laser pulses in photonic-crystal fibers," *Phys. Rev. E*, vol. 72, p. 056603, 2005.

6 C. Y. Teisset and **N. Ishii** and T. Fuji and T. Metzger and S. Köhler and R. Holzwarth and A. Baltuška and A. M. Zheltikov and F. Krausz, "Soliton-based pump-seed synchronization for few-cycle OPCPA," *Opt. Express*, vol. 13, pp. 6550–6557, 2005.

7 F. Tavella and K. Schmid and **N. Ishii** and A. Marcinkevičius and L. Veisz and F. Krausz, "High-dynamic range pulse-contrast measurements of a broadband optical parametric chirped-pulse amplifier," *Appl. Phys. B*, vol. 81, pp. 753–756, 2005.

8 E. E. Serebryannikov and A. M. Zheltikov and **N. Ishii** and C.Y. Teisset and S. Köhler and T. Fuji and T. Metzger and F. Krausz and A. Baltuška, "Soliton self-frequency shift of 6-fs pulses in photonic-crystal fibers," *Appl. Phys. B*, vol. 81, pp. 585–588, 2005.

9* **N. Ishii** and L. Turi and V. S. Yakovlev and T. Fuji and F. Krausz and A. Baltuška and R. Butkus and G. Veitas and V. Smilgevičius and R. Danielius and A. Piskarskas, "Multimillijoule chirped parametric amplification of few-cycle pulses," *Opt. Lett.*, vol. 30, pp. 567–569, 2005.

Contents

Chapter 1

Introduction

1.1 General introduction

After the first observation of the laser action in ruby [1], the temporal duration of optical pulses obtained from the laser has been shortened from microseconds, nanoseconds, picoseconds, and down to femtoseconds based on several techniques such as Q-switching and mode-locking as well as broadband laser media such as Nd:YAG, Nd:glass, and laser dye. Meanwhile since 1980s, the ultrafast spectroscopy, made possible by the highly coherent ultrafast laser pulses, has been established and pursued intensively with ultrafast dye lasers [2]. However, the dye lasers did not last in use for long due to the fact that they were difficult to handle and were unreliable, before being replaced by lasers based on Ti:sapphire [3, 4, 5] with chirped pulse amplification (CPA) [6, 7, 8]. The use of the Ti:sapphire laser with CPA has dominated the field of ultrafast optics and spectroscopy since the beginning of 1990s. Its reliability and easiness to use have enabled many ultrafast experiments: the real-time observation and coherent control of ultrafast dynamics in chemical reactions such as nuclear motion [9], the control of chemical reaction [10], multiphoton absorption by engineered pulses [11], and the dissociation and recombination of chemical bonds [12]. These works on the ultrafast phenomena have been categorised as "femtochemistry" [13] and Prof. A. H. Zewail was awarded the Nobel prize for Chemistry in 1999 for his contribution to this field.

By the end of the 20th century, at last, further advances in the high-energy, ultrashort Ti:sapphire laser have broken through the barrier of the femtosecond time scale into the attosecond regime [14]. Attosecond pulse generation based on optical high-order harmonics [15, 16] has brought on a new field of the attosecond optics and enabled the investigation of the attosecond ultrafast phenomena. The real-time dynamics ranging from a few femtoseconds to many attoseconds include the X-ray-generated photoelectron emission [17], the real-time observation of Auger electron decay [18], and the generation of single attosecond pulses with a few-cycle carrier-envelope phase (CEP) stabilized laser system [19]. These works have formed a new field called as "attosecond physics" [20, 21]. Although successful attosecond experiments have been performed exclusively by use of Ti:sapphire laser systems, the limitation of the output energy from the Ti:sapphire amplifier followed by external broadening in the hollow-core fiber filled

with a noble gas prevents the extension of the cut-off energy of high harmonics, the generation of high-intensity attosecond pulses, and the shortening of attosecond pulses.

To overcome these difficulties, in this thesis, we apply a novel optical pulse amplification technique, optical parametric chirped-pulse amplification (OPCPA) [22, 23, 24, 25], to the amplification of few-cycle high-energy laser pulses. We also demonstrate preliminary high-field and ultrafast experiments with such laser systems. These experiments include the generation of visible supercontinuum by infrared pump pulses, a unique CEP detection based on an f-to-$3f$ nonlinear interferometry , and the generation of extreme ultraviolet optical high-harmonics with the photon energy of up to 250 eV.

The topics included in this thesis are summarized as follows

Chapter 1: Review of optical pulse amplification techniques: CPA, OPA, and OPCPA and system consideration about an OPCPA system.

Chapter 2: Implementation of a few-cycle, high-energy, near-infrared OPCPA system with electronic synchronization.

Chapter 3: Application of a reliable all-optical synchronization scheme to a few-cycle, high-repetition-rate, near-infrared OPCPA system.

Chapter 4: Implementation of a few-cycle, high-repetition-rate, infrared OPCPA system with optical synchronization.

Chapter 5: Applications of infrared few-cycle pulses:

1. Generation of visible supercontinuum and its application to an f-to-$3f$ nonlinear interferometry for carrier envelope phase (CEP) detection.

2. Generation of 250-eV optical high harmonics.

In the later sections of Chapter 1, we will introduce the fundamental concept of OPCPA in comparison to CPA and OPA, and consider the general OPCPA performance and its dependence on various parameters. In Chapter 2, we describe the construction of a terawatt-class, few-cycle, high-energy (low repetition rate) near-infrared (around 800 nm) laser system based on OPCPA [26]. In Chapter 3, a novel optical synchronization scheme without the use of electronics [27], is proposed and implemented in the OPCPA system. The optical synchronization scheme is realized by the home-made Nd:YLF regenerative amplifier. This concept is applied to the few-cycle, high-repetition-rate, near-infrared pulse generation based on OPCPA. In Chapter 4, we describe the development of an infrared OPCPA system that produces few-cycle, high-energy, high-repetition-rate infrared optical pulses using an optically synchronized Nd:YLF amplifier. In Chapter 5, the infrared OPCPA system is applied to the generation of visible supercontinuum and a novel f-to-$3f$ nonlinear interferometry with the generated white light. This experiment demonstrates self-stabilization of the CEP in difference frequency generation process and the preservation of the CEP in the parametric amplifier and the stretcher and compressor pair. Another application of the infrared driver to optical high-harmonic generation shows the production of extreme ultraviolet photons with energies above 250 eV in argon.

1.2 Optical pulse amplification techniques

In this section, several methods used for amplification of optical pulses are reviewed and compared. These methods include CPA [28, 7], optical parametric amplification (OPA) [29], and a newly emerging technique, OPCPA [30, 22]. We emphasize features concerning our primary goal: amplification of broadband optical pulses to the mJ level.

So far high-energy ultrafast laser pulses, a key tool for the ultrafast spectroscopy and attosecond spectroscopy, have been produced [31] exclusively by CPA in Ti:sapphire [3, 4, 5]. Furthermore few-cycle, high-energy laser pulse generation used for single attosecond pulse generation and time-resolved attosecond experiments [32] are realized by external broadening of the Ti:sapphire amplifier output pulse in a hollow fiber filled with a noble gas [33], and external pulse compression by use of chirped multilayer coated mirrors [34]. With this scheme, few-cycle, several-hundred-microjoule pulses can be obtained and are used as a driver source for the spectroscopic applications mentioned previously in Section 1.1. Such laser sources have resulted in remarkable progress in high-harmonic generation (HHG), attosecond pulse generation, and spectroscopy [20, 35, 36]. Demand for shorter attosecond pulse generation, a higher photon energy up to keV, and higher-energy attosecond pulses for the nonlinear optics in the X-ray calls for a further upgrade of current laser sources. The energy of few-cycle pulses is limited to less than the mJ level because of the damage to the hollow-core fiber used for spectral broadening and the substantial loss due to the strong ionization of the noble gas contained in the fiber. To scale up the energy of ultrashort pulses, we have to rely on a different technology.

Another amplification technique of few-cycle pulses is OPA. Soon after the demonstration of the first laser [1], lasers had been used for the investigation of optical nonlinear phenomena such as second-harmonic generation (SHG) [37], third-harmonic generation [38, 39] OPA [29], and optical parametric generation (OPG) [40]. In the early days, OPA and OPG have served mainly as sources for tunable radiation. However, later, optical parametric amplifiers have also been recognized as a promising broadband amplification device. Especially, parametric oscillators [41, 42] and amplifiers [43, 44, 45, 46] using borate crystals [47] and noncollinearly phase-matching optical parametric interaction (NOPI) [48, 49, 50] have resulted in extensive investigations in few-cycle pulse generation, and their applications to the ultrafast spectroscopy. Ultrashort optical pulse amplification relying on NOPA has produced few-cycle, energetic pulses [51], although so far the energy of the few-cycle pulses obtained by NOPA is limited to the microjoule range. This energy range is usually suitable for the low-order nonlinear spectroscopy but is not for high-field physics.

An alternative, newly emerging amplification technique, OPCPA, which combines advantages of CPA and OPA, was first demonstrated in 1986 [30] and successively in 1992 [22]. In these experiments, the energy of stretched seed pulses was increased substantially in an optical parametric amplifier pumped by high-energy, long pulses. The energetic stretched pulses were recompressed in a pulse compressor. This technique had been left unnoticed until I. N. Ross *et al.* [23] recognized its advantages, showing the possibility of the generation of ultrabroadband high-energy pulses with a 10-petawatt peak power. The advantages include broadband amplification enabled by either NOPA or degenerate OPA, less accumulation of nonlinear effects due to extremely high gain possible in a thin crystal in contrast to a Ti:sapphire laser with CPA [52],

a negligible thermal load on a nonlinear crystal, and flexibility and the tunability of the gain spectral range.

At the same time, however, there exist several difficulties such as lack of the pump energy storage (parametric process), amplified superfluorescence (ASF) [40, 53] analogous to the amplified spontaneous emission (ASE) in CPA, and strict phase-matching, whose direction is dependent on the seed wavelength and might result in the spatial dispersion of the amplified beam and additional difficulty in the alignment of the amplifier. Without the pump energy storage, one needs to synchronize the pump and seed pulses strictly. This disadvantage is closely linked to one of its advantages, negligible heat load on the crystal, because the parametric process enables the exchange of the energy only between optical waves overlapped in time and space without loading energy in an intermediary nonlinear crystal. The comparison between CPA in Ti:sapphire and OPCPA using a 532 nm pump laser and noncollinear phase-matching (NCPM) in β-barium borate (BBO) (detailed descriptions available in Sections 2.3 and 2.4) is summarized in Tab. 1.1. Obviously from the table, the gain bandwidth of OPCPA is much broader than CPA in Ti:sapphire thanks to NOPA. This is a quite important feature for our aim of few-cycle broadband pulse amplification. Another advantage of OPCPA is a larger aperture size available

	OPCPA (NOPA)	CPA in Ti:sapphire
Gain bandwidth	> 100 THz at 850 nm	~ 30 THz at 800 nm
Single-pass gain	~ 10^6	~ 10
B-integral ([54])	< 1.0	> 1.0
Thermal load on a crystal	Negligible	Critical in a high-power system
Energy storage	No (instantaneous)	Yes (~ μs)
Background emission	Amplified superfluorescence	Amplified spontaneous emission
Gain tunability	Flexible	Fixed by Ti:sapphire

Table 1.1: Comparison of CPA in Ti:sapphire and OPCPA based on NOPA in BBO

for its nonlinear crystal, compared to the small cross section of the hollow-core fiber, in which the spectrum of the pulses from the laser amplifier is broadened in order to support few-cycle pulse generation. A BBO crystal can be grown to about 20 mm × 20 mm under the current technology. Assuming a pump intensity of 10 GW/cm^2 and a pump pulse duration of 100 ps, a BBO can stand a 5-J pump pulse energy, which can be easily converted to a 1-J amplified signal pulse energy, resulting in a 100-terawatt peak power assuming the compressed pulse duration of 10 fs. This peak power is about 1000 times higher than the current highest peak-intensity of the few-cycle pulses produced by external broadening and subsequent pulse compression following CPA in Ti:sapphire.

In summary, several features of OPCPA are found to be advantageous for few-cycle, high-energy pulse generation compared to the standard technique of CPA in a Ti:sapphire laser and external broadening. In the next section, we describe considerations od an amplifier based on OPCPA.

1.3 Parameters in an OPCPA system and their mutual dependence

1.3.1 Introduction

In this section, theoretical and physical considerations and numerical simulations for the OPA process are given to the OPA process and the design of an OPCPA system. Specifically we describe the performance of an OPCPA system and its dependence on parameters such as the pump intensity and duration, the optical parametric gain, phase-mismatch, the length of a nonlinear crystal, and so on. In addition, the optimization of OPA conversion efficiency and output pulse stability will be discussed.

The OPA process is one of the second order nonlinear optical effects (three-wave parametric interactions) and its behaviors can be fully described with coupled-wave equations [55]. In the OPA process, two conditions, the energy conservation and phase-matching conditions, have to be satisfied. These two conditions can be expressed as

$$\omega_p = \omega_s + \omega_i, \tag{1.1}$$
$$k_p \simeq k_s + k_i, \tag{1.2}$$

where ω_j and k_j represent the angular frequency and the wave vector with suffixes $j = p, s,$ and i representing the pump, signal, and idler waves, respectively. These conditions are derived from the coupled-wave equations. The phase-matching condition does not need to be satisfied rigorously and can have certain tolerance determined by the length of the three-wave interaction L as

$$\Delta k \equiv k_p - k_s - k_i, \tag{1.3}$$
$$|\Delta k| L < \pi, \tag{1.4}$$

where Δk is the wave-vector mismatch among the three involving waves. For the derivation and examples of the coupled-wave equations for the three-wave interaction, readers are also referred to references [56, 57, 58, 59] and books [60, 61, 62, 63]. An advanced formula including the group-velocity mismatch effect is found in Refs. [64, 65, 66, 67, 68].

A simple form for the gain calculation of OPA can be derived from the analytical solution of the coupled-wave equations, assuming the slowly-varying-envelope approximation, flat top spatial and temporal profiles, and no pump depletion. The intensity gain G of OPA can be expressed as

$$G = 1 + (gL)^2 \left(\frac{\sinh(\alpha)}{\alpha} \right)^2, \tag{1.5}$$

with

$$g = 4\pi d_{\text{eff}} \sqrt{\frac{I_p}{2\varepsilon_0 n_p n_s n_i c \lambda_s \lambda_i}}, \tag{1.6}$$

$$\alpha = \sqrt{(gL)^2 - \left(\frac{\Delta kL}{2}\right)^2}, \tag{1.7}$$

where $\Delta kL \equiv (k_p - k_s - k_i)L$ is the scalar phase mismatch, L is the interaction length in a nonlinear crystal, d_{eff} is the effective second order nonlinear coefficient of the nonlinear crystal, I_p is the pump intensity, ε_0 is the vacuum permittivity, n_j is the refractive index for the pump $j = p$, signal $j = s$, and idler wave $j = i$, respectively, c is the velocity of light in vacuum, and λ_j is the wavelength of the signal $j = s$ and the idler wave $j = i$, respectively. G can be simplified to G' with the assumption of exact phase matching ($\Delta k = 0$) as

$$G' \simeq (gL)^2 \left(\frac{\sinh(gL)}{gL}\right)^2 = \sinh^2(gL). \tag{1.8}$$

From this simple expression for the parametric gain, we can derive the relationship between the pump intensity and the length of the crystal. As can be seen in Eq. 1.8, G' returns the same value, if gL is constant, and gL can be related to the pump intensity I_p and crystal length L as

$$gL \propto \sqrt{I_p}L. \tag{1.9}$$

Therefore, the OPA gain would be constant provided

$$\sqrt{I_p}L = \text{const.}. \tag{1.10}$$

For example, a 10 times less pump intensity can be compensated by the increase of the crystal thickness by 3.16 times ($= \sqrt{10}$ times) in order to achieve the same gain. Later in this section, these formulas will be used to describe the OPA process.

1.3.2 Pump pulse intensity, duration and OPA gain bandwidth

In this section, relationships between the pump pulse intensity, duration, and OPA gain bandwidth are analyzed. First of all, we need to find a relationship between the pump intensity and the pulse duration. Generally speaking, the damage threshold intensity of an optical material (for instance, fused silica) is inversely proportional to the square root of the pulse duration within a certain pulse duration range [69]. Usually, the anti-reflection (AR) coating on the crystal is weaker than the crystal material itself. Experimentally, a standard AR coating can stand safely the pulse intensity of 10 GW/cm² for 100-ps pulses (in our experiment, the damage threshold of the AR coating proves to be about 20-30 GW/cm² for 30-50 ps pulses). For following calculations, we will adopt typical pulse intensities of 1 GW/cm², 10 GW/cm², and 100 GW/cm² for simplicity. From the experimental result and the above relationship between the optical pulse

duration and the damage threshold intensity, to some extent, 1 GW/cm², 10 GW/cm², and 100 GW/cm² could be considered as the damage threshold intensities for 10-ns, 100-ps, and 1-ps pulses, respectively.

Let us look into Eqs. 1.5, 1.6, and 1.7. As discussed previously, to achieve the same gain for the lower pump intensity, the crystal length has to be increased. Longer crystal length decreases α in Eq. 1.7 because the phase-mismatch ΔkL increases, and, consequently, lowers the gain G. If exact phase matching is satisfied in the entire gain bandwidth, the gain bandwidth would not be altered provided Eq. 1.10 is fulfilled. However such an ideal case cannot be realized in broadband parametric amplification and, consequently, a finite amount of phase mismatch exists for some wavelengths and tends to decrease the gain, in contrast to the case of exact phase matching, even when Eq. 1.10 is satisfied.   Examples of gain curves in the case of NOPA pumped by 532
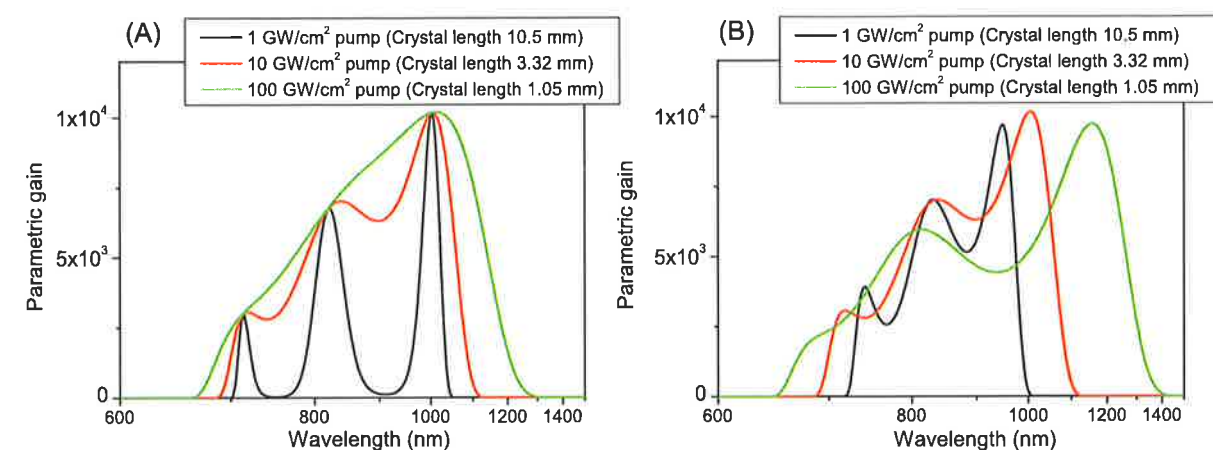
Figure 1.1: Relationship between the pump intensities and the OPA gain. (A): Calculated OPA gain curves with fixed parameters (noncollinearity angle and phase-matching angle) and three different pump intensities of 1 GW/cm² (black line), of 10 GW/cm² (red line), and of 100 GW/cm² (green line). A relative ratio of the crystal thicknesses is determined by the relation derived in Eq. 1.10. A total gain is arbitrarily chosen as 10^4 at the peak. (B): OPA gain curves with optimized parameters (noncollinearity angle and phase-matching angle) for a smooth gain spectrum at three different pump intensities of 1 GW/cm² (black line), of 10 GW/cm² (red line), and of 100 GW/cm² (green line).

nm radiation in a type I phase-matching BBO with three different pump intensities (a detailed description about NOPA and its gain calculation are available in Chapter 2) are shown in Fig. 1.1. In Fig. 1.1 (A), calculated OPA gain curves with fixed parameters (noncollinearity angle and phase-matching angle) and three different pump intensities of 1 GW/cm² (black line), of 10 GW/cm² (red line), and of 100 GW/cm² (green line) are shown. A relative ratio of the crystal thicknesses is determined from Eq. 1.10. A total gain is chosen as about 10^4 at the peak. In Fig. 1.1 (B), smoothed OPA gain curves with different optimized parameters (noncollinearity angle and phase-matching angle) and three different pump intensities of 1 GW/cm² (black line),

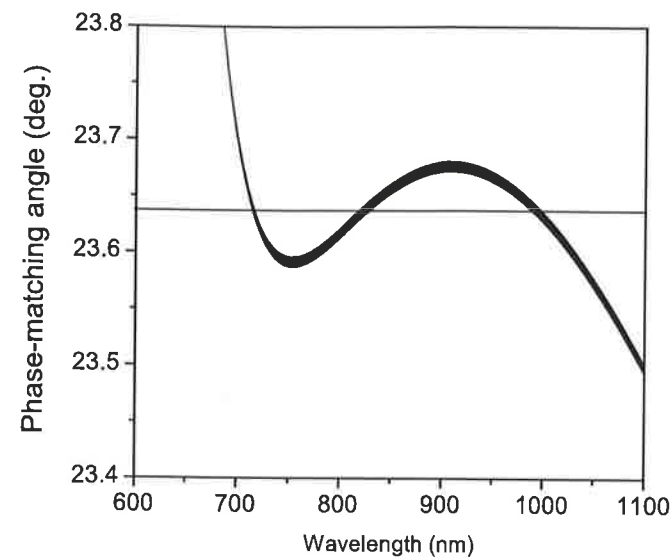Figure 1.2: Phase-matching region where a phase-mismatch is less than a certain value simulated with the same condition as the calculation plotted in Fig. 1.1 (A).

of 10 GW/cm^2 (red line), and of 100 GW/cm^2 (green line) are shown. Two conclusions can be drawn from these plots. One is that, even with the different pump intensity and crystal length, if the both parameters satisfy Eq. 1.10, the gain values at three peaks, where exact phase-matching is fulfilled, would be equal for three conditions. With the same calculation parameters for the gain shown in Fig. 1.1 (A), the behavior of phase-matching are plotted in Fig. 1.2. The phase-matching curve crosses 23.63° for three times where exact phase matching is achieved. The y-axis in Fig. 1.2 represents the angle between the optical axis of the nonlinear crystal and the pump beam propagation direction [70]. In the region other than the three points, finite phase mismatch results in a lower gain so that, to fill the gap between the three peaks in the gain curve, one needs to tune the parameters to obtain a smooth gain spectra for the lower pump intensity as shown in Fig 1.1 (B). The second conclusion is that the use of high pump intensity is preferable for the broadband amplification required for the few-cycle high-energy pulse generation, because the thin crystal does not accumulate phase mismatch, resulting in a relatively smooth gain spectrum such that a larger separation between the three gain peaks can be attempted to achieve a broader spectrum by the change of parameters as shown by the green line in Fig. 1.1 (B). However, as will be shown later, high pump intensity is not always preferable because of the resultant nonlinear effects and the timing-jitter problem arising from short pulse pumping. Deliberations on these issues will be presented later in this section.

1.3.3 B-integral, pump intensity, and gain

High-intensity short pulse generation and amplification always accompany inevitable nonlinear effects accumulated in the amplifier even with CPA, because of the high intensity of the amplified

stretched pulse [52]. As noted in Ref. [52], dependent on the amplifier design, a terawatt-class Ti:sapphire amplifier system exhibits a B-integral between 1 and 3. The definition of the B-integral from Ref. [54] is

$$B = \frac{2\pi}{\lambda_s} \int_0^L n_2 I_s(z) \mathrm{d}z, \tag{1.11}$$

where λ_s is the wavelength of the signal wave, L is the nonlinear crystal length, n_2 is the Kerr-effect nonlinear refractive index of the amplifier material, and $I_s(z)$ is the position-dependent signal intensity. The spatial and temporal beam quality of the amplified pulses is very important for the high-peak-intensity laser system and the recompression of the amplified stretched pulse down to the transform-limited pulse duration so that the amount of the B-integral is a key parameter for the design of a laser system. As listed in Tab. 1.1, I. N. Ross *et al.* [23, 71] pointed out that the value of B-integral could be kept less than 1 in a parametric amplifier, which is much less than that of a CPA system based on Ti:sapphire. This is because a high single-pass gain achievable in an OPA system requires less propagation in the nonlinear crystal than that in the laser crystal of a CPA system. However, the expression of the B-integral only includes self-nonlinear effects induced by the intense pulse itself, such as SPM [72, 73] and self-focusing [74, 75, 73]. This excludes cross-phase modulation (XPM) [76] between the strong pump, signal, and idler beams. However, because the OPA process is only possible by the spatial and temporal overlap between the pump and signal beams, the XPM should also be taken into account for the evaluation of the nonlinear effects accumulated during the OPA process. Therefore we propose a definition of a new B-integral B_{all} accounting for both nonlinear effects as

$$B_{all} = \frac{2\pi}{\lambda_s} \int_0^L n_2 \left(\gamma_{ps} I_p(z) + I_s(z) + \gamma_{si} I_i(z) \right) \mathrm{d}z, \tag{1.12}$$

where the same notations as in Eq. 1.11 are used and γ_{ps} and γ_{si} are the correction factors for a Kerr-effect nonlinear refractive index accounting for SPM and XPM.

γ_{ps} is equal to 2 when a pump polarization is parallel to a signal polarization and 2/3 when the pump polarization is orthogonal to the signal polarization [77], and the same applies for γ_{si} between the signal and idler beams. For example, γ_{ps} and γ_{si} are equals to 2/3 and 2 in the type I phase-matching condition, respectively. Because the pump intensity is usually much higher than that of the signal and idler, a B-integral B_{XPM}, which includes only the XPM effect between the pump and the signal, could result in a further simplified formula, from which one could derive the relationships between the B-integral, the pump intensity, and the crystal length. Using Eq.1.6 and Eq. 1.8, in a small-signal-gain regime, the relationship between the gain G' and the B_{XPM} can be derived as

$$G' = \sinh^2(gL) \simeq (gL)^2 \propto I_p L^2 \tag{1.13}$$

$$B_{XPM} \propto I_p L \propto \frac{G'}{L} \propto \sqrt{G' I_p} \tag{1.14}$$

where I_p is the pump intensity and L is the crystal length. From these equations, it can be concluded that the B-integral B_{XPM} is proportional to the gain and inversely proportional to the

length of the crystal. Alternatively, B-integral is proportional to the square root of the product of the gain and the pump intensity. The high pump intensity is preferable for the broadband gain but not good for the output beam quality due to the resultant high B-integral.

For a further detailed investigation, we performed a numerical simulation of the coupled-wave equations in order to demonstrate a more precise relationship and estimate a concrete value of the B-integral B_{all} including all possible effects. The B_{all} is calculated from the position-dependent values of pump, signal, and idler intensities given by a numerical solution to the coupled-wave equations. A 532-nm pump wave with the initial intensities of 1, 10, and 100 GW/cm^2 is used in a degenerate OPA, whose signal wavelength is 1064 nm, assuming exact phase-matching. The effective second-order nonlinear coefficient is chosen to be a typical value of 1 pm/V and the typical value of the Kerr-effect nonlinear refractive index coefficient n_2 is that of the fused silica (3.0×10^{-16} cm^2/W, see Appendix E for the value of the nonlinear refractive index). In Fig. 1.3 (A), the evolution of the pump (black line), signal (red line), and idler (green line) intensities are plotted with the propagation distance in the crystal. For this calculation we used a 10-GW/cm^2 pump intensity, a gain of 10^6, and a 5-kW/cm^2 input signal intensity. In Fig. 1.3 (B), using the same parameters, the calculated B-integral value (blue line) is plotted. The signal (red line) and idler (green line) are hardly distinguishable with each other. In the saturation regime, the slope of the B-integral increases because of the different values of $\gamma_{ps} = 2/3$ and $\gamma_{si} = 2$ in Eq. 1.12 although the sum of the three intensities is kept constant.
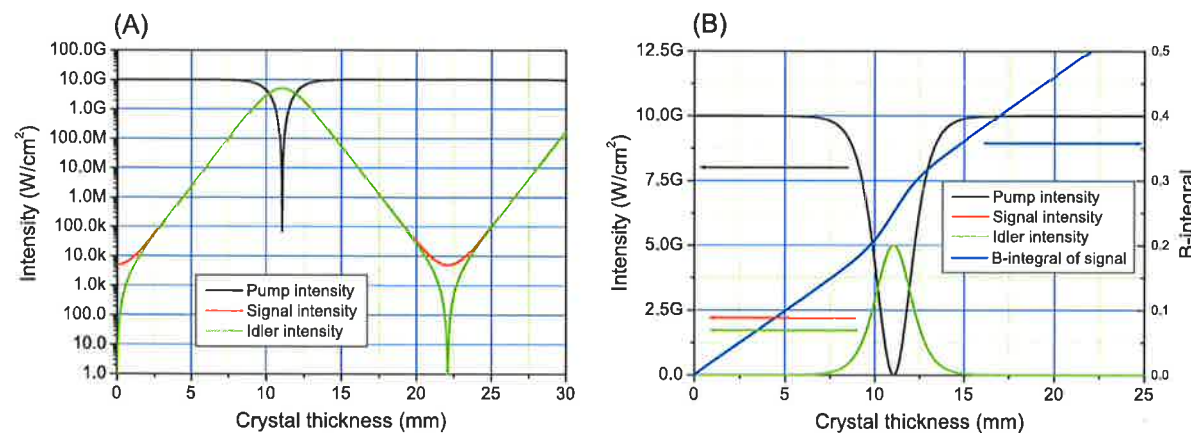

Figure 1.3: OPA process and simulated B-integral. (A): Evolution of pump (black line), signal (red line), and idler (green line) intensities. The 10-GW/cm^2 pump initial intensity, gain of 10^6, and the 5-kW/cm^2 signal initial intensity are used for the calculation. (B): Evolution of pump (black line) and signal (red line), which is hardly distinguishable from the idler (green line), intensities and a value of the B-integral (blue line). The 10-GW/cm^2 pump initial intensity, gain of 10^6, and the 5-kW/cm^2 signal initial intensity are used for the calculation.

Dependences of the B-integral value, which is obtained at the peak of the signal intensity, on the parametric gain is presented in Fig. 1.3 for three different pump intensities. From these plots, it
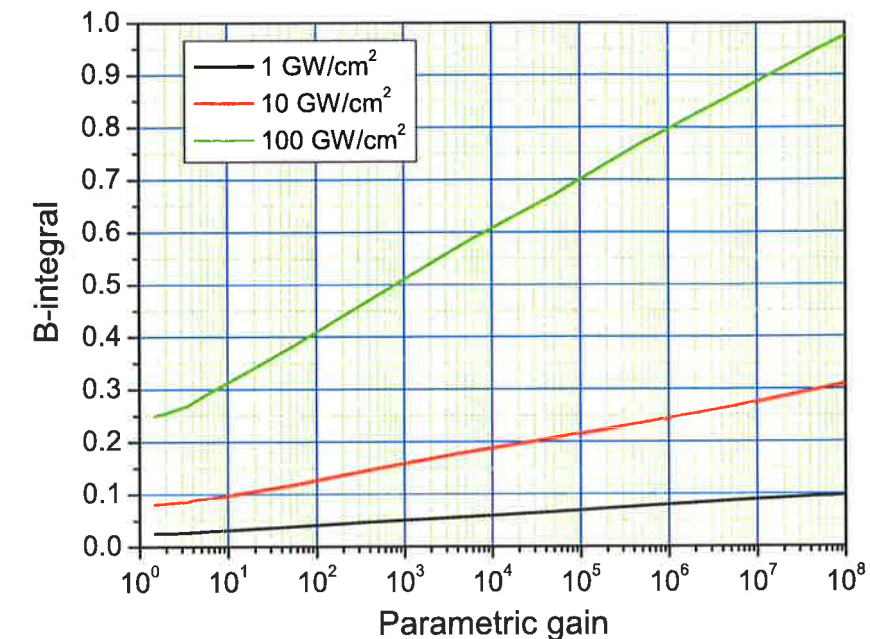
Figure 1.4: Dependencies of the B-integral on the parametric gain for three different pump intensities:1 (black line), 10 (red line), and 100 GW/cm^2 (green line). Note that the x-axis is represented in logarithmic scale.

is obvious that the B-integral in an OPA process is higher for the same gain with a higher pump intensity and a thinner crystal. The ratio of the B-integrals at the same gain value between the different intensities satisfies the relationship derived in Eq. 1.14. The B-integral is proportional to the square root of the pump intensity assuming the constant gain. When the total B-integral in a multi stage approach and a single stage for the same gain are compared, the total B-integral for the multiple stages becomes higher than the single stage. For example, 8 optical parametric amplifiers, where a gain of 10 in each stage is achieved, result in a total gain of 10^8 and a B-integral of $8 \times 0.32 = 2.56$, while a gain of 10^8 in a single stage leads to a B-integral of 0.97 with the pump intensity of 100 GW/cm^2. This means that a fewer-stage approach for the same amount of the gain is better in terms of nonlinear effect issues. However, from the practical and experimental point of view, the gain of 10^8 in a single stage has never been realized and the multi-amplifier-stage approach was experimentally verified to suppress more the ASF than a single stage approach.

1.3.4 Conversion efficiency, gain, initial signal intensity, and output stability

In this subsection, we investigate the dependence of energy conversion efficiency in the OPA process on the gain, the durations of the pump and signal pulses, and the input signal intensity. The stability of the amplified signal will be discussed. Although an exactly phase-matched op-

tical parametric amplifier using a pump beam with rectangular shapes in time and space gives maximum conversion efficiency equal to the quantum defect of one pump photon energy to one signal photon energy, however, Gaussian pump beams would be more practical for the experiment because an oscillator or regenerative amplifier cavity supports usually a Gaussian beam and it is easier to obtain and handle. We derive the energy conversion efficiency in an exactly phase-matched OPA using a Gaussian pump beam in time and space and Gaussian signal beam in space. The temporal shape of the signal pulse is assumed to be super-Gaussian. To simulate the conversion efficiency, the approximation of no pump depletion is invalid so that, in order to include the pump depletion, one has to solve numerically the coupled-wave equations. The coupled-wave equations are solved at every point in time and space. The pump and signal wavelengths are 1053 and 2106 nm, respectively. These wavelengths are used because the simulation was originally meant to account for the low efficiency in an infrared OPCPA system. The pump and signal intensities are 15 GW/cm^2 and 15 MW/cm^2, respectively, and a second-order nonlinear coefficient of 16 pm/V is chosen. For this numerical simulation, we used a 30-ps (FWHM),
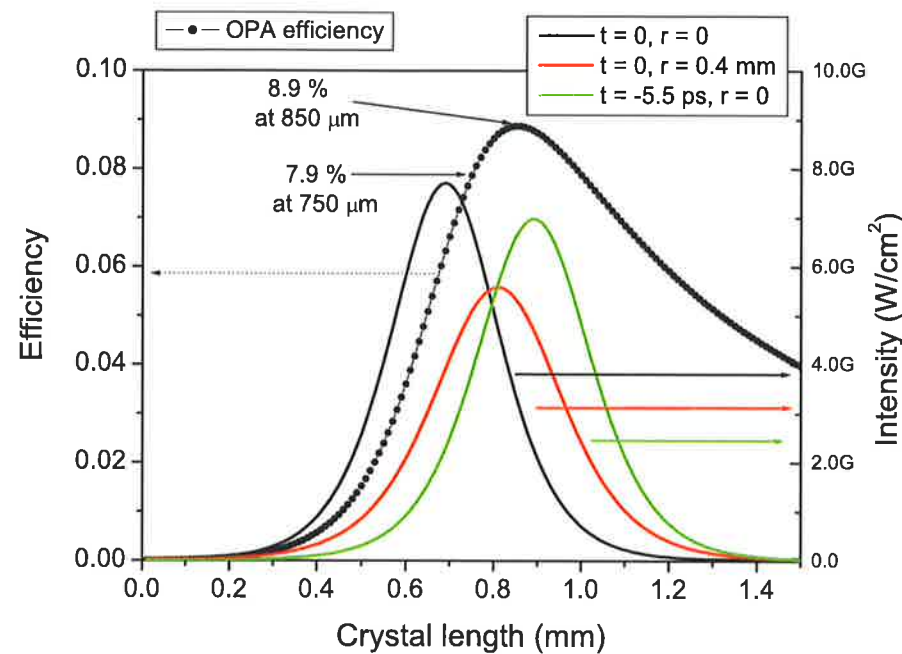

Figure 1.5: OPA conversion efficiency with Gaussian beams and signal intensities at several points. Black line: a signal intensity at time = 0 ps and the center of the signal beams in space, red line: a signal intensity at time = 0 ps and 0.4-mm-off from the center of the signal beams in space, green line: a signal intensity at time = -5.5 ps and the center of the signal beams in space, and black dotted-line: overall conversion efficiency.

1.2-mm-diameter (FWHM) pump beam and a 10-ps, 1.2-mm-diameter (FWHM) signal beam. In Fig. 1.5, amplified signal intensities at different points in time and space are plotted with black, red, and green solid lines. The black line shows a signal intensity at time = 0 ps and the center

of the signal beams in space. The red line shows a signal intensity at time = 0 ps and 0.4-mm-off from the center of the signal beams in space. The green line shows a signal intensity at time = -5.5 ps and the center of the signal beams in space. The signal intensity at each point in time and space saturates after different propagation lengths in the OPA crystal because, at each point, the intensity of the pump beam is different. This effect causes the decrease of overall conversion efficiency for the case of Gaussian pulses even with exact phase matching. Overall conversion efficiency obtained by the integration of all the spatial and temporal points is plotted with a black dotted-line in Fig. 1.5. In this case, the highest conversion efficiency is calculated as 8.9%. In
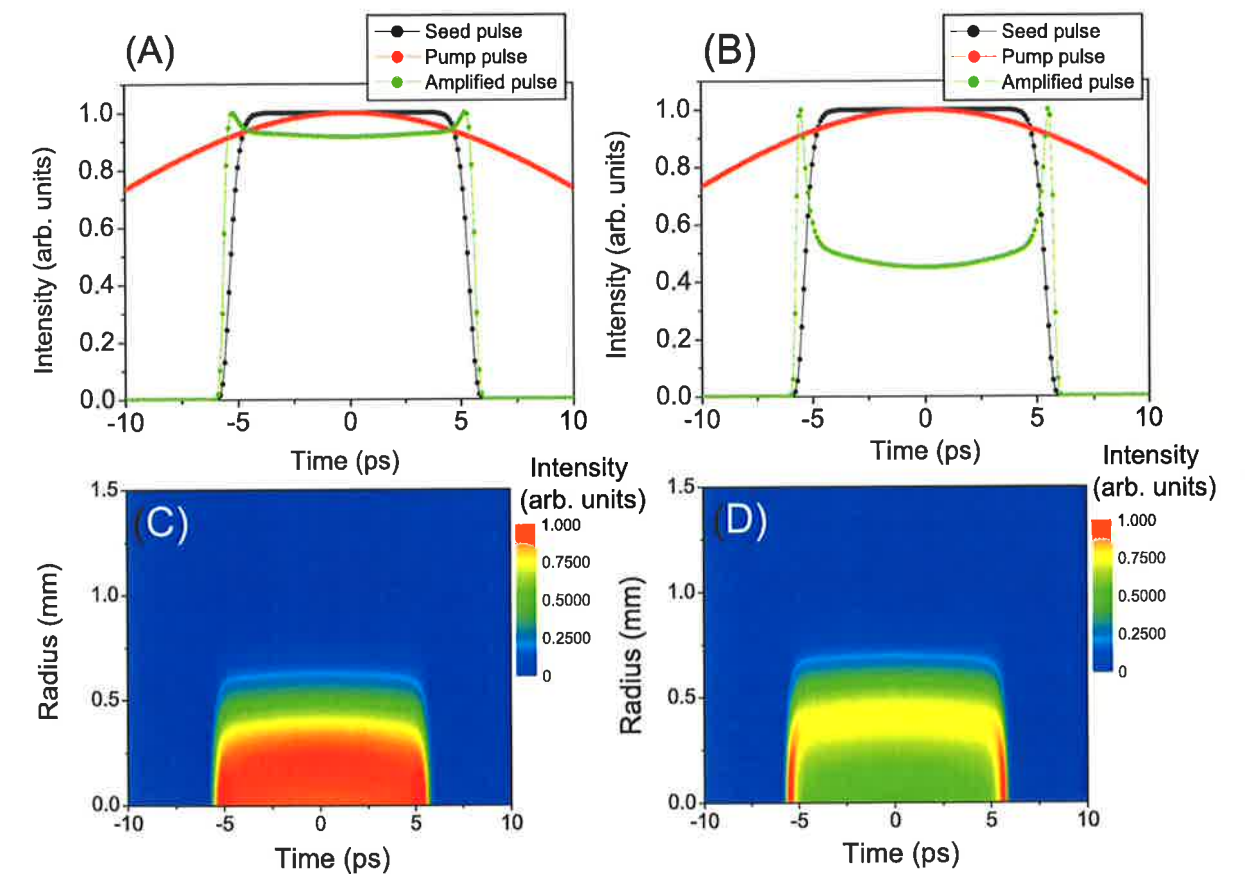
Figure 1.6: Pulse profile of the amplified signal after the propagation in the OPA crystal. (A): temporal profiles of an input signal (black line), an input pump (red line), and an amplified signal (green line) after 750-μm-long propagation in the OPA crystal and (B): temporal profiles of an input signal (black line), an input pump (red line), and an amplified signal (green line) after 850-μm-long propagation. (C): temporal and spatial profile of the amplified signal after 750-μm-long propagation and (D): temporal and spatial profile of the amplified signal after 850-μm-long propagation.

Fig. 1.6 (A), the temporal profiles of the input signal (black line), the input pump (red line), and the amplified signal (green line) after 750-μm-long propagation in the OPA crystal are shown. In Fig. 1.6 (B), the temporal profiles of the input signal (black line), the input pump (red line), and the amplified signal (green line) after 850-μm-long propagation are shown. Figs. 1.6 (C) and (D) show the spatial-temporal representation of the amplified signal after 750-μm-long propagation in the OPA crystal and after 850-μm-long propagation, respectively. Although the highest conversion efficiency of 8.9% can be obtained after 850-μm-long propagation in the OPA crystal, at this point, degradation of the pulse quality is clearly observed in Fig. 1.6 (B) and (D). Sharpe peaks in the temporal wing of the signal shown in Fig. 1.6 (B) would be converted to peaks in the amplified spectrum in the case of an OPCPA system, where the signal is temporally stretched. For example, despite the lower conversion efficiency of 7.9% after 750-μm-long propagation, the shape of the amplified signal is not altered dramatically and relatively high conversion efficiency could be achieved as shown in Fig. 1.6 (A) and (C). By the same method, we analyze the
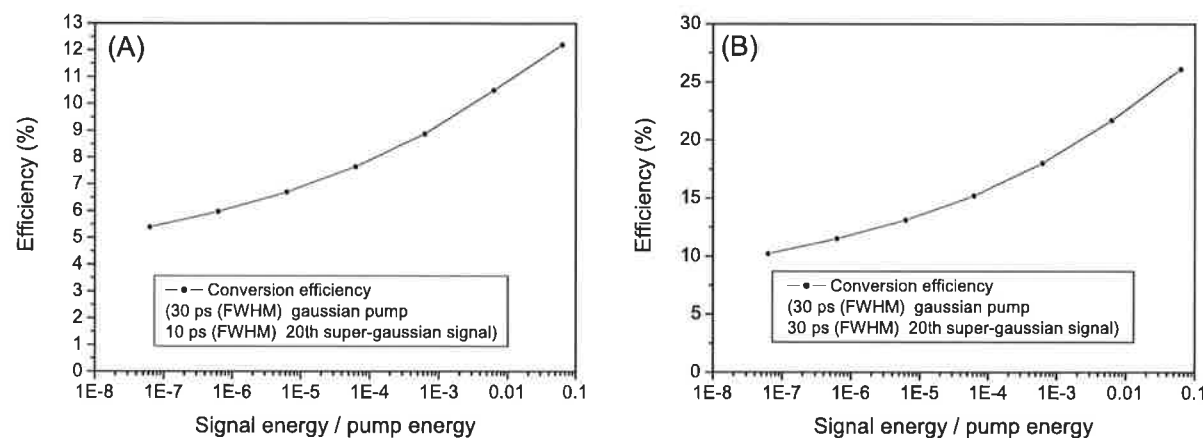

Figure 1.7: OPA efficiency dependence on the input signal intensity and the pulse duration ratio between the pump and signal pulses. (A): efficiency curve plotted with the energy ratio between the 10-ps input signal and 30-ps pump pulses. (B): efficiency curve plotted with the energy ratio between the 30-ps input signal and 30-ps pump pulses.

relationships between the conversion efficiency, the duration ratio between the pump and signal pulses, and the input signal intensity. In Fig. 1.7, the conversion efficiency of the parametric amplifier is plotted with the energy ratio between the input signal and pump pulses. The same parameters as those in the previous calculation are used except the pulse duration ratio. Fig. 1.7 (A) shows the conversion efficiency when the durations of the pump and signal pulses are 30 ps and 10 ps, respectively. Fig. 1.7 (B) shows conversion efficiency when the durations of the pump and signal pulses are 30 ps and 30 ps, respectively. Of course, a higher conversion efficiency is achieved when a longer signal pulse is used. The value obtained with the 30-ps-long pump and signal pulses corresponds well to the published reports of conversion efficiency [78, 79]. The efficiency increases with the increase of the input signal energy. A high conversion efficiency

is required always at the last stage in an amplifier chain so that the final OPA stage should be seeded with as energetic as possible a signal to achieve a high conversion efficiency.
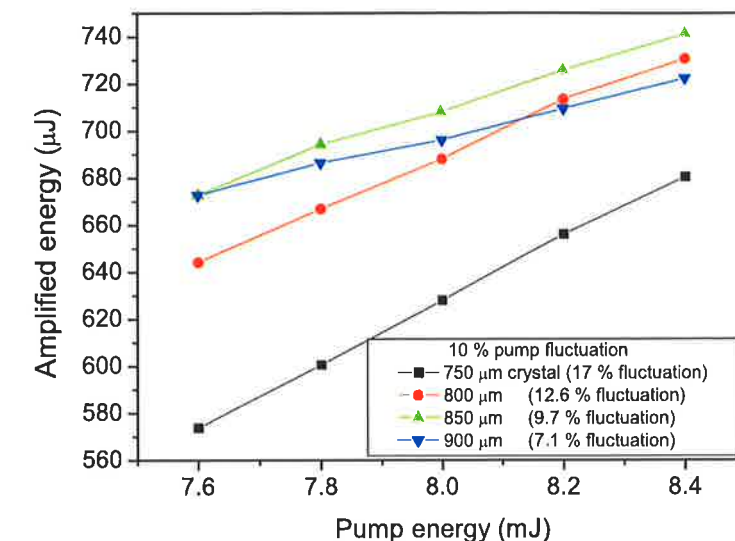

Figure 1.8: Amplified signal stability in OPA. Amplified signal energy fluctuation induced by 10% variation of the pump intensity with different crystal thicknesses: 750 μm (black line), 800 μm (red line), 850 μm (green line), and 900 μm (blue line).

At the same time, the stability of the amplified pulse energy is also an important topic. When rectangular spatial and temporal profiles of the pump and signal pulses were used in the parametric amplifier, the saturation and stabilization of an OPA output was demonstrated in Ref. [59]. This demonstration showed the stabilization of the amplified signal obtained after the OPA saturation.

Here the output pulse energy is calculated with several different pump pulse energies and several thicknesses of the crystal. Like previous calculations, Gaussian beams for the pump and signal are used. The pump pulse energy is changed by $\pm$ 5%. The calculated output energy is shown in Fig. 1.8. In Fig. 1.8, the OPA output pulse energies obtained after propagation of 750 μm (black line) in the OPA crystal, 800 μm (red line), 850 μm (green line), and 900 μm (blue line) are shown. Although plots show positive correlations, the slopes are different. In Fig. 1.8, the output energy after 850-μm-long propagation (green line) in the crystal fluctuates by 9.7% and this exhibits some stabilization effect of the output signal. However, as mentioned previously, the obtained output beam profile is not good for the practical use. The more acceptable output signal profile with the 750-μm-thick crystal would result in more fluctuation (17%) of the output energy than the pump energy.

In summary, we have investigated several characteristics of the OPA (OPCPA) process in detail. Several compromises have been found for the design and implementation of an OPCPA system. With these compromises, in the near-infrared OPCPA to be described in Chapter 2, we adopted a 60-ps pump pulse and a 40-50-ps-long stretched seed pulse. From these values, we

could expect a low B-integral, a relatively high conversion efficiency of more than 20%, and a broad OPA gain bandwidth. In the infrared OPCPA to be described in Chapter 4, we used a 40-ps pump pulse for OPA stages and a 10-ps-long stretched seed pulse. This was because we were unable to stretch the seed pulse to more than 10 ps with the only stretcher type available at the moment. In this case, broadband amplification would be easier to achieve but the conversion efficiency was lower than 10%.

Chapter 2

Generation of terawatt-class, few-cycle, near-infrared laser pulses by use of OPCPA

2.1   Introduction

In this chapter, a broadband optical parametric amplifier is designed and experimentally demonstrated. To obtain broadband amplification, NOPA scheme will be used in a parametric amplifier. We demonstrate the physical origin of a broadband parametric amplification mechanism based on NOPA by use of both mathematical procedure and numerical simulation. The choice of a nonlinear crystal is a key issue in an OPA experiment and will be carefully chosen with the help of numerical simulation. An OPCPA experiment requires the synchronization of pump and seed pulses. As seen in the last chapter, picosecond pump pulses seem to be optimum for our purpose, ultrabroadband high-energy pulse amplification. We use an electronic phase-lock loop (PLL) to synchronize two independent oscillators delivering picosecond pump and stretched seed pulses for an OPCPA system. This was, when it was constructed, the first trial to utilize repetition-rate-locked oscillators for an OPCPA system. We characterize the performance of a noncollinearly phase-matched optical parametric amplifier using a BBO crystal as a parametric crystal, a home-made broadband Ti:sapphire oscillator, a commercially available pump laser, and a simple pulse stretcher. After these test experiments, we describe the generation of few-cycle, terawatt-class, near-infrared optical pulses by use of a novel pulse stretcher and compressor pair in an OPCPA system.

2.2   Recent advances in ultrashort optical parametric devices

In this section we review recent advances in ultrashort laser pulse generation and amplification based on optical parametric interactions. Among many parametric interactions, noncollinearly phase-matched optical parametric interaction (NOPI), where three involving optical waves interact noncollinearly, exhibits unique features: extremely broadband parametric generation (superfluorescence) and amplification. Especially, the ultrabroadband parametric amplification of optical pulses is suitable for our purpose: the generation of few-cycle high-energy optical pulses.

As the first NOPI phenomenon, noncollinearly phase-matched OPG was observed in 1967, several years after the invention of the laser [48, 49]. In the early stage, researchers had made experimental demonstrations in many crystals and explained its physical mechanism [49]. In addition, a preliminary application of NOPI to walk-off compensation in optical parametric oscillation (OPO) was demonstrated[50]. However, its applications to ultrafast optics had needed to wait for reliable ultrafast laser sources, mainly Ti:sapphire laser, and new nonlinear crystals.

In 1985, a Chinese group invented a new crystal, BBO [47]. BBO has many interesting features such as the wide transparency range from infrared to ultraviolet, the large birefringence allowing many phase-matching conditions [80, 81], the relatively large nonlinear coefficient, and the high damage threshold. With the use of BBO and Ti:sapphire lasers, broadly tunable noncollinearly phase-matching OPOs [42, 41] were demonstrated owing to the cancellation of the spatial walk-off of an extraordinary pump beam from a signal beam. Although these demonstrations were not meant to generate broadband ultrashort optical pulses, soon, researchers had utilized the usefulness of BBO in NOPI for a broadband pulse generator and amplifier. The experimental demonstrations of broadband ultrashort OPOs with noncollinear phase-matching (NCPM) [82, 83] and broadband NOPAs resulting in the generation of energetic ultrashort pulses [44, 45, 46, 84, 85, 86], have been made shortly after the previous works mentioned above. Ultrashort energetic pulses, with the duration of from sub-20 down to a few femtoseconds, from a broadband NOPA have owed to also the compressible OPA seed source: supercontinuum (white light) [87, 72] generated by the self-phase modulation of an ultrashort pulse propagating a transparent material [88, 89]. Furthermore current state-of-art technologies ha resulted in the compression of a white-light-seeded NOPA by use of an adaptive optics following a parametric amplifier [90, 91, 92, 93]. The shortest pulse duration of 3.9 fs has been demonstrated so far by adaptive optics [94]. However relatively low output energy from a parametric amplifier, which does not exceed more than tens of μJ, limits the use of the generated ultrashort pulses in high-field experiments such as high-harmonic generation, attosecond pulse generation, and extremely nonlinear optics. To apply the advantage of an optical pulse amplifier based on a NOPA to high-field physics, we need to upscale output pulse energy from a parametric amplifier. The concept of NOPA, combined with the chirped-pulse amplification technique (noncollinearly phase-matched optical parametric chirped-pulse amplification (NOPCPA)), is one of quite promising schemes for a future few-cycle high-energy optical pulse generator.

In the next section, we will describe the physical mechanism of broadband phase-matching and resultant amplification and a choice of a nonlinear optical crystal.

2.3   Physics of noncollinearly phase-matched parametric interaction

In this section, we describe the physics of a NOPI phenomenon. This makes clear the physical origin of broadband NCPM compared to a standard collinear interaction.

As mentioned in Section 1.3, the two conditions, the energy conservation and phase-matching conditions, have to be satisfied to achieve efficient parametric interaction. These conditions are

represented in Eqs. 1.1 and 1.2. Whereas the energy conservation condition is automatically fulfilled in a parametric process, the phase-matching condition needs to be satisfied by use of several techniques: temperature-controlled phase-matching [40, 95] (typically used with non-critical phase-matching), angle-tuned phase-matching, and quasi-phase-matching. In this thesis, we used only type I phase-matching (angle-tuned phase-matching), in which a pump beam propagates as an extra-ordinary wave in a negative uniaxial crystal and seed and idler beams propagate as ordinary waves. This is because another type of phase-matching, type II phase-matching, does not provide broadband amplification as type I phase-matching does. In Fig 2.1, the illustration of pump, signal, and idler beams in NCPM and collinear phase-matching and their parameters are presented.
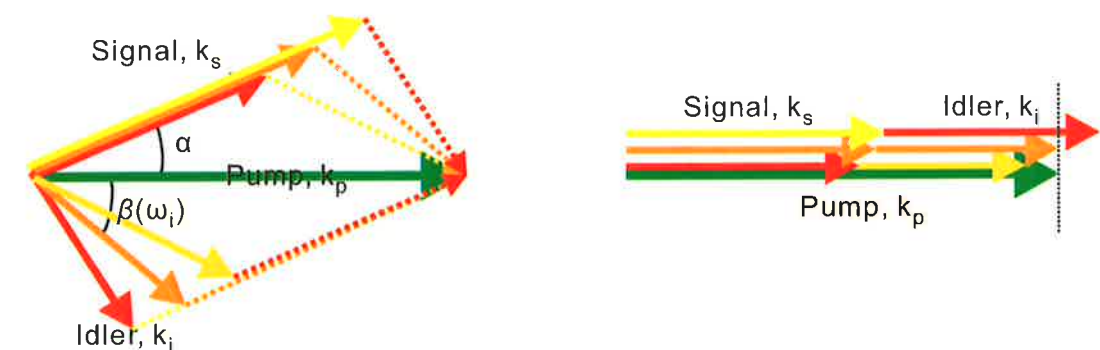

Figure 2.1: Noncollinear phase-matching and its parameters (left) and collinear phase-matching (right).

First of all, angular-frequency dependent phase mismatch in the case of collinear parametric interaction can be expressed as

$$\Delta k_c(\omega_s, \omega_i (\equiv \omega_p - \omega_s)) \equiv k_{cp} - k_{cs}(\omega_s) - k_{ci}(\omega_i), \qquad (2.1)$$

where k_{cp}, k_{cs}, and k_{ci} are the wave vectors of the pump, signal, and idler beams, respectively and ω_p, ω_s, and ω_i are the angular frequencies of the pump, signal, and idler beams, respectively. In this subsection, the pump wave is assumed to be monochromatic so that $\omega_p = $ const.. Here the derivative of the idler wave vector respect to the signal angular frequency can be written as

$$\frac{\partial k_{ci}(\omega_i)}{\partial \omega_s} = \frac{\partial (\omega_p - \omega_s)}{\partial \omega_s} \frac{\partial k_{ci}(\omega_i)}{\partial \omega_i} = -\frac{\partial k_{ci}(\omega_i)}{\partial \omega_i}. \qquad (2.2)$$

Because only one parameter, signal angular frequency, is independent, Eq. 2.1 can be simplified as

$$\Delta k_c(\omega) \equiv k_{cp} - k_{cs}(\omega) - k_{ci}(\omega), \qquad (2.3)$$

by use of $\omega_s = \omega$. Using Eqs. 2.2, 2.3, $\omega_0 \equiv \omega_{s0}$, and $\omega = \omega_0 + \Delta\omega$, the Taylor expansion of the phase-mismatch (Eq. 2.1) around the central angular frequency ω_0 can be written as

$$\Delta k_c(\omega_0 + \Delta\omega) = k_{cp} - k_{cs}(\omega_0) - k_{ci}(\omega_0) - \left(\frac{\partial k_{cs}}{\partial \omega}\bigg|_0 - \frac{\partial k_{ci}}{\partial \omega}\bigg|_0\right)\Delta\omega$$

$$- \frac{1}{2}\left(\frac{\partial^2 k_{cs}}{\partial \omega^2}\bigg|_0 + \frac{\partial^2 k_{ci}}{\partial \omega^2}\bigg|_0\right)(\Delta\omega)^2 + \mathcal{O}\left\{(\Delta\omega)^3\right\}, \tag{2.4}$$

$$= -\left(\frac{1}{v_{gs}(\omega_0)} - \frac{1}{v_{gi}(\omega_0)}\right)\Delta\omega - \frac{1}{2}\left(\frac{\partial^2 k_{cs}}{\partial \omega^2}\bigg|_0 + \frac{\partial^2 k_{ci}}{\partial \omega^2}\bigg|_0\right)(\Delta\omega)^2$$

$$+ \mathcal{O}\left\{(\Delta\omega)^3\right\}, \tag{2.5}$$

where exact phase-matching is assumed to be fulfilled at a signal central angular frequency ω_0 as

$$\Delta k_c(\omega_0,) = k_{cp} - k_{cs}(\omega_0) - k_{ci}(\omega_0) = 0. \tag{2.6}$$

The group velocities of the signal and idler waves at the central angular frequency

$$v_{gs}(\omega_s) \equiv \left(\frac{\partial k_{cs}}{\partial \omega_s}\right)^{-1} \text{ and} \tag{2.7}$$

$$v_{gi}(\omega_i) \equiv \left(\frac{\partial k_{ci}}{\partial \omega_i}\right)^{-1}, \tag{2.8}$$

are used for simplicity, respectively. From Eq. 2.5, the phase-mismatch linearly varies with the angular frequency owing to the group-velocity mismatch (GVM) between the signal and idler waves at the central frequency. Group-velocity mismatch (GVM) becomes zero in the case of degenerate OPA, where signal and idler wavelengths are identical, so that phase-mismatch in degenerate OPA would have parabolic dependence on an angular frequency. Therefore degenerate OPA could provide broader phase-matching and, to some extent, broader parametric gain bandwidth.

We apply the same mathematical procedure to NOPA phase-mismatch. We demonstrate a NOPI geometry with new parameters, noncollinearities between the pump and signal beams and the pump and idler beams, resulting in the cancellation of not only a first-order coefficient (GVM) but also a second-order coefficient. Detailed discussions about the cancellation of GVM are available in some articles [96, 44, 97] and another indication about "polychromatic phase matching" was made in Ref. [98] without mentioning to its physical origin. For practical use, the spatial dispersion of the seed beam would not be desirable and will be set zero. Therefore the noncollinearity angle between the pump and signal beams $\alpha(\omega) = \text{const.}(\equiv \alpha_0)$ is constant in angular frequency. We define the phase-mismatches perpendicular and parallel to the direction of the pump

$$k_\perp(\omega) \equiv k_s(\omega)\sin\alpha_0 - k_i(\omega)\sin\beta(\omega), \tag{2.9}$$

$$k_\parallel(\omega) \equiv k_p - k_s(\omega)\cos\alpha_0 - k_i(\omega)\cos\beta(\omega), \tag{2.10}$$

respectively. Assuming exact phase-matching in both directions at the central frequency as

$$k_\perp(\omega_0) \equiv k_s(\omega_0)\sin\alpha_0 - k_i(\omega_0)\sin\beta(\omega_0), \tag{2.11}$$

$$k_\parallel(\omega_0) \equiv k_p - k_s(\omega_0)\cos\alpha_0 - k_i(\omega_0)\cos\beta(\omega_0). \tag{2.12}$$

The first-order coefficients of the Taylor expansions of Eqs. 2.9 and 2.10 around the central angular frequency ω_0 become

$$k_\perp^{(1)}(\omega_0) = \left(\frac{\partial k_s(\omega)}{\partial \omega}\right)\bigg|_0 \sin\alpha_0 + \left(\frac{\partial k_i(\omega)}{\partial \omega}\right)\bigg|_0 \sin\beta(\omega_0)$$

$$+ k_i(\omega_0)\cos\beta(\omega_0)\left(\frac{\partial \beta(\omega)}{\partial \omega}\right)\bigg|_0, \tag{2.13}$$

$$k_\parallel^{(1)}(\omega_0) = -\left(\frac{\partial k_s(\omega)}{\partial \omega}\right)\bigg|_0 \cos\alpha_0 + \left(\frac{\partial k_i(\omega)}{\partial \omega}\right)\bigg|_0 \cos\beta(\omega_0)$$

$$- k_i(\omega_0)\sin\beta(\omega_0)\left(\frac{\partial \beta(\omega)}{\partial \omega}\right)\bigg|_0. \tag{2.14}$$

Eqs. 2.13 and 2.14 are simplified as

$$k_\perp^{(1)}(\omega_0) = \frac{\sin\alpha_0}{v_{gs}(\omega_0)} + \frac{\sin\beta(\omega_0)}{v_{gi}(\omega_0)} + k_i(\omega_0)\cos\beta(\omega_0)\left(\frac{\partial \beta(\omega)}{\partial \omega}\right)\bigg|_0, \tag{2.15}$$

$$k_\parallel^{(1)}(\omega_0) = -\frac{\cos\alpha_0}{v_{gs}(\omega_0)} + \frac{\cos\beta(\omega_0)}{v_{gi}(\omega_0)} - k_i(\omega_0)\sin\beta(\omega_0)\left(\frac{\partial \beta(\omega)}{\partial \omega}\right)\bigg|_0. \tag{2.16}$$

The first-order coefficients of the Taylor expansions become zero as

$$k_\perp^{(1)}(\omega_0) = 0, \tag{2.17}$$

$$k_\parallel^{(1)}(\omega_0) = 0, \tag{2.18}$$

provided

$$\frac{\cos(\alpha_0 + \beta(\omega_0))}{v_{gs}(\omega_0)} = \frac{1}{v_{gi}(\omega_0)}, \tag{2.19}$$

$$\left(\frac{\partial \beta(\omega)}{\partial \omega}\right)\bigg|_0 = -\frac{\tan(\alpha_0 + \beta(\omega_0))}{k_i(\omega_0)v_{gi}(\omega_0)}. \tag{2.20}$$

From another point of view, assuming Eq. 2.20, Eqs. 2.9 and 2.10 are expressed as

$$k_\perp(\omega_0 + \Delta\omega) = -\cos(\alpha_0)\left(\frac{1}{v_{gs}(\omega_0)} - \frac{1}{v_{gs}(\omega_0)\cos(\alpha_0 + \beta(\omega_0))}\right)\Delta\omega$$

$$+ \mathcal{O}\left\{(\Delta\omega)^2\right\}, \tag{2.21}$$

$$k_\parallel(\omega_0 + \Delta\omega) = \sin(\alpha_0)\left(\frac{1}{v_{gs}(\omega_0)} - \frac{1}{v_{gs}(\omega_0)\cos(\alpha_0 + \beta(\omega_0))}\right)\Delta\omega$$

$$+ \mathcal{O}\left\{(\Delta\omega)^2\right\}. \tag{2.22}$$

These equations demonstrate the cancellation of the first-order coefficients of the Taylor expansions, when Eqs. 2.19 and 2.20 are satisfied. The GVM between the signal and idler waves in the direction of the signal beam is an essential point to obtain broadband phase-matching in the case of NOPI. From Eqs. 2.9 and 2.20, one can determine the noncollinearity angle α_0, assuming $\sin(\alpha_0) \simeq \alpha_0$, as

$$\alpha_0 = \arccos\left(\frac{v_{gs}(\omega)}{v_{gi}(\omega)}\right)\left\{1 + \frac{k_s(\omega)}{k_i(\omega)}\right\}^{-1}. \tag{2.23}$$

As an example, we numerically simulate the noncollinearity angle using BBO refractive indices presented in Ref. [80, 99] and in Eqs. A.1 and A.2 in Appendix A. Fig. 2.2 shows the frequency-dependent noncollinearity angle calculated from Eq. 2.23, assuming the pump wavelength of 532 nm. As it follows from Fig. 2.2, the noncollinearity angle shows parabolic dependence
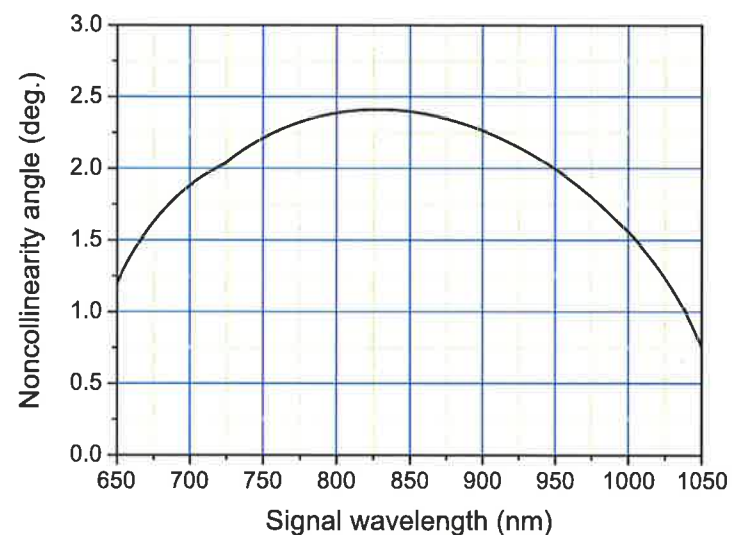

Figure 2.2: Noncollinearity angles optimized for lateral phase-matching and GVM

on the signal wavelength and has the plateau around 825 nm at 2.4°. The optimum value of a noncollinearity angle can be calculated by this method and, at the same time, the value of GVM is expected to be small in the wide spectral range around the plateau so that broadband amplification can be expected in this spectral range.

We further proceed the Taylor expansions to a second-order term. After several algebraic manipulations, we obtain the following formula for the second-order coefficients, $k_\perp^{(2)}$ and $k_\parallel^{(2)}$,

as

$$k_\perp^{(2)}(\omega_0) = \left(\frac{\partial^2 k_s(\omega)}{\partial \omega^2}\right)\bigg|_0 \sin\alpha_0 - \left(\frac{\partial^2 k_i(\omega)}{\partial \omega^2}\right)\bigg|_0 \sin\beta(\omega_0)$$
$$- 2\left(\frac{\partial k_i(\omega)}{\partial \omega}\right)\bigg|_0 \left(\frac{\partial \beta(\omega)}{\partial \omega}\right)\bigg|_0 \cos\beta(\omega_0) + k_i(\omega_0)\left\{\left(\frac{\partial \beta(\omega)}{\partial \omega}\right)\bigg|_0\right\}^2 \sin\beta(\omega_0)$$
$$- k_i(\omega_0)\left(\frac{\partial^2 \beta(\omega)}{\partial \omega^2}\right)\bigg|_0 \cos\beta(\omega_0), \tag{2.24}$$

$$k_\parallel^{(2)}(\omega_0) = -\left(\frac{\partial^2 k_s(\omega)}{\partial \omega^2}\right)\bigg|_0 \cos\alpha_0 - \left(\frac{\partial^2 k_i(\omega)}{\partial \omega^2}\right)\bigg|_0 \cos\beta(\omega_0)$$
$$+ 2\left(\frac{\partial k_i(\omega)}{\partial \omega}\right)\bigg|_0 \left(\frac{\partial \beta(\omega)}{\partial \omega}\right)\bigg|_0 \sin\beta(\omega_0) + k_i(\omega_0)\left\{\left(\frac{\partial \beta(\omega)}{\partial \omega}\right)\bigg|_0\right\}^2 \cos\beta(\omega_0)$$
$$+ k_i(\omega_0)\left(\frac{\partial^2 \beta(\omega)}{\partial \omega^2}\right)\bigg|_0 \sin\beta(\omega_0). \tag{2.25}$$

Equalizing $k_\perp^{(2)}(\omega_0)$ and $k_\parallel^{(2)}(\omega_0)$ to zero, and cancelling $\left(\frac{\partial^2 \beta(\omega)}{\partial \omega^2}\right)\bigg|_0$, these equations can be expressed by a simpler form

$$0 = -\left(\frac{\partial^2 k_s(\omega)}{\partial \omega^2}\right)\bigg|_0 \cos(\alpha_0 + \beta(\omega_0)) - \left(\frac{\partial^2 k_i(\omega)}{\partial \omega^2}\right)\bigg|_0 + k_i(\omega_0)\left\{\left(\frac{\partial \beta(\omega)}{\partial \omega}\right)\bigg|_0\right\}^2. \tag{2.26}$$

Using Eq. 2.20, one can derive the formula excluding any angular dispersion term as

$$0 = \underbrace{-\left(\frac{\partial^2 k_s(\omega)}{\partial \omega^2}\right)\bigg|_0 \cos(\alpha_0 + \beta(\omega_0))}_{A} \underbrace{- \left(\frac{\partial^2 k_i(\omega)}{\partial \omega^2}\right)\bigg|_0}_{B} + \underbrace{\frac{\tan^2(\alpha_0 + \beta(\omega_0))}{k_i(\omega_0)v_{gi}^2(\omega_0)}}_{C}. \tag{2.27}$$

Because further simplification seems to be impossible, we numerically evaluate the right three terms (A, B, and C) of Eq. 2.27. In Fig. 2.3, the calculated values of the first term (A in Eq. 2.27, red line), the second term (B in Eq. 2.27, green line), the third term (C in Eq. 2.27, blue line), and their sum (black line) are plotted. For this calculation, we used a 532 nm extraordinary pump wave. In Fig. 2.3, it can be clearly seen that the black line, the sum of the three terms, crosses zero around 827 nm. At this signal wavelength, the second-order coefficients of the phase-mismatch disappear and phase-mismatch shows cubic dependence around 827 nm. This is a unique feature in NOPI and extremely broad parametric amplification can be expected around this region. Actually, this wavelength range coincides to the central wavelength of the plateau of the noncollinearity angle in Fig. 2.2.

In summary, we analyzed the NOPI and collinear phase-matching interactions (degenerate interaction) and demonstrated the physical origin of the broadband phase-matching in the case of the degenerate interaction and the NOPI. In the next section, considerations about the choice of a nonlinear crystal to be used in an OPCPA system and detailed calculations of a gain bandwidth in NOPA will be carried out to envisage important parameters for the construction of an OPCPA system.
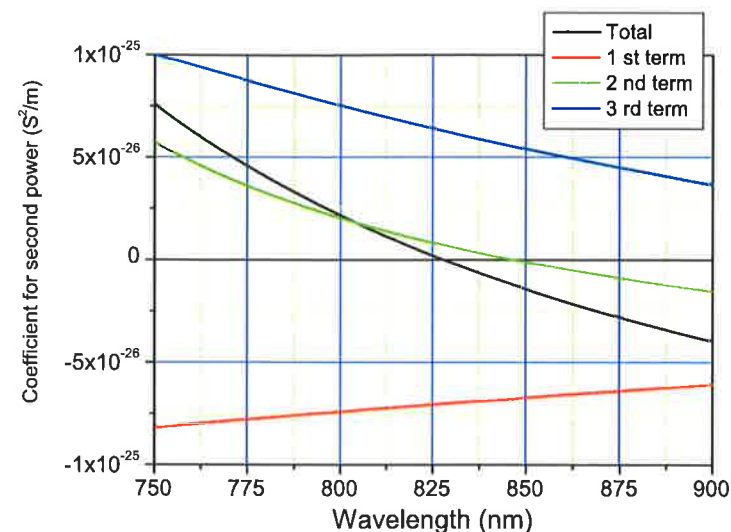
Figure 2.3: Plot of three terms (first term (A): red line, second term (B): green line, and third term (C): blue line) of Eq. 2.27 and their summation (black line) showing the cancellation of second-order phase-mismatch around 827 nm in the case of the NOPI in the BBO crystal. A x-axis represents the signal wavelength and pump wavelength is chosen as 532 nm.

2.4   NOPA and choice of its crystal

In this section, an OPA crystal for a NOPCPA system will be selected out from many crystals. Frequently used crystals for ultrashort pulse generation are mainly borate crystals including BBO, Lithium Triborate (LBO), and Cesium Lithium Borate (CLBO) because of several reasons such as high damage threshold, wide transparency range, short-wavelength absorption edge in the ultraviolet, high second order nonlinear coefficient, large birefringence, and relatively large aperture available. The disadvantage of the borate crystals is its low resistance to humidity, especially, CLBO. Other well-known crystals such as AgGaSe (AgGaS), KTP (KTA), KDP and $LiNbO_3$ (KNbO₃) have potentials for OPA applications and are even used for ultrafast pulse generation, mainly, in the infrared. AgGaSe, KTP, and $LiNbO_3$ have long-wavelength absorption edges around 710, 350, and 330 nm, respectively. Therefore this long-wavelength absorption restricts their use in the parametric amplifier pumped by visible intense pulses at 532 nm. because of problems of the linear and two-photon absorption of strong pump radiation. Also KTP (KTA) is not used usually for type I phase-matching because of its small second order nonlinear coefficient for this phase-matching. KDP and DKDP are good candidates because of short-wavelength absorption edge in the deep UV and its available large aperture size. However these crystals do not have enough transparency in the near infrared so that amplification of shorter wavelengths than 800 nm is difficult when a 532-nm laser pulse is used as a pump pulse. Therefore, for our purpose, only two borate crystals, BBO and LBO, remain as a candidate because CLBO is too deliquescent to handle in a normal laboratory environment. We compare the properties and features of BBO and LBO. The NCPM curves with BBO and LBO pumped by a 532-nm
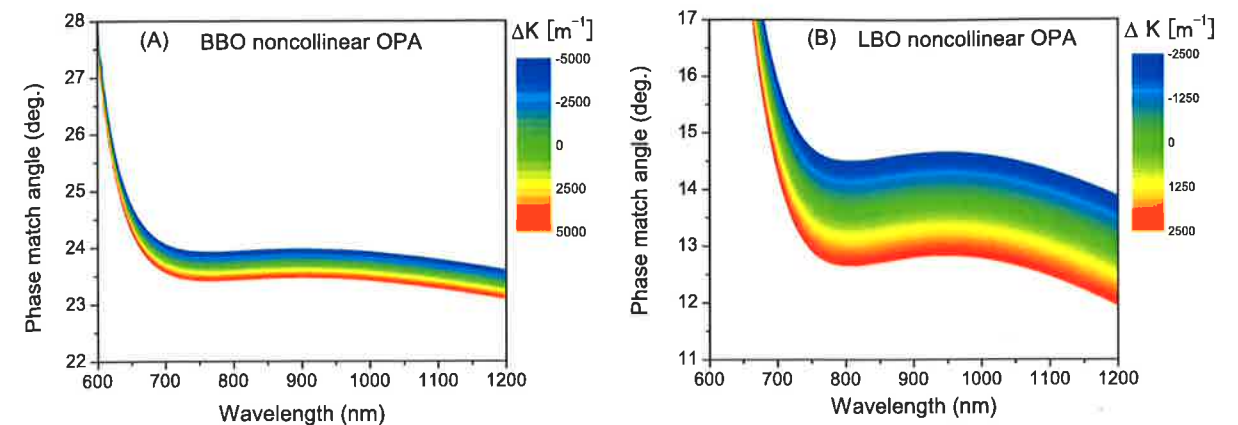
Figure 2.4: Phase-matching curves in the NOPI for the BBO (A) and LBO (B) crystals pumped by a 532-nm monochromatic wave.

monochromatic wave are shown in Fig. 2.4 (A) and (B), respectively. Parameters are chosen such that the flat phase-matching curves are obtained. Two conclusions can be drawn from these curves. The first conclusion is that the flat phase-matching for BBO lies in the shorter wavelength range than for LBO. This difference is important for our purpose because our broadband Ti:sapphire seed oscillator has a spectrum from 650 to 1000 nm and this oscillator spectrum is better overlapped with the phase-matching curve of BBO than LBO. The second conclusion is that the phase-matching curve of LBO has the wider acceptance angle than BBO. Wide angle acceptance is an attractive feature because narrow angle acceptance might result in the drop of pump-signal conversion efficiency and the spatial chirp (non-uniform beam profile for each wavelength) [100]. Notice that the color scale of the z-axis of BBO and LBO plots are two times different because the second-order nonlinear coefficient of LBO is two times lower than of BBO and therefore two-times longer interaction is required for LBO than BBO in order to obtain the same amount of gain. We numerically simulate the gain curves of noncollinearly phase-matched parametric amplifiers based on LBO and BBO. We use the formula for the intensity gain calculation shown in Eq. 1.5. The beam geometry and the parameters are found in Fig. 2.1 and the amount of phase-mismatch can be obtained by Eqs. 2.9 and 2.10. From Eqs. 2.9, the noncollinearity angle α_0 between pump and signal beams determines the frequency-dependent noncollinearity angle $\beta(\omega)$ of an idler beam. The obtained α_0 and $\beta(\omega)$ are used for the calculation of the phase-mismatch 2.10 parallel to a pump beam direction. The refractive indices of LBO and BBO used in this calculation are available in Eqs. A.1, A.2, A.5, A.6, and A.7 in Appendix A. Fig. 2.5 plots the spectrum of a home-made Ti:sapphire oscillator (black line) and calculated NOPA gain spectra for BBO (red line) and for LBO (green line). The parameters used for these calculations are, the common pump intensity I_p: 10 GW/cm², the effective second-order nonlinear coefficient d_{eff}: 2.0 pm/V for BBO and 1.0 pm/V for LBO [99, 101], the interaction length L: 4.0 mm for BBO and 7.4 mm for LBO, the signal noncollinearity angle α_0: 2.28° for BBO and 1.3° for LBO, and the phase-matching angle, which is the angle from an optical axis
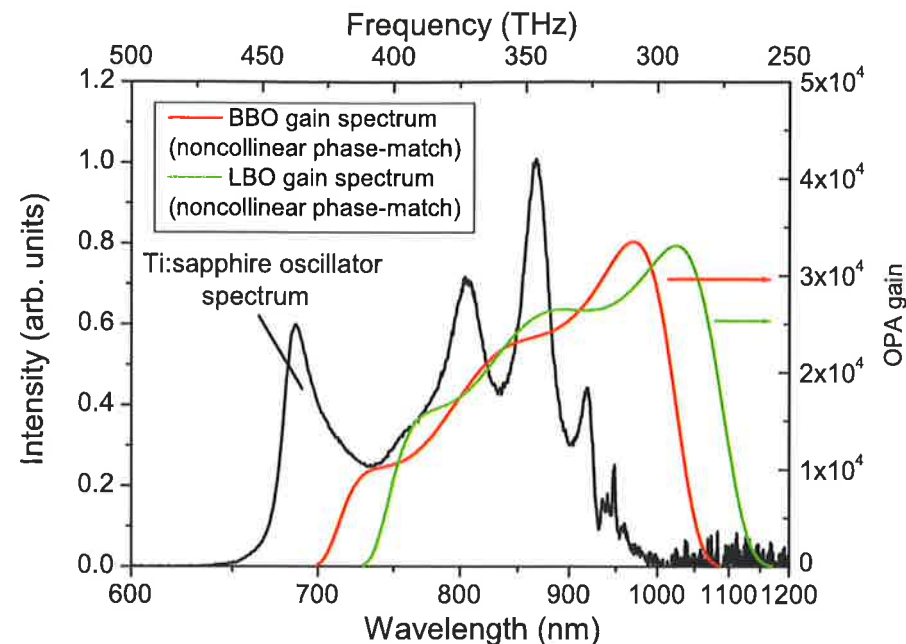
Figure 2.5: Seed spectrum from a Ti:sapphire oscillator (black line) and simulated gain spectra of NOPA using BBO (red line) and LBO (green line)

to pump beam propagation direction: $23.7°$ for BBO and $13.7°$ for LBO. In the case of LBO, pump, signal, and idler beams are in the X-Y plane and the polarization of the pump wave lies in the X-Y plane and the signal and idler waves are polarized along z-axis. In Fig. 2.5, it is shown that the gain spectrum of NOPA using BBO is more overlapped with the Ti:sapphire seed oscillator than LBO. The shortest pulse duration calculated by the Fourier transformation of the BBO gain spectrum assuming a flat spectral phase is about 6.1 fs (FWHM of the intensity). This corresponds to 2.2 cycle at the central wavelength of 840 nm. Although OPA results using LBO will not be described here, we have experimentally tested LBO as a parametric crystal. This experiment showed us more red-shifted gain spectrum than BBO. Because of the better spectral overlap between the BBO gain and the Ti:sapphire spectrum, we use exclusively BBO for the near-infrared OPCPA system described later.

2.5   Pump-seed synchronization

We review several synchronization methods used in previous works on OPCPA and give considerations about a synchronization scheme applicable to an OPCPA using picosecond pump pulses. For parametric three-wave interactions (including OPA), pump and seed pulses must have temporal and spatial overlap with each other to exchange energy between them because of lack of an energy storage in a parametric process. Therefore an OPCPA system imposes strict synchronization between pump and seed pulses. The stable operation of an OPCPA system re-

quires the stabilization of relative timing jitter between pump and seed pulses within less than a fraction of their pulse durations. Timing jitter of more than 10% of pump and signal pulse durations severely might degrade amplified pulse compressibility, energy stability, and the stability of amplified spectrum and the intensity of compressed amplified seed pulses. Although about 20 years has passed since the first demonstration of OPCPA, the issue of synchronization is still a common problem and not completely solved yet even in real working systems. Dependent on an pump pulse duration, an output energy level, a required output pulse duration, and so forth, only two synchronization methods had been used in OPCPA systems.

1. Single narrowband oscillator approach

2. Electric trigger synchronization

and they will be discussed in the following subsections.

Single narrowband oscillator approach

An approach that one narrowband oscillator delivers seed pulses to a parametric amplifier and a pump amplifier has been widely used since the use in the first demonstration of OPCPA [30, 22]. As a typical example of this approach, in Ref. [22], a Nd:glass oscillator seeded simultaneously a Nd:glass regenerative amplifier for pump pulse generation and an OPCPA system. Stretched seed pulses from the oscillator were amplified in a degenerate optical parametric amplifier pumped by the frequency-doubled output from the regenerative amplifier. Many works using this approach have been demonstrated [102, 103, 104, 105, 106] and they inevitably rely on an optical parametric amplifier operating at the degeneracy point because the choice of available wavelengths for pump and seed pulses is limited to the fundamental and its harmonics. However, we could not use this approach because of lack of spectral overlap between our Ti:sapphire and an Nd:YAG amplifier, which will be used as a pump laser for our OPCPA system. This method cannot meet our requirement, high-energy few-cycle pulse generation, because degenerate OPA provides usually narrower gain bandwidth than NOPCPA except one special case [104] and the difficulty in high-energy pump laser development based on Ti:sapphire necessary for this approach. In Ref. [104], spectrally broadband pump pulses are specially engineered in time and space to be able to amplify extremely broadband (from 630 to 1050 nm) seed spectrum obtained by a photonic crystal fiber. This idea is quite attractive for low-energy ultrabroadband pulse amplification. However this special case cannot be applicable for high-energy pulse generation simply because of its low energy conversion efficiency due to the complicated system and a Ti:sapphire amplifier required for pump pulse generation. This scheme could be a good approach when femtosecond high-energy pulses from an laser amplifier based on emerging Yb^{3+}-doped host materials will be able to serve as pump and seed sources for an OPCPA system. The second harmonic of femtosecond high-energy pulses can be used as a pump source for an optical parametric amplifier of supercontinuum generated by the small portion of femtosecond high-energy pulses from an Yb laser amplifier.

Pump-seed synchronization by an electric trigger

an electric trigger is frequently used to synchronize optical pulses. For example, this is used for the synchronization between Ti:sapphire oscillator pulses and Q-switch Nd:YAG laser pulse pumping a Ti:sapphire amplifier. Limitation of this method is possible precision of an electric signal respect to optical pulses. The precision of an electric signal is sub-nanosecond under the current technology. Therefore the synchronization of picosecond pulses is hardly achievable by electronics. Usually nanosecond Q-switched or injection-seeded lasers are used as a pump source with this synchronization method. Advantages of this method includes its simplicity and easiness in use, wavelength tunability of a pump laser, available high-energy pump pulse, and commercial availability of well-developed inexpensive nanosecond lasers. At the same time, there exist several disadvantages such as narrow OPA gain bandwidth, inability for broadband few-cycle pulse amplification, low conversion efficiency, and multiple pulse amplification in a nonlinear crystal. Narrower gain bandwidth results from large phase-mismatch accumulated during propagation in a long OPA crystal because a damaged threshold intensity is lower for nanosecond pulses than picosecond pulses [69] so that a longer parametric crystal is necessary for nanosecond pump pulses. Detailed considerations about this topic will be given in Section 1.3. Another difficulty in the recompression of ultrabroadband stretched pulses from nanosecond to sub-10-fs restricts the practical use of nanosecond pump pulses for few-cycle, high-energy pulse generation. So far, the recompression of 300-ps stretched pulses down to sub-10-fs pulses has been demonstrated with the help of adaptive optics [107]. Conversion efficiency of a parametric amplifier using nanosecond pump pulses tends to be low because of typical unmatched durations between pump and seed pulses. A Q-switched laser has typically a duration of more than 5 ns, while seed pulses can be stretched to less than few nanoseconds at most. This mismatch results in lowering the energy conversion efficiency from a pump pulse to a seed pulse. Multiple pulse amplification, caused by reflections of amplified pulses on the surfaces of an OPA crystal, has been demonstrated in our group for the first time [108]. A high gain in a parametric amplifier is one of advantages of OPA or OPCPA. However reflections of a highly amplified pulse on the surfaces of an OPA crystal cannot be neglected any more in such an high gain operation of a parametric amplifier. A reflected pulse become a seed to be amplified again by a long pump pulse when pump pulse length is much longer than a crystal thickness and a high OPA gain overcomes substantial losses at the anti-reflection coated surfaces of a crystal. As an example, 1% reflection at both surfaces can be easily compensated by an OPA gain of 10^4, which is not so rare in the case of OPA. In the worst case, this mechanism causes parametric oscillations (optical parametric oscillation) between the surfaces of a nonlinear crystal [109]. This effect is schematically illustrated in Fig. 2.6. The scheme of retro-reflection and re-amplification ((A)-(C))and the high-dynamic range autocorrelation trace (D) of amplified signal pulses in an OPCPA system after pulse compression are shown in Fig. 2.6 (Courtesy of Mr. Tavella Franz, the Max-Planck-Institute for Quantum Optics, Garching, Germany). Fig. 2.6 (A) illustrates pump pulse (green), whose spatial duration is longer than a crystal, and stretched seed pulses (from yellow to orange) coming into an OPA crystal. Fig. 2.6 (B) shows reflection of an amplified seed pulse at the back surface of the crystal. Fig. 2.6 (C) the re-reflection and re-amplification of the reflected amplified seed pulse. Fig. 2.6 (D) shows the high-dynamic range autocorrelation trace of multi-
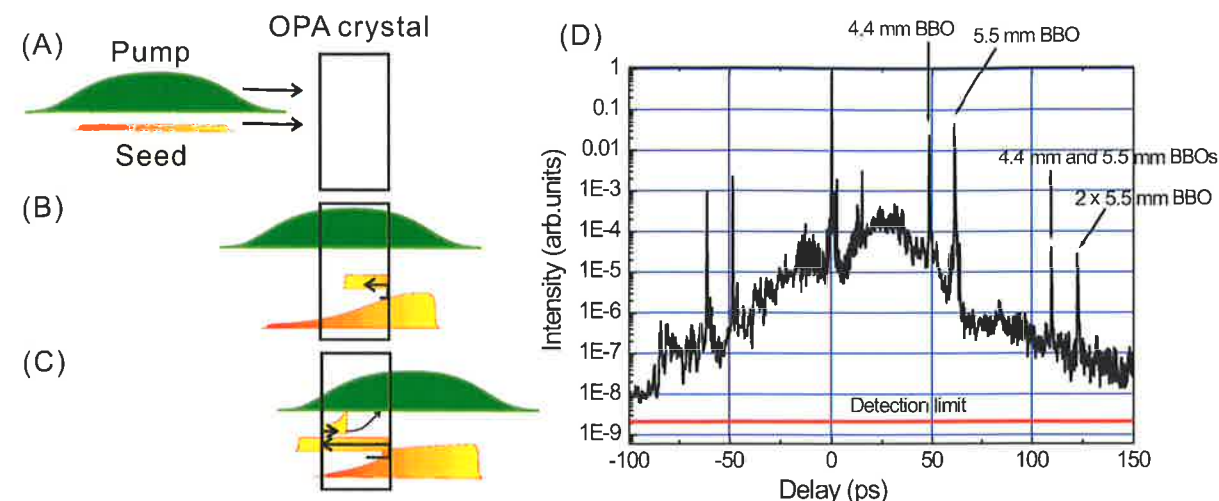
Figure 2.6: (A)-(C): Schematic illustrations of the retro-reflection in the OPA stage by use of a pump pulse with the duration longer than the crystal thickness. (B): High-dynamic range autocorrelation trace of multi-millijoule few-cycle near-infrared pulses based on OPCPA [108] (Courtesy of Mr. Tavella Franz, the Max-Planck-Institute for Quantum Optics, Garching, Germany). See the main text for details.

milljoule few-cycle near-infrared pulses generated from a near-infrared OPCPA system. In Fig. 2.6 (D), two pre-pulses do not exist and are ghosts [108] of two post-pulses around 50 ps (one peak at 48 ps from a 4.4-mm-long BBO crystal and the other at 61 ps from a 5.5-mm-long BBO crystal). The other two post-pulses after 100 ps are created by two-times retro-reflection (one at 110 ps from the 4.4-mm- and 5.5-mm-long BBO crystals and the other at 123 ps from the two times in the 5.5-mm-long BBO crystal). The ASF contributes to a smooth pedestal in the range from -100 ps to 150 ps, which would be a critical issue for high-intensity applications using solid targets (e.g. high harmonic generation on a solid). However, generally, higher-contrast amplified pulses have been demonstrated by use of OPCPA in contrast to amplified pulses obtained by CPA in Ti:sapphire [110, 111]. In a high-contrast OPCPA system, even small ripples of a pump pulse obtained from a Q-switched laser imprints the modulation in an amplified spectrum, causing the degradation of a pulse contrast [112]. Proposals for further improvement of the pulse contrast of an parametrically amplified pulse have been made by use of cascaded OPAs [113] and by use of a third-order nonlinear effect in a MgF_2 plate [114].

An electric trigger method has been applied to the synchronization method of an OPCPA system since 1998 when A. Galvanauskas *et al.* [115] demonstrated the first application of electric trigger synchronization and a Q-switch laser. Especially, after a proposal [23] made by I. N. Ross *et al.* , which pointed out an OPCPA method applicable for extremely high-peak-intensity ultrashort laser pulse generation up to 10 PW, large institutes in the world have applied an OPCPA approach to the development of high-energy, high-intensity, and ultrashort laser pulse systems [116, 117, 118, 119, 120, 121, 122]. In these demonstrations, a high-energy

nanosecond Q-switched laser is exclusively use as a pump source. So far, the highest pulse peak intensity reaches up to more than 100 terawatt in sole OPCPA systems, respectively [123, 124]. More than 1 petawatt (PW) peak intensities in the hybrid amplifier systems comprising an OPCPA front-end and Nd:glass power amplifiers have been realized [125, 120]. Notice that the first PW laser built in Lawrence Livermore National Laboratory [126] relied on Ti:sapphire regenerative amplifiers operating at 1053 nm as a front-end of the petawatt laser system [127] , instead of using an OPCPA as a front-end simply because, at that moment, OPCPA was not widely noticed. Apart from these high-energy OPCPA systems, this approach has been employed in a hybrid system using OPCPA and Ti:sapphire amplifiers [128, 111] and OPCPA systems using periodically poled KTP [129] and periodically poled LiTaO$_3$ [130]. All experiments listed above have demonstrated high-energy and/or more than tens of femtosecond laser pulse generation. The electronic synchronization approach has been applied to narrowband amplification and relatively long pulse amplification and not been used for few-cycle pulse amplification.

Picosecond pump and seed pulses synchronization by use of a phase-lock loop

As mentioned above, synchronization of picosecond pump and seed pulses cannot be achieved by an electronic synchronization method. However, few-cycle ultrabroadband pulse amplification based on an OPCPA scheme requires the use of picosecond pump pulses, therefore, synchronization in the picosecond range. The precise synchronization and timing-jitter reduction of optical pulses have been one of topics in laser physics [131, 132, 133, 134, 135]. A repetition rate of a laser oscillator was stabilized by use of an electronic phase-locked loop (PLL) using a double balanced mixer [131]. The timing-jitter of optical pulses respect to a reference clock was reduced to less than a picosecond (rms jitter of 0.3 ps in the frequency range from 0.25 Hz to 25 kHz) by use of Nd^{3+} oscillators [132]. Further reduction of timing jitter was achieved by use of a self-mode-locked Ti:sapphire oscillator (150 fs (100−500 Hz) and 80 fs (500−5000 Hz)) [134]. Two picosecond oscillators were synchronized within timing jitter of 20 fs and applied to a time-resolved anti-Stokes Raman scattering measurement [135]. We have chosen an electronic PLL repetition-rate stabilization for pump-seed synchronization in our OPCPA system. At the same time or after our demonstration, this scheme has been recognized as a pulse synchronization method for picosecond OPCPA systems [136, 137, 138]. Fig. 2.7 shows a detailed synchronization scheme. See Section 2.6 for details about oscillators, an amplifier, and an OPA and Section 2.7 for a stretcher. A synchronization unit is based on a PLL electronic circuit by use of a double balanced mixer and stabilizes repetition rates of two oscillators, an actively mode-locked Nd:YVO$_4$ used for a pump seed and a Ti:sapphire used for a OPCPA seed. To increase the precision of repetition-rate lock, actually, we lock a fourth harmonics of the repetition rate frequency. We checked its timing precision by the cross-correlation between the oscillators based on sum-frequency generation. The Ti:sapphire oscillator pulses are not intentionally stretched in time. The cross-correlation trace (B) and the autocorrelation trace of the actively mode-locked Nd:YVO$_4$ oscillator (A) are shown in Fig. 2.8. The pump oscillator pulse duration of 62 ps deconvolved from the 87-ps-wide autocorrelation trace well corresponds to the cross-correlation
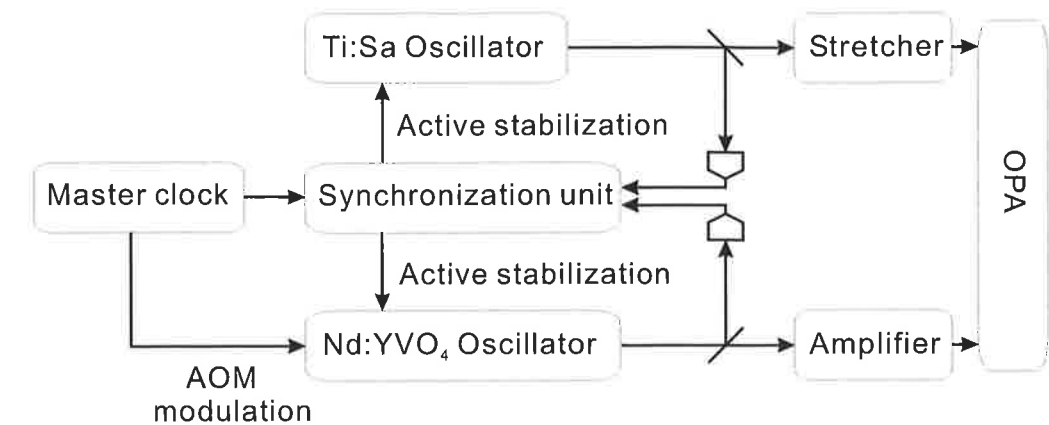
Figure 2.7: Scheme of synchronization of picosecond pump and seed pulses in the OPCPA system by use of a PLL. Master clock:, synchronization unit: PLL electronic circuit using a double balanced mixer, stretcher: seed pulse stretcher prior to the OPA stage, amplifier: Nd:YAG amplifier for the pump pulse generation, and OPA: optical parametric amplifier adopting a BBO crystal.
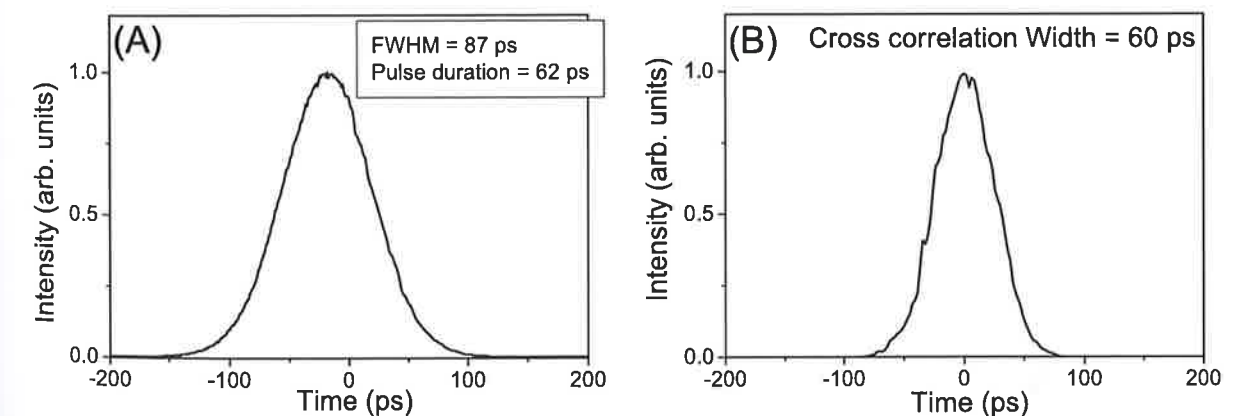

Figure 2.8: Autocorrelation of pump pulses and cross-correlation between the synchronized pump and seed pulses. (A): autocorrelation trace of the actively mode-locked Nd:YVO$_4$ oscillator. (B): cross-correlation trace between the Nd:YVO$_4$ oscillator and the Ti:sapphire oscillator.

width of 60 ps. Because this method does not provide enough precision necessary of an OPCPA application, another method [135] is used to determine timing-jitter more precisely. The short pulse from the Ti:sapphire oscillator is placed at half peak of the long picosecond pump pulse, where the slope of the pump pulse is steepest, and the fluctuation of sum-frequency intensity is measured to estimate the timing-jitter. Of course this method requires a stable oscillator but can determine the worst possible value of timing-jitter. The obtained value of timing-jitter in short term is less than 4.5 ps, which is less than 10% of the pump pulse duration. Details about this measurement can be found in Ref. [139]. During this measurement we found a long term timing drift, which is attributed to a double balanced mixer employed in our PLL circuit. The double balanced mixer has critical disadvantages such as thermal phase shift and phase noise affected by an amplitude noise [132]. These drifts change the relative timing of pump and seed pulses in time scale of an hour. Later this effect will be solved by use of the optical synchronization between pump and seed pulses, which was developed after this near-infrared OPCPA system. Details about optical synchronization will be described in Chapter 3. A comparison between the electronic and optical synchronizations is summarized in Appendix B.

2.6   Broadband near-infrared OPCPA

First we describe NOPCPA using BBO and a Ti:sapphire seed pulse stretched in SF57 glass blocks in order to investigate the characteristics of a parametric amplifier. The layout of our
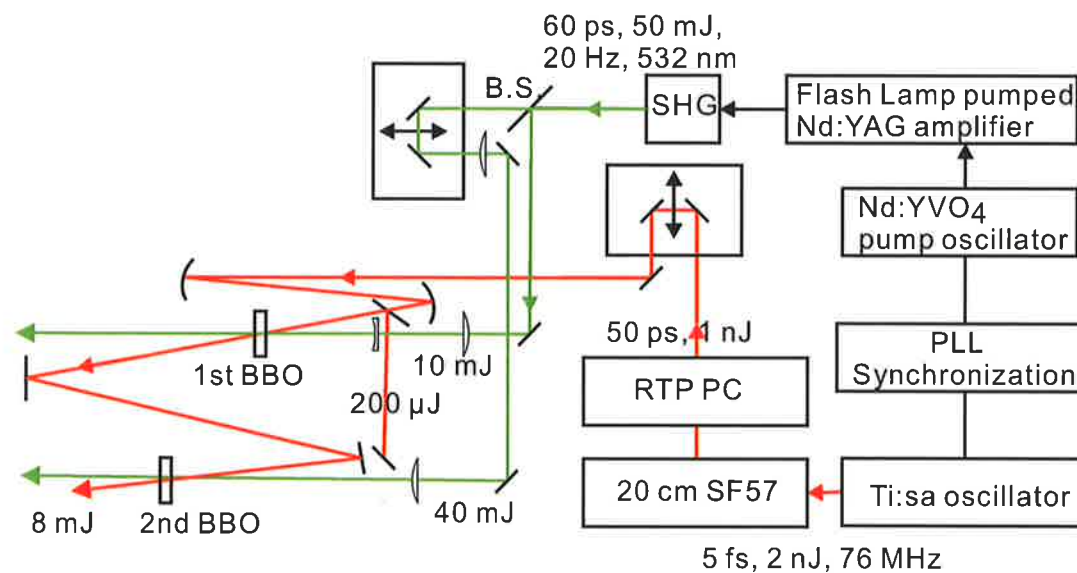

Figure 2.9: Layout of the NOPCPA system with the bulk stretcher. PPL: phase-lock loop for oscillators' repetition-rate lock; RTP PC: RTP Pockels cell; SHG: second-harmonic generator (type I phase matching KD*P); B.S.: beam splitter.

NOPCPA system with the bulk stretcher is presented in Fig. 2.9. The home-made broadband

Ti:sapphire oscillator has been employed as the seed source for the parametric amplifier. The repetition rate of the Ti:sapphire seed laser is locked to that of an actively mode-locked 60-ps Nd:YVO$_4$ pump oscillator by use of a PLL electronics. Relative timing between these oscillators' pulses is stabilized to less than 5 ps. Details about the active synchronization of the pump and seed pulses are described in Section 2.5. The pulses from the picosecond Nd:YVO$_4$ pump oscillator are amplified to 100 mJ at a 20-Hz repetition rate in a flash-lamp-pumped Nd:YAG amplifier (EKSPLA). 50-mJ pump pulses at 532 nm for the OPCPA system are obtained by frequency-doubling the output from the Nd:YAG amplifier in a type I phase-matching KD*P crystal. The seed pulses for OPCPA from the Ti:sapphire oscillators are temporally stretched by 20-cm-long propagation in the SF57 blocks. The seed-pulse repetition rate is reduced to 20 Hz from 76 MHz by a RTP pulse picker, otherwise the 76-MHz seed pulses from the oscillator would be too powerful for any measurement of the low-repetition-rate amplified pulse. The SF57 blocks and the RTP Pockels cell temporally stretch the seed pulse to about 50 ps (700 - 1000 nm) to achieve both good efficiency. The seed beam is recollimated by a pair of concave silver mirrors to have good spatial overlap with the pump beam at a first OPA stage. 3-mm- and 4-mm-thick AR-coated type I phase-matching BBO crystals are used in the first and second parametric amplifier stages, respectively. In the first amplifier stage, the pump beam at the first OPA stage has a 500-μm diameter by the recollimation of an amplifier output beam by a pair of positive and negative lenses. In the second amplifier stage, the output beam from the Nd:YAG amplifier [140] is relay-imaged from the second-harmonic generator to the OPA stage and collimated down to 2.5 mm in diameter. The pump beam profile at the second stage is shown in Fig.
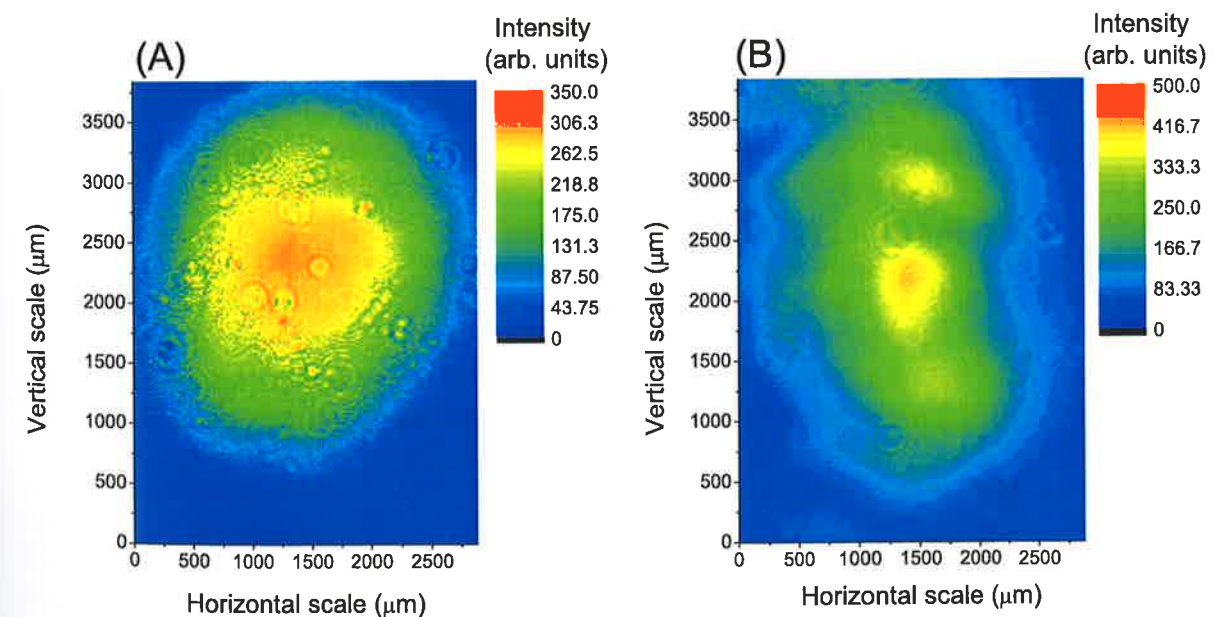

Figure 2.10: Near-field beam profiles of the pump (A) at the second stage and of the amplified seed (B) after the second stage.

2.10 (A). The pump beam sizes in the first and second stages are determined by a compromise between the gain bandwidth and the amount of gain. The use of a thinner crystal results in a broader OPA gain bandwidth in exchange of a less gain [71], although a strong pump intensity, which is limited by a damage threshold of optics, is necessary to obtain a required gain in a thin crystal. The pump intensities are set about 20 GW/cm^2 at the first stage and 10 GW/cm^2 at the second stage, respectively. Under these conditions, a B-integral value by the XPM of the amplified seed pulse by the pump pulse is estimated to be 0.3. The third-order nonlinearity refractive index of the BBO crystal is available in Appendix E. The internal noncollinearity angle between the pump and seed beams is set at approximately 2.3° for both stages to provide broadest gain bandwidth. The corresponding external angle is about 3.7°.
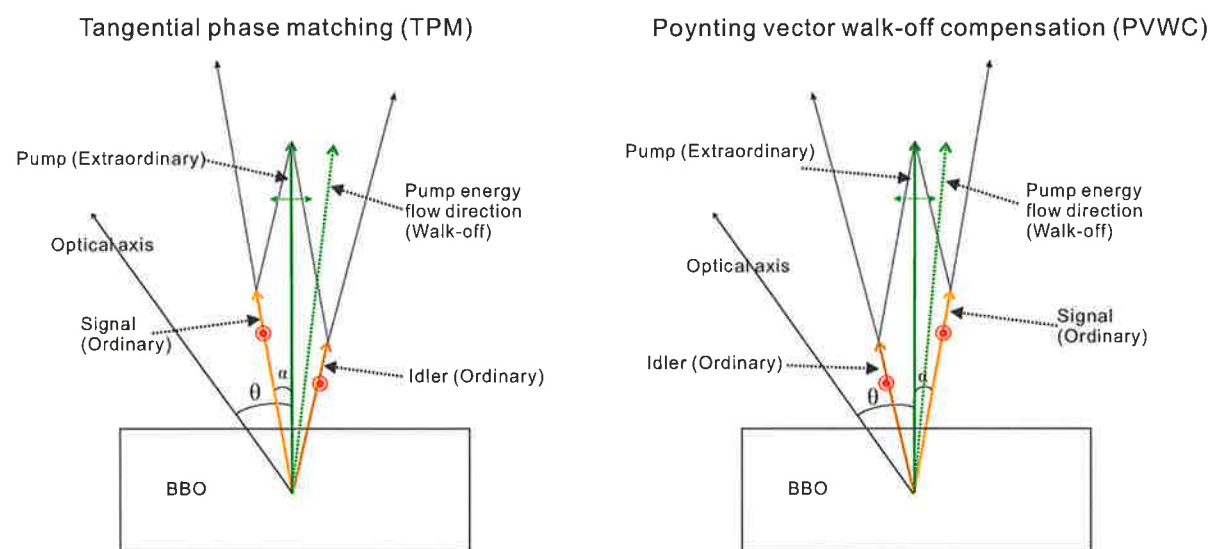

Figure 2.11: Schematics of two possible beam geometries in NOPA: tangential phase matching (TPM) (left) and Poynting-vector walk-off compensation (PVWC) (right).

There exist two possible beam geometries in NOPA, both of which we have tested, illustrated in Fig. 2.11. Their difference is the seed-beam propagation direction relative to an optical axis of a uniaxial crystal and the pump beam direction [83]. In a negative uniaxial crystal, the direction of a pump wave vector lies between the direction of a pump Poynting vector and the optical axis [99, 83]. Tangential phase matching (TPM) is the beam geometry where the direction of a signal beam lies between a pump beam and the optical axis. The other geometry is called Poynting vector walk-off compensation (PVWC). Experimentally, a TPM configuration resulted in a higher gain and a more efficient OPA operation and, in addition, less second-harmonic generation (SHG) of an amplified seed. This is because an angle between the propagation direction of the amplified seed and the optical axis is 24° so that the SHG of the amplified seed cannot be phase-matched in this direction. Phase-matching angles for SHG of 800 and 900-nm lights are about 29° and 26° in the case of type I phase-matching BBO, respectively. In contrast to

the TPM geometry, the PVWC configuration leaded to less gain and the generation of strong blue radiation (second-harmonics of the amplified seed) because the angle of the amplified seed beam direction from the optical axis is close to 26-29 °, which are the phase-matching angles of near-infrared radiation. Fig. 2.12 shows the photograph of superfluorescence generated by
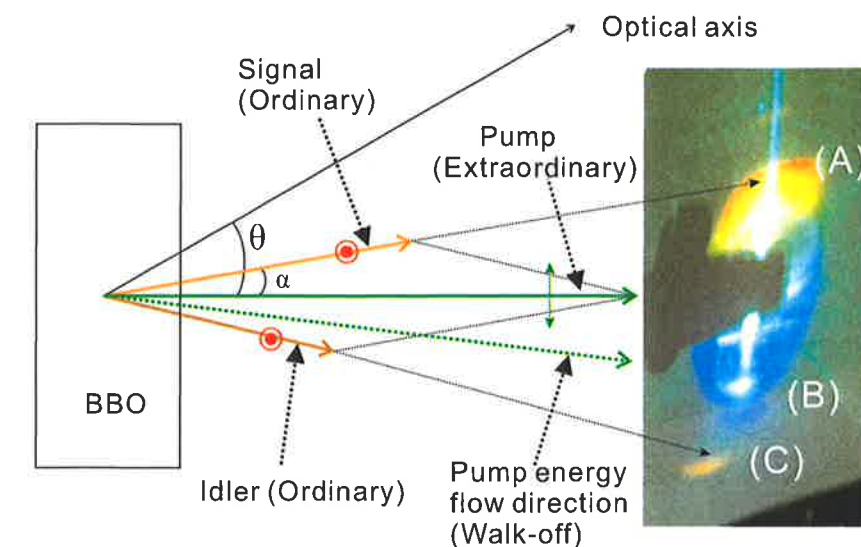

Figure 2.12: Photograph of the superfluorescence and schematic illustration of the pump, signal, and idler beams in the TPM geometry and the optical axis of BBO.

strong 532-nm pumping pulses. The TPM beam geometry used in our experiment is also illustrated correspondingly with the photograph. The strong red light indicated by (A) in Fig. 2.12 should be closer to the optical axis than the strong blue light direction indicated by (B) in Fig. 2.12 because of the SHG phase-matching condition above mentioned. Fig. 2.12 (C) shows the second-harmonics of the idler. In this picture, the stronger superfluorescence is observed in the direction (A) and this also indicates that the efficient amplifier operation is possible when a seed beam is sent into the direction (A). With the TPM geometry, the amplified pulse energy from the first stage is obtained up to 250 μJ, which is 2.5 times more than 100 μJ output energy obtained with the PVWC geometry. The 250 μJ output energy corresponds to the OPA gain of about 2.5×10^5. We checked high energy contrast between the generated superfluorescence (uncompressible parametric noise) [53, 40] and the amplified seed output at the first stage. The diverging output beam from the first OPA stage is collimated by a curved mirror (not shown in Fig. 2.9) and sent to the second OPA stage. The lower pump intensity at the second stage than at the first stage resulted in the gain of 30 and the signal pulse is amplified up to 8 mJ with a 40-mJ pump pulse. The low gain is favorable to increase the conversion efficiency as discussed in Section 1.3. Amplified superfluorescence has the energy of 3 mJ when the seed beam is blocked. Onset of the seed pulse reduces the amount of the superfluorescence so that the output pulse can have more than 5 mJ. When the signal beam path between the first stage and the second stage is blocked, we do not observe any superfluorescence from the second stage. Therefore, it can

be concluded that the superfluorescence is generated and successively amplified in the first stage and further amplified in the second stage. The amplified seed beam profile is shown in Fig. 2.10 (B). The cause of modulation in the beam profile can be attributed to the consequence of cumulative nonlinear effects, space-dependent saturation effect as shown in Fig. 1.6, and/or the little modulation of the pump beam profile. The ellipticity of the amplified seed beam results from different phase-matching tolerances in the horizontal and vertical planes [141, 84, 142]. The measured spectra of the seed (red line) and the amplified seed from the second stage OPA (black line) and the calculated BBO gain spectrum (blue line) are plotted in Fig. 2.13. The amplified spectrum is well consistent with the overlapped region between the calculated BBO gain and the oscillator spectra. The short-wavelength cut-off of the amplified spectrum is due to the phase-matching condition of NOPA pumped by the second-harmonics of a Nd:YAG laser. The long wavelength cut-off of the amplified spectrum around 1000 nm is due to lack of the Ti:sapphire oscillator spectrum. Energy conversion efficiency of a parametric amplifier stage is an impor-
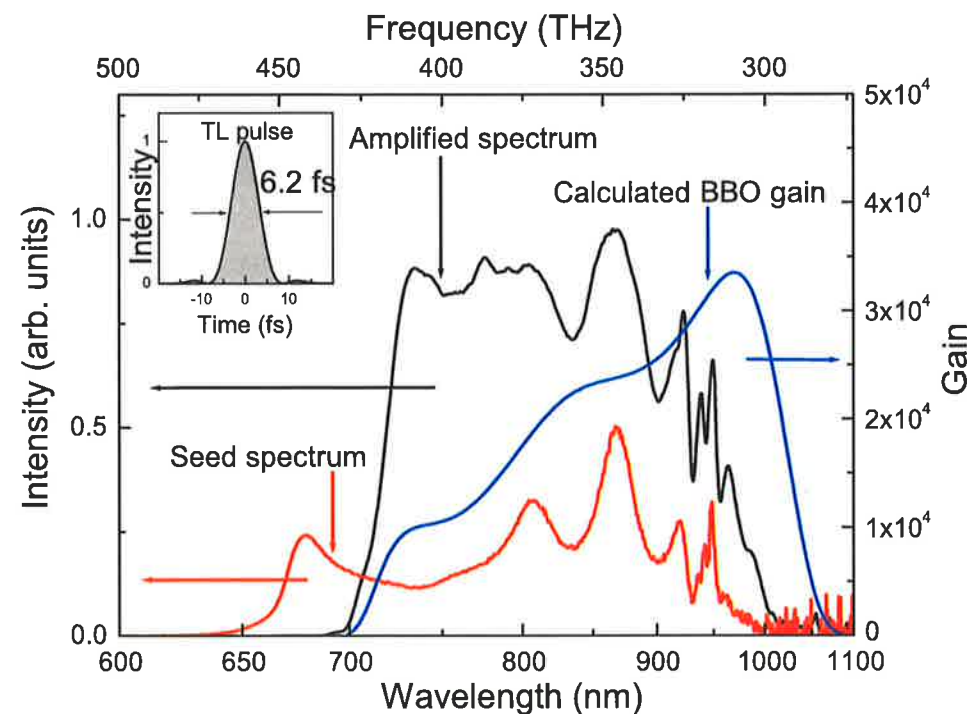

Figure 2.13: Spectra of amplified seed (black line), seed (red line), and calculated gain (blue line) with the bulk stretcher. Inset: Transform-limited pulse profile calculated from the amplified spectrum assuming a flat spectral phase. This pulse has the duration of 6.2 fs (FWHM).

tant issue in a high-energy OPCPA system. The pump-to-signal energy conversion efficiency in the first and the second stage is summarized in Fig. 2.14 (A) and (B), respectively. Notice that constant conversion efficiency means that an amplified seed output is proportional to an pump input energy. Therefore the stability of the output energy is the same as that of the pump energy. With the Gaussian temporal and spatial beam profile of the pump pulse, the peak pump-to-signal

conversion efficiency in the second stage reaches 27% (Fig. 2.14 (B)). At the maximum conversion efficiency, the energy stability of the amplified pulses after the second parametric stage is measured to be 2.9% rms, whereas the pump energy stability is 1.5% rms.
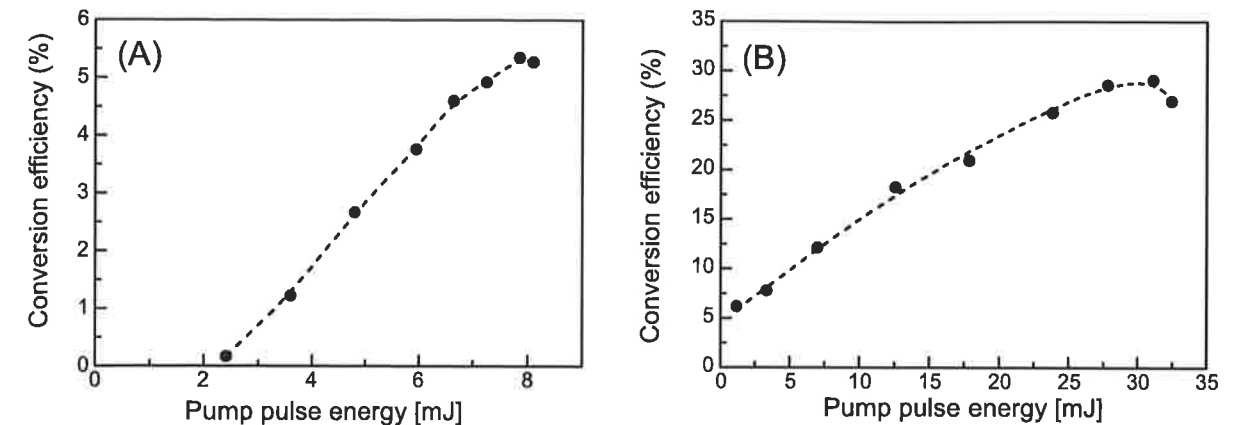

Figure 2.14: Conversion efficiency in the first stage (A) and the second stage (B).

In summary, we demonstrated the ultrabroadband high-energy NOPCPA system. This system employs a broadband chirped pulse as a seed, the high-energy frequency-doubled output from the Nd:YAG amplifier as a pump, and the BBO crystal as an amplifier medium. The efficient operation of the parametric amplifier is demonstrated and results in the 8-mJ broadband amplified output pulse obtained with the 40 mJ pump pulse. The broadband amplified pulse has the potential bandwidth, which could support generation of the ultrashort pulses with the duration of 6.2 fs assuming a flat spectral phase. As a result, from these experiments, terawatt-class laser pulse generation would be possible with an appropriate pulse stretcher and compressor. In the next section, we will describe few-cycle pulse generation based on broadband NOPCPA with an inverse stretcher and compressor pair.

2.7   Few-cycle terawatt-class optical pulse generation by use of OPCPA

In this section, we introduce a pair of a novel down-chirping pulse stretcher and an up-chirping pulse compressor in the NOPCPA system described in the last section in order to achieve the amplification of few-cycle high-energy pulses. The down-chirping stretcher gives negative dispersion to seed pulses prior to the parametric amplifier. The down-chirped amplified pulses are temporally compressed by the up-chirping pulse compressor. Obtained high-energy pulses from the NOPCPA system are characterized by spectral phase interferometry for direct electric-field reconstruction (SPIDER) [143, 144]. The generation of high-intensity ultrashort pulses always

accompanies the use of the chirped-pulse amplification (CPA) technique [7], otherwise high-energy ultrashort pulses would suffer from the damage of optics and severe nonlinear effects. The invention of CPA [7], which used a fiber stretcher and a Treacy grating compressor [145], has been followed by many stretching and compression schemes: a positively chirping grating stretcher [146] and a grating compressor [8], a quintic-phase limited pulse stretcher and a grating compressor [147], an all-reflective stretcher and a grating compressor [148], a stretcher based on an Öffner type magnification system [149, 150, 151] and a grating compressor [152, 153], and additional adaptive optics to a standard grating stretcher and compressor supporting sub-20-fs spectral bandwidth [154, 155, 156]. So far the shortest pulse duration of 8.9-fs has been achieved by the recompression of 300-ps stretched pulses with the help of adaptive optics[107]. However the recompression of 50-ps stretched pulses down to few femtoseconds has not been demonstrated yet even with adaptive optics, a grating stretcher, and a grating compressor. Recently a novel CPA technique by use of a pair of a down-chirping stretcher and a up-chirping compressor, which is opposite to a pair of a up-chirping stretcher and a down-chirping compressor used in the standard CPA technique, has been used in the high-power Ti:sapphire amplifier system [157, 158]. As mentioned in Ref. [157], this inverse CPA (down-chirped-pulse amplification) technique is quite suitable for the stretching and recompression of extremely broadband pulses because a seed pulse with a broadband spectrum can be easily stretched to several tens of picosecond by the small amount of chromatic dispersion. In down-chirped-pulse amplification, a seed pulse is negatively chirped using a grating stretcher and/or a prism pair prior to an amplifier. Amplified stretched pulses from the amplifier chain are recompressed by positively dispersive materials such as SF57, SF11, and fused silica. An advantage of an up-chirping compressor is the high transmittance (close to unity) of broadband amplified pulses through a compressor. The pulse stretching and compression scheme used in this development is illustrated in Fig. 2.15 (A). The seed pulse from the oscillator is negatively chirped by a grating-based stretcher and sent into an acousto-optic programmable dispersive filter (Dazzler, Fastlite), which will be used later for correction of a residual phase measured with a SPIDER apparatus. After the parametric amplifier, the stretched amplified pulse is recompressed by a sequence of dispersive optical materials, SF57 and FS, and custom-made designed positively dispersive chirped mirrors. Fig. 2.15 (B) plots group delays given by dispersive components: the 45-mm-long TeO_2 (black line), BBO crystals used (red line), the 150-mm-long SF57 (green line), the 100-mm-long fused silica (blue line), and the grating-based stretcher (light blue). The group delay of the stretched pulse in the amplifier (pink line) is also shown in Fig. 2.15 (B). The refractive indices of BBO, TeO_2, SF57, and fused silica are available in Appendix A. In the grating stretcher, shown in Fig. 2.16 (left photograph), the seed beam is dispersed by a 900-grooves transmission grating (Wasatch Photonics) and collimated by a parabolic lens (f=80 mm) to make a Fourier plane at the focus of the lens where a micromachined fused silica plate is inserted. The fused silica plate corrects for higher-order spectral dispersion given in a compressor chain (mainly 3rd-order dispersion later given by the glass compressors). Fig. 2.16 (B) plots the input seed spectrum (black line), the measured seed spectrum behind the stretcher (red line), the calculated transmitted seed spectrum behind the stretcher (blue line), the single diffraction efficiency of the transmission grating (green dashed line), and the four-times diffraction efficiency of the grating (orange dashed line). Although the shape of the seed spectrum was dramatically altered after the stretcher, 50% energy
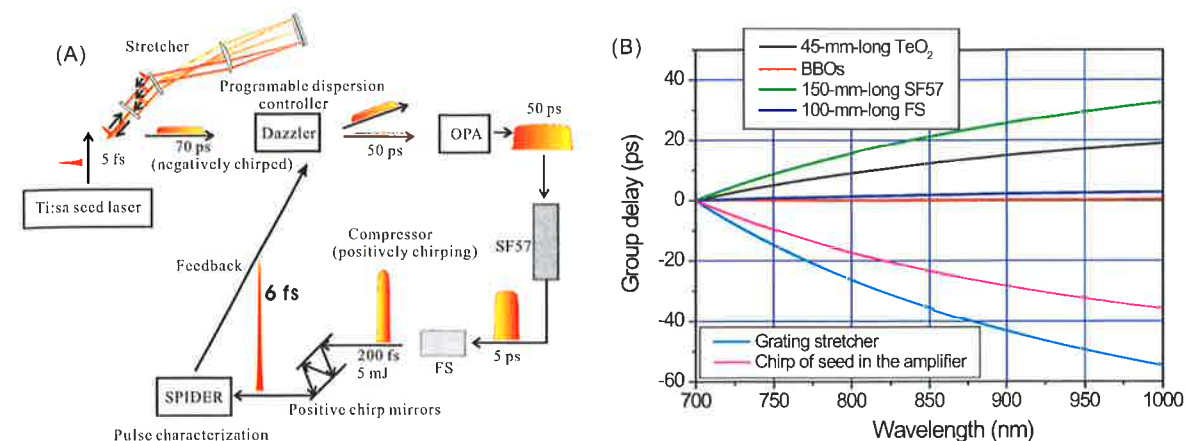
Figure 2.15: (A): Stretching and compression scheme and a feedback system from a SPIDER apparatus to a Dazzler. OPA: Noncollinearly phase-matched optical parametric amplifier using BBO; SPIDER: spectral phase interferometry for direct electric-field reconstruction; Dazzler:an acousto-optic programmable dispersive filter (Dazzler, Fastlite). (B): Group delay of components in the stretcher and compressor of the NOPCPA system. Group delay in a 45-mm-long TeO_2 (black line), BBO crystals used (red line), a 150-mm-long SF57 (green line), a 100-mm-long fused silica (blue line), a grating-based stretcher (light blue), and a group delay of the stretched pulse in the amplifier (pink line).

transmittance is achieved and The necessary seed spectrum for the parametric amplifier remains after the stretcher. The Dazzler made of a 45-mm-long TeO_2 diffracts an input pulse through the interaction between an optical wave and an acoustic wave [159, 160]. A monochromatic input optical wave polarized along one of two optical axes is diffracted by an acoustic wave in TeO_2 to another optical wave polarized along the other axis, when a certain phase-matching condition is satisfied by the acoustic wave. Each monochromatic wave of a broadband pulse propagates with different time determined by the position where the diffraction occurs in the TeO_2 crystal because of the different refractive indices along the two axes. Therefore, arbitrary dispersion can be given to an optical pulse by a programmable acoustic wave. The arbitrary control of a spectral phase of optical pulses has been demonstrated by use of ultrashort laser pulses [161]. A disadvantage of the Dazzler is its low diffraction efficiency of about 10% in our case of the 300-nm-wide band input pulse. The NOPCPA system, whose layout is shown in Fig. 2.17, is slightly modified from that described in the last section since the input seed energy is reduced substantially after the stretcher and the Dazzler to less than 5% of the pulse energy obtained from the oscillator. 50-pJ seed pulses behind the stretcher and the Dazzler can be used as seed pulses for the first OPA stage (3-mm-thick AR-coated type I phase-matching BBO). After first-pass amplification in the first stage, the retro-reflected amplified pulse is amplified again in the same crystal by the residual retro-reflected pump pulse and the resultant 250-μJ amplified pulses are
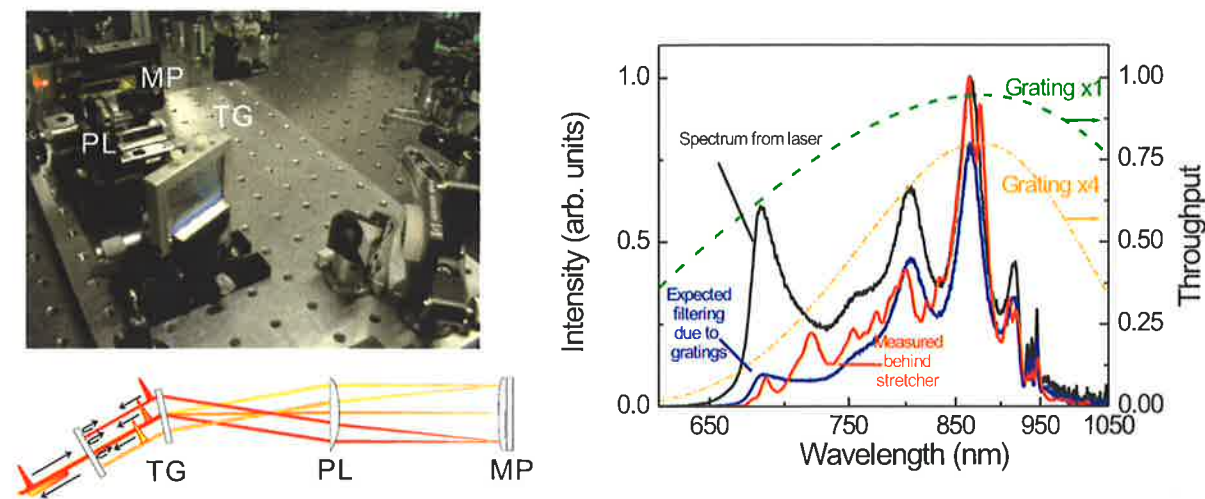
Figure 2.16: (A): Photograph and illustration of the down-chirping stretcher. TG: 900-grooves transmission grating; PL: parabolic lens (f=80 mm); MP: micromachined plate. (B): Transmittance of the grating and the stretcher. Input seed spectrum (black line), measured seed spectrum behind the stretcher (red line), calculated transmitted seed spectrum behind the stretcher (blue line), single diffraction efficiency of the transmission grating (green dashed line), and four-times diffraction efficiency of the grating (orange dashed line).

Figure 2.17: Layout of the near-infrared NOPCPA system with the grating stretcher and bulk compressor. PPL: phase-lock loop; SHG: second-harmonic generator (type I phase-matching KD*P); B.S.: beam splitter for 532 nm; SPIDER: spectral phase interferometry for direct electric field reconstruction.

ejected from the first stage. In the second parametric amplifier stage (4-mm-thick AR coated type I phase-matching BBO) following a beam collimator of the amplified beam from the first stage, two-pass amplification in the second stage boosts the pulse energy from 250-μJ to 5 mJ. The 5 mJ output was limited by the onset of uncompressible ASF, which is more prominent than in the previous amplifier chain because of the reduced seed energy. The beam distortion of the input seed in the stretcher also contributes to loss of the effective seed energy. The obtained amplification results in the NOPCPA system using the grating stretcher are summarized in Fig. 2.18. The Fourier transform of the amplified spectrum, assuming a flat spectral phase, results in the pulse duration of 7.3 fs. The narrower amplified spectrum can be attributed to gain narrowing accumulated during longer propagation length in the parametric crystals and the narrower spectrum of the seed pulse after the pulse stretcher. The energy stability and the mode profile of the amplified pulse are not changed dramatically from the previous results obtained with the bulk stretcher. Because of twice long propagation length in BBO crystals compared to the previous OPA experiment using the bulk pulse stretcher, the total estimated B-integral is about 0.6. After the parametric amplifier, the amplified output beam was expanded to 3 cm in diameter (FWHM) and sent into a compressor chain consisting of the 15-cm-long SF57 glass (Schott), the 10-cm-long Suprasil glass (Heraeus), and a set of three custom-made positive-dispersive dielectric chirped mirrors. This stepwise pulse compression reduces pulse distortion by nonlinear effects inside the bulk materials. Fig. 2.19 (A) plots the pulse duration (dashed line) during compression in the bulk compressors and the calculated B-integral (solid line). The amount of the B-integral in
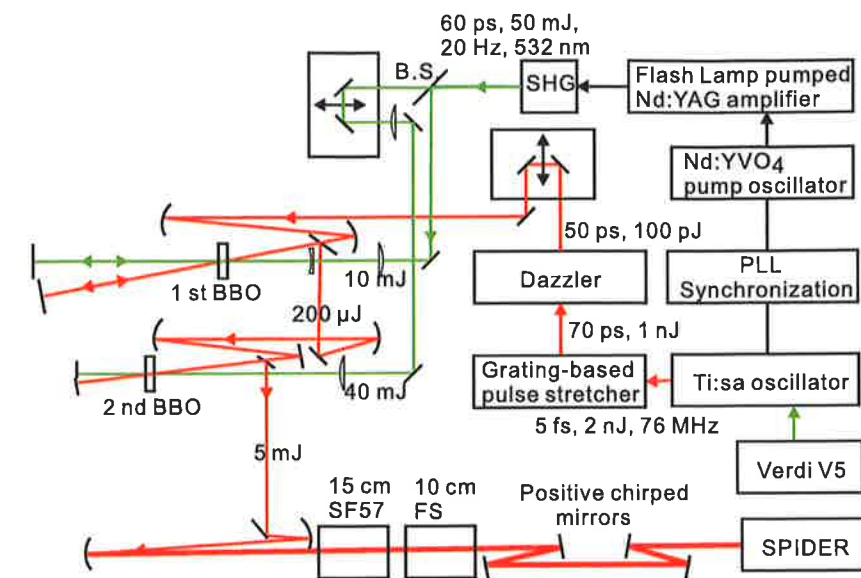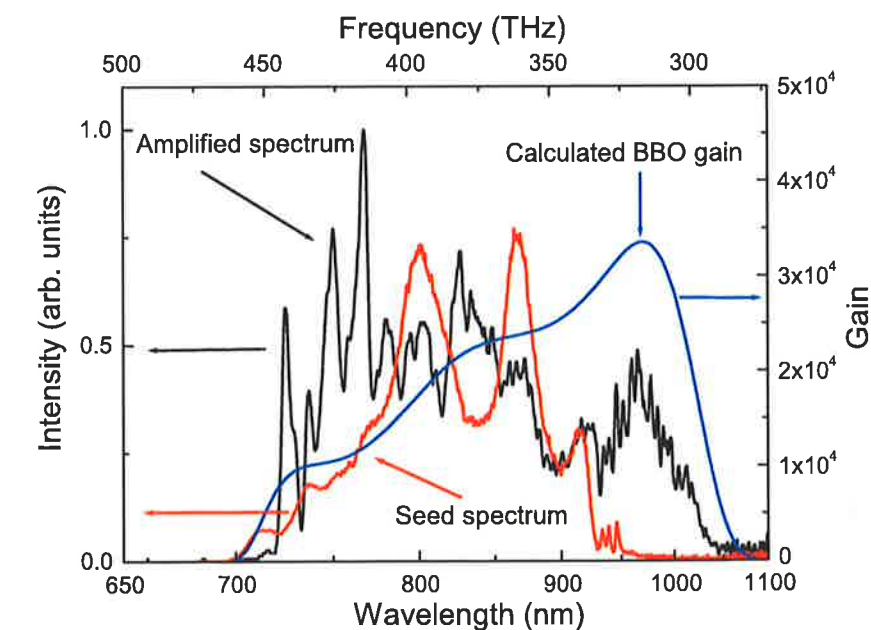
Figure 2.18: Amplification results in the near-infrared NOPCPA system using the grating stretcher. Seed spectrum behind the stretcher (red line), amplified spectrum (black line), and calculated BBO gain spectrum (blue line).

the compressor chain for the 5-mJ amplified pulse is estimated below 0.45. Therefore the estimated total B-integral in the NOPCPA system is about 1. Fig. 2.19 (B) shows the group-delay dispersion of the specially designed up-chirping dielectric mirror. The total measured loss in the compressor chain is measured to be below 4%. After the down-collimation of the output beam
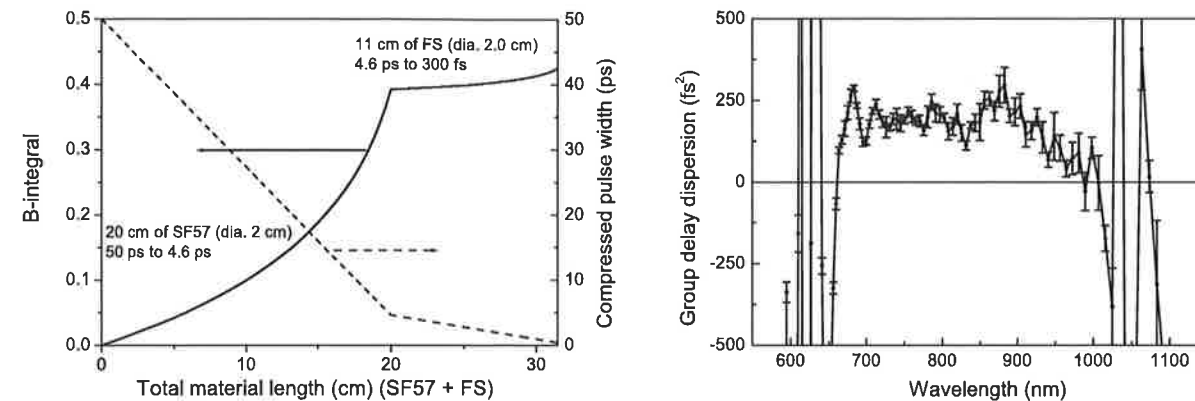

Figure 2.19: (A): Pulse duration (dashed line) in the compressor and the B-integral (solid line) accumulated in the bulk materials (calculated using 20 cm of SF57 and 11 cm of FS for the worst case scenario). The energy and the duration of the amplified pulse are 5 mJ and 50 ps for this calculation, respectively. (B): Measured group-delay dispersion of the up-chirping dielectric mirror.

from the compressor chain, the compressed pulse is characterized by the home-made SPIDER apparatus [143, 144]. Using the feedback from a SPIDER result, dispersion controlled by the Dazzler compensates a residual phase of the amplified pulses. The example of the feedback is demonstrated in Fig 2.20 (A) and (B). Fig. 2.20 (A) shows the spectral phases of the amplified pulses before the feedback (black line) and after the feedback (red line). Fig. 2.20 (B) shows the amplified temporal pulse profiles before the feedback (black line) and after the feed back (red line). The shortest pulse duration of 9.6 fs (FWHM) has been obtained and the SPIDER measurement results are summarized in Fig. 2.21. Fig. 2.21 (A) shows the measured SPIDER trace. Fig. 2.21 (B) shows the seed spectrum behind the stretcher (black line), the amplified spectrum (red line), and the retrieved residual group delay (blue line). Fig. 2.21 (C) shows the reconstructed pulse with the duration of 9.6 fs (FWHM) (black line), the transform-limited pulse with the duration of 7.3 fs (FWHM) (red line) calculated from the amplified spectrum assuming a flat spectral phase, and the retrieved residual temporal phase (blue line). The shot-to-shot variation of the pulse duration and the spectral phase has been observed and could be attributed to the pulse-to-pulse change of accumulated nonlinear phase modulation in time and space caused by the pump pulse intensity fluctuation and/or timing-jitter between the pump and seed pulses. The intensity fluctuation of the pump changes a nonlinear phase given in the BBO parametric amplifiers and the successive compressor chain. A single-shot pulse characterization device such as a single-shot SPIDER [162, 163] and a GRENOUILLE (Swamp Optics) would help to investigate
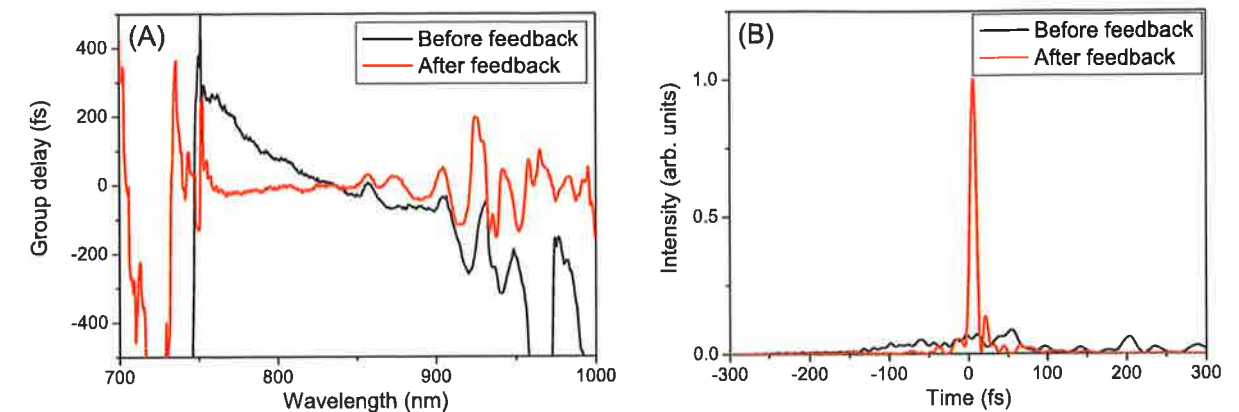
Figure 2.20: Optimum pulse compression by the feedback system using the Dazzler and the SPIDER. (A): Spectral phases before the feedback (black line) and after the feedback (red line) and (B): reconstructed temporal profiles before the feedback (black line) and after the feedback (red line).

shot-to-shot variations of an output pulse duration and a spectral phase [164].

   In summary, we have achieved the generation of more than 0.5-terawatt (5 mJ, 9.6 fs) optical pulses by use of NOPCPA with the unique pulse stretching and compression technique. Because of the absence of thermal load on the nonlinear optical crystal, the demonstrated concept is scalable both in an output energy and a pulse repetition rate. The limitation of output energy would be determined by an available aperture size of nonlinear crystals. Although current highest peak-intensity is achieved by our colleagues [165], this work was the demonstration of the highest-peak intensity optical pulse generation at that time and opened the way toward not only the generation of few-cycle high-peak-intensity near-infrared pulses but also the generation of few-cycle infrared OPCPA pulses which will be described later in virtue of wavelength tunability of an OPCPA approach.
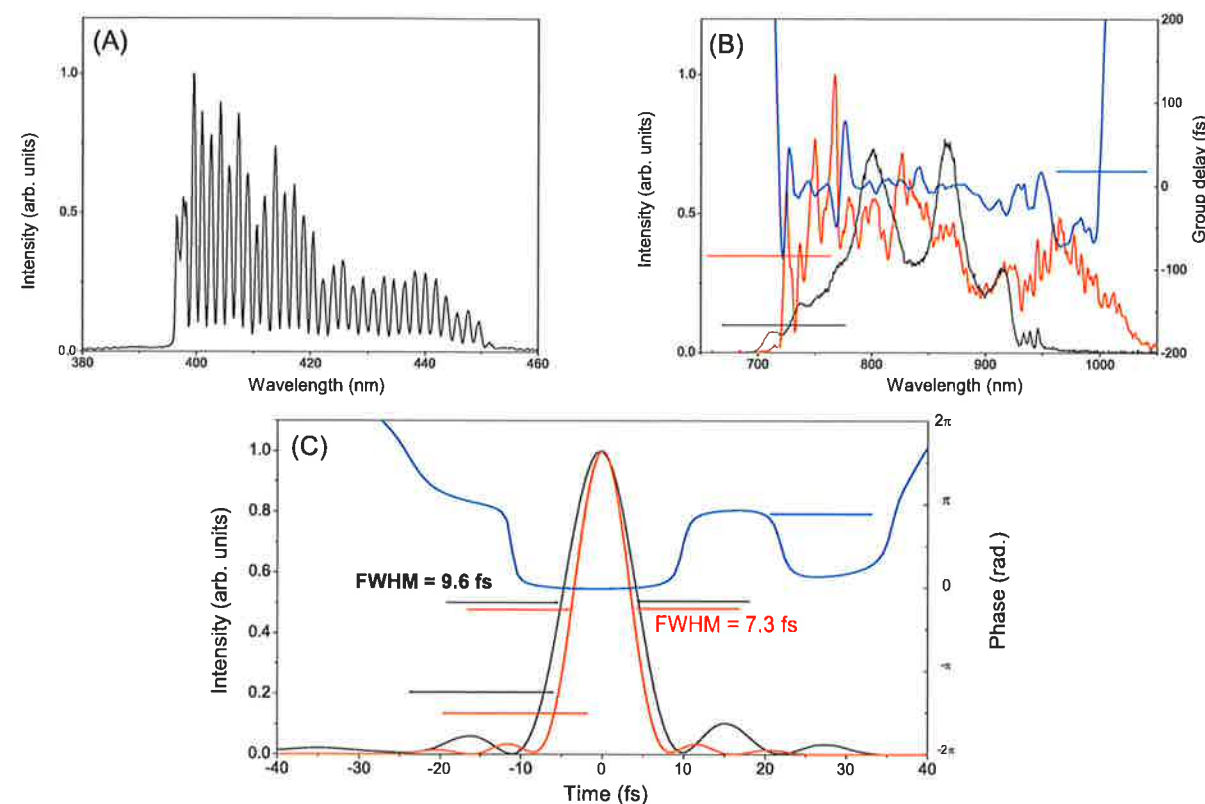
Figure 2.21: SPIDER results of the near-infrared few-cycle terawatt-class optical pulses from the NOPCPA system. (A): measured SPIDER trace. (B): measured amplified spectrum (red line), seed spectrum behind the stretcher (black line), and residual group delay (blue line). (C): reconstructed temporal pulse profile with the duration of 9.6 fs (FWHM) (black line), transform-limited temporal pulse profile with the duration of 7.3 fs (FWHM) (red line), and residual temporal phase (blue line).

Chapter 3

Optical synchronization between the pump and seed pulses in an OPCPA system

3.1 Introduction

In this chapter, we describe the demonstration of a novel pump-seed synchronization scheme in an OPCPA system. This synchronization method is achieved by a single ultrabroadband Ti:sapphire oscillator, which seeds both an OPCPA pump laser and an optical parametric amplifier. The Ti:sapphire oscillator is modified to have a wider spectrum reaching beyond 1 μm. We build a diode-pumped high-repetition-rate Nd:YLF amplifier to test its seeding with a Ti:sapphire oscillator. The Nd:YLF regenerative amplifier is carefully characterized and an intracavity etalon is introduced to control the pump pulse duration to make it suitable for our OPCPA application. This scheme has a potential for the optical synchronization of the pump and seed pulses in an OPCPA system because the method only relies on light pulses without any electronics. We also discuss about issues of residual timing jitter and drift in an optically synchronized amplifier. This amplifier is applied to a few-cycle near-infrared OPCPA system, experimentally demonstrating the usefulness of the optical synchronization in an optical amplifier. This scheme realizes a reliable and simple synchronization technique, resulting in the development of an experimentally applicable OPCPA system.

3.2 Advanced pump pulse synchronization methods

In the previous near-infrared OPCPA system described in Chapter 2, we used the electronic PLL to stabilize two oscillators' repetition rates and, therefore, the timing between the pump and seed pulses at the parametric amplifiers. However the OPCPA system performance was affected by a long term timing drift, which comes from a phase drift in a double balanced mixer used in the PLL circuit. These effects cause a long term timing drift in the time scale of an hour. However, to build a usable OPCPA system for spectroscopic applications, this issue has to be solved.

There exists a novel synchronization method using a digital phase detector for a electronic PLL [166]. This type of a PLL without using a mixer is potentially insensitive to thermal drift

and the amplitude drift and noise of laser oscillators. Timing jitter of less than 20 fs (25 mHz − 10 kHz) was demonstrated by use of a PLL electronics using a digital phase detector. However, this system is fairly complex and its long-term stability has not yet been proven, whereas such tight synchronization precision is superfluous. Even with rigorous cavity synchronization of the two master oscillators in an OPCPA system, the actual pump-seed timing at the nonlinear crystal is affected by the thermal expansion of the beam path length. The beam path length can reach many tens of meters in a typical regenerative or multipass amplifier, which results in the timing drift between the pump and seed pulses by hundreds of femtoseconds.

We have found three possible candidates for the pulse synchronization in an OPCPA system.

K. Finsterbusch *et al.* [167] employed an OPO as a frequency converter device of a pump oscillator to generate new radiation used as seed pulses in an optical parametric amplifier. They used the half of an output from a 1-μm master oscillator as a pump pulse and the other half to pump an optical parametric oscillator generating new radiation around 2 μm to be used as a seed pulse in the parametric amplifier.

H. Zeng *et al.* [168] demonstrated the generation of synchronized seed pulses for a pump amplifier by use of OPA. The pump amplifier was seeded with femtosecond idler pulses of an optical parametric amplifier pumped by femtosecond pump laser pulses, which parametrically amplified and created femtosecond pulses from a CW seed laser.

C. Y. Teisset, the author, and others [169] demonstrated the generation of seed pulses for a pump amplifier using a soliton self-frequency shift phenomena [170] in a photonic crystal fiber (PCF) [171]. A frequency-shifted radiation around 1064 nm was obtained from the PCF injected by a portion of a Ti:sapphire oscillator output pulse[172] and the resulting frequency-shifted radiation was amplified up to sub-mJ level in a diode-pumped Nd:YAG regenerative amplifier. Later not only the frequency-down-shifted radiation but also frequency-up-shifted Čerenkov radiation was used as a seed source for an OPA system [173]. The use of frequency conversion in a nonlinear process is a promising way for tunable seed source generation. However its energy instability and sensitivity to alignment might restrict the performance of an amplifier.

In the next section, thanks to an extremely broadband Ti:sapphire oscillator, we demonstrate the direct seeding of a Nd:YLF regenerative amplifier from a home-made ultrabroadband Ti:sapphire. With this scheme we establish all-optical pulse synchronization for amplifier systems including an OPCPA. We investigate performances of the Nd:YLF amplifier and discuss about issues in this seeding method.

3.3   Seeding of a Nd:YLF amplifier with a Ti:sapphire oscillator

In this section, we describe the development of a home-made Nd:YLF regenerative amplifier and the seeding of the regenerative amplifier with a broadband Ti:sapphire oscillator. The way to control the pump pulse duration is proposed and experimentally demonstrated by use of an etalon in the regenerative amplifier cavity.

Broadband Ti:sapphire oscillator

A key tool for optical synchronization is the broadband Ti:sapphire oscillator , whose spectrum needs to cover the wavelength range from 700 to more than 1000 nm. This is because, high-energy picosecond pulse amplification is possible by use of Nd^{3+}-doped host materials, which have their emission line beyond 1000 nm.

Ti:sapphire has been known as a widely tunable solid-state laser medium [3, 5, 4]. In the 1990s, Ti:sapphire has brought revolutionary advances in laser physics and ultrafast optics. These progresses include a continuous wave lasing operation [174], ultrashort femtosecond laser pulse generation from oscillators [175, 176, 177, 178, 179, 180] enabled by wide-spectral-range dispersion control by use of a prism pair [181, 182, 183]. A new self-mode-locking mechanism, Kerr-lens mode-locking, has enabled simple and reliable operation of the generation of ultrashort laser pulses from a solid-state laser oscillator [184, 185, 186, 187, 188]. Another invention, chirped multilayer coatings (chirped mirror) [34], capable of ultra broadband dispersion control has pushed the limitation of the duration of Ti:sapphire oscillator pulses to the sub-10 fs regime [189, 190, 191, 192]. Further advance in the designing and fabrication technique of chirped mirrors enables simultaneous oscillation in the whole emission bandwidth of Ti:sapphire, resulting in few-cycle laser pulse generation from laser oscillator without external spectral broadening [193, 194, 195, 196]. These ultrabroadband Ti:sapphire oscillators can have its spectrum beyond 1000 nm and make possible the direct seeding of Nd^{3+} amplifiers from a Ti:sapphire oscillator. In this demonstration, we use our home-made ultrabroadband prism-less Ti:sapphire oscillator [196]. In addition, the use of a broadband Ti:sapphire oscillator with megahertz-repetition-rate CEP stabilization [195, 197, 198, 199] permits further straightforward amplification of CEP-controlled pulses in a kilohertz-repetition-rate OPCPA system [103, 136].

Nd:YLF regenerative amplifier

For a home-made diode-pumped laser amplifier used as an OPCPA pump source, we have chosen Nd:YLF as a gain medium from several Nd^{3+}-doped host materials (Nd:YAG, Nd:YLF, Nd:YVO$_4$, and Nd:glass). Nd:YLF has several advantages over other Nd^{3+}-doped host materials such as

1. Natural birefringence (uniaxial crystal)

2. Weak and negative thermal-induced lensing effect [200, 201, 202]

3. Long fluorescence lifetime (500 μs) [203]

4. Low stimulated emission cross section (= 1.8×10^{-19} cm^2 (π, c-axis, 1047 nm) and 1.2×10^{-19} cm^2 (π, a-axis, 1053 nm)) [204, 200]

5. Moderate thermal conductivity (0.06 W/cm/K, two times lower than YAG).

At the same time, Nd:YLF has several disadvantages such as fragility and low pump power fracture limit, low single-pass gain, long population decay time from a terminal lasing level to

the ground state [205, 206], excited-state absorption of laser wavelengths [207, 202], and the difficulty in crystal growth, cutting and polishing processes [208]. Weak thermal lensing and natural birefringence are quite attractive in spite of several disadvantages. The weak thermal lensing simplifies the design of a regenerative amplifier cavity and its compensation. The natural birefringence suppresses thermal-induced depolarization, which is typical in a high power Nd:YAG amplifier and effectively reduces the usable energy. Nd^{3+}-doped YLF has different fluorescence emissions along a-axis and c-axis (optical axis) at 1053 nm and 1047 nm, respectively. In this experiment, because of the weaker thermal lensing along a-axis (1053 nm), the 1053-nm fluorescence line has been chosen for the development of a regenerative amplifier.

Q-switch operation of the amplifier cavity

Picosecond pulse amplification based on Nd^{3+}-doped host materials has been extensively investigated from 1980s both in a multipass amplifier [209] and a regenerative amplifier [210, 211, 212]. Current technologies required for picosecond pulse amplification have been well established and even a picosecond amplifier is commercially available. Therefore we describe briefly the development of the Nd:YLF regenerative amplifier. Fig. 3.1 illustrates the layout of the home-made
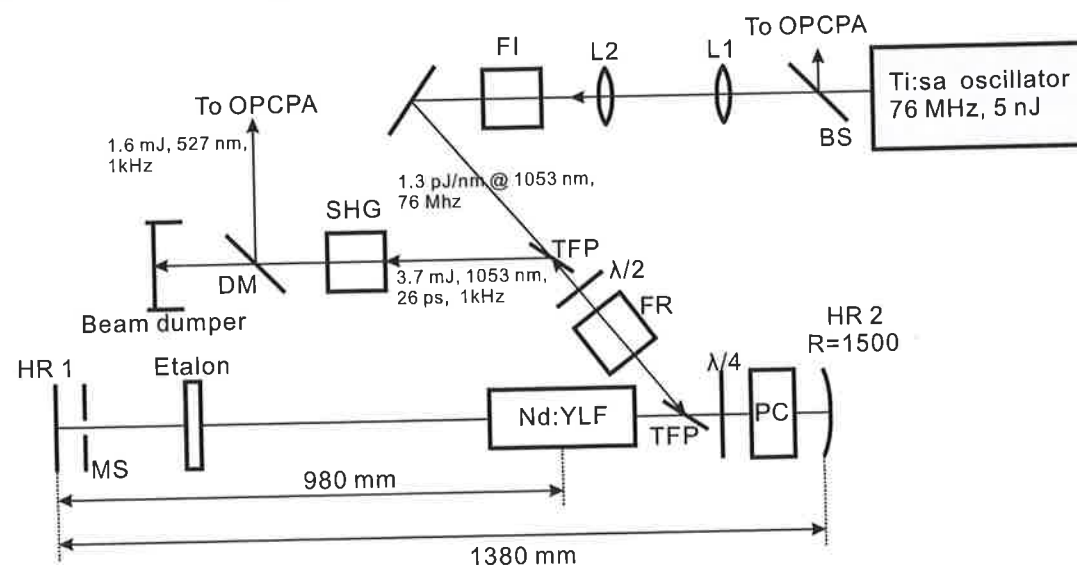

Figure 3.1: Layout of the home-made Nd:YLF regenerative amplifier with the Ti:sapphire seeding scheme. OPCPA: near-infrared optical parametric chirped-pulse amplifier; BS: broadband 50% beam splitter; L1, L2: mode-matching lenses (f_{L1} = 100 mm, f_{L2} = 50 mm); FI: Faraday isolator; TFP: thin-film polarizer; $\lambda/2$: half-wave plate; FR: Faraday rotator; $\lambda/4$: quarter-wave plate; PC: KD*P Pockels cell; ND:YLF: continuous-diode-pumped Nd:YLF laser head; MS: mode selector (pinhole); HR 1: 100% high reflector (radius of curvature = ∞); HR 2: 100% high reflector (radius of curvature = 1500 mm); SHG: second-harmonic generator (10-mm-long type I phase-matching LBO); DM: Dichroic mirror reflecting second harmonics at 527 nm and transmitting fundamental radiation at 1053 nm.

Nd:YLF regenerative amplifier with several optics necessary to utilize a weak seed pulse. A laser crystal, 63-mm-long 3-mm-diameter a-cut Nd:YLF rod, is mounted in a continuous-diode-pumped gain module (model RD40, Northrop Grumman Cutting Edge Optronics). The thermal-lensing focal distance of the diode-pumped rod is measured to be from -2 to -5 m dependent on the pump power. A single-pass gain of about 1.5 is obtained at a pump level above which YLF rods were cracked. The weak thermal lens allows a relatively simple cavity comprising one con-
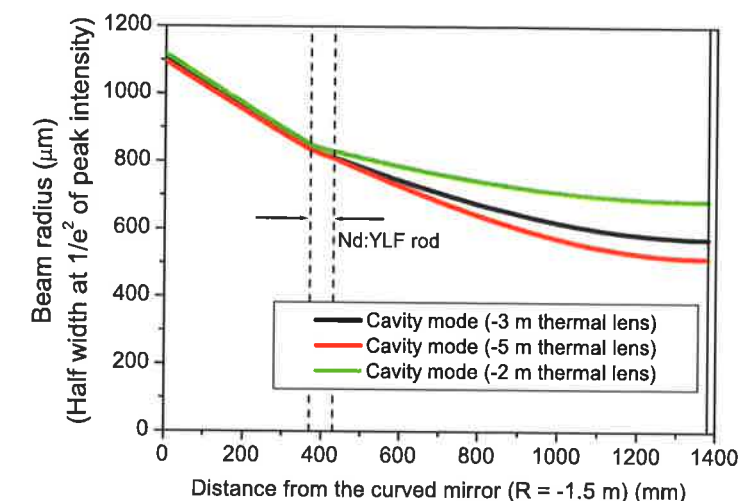

Figure 3.2: Eigenmodes of the Nd:YLF regenerative amplifier cavity with three different thermal lenses.

cave mirror and one flat high reflectors separated by 1.38 m. A calculated cavity eigenmode for three focal distances of the thermal lens are shown in Fig. 3.2, including the effect of propagation in the long YLF rod and the thermally induced lensing effect [54, 69]. The calculation confirms the stable operation of the regenerative amplifier with different thermal lensing focal distances from -2 to -5 m. The AR coating on the Pockels cell crystal is found to be the weakest against the optical damage and, therefore, it is placed close to the curved HR side where the beam size is the largest. Under this condition, after the 400-ns-long opening of the regenerative cavity, ejected Q-switched nanosecond pulses have the energy of above 3 mJ at 1 kHz. The evaluation of the output power and energy with respect to the saturation fluence and power of Nd:YLF and a formula for the estimation of the effective power and energy in the regenerative amplifier are described in Appendix C.

Seeding of the regenerative amplifier

A standard oscillator-amplifier system is seeded with the pulse energy of more than a nanojoule from an oscillator. In this case, amplified spontaneous emission (ASE) would not be a problem because the strong seed could be amplified to the required energy without producing a noticeable amount of ASE. However, in our case, the quite low pulse energy around 1053 nm is available from the Ti:sapphire oscillator whose spectrum is shown in Fig. 3.3(A). The reason is that

the Ti:sapphire oscillator pulses have a weaker spectral intensity at 1050 nm than the central wavelength and the spectral intensity itself is not strong because of its wide spectral breadth. The regenerative amplifier has to be seeded carefully with the weak pulse and characterized because the competition between amplification of the seed and ASE might result in a useless amplifier operation. A spectrum after a 10-nm-wide interference filter at 1050 nm is shown in Fig. 3.3 (B) and this filter is used for estimation of the seed energy. A transmitted seed power after the 10-nm-wide, 50%-transmitance interference filter was about 380 μW at a 76-MHz repetition rate, from which the spectral intensity can be calculated as 1.0 pJ/nm around 1050 nm. An effective seed energy, defined as the spectral width (FWHM) of the Nd:YLF fluorescence (1.3 nm) multiplied by the spectral intensity (1.0 pJ/nm), is 1.3 pJ, which is 2-3 order of magnitude less than the usual seed energy. As seen in Fig. 3.1, we used a mode-matching
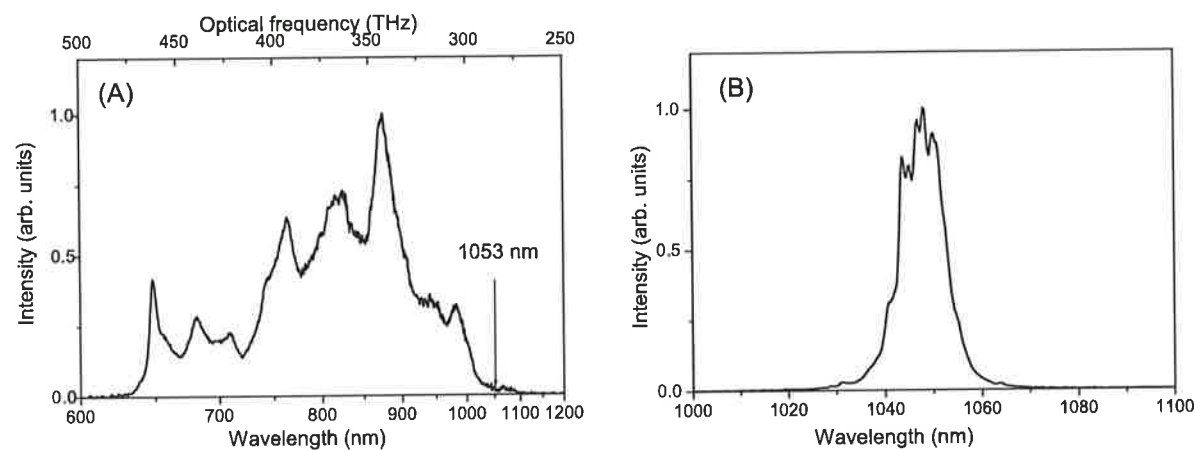

Figure 3.3: (A): Spectrum of the home-made broadband Ti:sapphire oscillator (output power: 400 mW; repetition rate: 76 MHz). (B): Spectrum of the Ti:sapphire oscillator after a 10-nm-wide transmittance interference filter at 1050 nm.

telescope (L1 and L2) and a Faraday isolator (FI) for the seeding procedure. In addition, a translation stage attached to one of the mode-matching lenses allows the fine adjustment of the seed beam divergence to match itself into the regenerative amplifier cavity mode and increase the coupling efficiency. The Faraday isolator was employed to protect the oscillator from the feedback of the regenerative amplifier, which might cause the unstable operation of the oscillator and the cw emission in the mode-locked oscillator. With the careful seed beam alignment, the 1.3-pJ seed pulse was successfully amplified up to 3.7 mJ after 35 round trips in the regenerative amplifier. The maximum output pulse energy of 3.7 mJ is limited by the average-power saturation at the 1-kHz repetition rate [210, 211, 212]. This fact can be seen in Fig. 3.4 where an intracavity pulse train (black line) and an output pulse (red line) of the Nd:YLF regenerative amplifier are shown. The single amplified pulse cannot be saturated by itself because additional round trips did not increase the output energy of the amplified pulse and shifted the whole pulse train by

corresponding round trips. Details about the roll-off frequency between the power and energy saturation are given in Appendix C. The single-pass gain of the amplifier operated at 1 kHz for
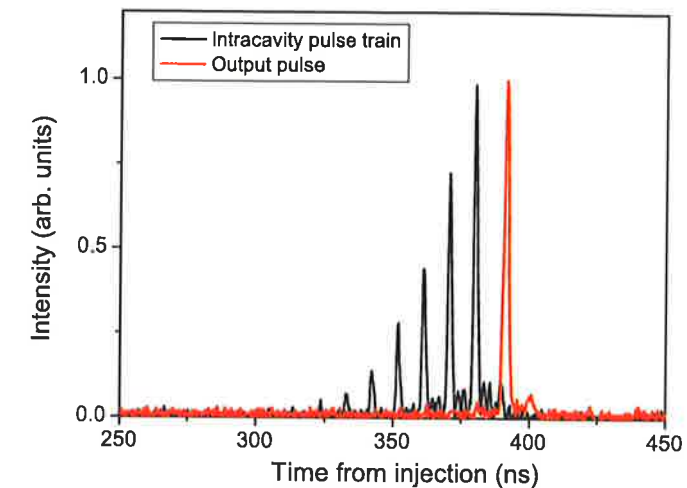

Figure 3.4: Intracavity pulse train (black line) and output pulse (red line) of the Nd:YLF regenerative amplifier.

a certain pulse is estimated to be dependent on the output energy of a 1-ms separated previous pulse. Therefore high energy extracted from the Nd:YLF rod by the previous pulse decreases the gain for a successive pulse. This is a reason why the pulse train was shifted when further round trips were added. This is quite dangerous for the amplifier operation, especially, at a high-repetition rate because the first pulse after a long interception of the injection seed will be amplified more strongly than those in the stationary operation and might cause a damage in the amplifier. Autocorrelation traces of the output pulses from the Nd:YLF amplifier are measured with and without the etalon (a 0.8-mm-thick fused silica plate) in the amplifier cavity and shown in Fig 3.5(A). As can be seen in Fig. 3.5 (A) (red line), the short pulses amplified in the regenerative amplifier without the etalon have a ripple in the temporal pulse profile because self-phase modulation caused by the intense short pulse results in spectral broadening, multiple-pulse production, and self-compression [209, 211]. Therefore we stretch the pulse during amplification in the regenerative cavity by use of an etalon. Smooth amplified pulses with a duration of 26 ps assuming a Gaussian temporal pulse profile are obtained with the 0.8-mm-thick etalon. An output temporal pulse profile is numerically simulated including the effects of etalon spectral filtering and gain narrowing of Nd:YLF. An autocorrelation trace shown in Fig. 3.5(A) (green line) is reconstructed from the simulated pulse. The simulated and measured autocorrelation correspond well with each other. With this simulation, the pulse duration can be predicted and engineered arbitrarily with an appropriate etalon. An analysis of the etalon effect is described in Appendix D. The insertion of the etalon results in a smooth, narrow spectrum (Fig. 3.5(B) (black line)), which corresponds to a spectral resolution of an optical frequency analyzer (AQ6315B, Ando). The spectral width of the amplified pulse can be calculated as 0.04 nm assuming the chirp-free pulse, which is much narrower than the spectral resolution of the optical frequency
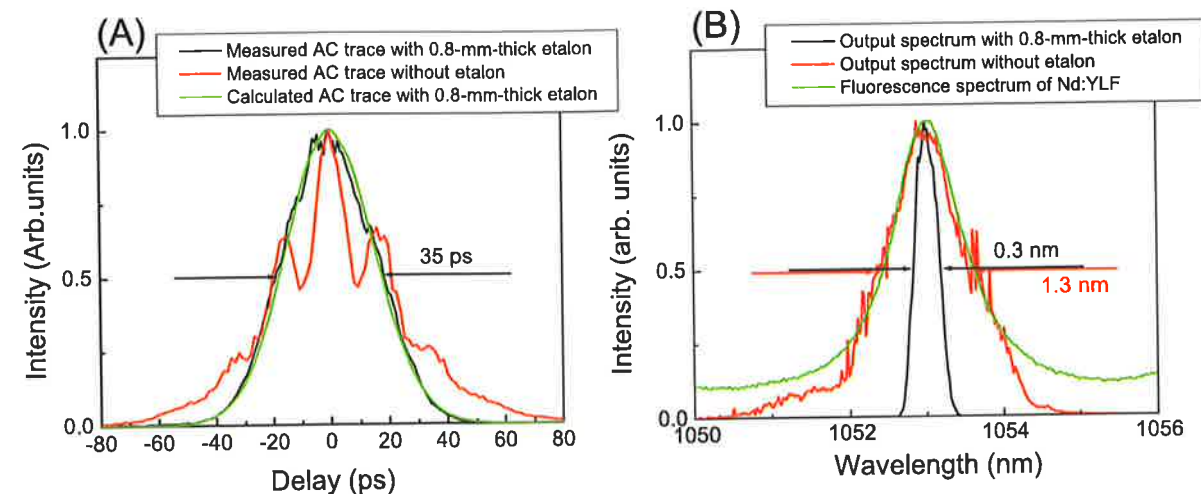
Figure 3.5: (A): Autocorrelation traces with (black line) and without the intracavity etalon (red line) and a calculated autocorrelation trace (green line). (B): Output pulse spectra with the 0.8-mm-thick intracavity etalon (black line) and without the etalon (red line) and a fluorescence spectrum of Nd:YLF (green line). Note that a resolution of the spectrometer is 0.3 nm.

analyzer. In Fig. 3.5(B) (red line), an amplified pulse spectrum without the etalon is shown. This broad spectrum, in contrast to the amplified pulse spectrum with the etalon, indicates the spectral broadening effect due to self-phase modulation in the Nd:YLF rod and KD*P Pockelscell. With the etalon, an estimated B-integral accumulated in the Nd:YLF rod and a KD*P Pockels cell is 7.4. Nonlinear refractive indices of YLF and KD*P are listed in Appendix E. To utilize the output
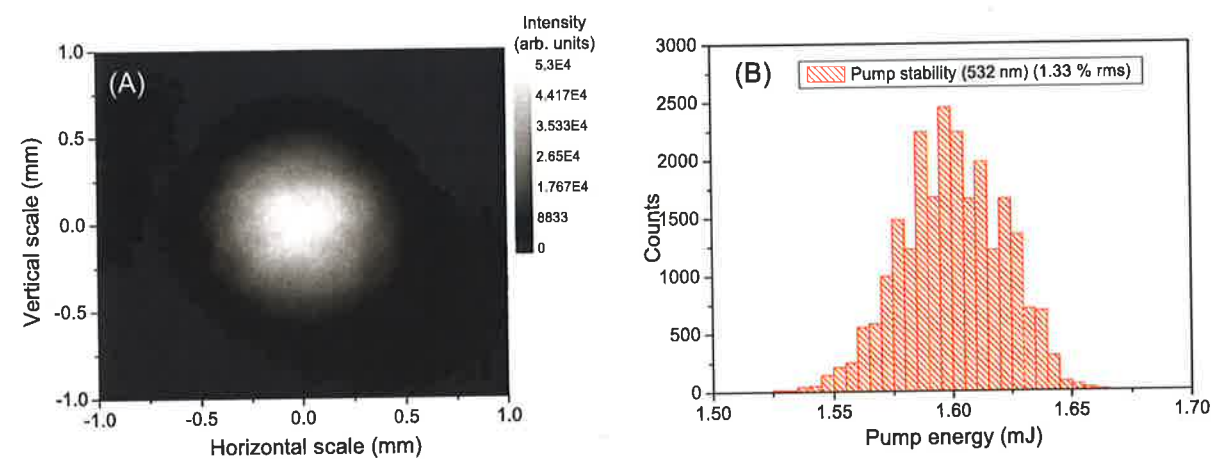

Figure 3.6: (A): Near-field beam profile of second harmonics (527 nm) of the output pulses from the Nd:YLF amplifier. (B): Histogram of shot-to-shot output energies of the second harmonics

pulses from the regenerative amplifier as pump pulses for near-infrared OPCPA, a 1.6-mJ second-harmonic pulse at 527 nm is obtained by frequency-doubling in a 10-mm-long type I phase-matching LBO crystal. A near-field beam profile of second harmonics is shown in Fig. 3.6(A) and has good quality because of the beam mode confined with the pinhole (mode selector) in the regenerative amplifier. The measured energy stability of second-harmonics is 1.33% rms because of average-power saturation. Its histogram is shown in Fig. 3.6(B). Without the seed pulse into the amplifier, the Q-switched pulse produces a 200-μJ second-harmonic pulse. Because ASE would be suppressed with the onset of the seed injection, at least, the energy of 1.4-mJ can be assumed to be contained in the picosecond range. Later, in Section 3.4, a pulse contrast in a picosecond and nanosecond range will be measured and a necessary seed energy to overcome the ASE will be discussed.

Conclusion

In summary, the weak seed pulses from the broadband Ti:sapphire oscillator are successfully amplified in the picosecond Nd:YLF regenerative amplifier. Resultant amplified pulses at 1053 nm have the output energy of 3.7 mJ at the repetition rate of 1kHz and the duration of 26 ps. The smooth temporal profile and spectrum of the amplified pulse are obtained with the insertion of the etalon in the regenerative cavity. The estimated B-integral accumulated in the Nd:YLF regenerative amplifier is 7.4 with the intracavity etalon. The 1.6-mJ, out of which the 1.4-mJ is contained in the picosecond range, second-harmonic pulses with good beam quality and energy stability of 1.33% rms were obtained by frequency-doubling in the LBO crystal.

This picosecond amplifier will be used as a pump source of an optically synchronized near-infrared OPCPA system. The seeding method, demonstrated here, also could be applied to all-optical synchronization of amplifiers based on different gain media in the spectral range from 600 to 1100 nm. This spectral range covers workhorse solid-state laser media such as Ti:sapphire, Yb^{3+}-doped, and Nd^{3+}-doped host materials.

3.4   Picosecond pump pulse contrast measurement

In this section we describe the contrast measurement of the picosecond output pulses from the Nd:YLF regenerative amplifier seeded with the broadband Ti:sapphire oscillator pulses. The pulse contrast is measured by a high-dynamic-range autocorrelator based on third-harmonic generation (THG). The contrast between the main picosecond pulse and background nanosecond ASE will reveal the ratio between the energies contained in the picosecond and nanosecond range. This is important because the seed pulse energy into the amplifier is weak, and the growth of the ASE may severely reduce the amount of the useful energy in the picosecond time scale.

In the previous section, the lowest limit of the amplifier output energy was estimated by a comparison of the amplifier output energies with and without the seed. However, the onset of the amplified seed pulse reduces the gain of the Nd:YLF amplifier (especially in the saturation regime) and, therefore, suppresses ASE. The precise pulse contrast between the picosecond amplified seed and the nanosecond background can be measured by use of a high-dynamic-range

autocorrelator [213, 214, 215]. From this contrast measurement, we could estimate the actual energy ratio in the picosecond and nanosecond range.   The layout of the high-dynamic-range
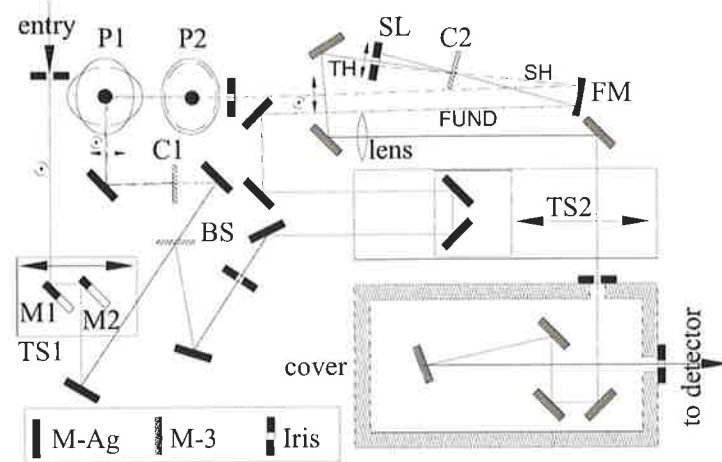

Figure 3.7: Layout of the high-dynamic-range autocorrelator based on THG. TS1: translation stage; M1, M2: partially coated mirrors; BS: pellicle beam splitter; C1: second-harmonic generation crystal; M-Ag: silver mirrors; P1: periscope; P2: height-changer. P1 and P2 are equipped with dichroic mirrors for second harmonics. FM: focusing mirror (f = 100 mm); M-3ω: dielectric mirrors reflecting only third harmonics; C2: third-harmonic generation crystal; SL: slit; lens: f=100 mm; TS2: translation stage for time delay.

autocorrelator is shown in Fig. 3.7. Its detailed description is available in Ref. [108]. The amplifier was modified from the one described in Section 3.3. 2.5-mJ output pulses from the regenerative amplifier are successively amplified up to 6 mJ by two-pass amplification in a post-amplifier comprising a five-diode-pumping home-made gain module with a 4-mm-in-diameter 12-cm-long a-cut Nd:YLF rod. The 6-mJ output pulses are characterized with the above described autocorrelator. The measured autocorrelation traces are shown in Fig. 3.8. To collect these data, we varied the seed energy and adjusted correspondingly the round-trip number to maintain a constant output power from the amplifier. The inset in Fig. 3.8 shows the relative fraction of the Q-switched pulse energy obtained by the interception of the seed with respect to the total amplifier output energy when the seed pulse is injected. Unfortunately, the scanning range of the third-order autocorrelator does not cover the entire extent of the nanosecond pedestal. It is shown in Fig. 3.8 that the increase of the nanosecond background results from the decrease of the seed energy. In the autocorrelation trace, the intensity of the leading pedestal is higher than the tailing pedestal. This is because the population inversion of the gain medium (Nd^{3+}) decays during the passage of the amplified pulse so that, always, the leading edge of the pulse feels higher gain than the tailing edge and is more amplified [54, 216, 31]. We assume that the intensity of the nanosecond background is flat in time and has a duration of 6 ns, which is determined by the switching time of the Pockels cell. Under these assumptions, only a 2.3% fraction of the total output energy is contained in the nanosecond pedestal if the nanosecond pedestal has the relative intensity of
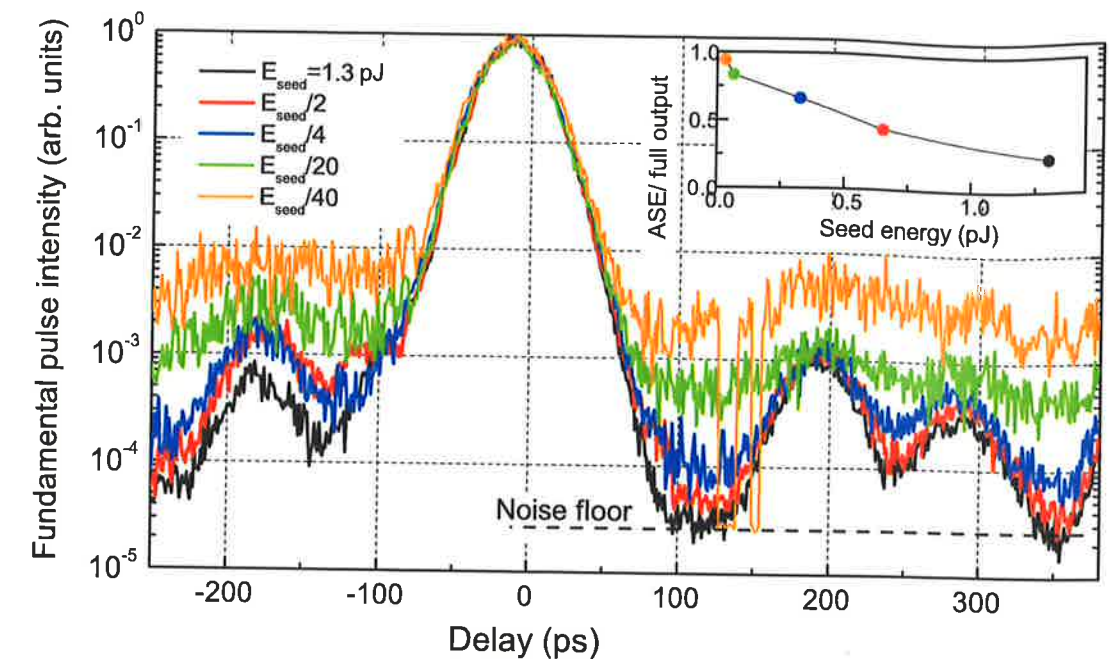
Figure 3.8: High-dynamic-range autocorrelation traces of the output pulses from the Nd:YLF amplifier chain seeded with the full seed energy (black line) from the broadband Ti:sapphire oscillator, half energy (red line), quarter energy (blue line), one-twentieth energy (green line), and one-fortieth energy (orange line). Inset: ratios between output power of seeded regenerative amplifier and Q-switched output power in the absence of the seed pulse. Seed energies and color notations are the same as in main panel.

10^{-4} respect to the picosecond peak intensity. If the nanosecond background intensity is a 10^{-3} level, the fractional energy of the nanosecond pedestal increases to 18.8%. The measurements, presented in Fig. 3.8, prove that the seed energy of 1.3 pJ is sufficiently high to suppress the ASE background and produce a reasonably clean picosecond pump pulse for the OPCPA system. It could be concluded that the ASE energy is strongly reduced when the seed is injected because the estimated energy of the nanosecond background, when the seed is injected, from the autocorrelation trace is not equal to the output energy of the Q-switched pulses. For example, for the half seed energy (red line) in Fig. 3.8, the nanosecond background energy can be estimated as much lower than 18.8% because of its intensity is lower than 10^{-3} of the peak intensity. However, in the inset of Fig. 3.8, the Q-switched pulses without the seed pulse is almost 50% of the total output. Amplification of ASE is reduced by at least 3 times by the onset of the seed pulse injected. As an empirical criterion, when the Q-switched pulse energy is less than the half of the amplified seed energy, we noticed that nanosecond background is reasonably suppressed and the main picosecond pulse contains the substantial amount of the output energy. Preferably, this criterion is only dependent on the output energies from the amplifier with and without the seed pulse. Notice that, in some case, this criterion could not be applicable, if the cavity mode dramatically changes with the seeded and unseeded amplifier operation by the different thermal

condition and different nonlinear effects.

In summary, we have characterized the output pulses from the regenerative amplifier seed with the broadband Ti:sapphire oscillator by use of the high-dynamic-range autocorrelator based on THG. The third-harmonic autocorrelation characterization determines the intensity contrast of the main picosecond pulse and the nanosecond ASE, consequently, the energy ratio between them. The measured data confirmed the reasonably clean pulse obtainable with the weak seed pulse from the Ti:sapphire oscillator. The criterion for clean pulse amplification have been derived and can be applied to general cases when the seed energy is low.

3.5   Timing-jitter and drift problems in the OPCPA system

In the previous section, we demonstrated the seeding of the home-made Nd:YLF regenerative amplifier with the Ti:sapphire laser and the characterization of its output pulses by use of high-dynamic-range autocorrelation. Originally, the main motivation of this development is to eliminate timing jitter and drift between the pump and seed pulses in the OPCPA system. In Chapter 2, electronic synchronization of two oscillators used in the near-infrared system demonstrated its excellent short-term timing lock within 5 ps. However we have observed long-term timing drift resulted from the thermal effect of the double-balanced mixer and its phase noise converted from the laser amplitude noise, which are critical for spectroscopic applications such as high-harmonic generation, attosecond pulse generation, and attosecond real-time spectroscopy. We discuss about possible source for residual timing jitter and drift existing in optically synchronized amplifiers. We separate the timing issues into two types, namely, short-term timing jitter (shot-to-shot fluctuation) and long-term timing drift and discuss them one by one.

Short-term jitter

We used a cross-correlation technique based on OPA to examine timing fluctuation within tens of minutes [217]. The experimental set up is described in Fig. 3.12 in the next section. The second-harmonic pump pulses from the regenerative amplifier followed by the frequency-doubling LBO crystal are cross-correlated with unstretched pulses directly from the broadband Ti:sapphire oscillator. The second harmonics and the unstretched pulses act as the pump pulses and seed pulses in type I NOPA by use of BBO. This cross-correlation technique provides the highest temporal resolution to assess the timing jitter between the OPCPA seed and pump pulses. We artificially shortened the amplified pulse from the Nd:YLF amplifier by removing the intracavity etalon so that the self-compressed laser pulse train was obtained and used for the parametric cross-correlation. The measured trace, shown in Fig. 3.9, has the width of only 1 ps (FWHM), which gives the upper limit of the possible synchronization imperfection in our system. This short temporal resolution is obtained not only by the self-compressed pulse but also by the extreme nonlinearity of OPA, effectively improving the correlation resolution to less than the pump pulse duration. Although the shot-to-shot timing fluctuation is difficult to assess, a novel work to examine shot-to-shot timing fluctuation between output pulses from a Ti:sapphire regenerative amplifier and from a Ti:sapphire oscillator has been achieved by use of the detection of the
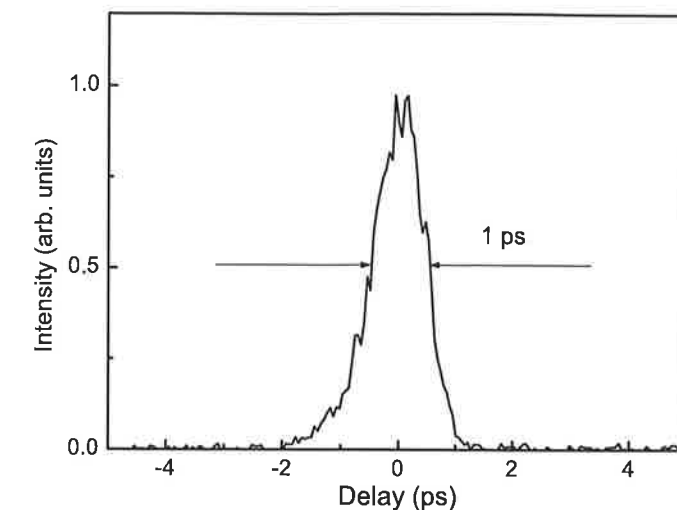
Figure 3.9: OPA-based cross-correlation trace, showing the upper limit of the timing-jitter of less than 1 ps.

sum-frequency spectrum between the chirped and chirp-free pulses [218]. With this method, they have observed pulse timing fluctuation of less than $\pm$ 20 fs (100-m-long propagation in the regenerative amplifier cavity and the oscillator). They found the cause of the short-term timing fluctuation related to the frequency of the alternating current of the power supply. The result of the work [218] is consistent with our experimental result and shows potential precise synchronization of much less than picosecond time scale.

Long-term timing drift

The long-term drift, regardless of the type of pump and seed pulse synchronization, is related to the thermal expansion of the cavities of the pump amplifier and the seed oscillator. An illustration of the timing synchronization scheme in the OPCPA system is shown in Fig. 3.10. The timing-drift problem results from the relative path length drift between two arms from a splitting optic to a combining optic. In the case of the OPCPA system, shown in Fig. 3.10, the path length corresponds to the distance from the output coupler to the OPA stage through the laser amplifier. Note that the splitting optic in this case is not the beamsplitter but the output coupler. This can be understood by the fact that, in principle, the beamsplitter can be replaced by the Pockels cell, which can select out a seed for the laser amplifier and the other seed for the parametric amplifier at a different time. A seed pulse 1 (seed 1 in Fig. 3.10) picked up by the Pockels cell (PC in Fig. 3.10) travels in the amplifier, while another seed pulse 2 (seed 2 in Fig. 3.10) is stored in the oscillator and waits for the amplified seed pulse 1 to be ejected from the amplifier. Then, when the amplified seed pulse 1 is ejected from the laser amplifier, the seed pulse 2 is ejected from the oscillator and the two pulses are temporally and spatially overlapped at the OPA crystal. The amount of timing drift depends on relative thermal variation of the pump and seed arms. The pump arm length is governed by the total path length in the laser amplifier (for the case of the
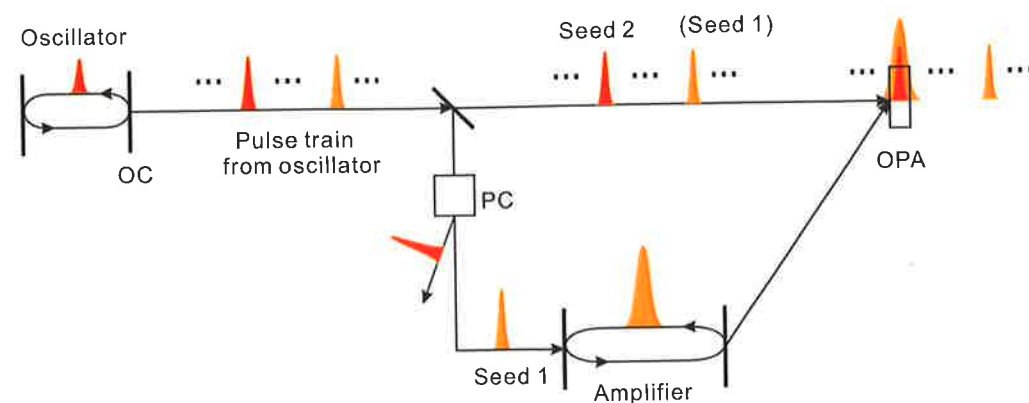
Figure 3.10: Illustration of the optical synchronization scheme in the OPCPA system. OC: output coupler; BS: beam splitter; PC: Pockels cell; OPA: optical parametric amplifier; seed 1: seed pulse used for the laser amplifier; seed 2: seed pulse used for the parametric amplifier
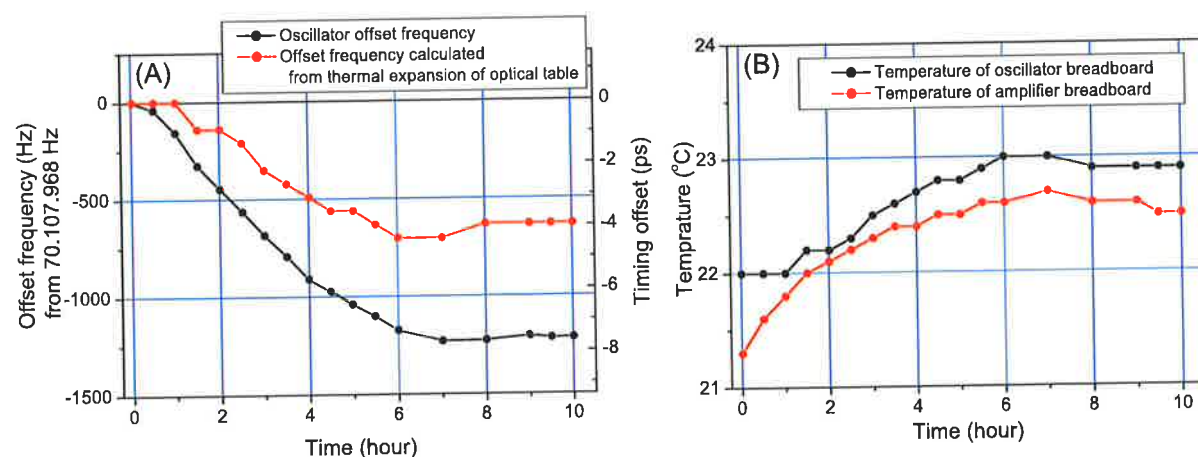

Figure 3.11: (A): Repetition rate drift of the Ti:sapphire oscillator (black curve) and calculated repetition rate drift (red curve) from the temperature drift of the oscillator breadboard. A right y-axis represents the corresponding timing drift after the 700-ns-long (210-m-long) travel in the regenerative amplifier. (B): Temperature drifts of the oscillator (black curve) and the amplifier breadboards (red curve).

regenerative amplifier, the cavity length in one round trip × the round-trip number). The seed arm length is governed by the oscillator cavity length × its round-trip number. For example, assuming a 100-m path length on a stainless steel breadboard, a relative temperature change by 0.1 K between the seed and the pump arms causes 0.3-ps timing shift. 0.1-K temperature stabilization of the optical table represents the practical limit for the laboratory environment. Further improvement of the timing synchronization has to rely on active stabilization of both the oscillator and the regenerative amplifier cavities [219]. Such measures would be required for pump and seed pulses with the duration of less than a couple of picoseconds. The thermal drift of the oscillator and the laser amplifier bases was measured to estimate the amount of the slow drift in our infrared OPCPA system, which will be described later in Chapter 4. In Fig. 3.11 the repetition rate ((A) black curve) of the Ti:sapphire seed oscillator and the temperature of the oscillator breadboard ((B) black curve) and the regenerative-amplifier breadboard ((B) red curve) are shown. In Fig. 3.11(A) (red curve), expected oscillator-repetition-rate shift is calculated from temperature drift of the oscillator breadboard, shown in Fig. 3.11(B) (black curve). This relationship verifies that the oscillator frequency shift is related with the thermal expansion of the breadboard. However the factor of two difference between the frequency shifts, shown in Fig. 3.11(A), has not been attributed yet. The estimated timing drift amounts to about 8 ps in the oscillator cavity. However the similar tendency of the temperature drift between the oscillator and the amplifier breadboard could result in the cancellation with each other. Several-hour-long warming up time also stabilizes the optical table and breadboard temperatures, resulting in less than 2-ps drift after warming up. Although day-to-day timing shift in OPCPA systems has been observed because of the repetition-rate shift of the oscillator and the environmental temperature change, any shift in one day has not been noticed so far.

In summary, in this section, short term and long term timing drifts have been investigated by the cross-correlation technique based on OPA and estimated by temperature drifts in the oscillator and the amplifier, respectively. 100-m beam path length on the stainless steel would cause 0.3-ps timing drift by 0.1-K temperature change. Comparison between electronic and optical synchronization for an OPCPA system is summarized in Appendix B.

3.6 Near-infrared OPCPA system with optical synchronization

In this section, we apply the optically synchronized picosecond pump pulses from the Nd:YLF regenerative amplifier to a near-infrared OPCPA system similar to the one represented in Chapter 2. The scheme of the optically synchronized OPCPA system is illustrated in Fig. 3.12. A Ti:sapphire oscillator pulse is split by a 50% broadband beamsplitter and one of the pulses is directed into the OPA stage following a pulse stretcher chain to expand temporally the seed pulse approximately to 22 ps to ensure appropriate overlap with the 26-ps pump pulse. The stretcher chain consists of a SF57 prism pair, the Dazzler, and a 10-cm-long SF57 block. The energy of the transmitted seed pulse after the stretchers is reduced to 50 pJ from about 2.5 nJ (2% throughput) because of the low diffraction efficiency of the broadband Dazzler and losses of the optics. The
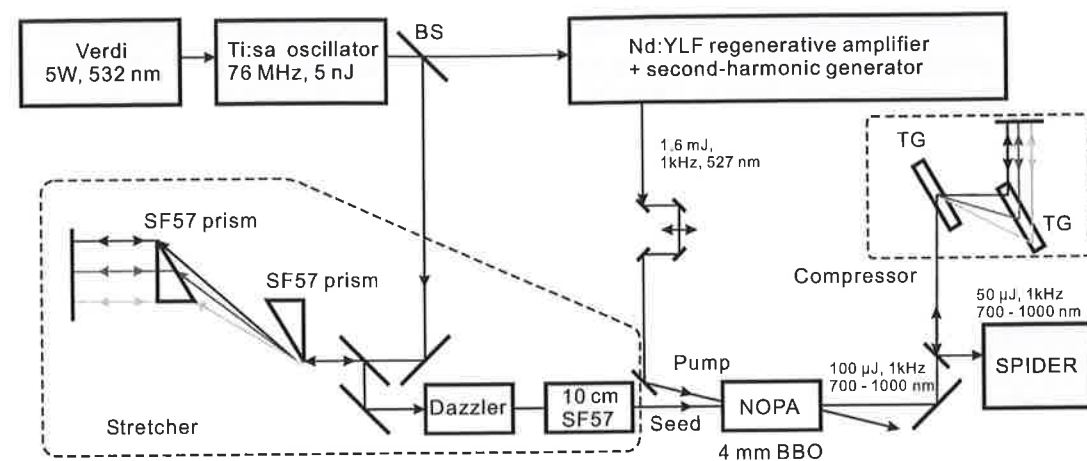
Figure 3.12: Near-infrared OPCPA system by use of the optically synchronized pump laser. BS: broadband 50% beam splitter; NOPA: noncollinearly phase-matched optical parametric amplifier using BBO; TG: transmission grating; SPIDER: SPIDER apparatus.

noncollinear parametric amplifier employs a single-pass geometry in a 4-mm-long type I phase-matching BBO. We used the same noncollinearity angle and phase-matching angle as for the first parametric amplifier stage in the near-infrared OPCPA system described in Chapter 2. The pump intensity on the BBO crystal is estimated as about $15\text{GW}/\text{cm}^2$ assuming the pulse duration of 26 ps for the second harmonic. The near-field beam profile of the amplified seed pulse with the energy of 100 μJ (corresponding gain of 2×10^6) is shown in Fig. 3.13(A). The shot-to-shot energy stability was measured as 11% (RMS) and its histogram is shown in Fig. 3.13(B). Although we did not observed the shot-to-shot shift of the amplified spectrum, which could result from the timing-jitter between the pump and the stretched seed, the unsaturated operation in the parametric amplifier causes degradation of the energy stability of the output pulses. This can be easily solved by use of a new second OPA stage by use of a stronger pump laser. However, in this section, we concentrate on the development of the OPCPA system based on the optical synchronization and its characterization. In Fig. 3.13 (A), the ellipticity of the amplified-beam results from the different phase-matching tolerances along the signal polarization direction and along the pump polarization direction [141, 84, 142]. The amplified pulses are recompressed in a compressor consisting of a pair of 900 lines/mm transmission gratings (Wasatch Photonics) separated by about 14 mm. The throughput of the pulse compressor is about 50%. The amplified spectrum after the grating compressor (solid line) is shown in Fig. 3.14 (A). The compressed pulses were characterized by SPIDER. The residual spectral phase retrieved by a SPIDER analysis program was corrected for by use of the feedback mechanism from a SPIDER system to the Dazzler.

The residual spectral phase (dashed line) obtained after several feedbacks is plotted in Fig. 3.14(A). Fig. 3.14(B) depicts the retrieved temporal pulse profile with the duration of 11.3 fs (FWHM) (solid line), a transform-limited pulse profile (dashed line) calculated from the amplified spectrum (its duration is 8.3 fs (FWHM)), and the retrieved temporal phase (dotted line).
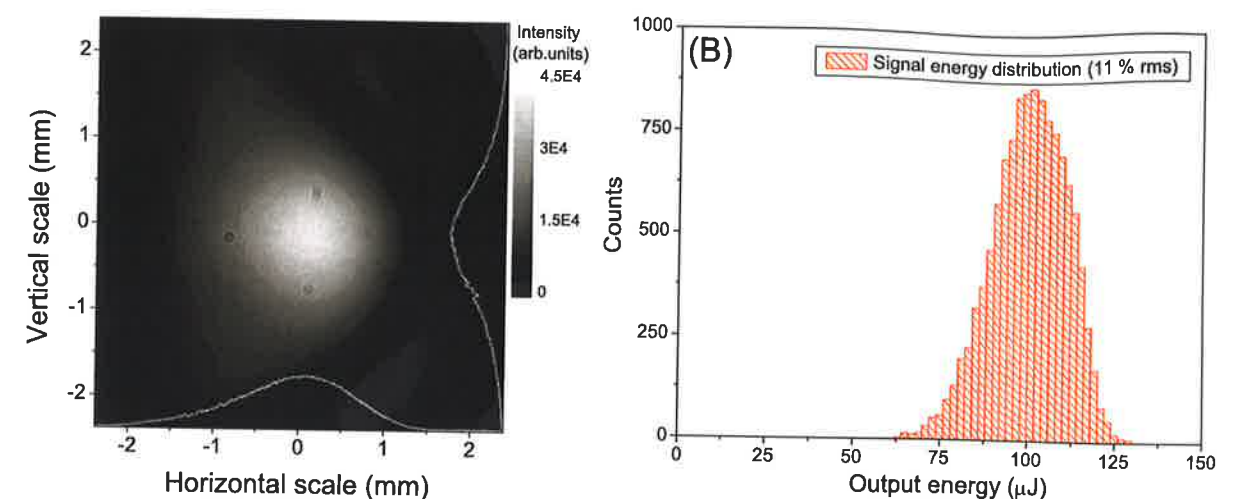
Figure 3.13: (A): NOPA output beam profile. (B) Shot-to-shot output energy histogram. The energy stability is 11% RMS.

Figure 3.14: SPIDER results of the amplified pulses from optically synchronized NOPCPA. (A): measured amplified spectrum (solid line); retrieved spectral phase (dashed line). (B): retrieved temporal pulse profile (solid line); transform limited pulse calculated from the measured amplified spectrum assuming flat spectral phase (its duration is 8.3 fs (FWHM)); retrieved spectral phase (dotted line).
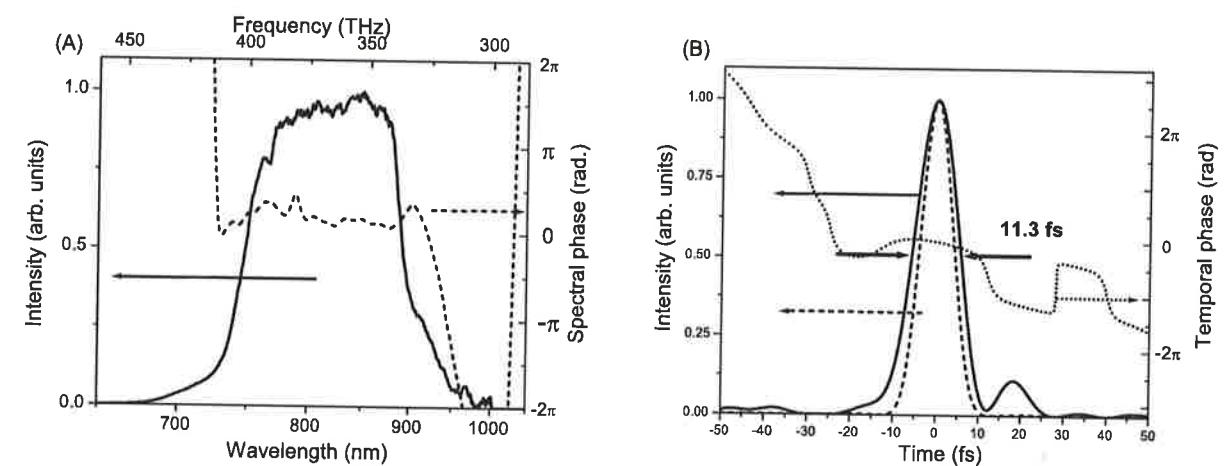
High-order dispersion (mainly third-order dispersion) of the 10-cm-long SF57 block could not be fully compensated over the entire spectral range of interest because of the limited aperture of the second prism in the prism pair and the limited dispersion tuning range of the Dazzler.

In summary, the optically synchronized pump amplifier is applied to the 11-fs near-infrared OPCPA system. These amplifiers are seeded with the common single broadband Ti:sapphire oscillator. The main problem, the timing-jitter are substantially reduced so that we could not notice any timing-drift during the experiment and the fluctuation of the amplified spectrum, which would result from the short-term timing fluctuation.

3.7   Upscaling of output pulse energy from an amplifier seeded with weak pulses

Upscaling of the output energy from an amplifier chain seeded with a several-picojoule pulse is an interesting topic. In our laboratory, Ti:sapphire oscillators are being modified to further extend the infrared wing of the output spectrum to attain the strong infrared spectral intensity. As a result, so far, a modified Ti:sapphire oscillator has produced five times more energy at 1053 nm compared to the oscillator used in the seeding experiment. With this seed, two post amplifiers following the Nd:YLF regenerative amplifier boost the pulse energy from 4 mJ to 11 mJ. The ratio between the output energies with and without seed pulses is kept below 0.5, which satisfies the criterion described in this section. As an example, a much larger 100-ps, 1.5-J, 10-Hz Nd:YAG amplifier system [220] is successfully seeded with the frequency-shifted output pulse from the photonic crystal fiber [169]. A 1-mJ output pulse from a Nd:YAG regenerative amplifier seeded with an about 1-pJ pulse from a photonic crystal fiber is further amplified to 1.5 J in a chain of post-amplifiers. The fundamental energy of the Q-switched pulse in the absence of the seed pulse is measured as 150 mJ. This Q-switched pulse energy, based on the same criterion, corresponds to the less than 2% ASE energy contained in the 1.5-J output. Therefore, we could conclude that the main source of the contrast deterioration of the amplifier output pulses is the regenerative amplifier because of its very high gain, typically 10^9 in the case of weak seeding. Consequently, an unsaturated power booster following the regenerative amplifier does not enhance the ASE background so much because of its low gain.

3.8   Conclusion

We have implemented direct optical seeding of the picosecond Nd:YLF regenerative amplifier amplifier with the broadband Ti:sapphire oscillator. This novel scheme established reliable optical synchronization of two amplifiers operating in non-overlapping spectral ranges. This method was applied to the broadband OPCPA system by use of the optically synchronized pump source. The use of a common Ti:sapphire oscillator dramatically simplifies the whole OPCPA system in comparison with OPCPA schemes adopting two oscillators synchronized by use of the PLL electronics. This work also offers a blueprint for building large-scale OPCPA systems that would be particularly suitable for the applications in high-field physics, extreme nonlinear optics, and

attosecond spectroscopy. The demonstrated simple OPCPA system would be necessary for the attosecond real-time spectroscopy, high-harmonic generation, and attosecond optics. In addition, the demonstrated synchronization method opens a new way for all-optical synchronization of high-intensity laser amplifiers based on various gain media that do not have mutual spectral overlap. This optically synchronized Nd:YLF amplifier system will serve as a pump source of an infrared OPCPA system in the next chapter with additional boosting power amplifiers after the regenerative amplifier.

Chapter 4

Few-cycle high-energy infrared pulse generation by use of OPCPA

4.1   Introduction

In this chapter, we will describe the design and experimental implementation of an broadband optical parametric amplifier of chirped pulses in the infrared. Unique high-energy, ultrafast optical pulses at 2.1 μm are generated by this OPCPA system. Seed pulses are generated by difference frequency generation (DFG) and their CEP is self-stabilized [221, 222, 223]. We use the Nd:YLF amplifier seeded with a Ti:sapphire oscillator, whose development was described in Chapter 3, as a pump source for the infrared OPCPA system. A pump amplifier chain is upgraded by additional post amplifiers following the regenerative amplifier and produces 11-mJ, 40-ps, 1053-nm pulses at 1kHz.

In Chapter 5, we demonstrate preservation of the CEP of the seed pulses during parametric amplification. The obtained few-cycle infrared pulses are applied to generation of the visible supercontinuum. The supercontinuum and THG of the fundamental pulses make possible a novel f-to-$3f$ nonlinear interferometry and the detection of the CEP of the infrared pulses.

4.2   Infrared seed pulse generation by use of difference frequency generation

In this section, we review infrared optical light sources and describe generation of an infrared broadband seed source for the infrared OPCPA system based on DFG [224] in periodically poled lithium niobate (PPLN). High-energy pulses from a commercial Ti:sapphire amplifier are spectrally broadened by self-phase modulation (SPM) and used as pump pulses of DFG.

A straightforward way to obtain infrared seed pulses is to use a broadband oscillator based on a laser medium. However so far the shortest pulse duration of laser oscillators operating around 2 μm has been limited to sub ps [225].

Because of the lack of an appropriate ultrafast laser oscillator, in the infrared, an optical

parametric oscillator (OPO) [226, 227, 228] has been used as an ultrashort tunable light source. However, for our purpose, the OPO does not provide an important feature: few-cycle pulse generation.

Another approach to obtain the infrared radiation is optical rectification of the broadband optical pulses. This scheme as well as the use of a photoconductor and the electro-optic effect is frequently used in ultrafast terahertz (THZ) optics and spectroscopy [229, 230, 231]. Recent advance in the ultrabroadband laser oscillator in the visible has naturally resulted in generation of high-photon-energy THZ radiation, which has reached the mid-infrared range. Mid-infrared pulses at 7 μm has been demonstrated by use of optical rectification (DFG) of sub-20-fs Ti:sapphire oscillator pulses [232]. Few-cycle or even mono-cycle pulses with the stable electric field, which indicates the stabilization of the CEP of the THZ radiation, is exactly what we want to have as a seed source except its wavelength.

By use of DFG and its self-stabilization mechanism of the CEP, a previous work by T. Fuji et $al.$ in our group demonstrated detection and stabilization of a carrier-envelope offset (CEO) frequency based on the interference between a 1.4-μm difference frequency (DF) and Ti:sapphire fundamental spectral components at this wavelength [198]. This mechanism satisfies two important requirements for the OPCPA seed source. First, with an appropriate nonlinear crystal, 2-μm broadband radiation could be expected to be acquired simply because of less requirement of the bandwidth of the Ti:sapphire oscillator spectrum. Secondly, the CEP of the DF generated by the CEP-unlocked pump laser pulse is automatically self-stabilized [233, 221, 222, 223]. The mech-
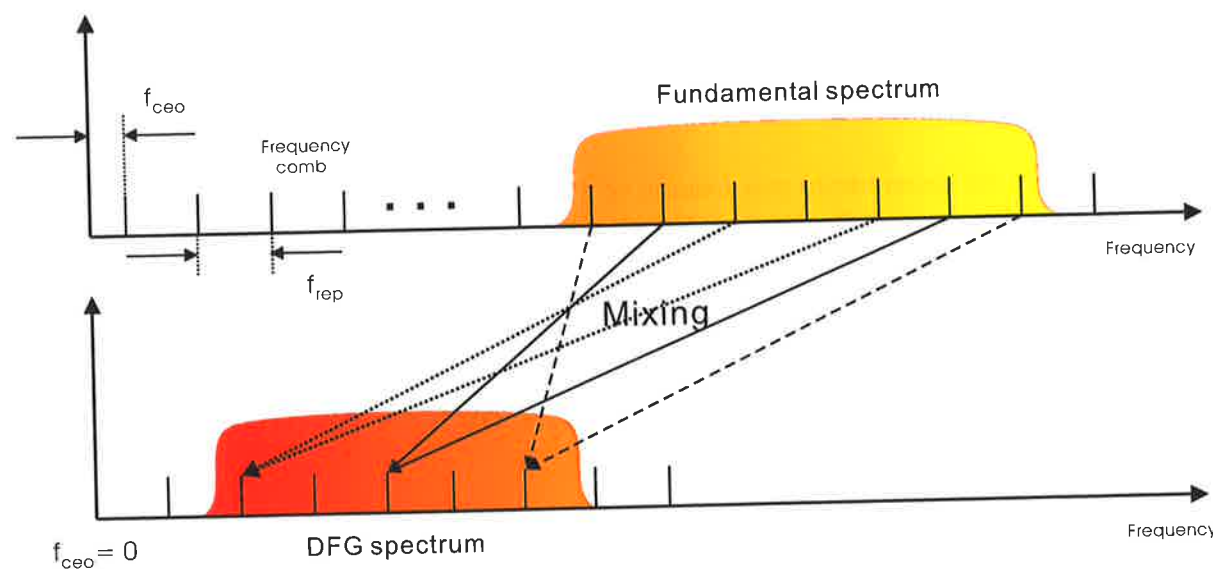

Figure 4.1: CEP stabilization and CEO frequency stabilization in a DFG process. f$_{ceo}$: CEO frequency and f$_{rep}$: laser repetition-rate frequency.

anism of DFG and its CEP stabilization is illustrated in Fig. 4.1. This can be easily understood by the spectral domain representation of pump laser frequency combs. An optical frequency

of each comb in the DF spectrum is the laser repetition rate multiplied by an integer because each comb is generated by parametric mixing between the different combs of the fundamental spectrum whose offset frequencies are the same and these offset frequencies are cancelled out through the DFG process. This can be confirmed by use of simple mathematics. A DF (f_{DFG}) generated by the difference frequency mixing between the oscillator combs ($nf_{rep} + f_{CEO}$) and ($mf_{rep} + f_{CEO}$) depends only on the laser repetition rate f_{rep} as

$$f_{DFG} = nf_{rep} + f_{CEO} - (mf_{rep} + f_{CEO}) = (n-m)f_{rep} \qquad (4.1)$$

, where f_{rep} and f_{CEO} represent the laser repetition rate and the CEO frequency, respectively. Therefore, the pulse-to-pulse CEP does not change and every DF pulse has a temporal phase defined by the exciting-pulse envelope. Resultant self-stabilization of the CEP is a quite useful feature, when few-cycle laser pulses are used as a driver for HHG and attosecond optics and spectroscopy [19], because a peak value of the electric-field amplitude of the few-cycle optical pulse becomes dependent on the CEP [234]. In a previous infrared OPCPA system described in Ref. [235], a home-made broadband Ti:sapphire oscillator was used for DFG, resulting in a DF with the energy of 2 pJ. An infrared parametric amplifier seeded with this weak DF produced about 50-μJ, 20-fs pulses around 2 μm. The energy is limited to 50 μJ because further amplification just results in the dramatic increase of the ASF and it is difficult to distinguish the amplified pulse energy from the ASF energy. Therefore, higher-energy seed pulses are required to achieve the higher output energy without suffering from the ASF. Since then we have changed the method to generate the seed pulse by use of DFG, aiming at the high-energy seed source. High-energy 100-fs, 1-mJ, 1-kHz pulses at 800 nm are obtained from a commercial Ti:sapphire regenerative amplifier followed by an additional two-pass post amplifier (Spitfire, Spectra physics) and are sent into a gas cell containing 3-bar Kr to broaden its spectrum by SPM. The output beam is weakly focused with a 1-m lens into the gas cell, forming a long single filament visualized by ionization of Kr atoms. This long filament is sustained by the balance of three effects: self-focusing, natural divergence of the laser beam, and plasma defocusing [236, 237, 238]. The narrowband 100-fs pulse is spectrally broadened in the long filament where the high laser intensity is kept to enhance spectral broadening based on SPM. Generated broadened pulses show, recently, self-compression phenomena in the filament, leading to few-cycle high-energy pulse generation [239, 240, 241, 242]. Note that this is one of promising ways toward high-energy, few-cycle, near-infrared laser pulse generation, although the infrared few-cycle pulses can be uniquely obtainable by use of the OPA process under current technology. Fig. 4.2 (A) shows the fundamental spectrum (black line), the broadened spectrum before band-stop mirrors (red line), and the broadened spectrum after the band-stop mirrors (green line). Fig. 4.2 (B) shows the spectrum of the supercontinuum before the band-stop mirrors in logarithmic scale. The home-made band-stop mirrors are used behind the gas cell to eliminate the strong central part of the output broadened spectrum from the gas cell, while maintaining smooth variation of the spectral phase of the reflected pulse.

The broadened pulse is temporally compressed by use of a set of chirped mirrors after the band-stop mirrors. The pulse compression by 4 bounces on chirped mirrors seemed to be optimum for generation of the broadband DF spectrum in 1-mm-long MgO-doped periodically-poled stoichiometric lithium niobate (MgO:PPSLN) crystals. After 4 bounces on the chirped mirrors,
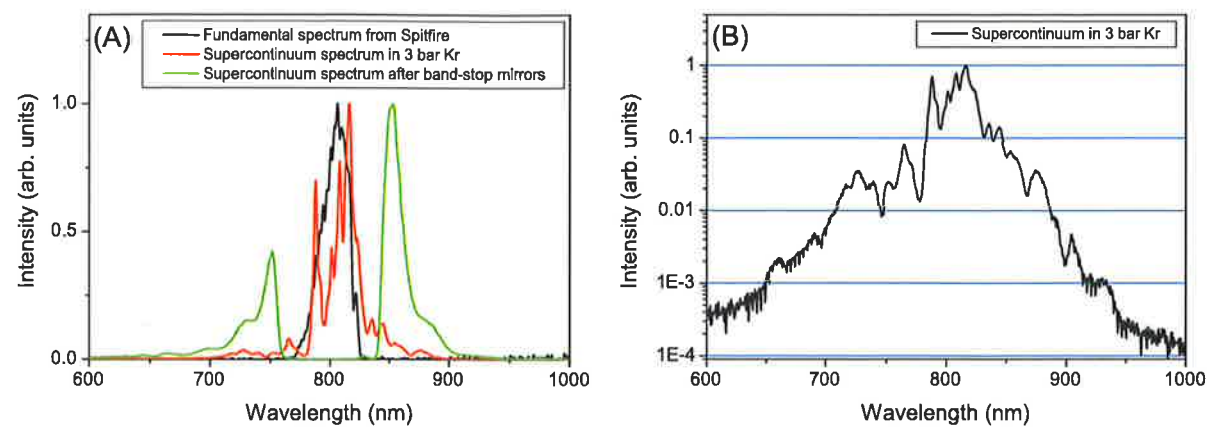
Figure 4.2: (A): Fundamental spectrum (black line), broadened spectrum before the band-stop mirrors (red line), and broadened spectrum after the band-stop mirrors (green line). (B): broadened spectrum before the band-stop mirrors in logarithmic scale.
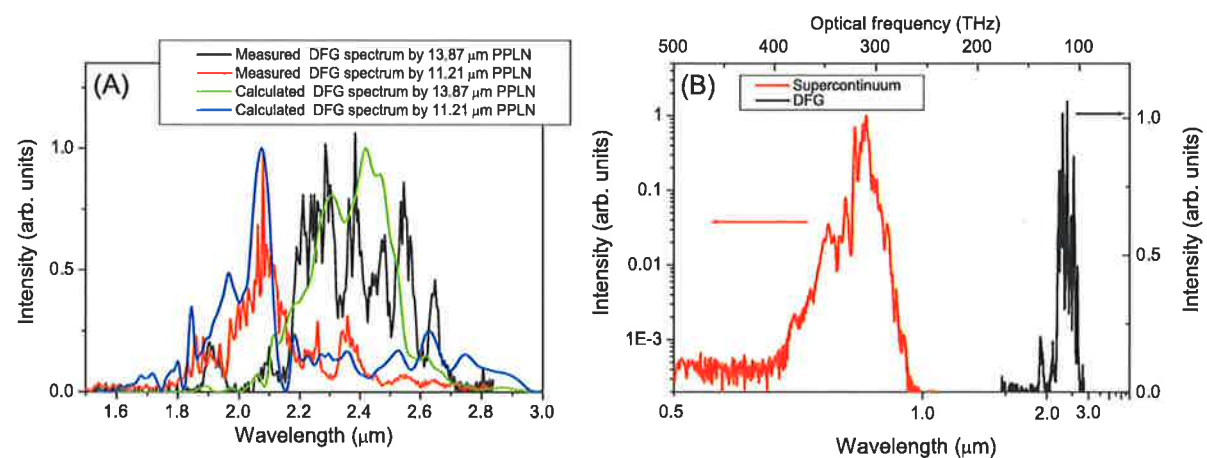

Figure 4.3: (A): Measured DF spectra generated in the MgO:PPSLNs with the quasi-phase-match (QPM) period of 13.87 μm (black line) and 11.21 μm (red line). Simulated DF spectra with the QPM period of 13.87 μm (green line) and 11.21 μm (blue line). (B): Broadened spectrum before the band-stop mirrors (red line) and DF (black line) spectra in the frequency domain, showing correspondence of the central frequency of the DF to the frequency width between the blue and red wings of the broadened spectrum.
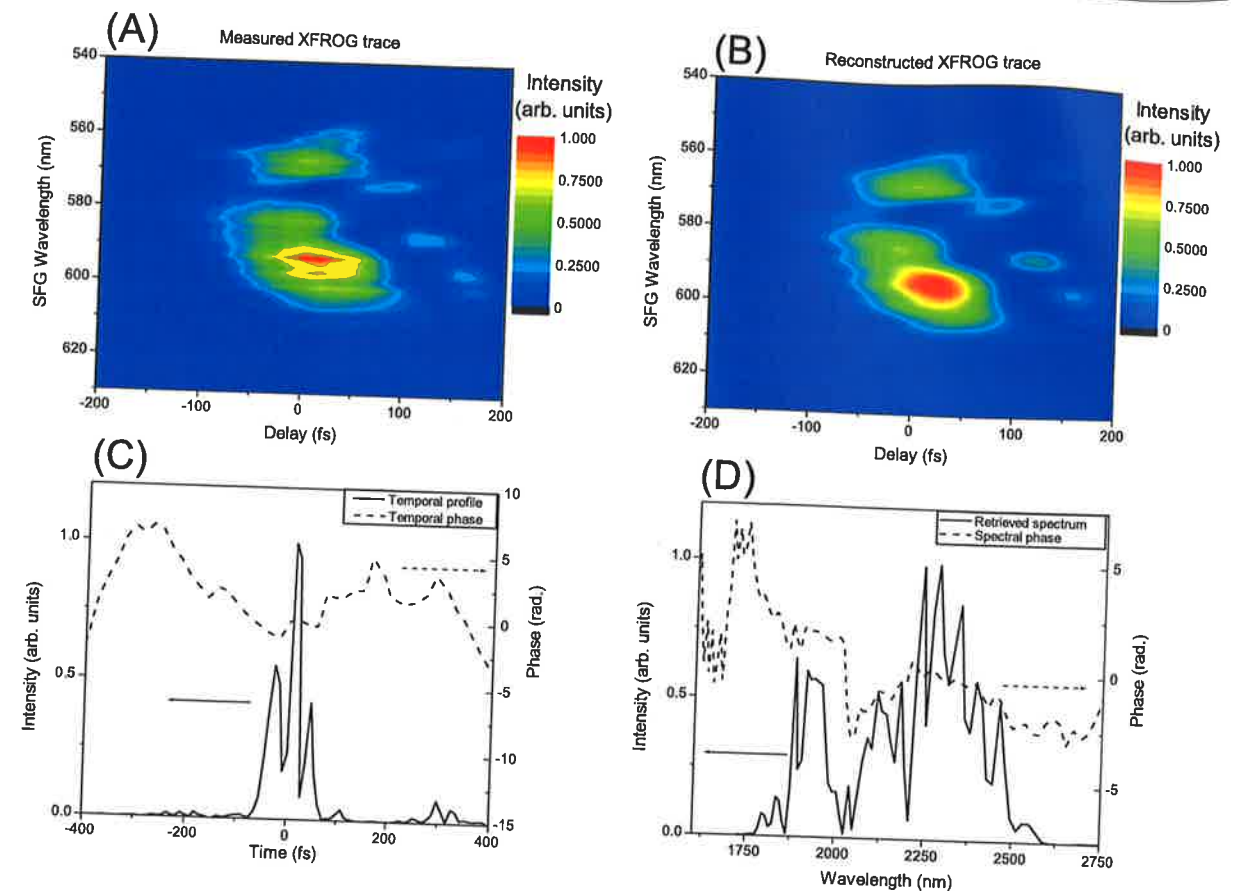
Figure 4.4: Characterization of the DF pulses by use of XFROG. (A): Measured XFROG trace, (B): reconstructed XFROG trace, (C): retrieved temporal pulse profile (solid line) and temporal phase (dashed line), and (D): retrieved spectrum (solid line) and spectral phase (dashed line).

the energy of the supercontinuum pulse is measured as 50 μJ. We tried two MgO:PPSLN crystals with different quasi-phase-match (QPM) periods of 11.21 and 13.87 μm for DFG. Fig. 4.3 plots the DF spectra generated by the MgO:PPSLN crystals with the QPM periods of 11.21 μm (red line) and 13.87 μm (black line). In Fig. 4.3, numerically simulated DF spectra by use of the MgO:PPSLN with the QPM periods of 11.21 (blue line) and with the QPM periods of 13.87 μm (green line) are compared with the experimentally obtained DF spectra. A theoretical description about the simulation of the DFs is given in [61, 243, 244, 245]. This calculation uses the spectral intensity and phase of the broadened spectrum by use of frequency-resolved optical gating based on second-harmonic generation (SHG FROG) [246].

To examine the compressibility of the DF, we characterize the spectral phase and intensity of the DF by use of a cross-correlation FROG (XFROG) based on the sum-frequency generation between the DF and the fundamental pulse from the Spitfire. In this pulse characterization, the MgO:PPSLN with the QPM period of 11.21 μm was used. Fig. 4.4 shows a measured

XFROG trace (A), a reconstructed XFROG trace (B), a retrieved temporal pulse profile (solid line) and a temporal phase (dashed line) (C), and a retrieved spectrum (solid line) and a spectral phase (dashed line) (D). From these traces, although the chirp of the DF pulses are not only governed by the second-order chromatic dispersion but also other higher-order dispersion, the smooth variation of the group delay of the DF pulses could be a proof for the possible pulse compression with suitable adaptive optics. The energy of the DF is measured as 50 nJ with the maximum pump energy. However, the DF generated by the maximum pump energy turned out to be useless due to the bad quality of its temporal pulse profile showing multiple peaks. This might be attributed by the onset of the nonlinear effects in the MgO:PPSLN generating the DF by the strong compressed supercontinuum. The pump pulse energy was reduced and the resultant DF was checked as described above to have the clean temporal pulse profile. The energy of the reduced DF pulses was hardly measurable because of their weakness.

In summary, we have demonstrated a broadband DF around 2 μm by use of the broadened Ti:sapphire amplifier output pulses. The fundamental pulses broadened in the long-distance filament formed in 3-bar Kr are used as the pump source for DFG in the MgO:PPSLN. The generated DF has been characterized with XFROG, showing its potential compressibility. This energy is much higher than the previously used seed energy of 2 pJ and, consequently, the high-energy output from the infrared OPCPA system is expected.

4.3   Infrared optical parametric amplifiers

In this section, we review past works on infrared OPAs, which give us helpful ideas for the development of an infrared OPCPA system. Especially our attention will be paid to broadband and high-energy amplification and ultrashort laser pulse generation. The optically synchronized, 1053-nm pulses, which are produced by an upgraded Nd:YLF amplifier chain to be described in Section 4.4, are used as a pump source for amplification of the broadband seed source around 2 μm obtained in the last section. Therefore only degenerate optical parametric amplification would provide broad gain bandwidth necessary for few-cycle pulse amplification. A suitable OPA crystal for this purpose will be selected out from many possible candidates.

Here we look through demonstrations of OPAs and OPCPAs for ultrashort infrared pulse amplification with bulk nonlinear crystals (experiments using periodically-poled crystals will be discussed later): 200-fs pulse generation at 3-4 μm by use of KNbO$_3$-based OPA [247], 125-fs pulse at 3 μm by use of a bulk LiNbO$_3$ (LN) [248], 5-cycle at 3 μm using MgO-doped LN (MgO:LN) [249], a review of femtosecond OPAs with KTP, KTA, and KNbO$_3$ crystals in Ref. [250], 75-fs pulses at 5 μm with dispersion compensation in transparent materials [251], and 65-fs pulses tunable from 2.7 to 4.5 μm based on a KNbO$_3$ [252]. From the papers above, so far, the shortest pulse duration is 5-cycle around 3 μm. However its output energy is less than 10μJ and they generate ultrashort laser pulses by slicing a long seed pulse using ab ultrashort pump pulse. Although 5-cycle optical pulses around 3 μm have been demonstrated by use of MgO:LN, the broadband seed spectrum, described in the last section, prefers a wider parametric amplification bandwidth to achieve high-energy few-cycle pulse generation. Recently a new type of infrared ultrafast pulse generation has been demonstrated: broadband (not compressed yet) phase-stable

near-infrared (1.2-1.5 μm) pulses by use of DFG followed by boosting OPA [253]. This is quite interesting but there seems to be several problems such as the rather complex setup to be used and the unreliable phase-stabilization scheme dependent on the interferometer.

Two things can be considered to enhance the gain bandwidth: higher pump intensity and the use of thin crystals. The use of the high pump intensity is, in any case, limited by the damage threshold of the optics (mainly bulk damage and surface damage of the crystal). As pointed out in Section 1.3, shorter pump pulses would result in broadband parametric amplification because the parametric amplifier could be pumped by the higher-intensity pump. However the shortest duration of the amplified pulse from the Nd:YLF amplifier is limited by amplifier gain narrowing and the damage of the amplifier optics so that dramatic increase of the pump pulse intensity is implausible. The second idea, the use of thin crystals, are not easy to implement because a certain amount of gain has to be realized to amplify the weak seed energy to millijoule-level. However the higher second-order nonlinearity coefficient could compensate for the gain decreasing due to the thin nonlinear crystal. From the formulas for the gain calculation described in Eqs. 1.5, 1.6, and 1.7, small gain coefficient g multiplied by the interaction length L can be expressed by the second-order nonlinearity coefficient d_{eff}, the pump intensity I_p and L as

$$gL \propto d_{\mathrm{eff}}\sqrt{I_pL}.$$

(4.2)

Therefore, to sustain a certain gain, the crystal length L can be reduced when d_{eff} is larger, resulting in broadband parametric amplification due to less phase mismatch. Actually, recently emerging periodically-poled nonlinear crystals have an extremely high second-order nonlinearity coefficient so that the use of thin periodically-poled nonlinear crystals could result in the broadband and high gain at the same time.

In 1993, first fabrication of periodic antiparallel domains in the ferroelectric crystal, LiNbO$_3$, by use of the electric external field was demonstrated[254]. The use of the QPM technique, which was predicted initially by a first theoretical paper concerning OPA [55] and later theoretically explained in detail [255], has been widespread owing to this relatively easy fabrication technique of periodically-poled crystals by use of the electric field. In the QPM technique, periodic reversal of the domains in the crystal causes the periodic reversal of the sign of the second-order nonlinear coefficient. This modulation compensates for phase-mismatch accumulated among the three waves involved in the parametric interaction and enables effective parametric interactions. Advantageous features of the QPM method include the noncritical phase-matching possible for any three-wave interaction within the transparency of the material, if fabrication techniques allow a required domain reversal, and the use of the largest second-order nonlinear coefficient.

For periodically-poled crystals, many interesting experiments in the infrared regime and advances in crystal fabrication and engineering have been demonstrated: early demonstration of an OPO by use of MgO:PPLN [256], fabrication of MgO-doped stoichiometric LiTaO$_3$ (MgO:PPSLT) [257], OPA and OPO applications by use of MgO:PPLN [249] and [258], respectively, a high-power OPO operation using large aperture MgO:PPLN [259], and relatively broadband OPG by use of MgO:PPSLT [260]. Not only OPAs but also several OPCPAs have been demonstrated with periodically-poled crystals: high-energy femtosecond OPCPA by use of a Q-switched laser as a pump source [115], ultrashort pulse generation based on periodically-

poled KTP (PPKTP) [129], first use of MgO:PPSLT in an OPCPA [130], broadband amplification of mid-infrared pulses in PPKTP [261], and high-contrast OPCPA system using PPKTP [110]. The periodically poled crystals have been applied to many OPAs and OPCPAs and shown its potentials and, especially, the highest second-order nonlinear coefficient for the parametric interaction is quite favorable.

We numerically calculate the OPA gain bandwidth by use of the Eqs. 1.5, 1.6, and 1.7 for three crystals (MgO:PPSLN, MgO:PPSLT, and bulk-LN). This simulation clarifies the effect of the high second-order nonlinear coefficient value on the gain bandwidth. The calculation of the OPA gain adopting 1st-order QPM with the duty cycle of 50% does not change the OPA gain formula except the notation of the phase-match condition and the replacement of the second-order nonlinear coefficient [255]. The wave-vector mismatch can be expressed as

$$\Delta k \equiv k_p - k_s - k_i - \frac{2\pi}{\Lambda_{QPM}}, \qquad (4.3)$$

where Λ_{QPM} is the QPM period of the periodically poled crystal. The effective second-order nonlinear coefficient d_{eff} in Eq. 1.6 has to be replaced by that for QPM d_{QPM} [255]. Their relationship can be expressed as

$$d_{QPM} = \frac{2}{\pi} d_{eff}. \qquad (4.4)$$

Values of the second-order nonlinear coefficients of SLT and SLN are $d_{33} = 25.0$ pm/V [262] and $d_{33} = 15.7$ pm/V [262, 263] both in the case of zzz interaction, respectively, resulting in effective second-order nonlinear coefficients of $d_{QPM} = 16$ pm/V for PPSLN and 10 pm/V for PPSLT, respectively. Temperature dependent extraordinary refractive indices of MgO:LN from HC Photonics and SLT are available from Eqs. A.10 and A.11 in Appendix A, respectively. Refractive indices of 5 mol% MgO-doped congruent LN are available from Eqs. A.8 and A.9 in Appendix A. Calculated gain curves with MgO:PPSLN (black line), MgO:PPSLT (red line), and bulk MgO:LN (green line) are shown in Fig. 4.5 (A). The obtained seed spectrum (blue line) is plotted in Fig. 4.5 (A). Fig. 4.5 (B) depicts temporal pulse profiles, assuming flat spectral phase, calculated from the gain spectra with MgO:PPSLN (black line), MgO:PPSLT (red line), and bulk MgO:LN (green line), respectively. For the calculations, the following parameters are used: common pump intensity: 5 GW/cm², QPM periods of MgO:PPSLN and MgO:PPSLT: 30.2 and 31.8 μm, temperature of MgO:PPSLN and MgO:PPSLT: 300 and 100 °C, and crystal length of MgO:PPSLN and MgO:PPSLT: 2 and 2.9 mm. The crystal length, phase-matching angle, and second order nonlinear coefficient of MgO:LN are 6.5 mm, 42.93 °, and 5 pm/V, respectively. Nearly two-cycle pulses could be amplified by use of MgO:PPSLN (carrier period at 2.1 μm is 7 fs), while even the narrowest gain bandwidth obtained with bulk MgO:LN is expected to support amplification of less than 3-cycle pulses.

In summary, we have conducted the OPA gain calculation using MgO:PPSLN, MgO:PPSLT (red line), and bulk MgO:LN. The high second-order nonlinear refractive index, enabled by the QPM technique and periodically poled crystals, resulted in broadband gain, making possible amplification of few-cycle pulses in the infrared regime. In this experiment, we will adopt exclusively MgO:PPLNs because of the broader gain bandwidth and available large-aperture (5
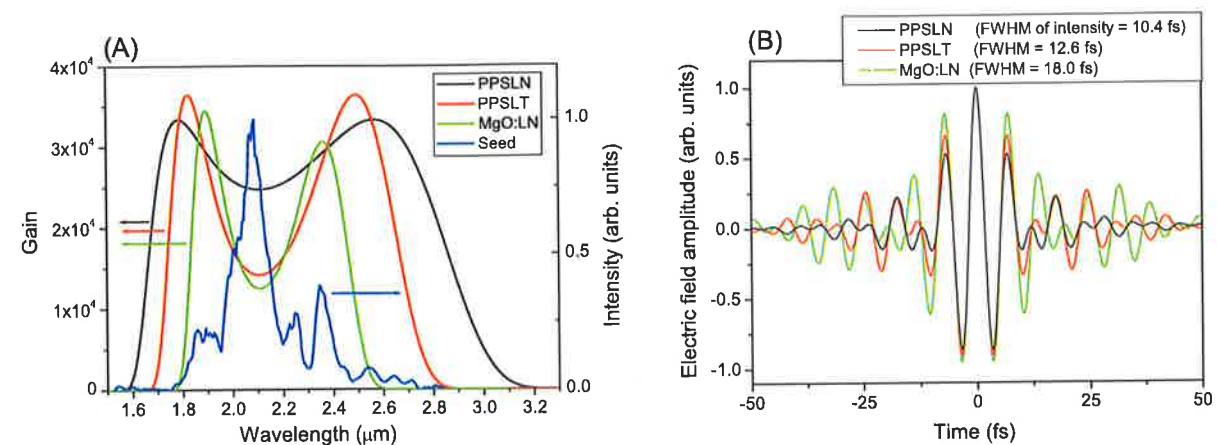
Figure 4.5: (A): Calculated OPA gain spectra in the infrared by use of MgO:PPSLN (black line), MgO:PPSLT (red line), and bulk MgO:LN (green line) and the obtained seed spectrum (blue line). (B): Temporal pulse profiles, assuming flat spectral phase, calculated from the gain spectra with MgO:PPSLN (black line), MgO:PPSLT (red line), and bulk MgO:LN (green line).

mm × 5 mm) crystals [264] supplied by a collaborating institute, Dr. H. Ishizuki and Prof. T. Taira (Institute for Molecular Science, Okazaki, Japan). With this MgO:PPLN, amplification of the whole seed spectrum is expected, leading to few-cycle pulse generation in the infrared. Although MgO:PPSLT and bulk MgO:LN are not used in this experiment, especially, in the case of higher-energy pulse amplification, a higher damage threshold of MgO:SLT and much larger available aperture size of bulk LN might be superior to the low damage threshold and a limited aperture size of MgO:SLN. Other periodically-poled nonlinear crystals such as PPKTP and PP-KTA and bulk crystal KNbO₃ also have not been tried. This is because their use is rare and their properties for the OPA application are equivalent or inferior compared to PPSLN, although they exhibit stronger tolerance for the photorefractive effect and this advantage could be preferable for some cases.

4.4 Upgrade of the Nd:YLF pump amplifier for the infrared OPCPA system

In this section, we describe upgrade of the optically synchronized Nd:YLF regenerative amplifier established in Section 3.3. Additional post amplifiers are placed after the Nd:YLF regenerative amplifier seeded with the Ti:sapphire oscillator in order to increase the picosecond output pulse energy to more than 11 mJ. Because of cumulative nonlinear effects in the Nd:YLF amplifier, two intracavity etalons are used to stretch the amplified pulse duration, resulting in smoother high-energy, high-intensity pulse generation from the amplifier chain. Details about the two etalon approach is described in Appendix D.

In the Nd:YLF amplifier, the KD*P Pockels cell has been exchanged with a BBO Pockels cell. This exchange enables higher-energy and higher-power operation of the regenerative amplifier [265] because of the low absorption of the fundamental light at 1053 nm and BBO's stronger resistance to the heat deposition than KD*P. A better thermal property of BBO and the improvement of the amplifier cavity resulted in the higher output energy of more than 4 mJ at 1 kHz repetition rate and saturation of the amplified pulses. Saturation of the amplified pulse is caused by a nonlinear loss of the fundamental amplified pulse because a part of the amplified pulse is converted to second harmonics generated in the BBO Pockels cell in contrast to the KD*P Pockels cell. The stronger amplified pulse loses more energy due to the higher conversion of the fundamental pulses into the second harmonics.

To examine picosecond amplification with the weak seed pulse, we tried to compare the output between the Q-switched and the seeded operations as described in Section 3.4. However we could not precisely measure the output ratio of the modified Nd:YLF regenerative amplifier between the Q-switched and the seeded operations. This is because a cavity design is dramatically dependent on the thermal condition of the Nd:YLF rod. Therefore the round-trip gain and the amplifier performance become dependent on the thermal load on the Nd:YLF rod and, consequently, its output power itself. A less output energy in the Q-switched operation, compared to the output of the seeded amplifier, changes the amplifier performance from the seeded operation so that simple comparison of the output powers between the Q-switched and the seeded operations is not possible anymore. Therefore, as shown in Fig. 4.6, we measured the shot-to-
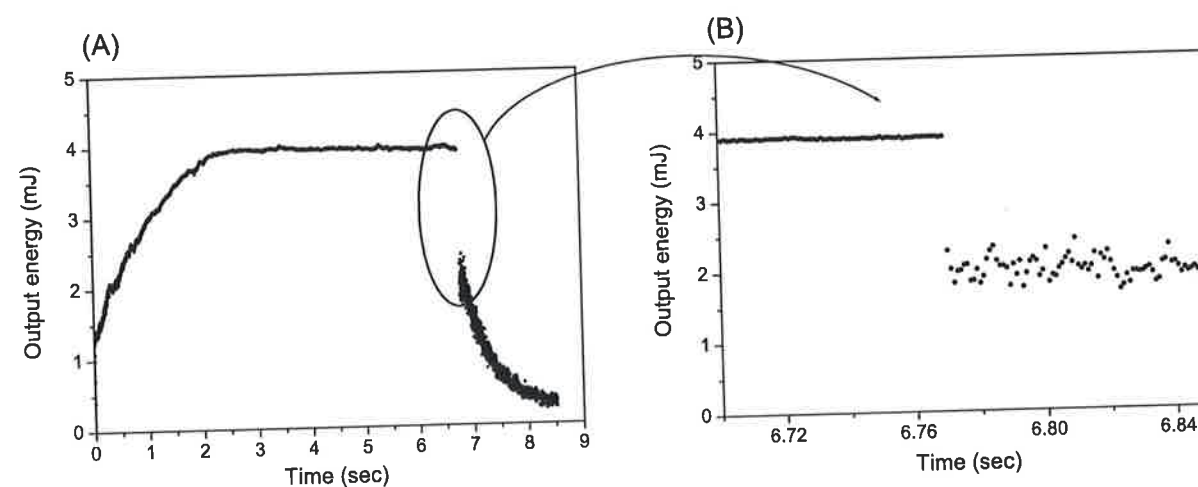

Figure 4.6: Regenerative amplifier output energy with and without the seed. (A): Output energy change due to the variation of the thermal condition in the cavity. (B): Expanded plot around the seed interception.

shot output energy with and without the seed pulse. The output energy after the seed injection slowly increases for about 2.5 seconds to reach saturation around the 4-mJ output energy and the Q-switched output also decreases slowly with the same time scale after the seed blocked.

By comparing the output energy just before and after the seed interception, the output energy ratio between the Q-switched and the seeded operations can be determined from the plot as 1/2 because, in such a time scale, thermal condition of the Nd:YLF rod is not changed so much. This value satisfies the criterion for clean pulse amplification defined in Section 3.4. This ratio is improved from the previous amplifier configuration mainly because of the 5 times higher spectral intensity around 1053 nm of an improved Ti:sapphire oscillator.

The 4-mJ output pulses from the regenerative amplifier are sent to a post-amplifier chain consisting of two home-made continuous-diode-laser Nd:YLF gain modules. A first module (Nd:YLF 2 in Fig. 4.10) contains a 63-mm-long 3-mm-diameter a-cut Nd:YLF rod. This module exhibits a single-pass gain of about 2 with the diode-laser power well below the fracture limit of the Nd:YLF rod (about 50-60 W/cm in our case). A second module (Nd:YLF 3 in Fig. 4.10) contains a 120-mm-long 4-mm-diameter a-cut Nd:YLF rod and exhibits a slightly less single-pass gain of 1.8. These Nd:YLF crystals of the two modules are oriented such that their c-axes become orthogonal with each other. This configuration helps to compensate the elliptical thermal lens of the YLF crystal. Additionally a cylindrical lens is placed between the modules for further compensation of the ellipticity of the beam. Taking into account self-focusing of the amplified beam propagating in the long Nd:YLF rod, the beam size is optimized by an appropriate lens such that the clipping of the transmitted beam by the Nd:YLF rod disappears at the highest output operation. With this optimization, a maximum output energy of 12 mJ at 1 kHz is achieved using high pump-diode input power close to the fracture limit. A lower safe pump power results in the less output energy of 11 mJ at 1 kHz. Its beam profile is shown in Fig. 4.7 (A). We have
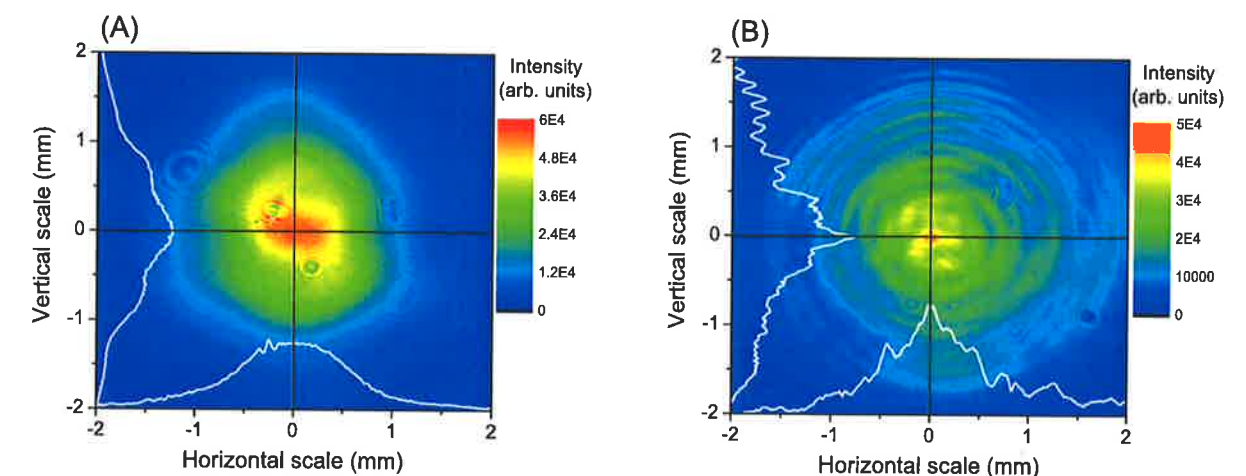
Figure 4.7: Output beam profiles from the Nd:YLF amplifier chain. (A): Beam profile of 11.2-mJ output pulses from the two post-amplifiers following the Nd:YLF regenerative amplifier. (B): Beam profile of 15.1-mJ output pulses from the three post-amplifiers.

measured autocorrelation traces of the output pulse from the post amplifier chain following the Nd:YLF regenerative amplifier with a single etalon inside. We observed multiple prominent
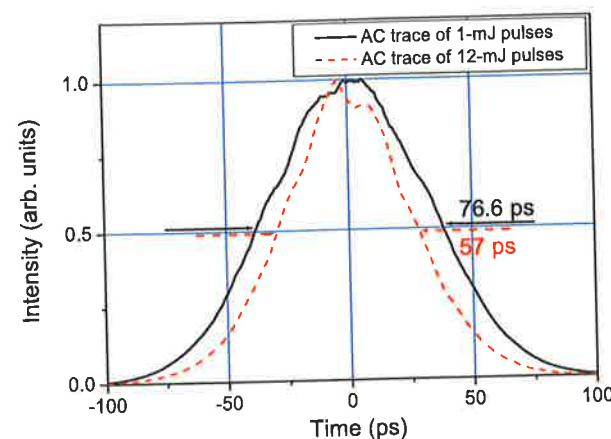
Figure 4.8: Autocorrelation traces of the amplified output pulses from the post amplifier. Autocorrelation traces of the post-amplifier 1-mJ output pulses (black line) and of the post-amplifier 1-mJ output pulses (red dashed line), clearly indicating the pulse temporal narrowing effect.

peaks in the autocorrelation trace and attributed this phenomenon to a shallow ripples introduced by a single etalon and its enhancement by a self-compression effect caused by SPM and gain narrowing [209, 211]. Therefore, to stretch the amplified pulse more and remove the ripples, two etalons are inserted in the regenerative cavity. This two-etalon approach is theoretically demonstrated to cancel out ripples introduced by indvidual etalons and its details are described in Appendix D. Fig. 4.8 shows the measured autocorrelation traces of resultant 1-mJ and 12-mJ output pulses from the post-amplifier chain adopting the two etalon inside the regenerative cavity. Because the 1-mJ pulses are obtained by attenuating the regenerative amplifier output cavity. Because the 1-mJ pulses are obtained by attenuating the regenerative amplifier output pulses in front of the post amplifier, difference of the pulse durations of 1-mJ and 12-mJ output pulses is caused by the self-compression effect caused by SPM and gain-narrowing in the post amplifiers [209, 211]. The pulse duration at the full output energy operation is 40 ps, assuming a Gaussian pulse temporal profile. Although we have succeeded in obtaining an output energy of 17 mJ from an additional third Nd:YLF amplifier using the same crystal as in the second module, the output pulses from the three post amplifiers are severely distorted so they are less usable as OPCPA pump pulses than the 11-mJ pulse from the two amplifiers. This is because the critical degradation of the spatial and temporal pulse profile effectively reduces the usable energy. A beam profile presented in Fig. 4.7 (B) shows the sharp peak at the center of the beam due to the self-focusing in the last amplifier, although the diffraction at the exit of the third amplifier clips an output beam profile, causing the diffraction pattern. This is because the intense part of the input beam self-focuses more strongly during propagation in the third post amplifier than the wings. The B-integrals accumulated in the post-amplifiers are estimated as 0.54 for 2 stages and 1.14 for 3 stages.

In summary, the optically synchronized Nd:YLF amplifier chain is upgraded with the two additional boosters and produces the 11-mJ pulses at the 1-kHz repetition rate. These output pulses will be used as a pump source for the infrared OPCPA system to be described in the next section. Further upgrade of the amplifier seems to be difficult and, at least, the rod aperture size

has to be increased to avoid nonlinear effects in a long Nd:YLF rod.

4.5   Few-cycle high-energy infrared optical pulse generation by use of OPCPA

Introduction

In this section, we demonstrate the experimental implementation of a MgO:PPSLN OPCPA system by use of the optically synchronized Nd:YLF pump laser. Similar to the stretching and compression method adopted in near-infrared OPCPA, we used a novel down-chirping stretcher and up-chirping compressor for the dispersion control in the OPCPA system. The infrared seed pulses are negatively stretched in a Dazzler prior to the parametric amplifiers. The stretched pulses are amplified in two OPA stages using MgO:PPLNs. The amplified pulses are compressed by the chromatic dispersion of silicon (Si) down to about 20 fs. The compressed pulses are characterized by FROG using surface-third-harmonic generation (THG FROG) [266].

Pulse stretching and compression

The infrared Dazzler functions as both a main stretcher and a residual dispersion compensator in infrared OPCPA (IR OPCPA) in contrast to the near-infrared OPCPA. After coarse pulse compression, the Dazzler corrects for the residual spectral phase whose information is obtained by the THG FROG measurement. The Dazzler gives negative dispersion to the infrared seed pulses, stretching it to about 13 ps in the spectral range from 1.8 to 2.8 μm. After amplification of the down-chirped seed pulses, positively dispersive 50-mm-long Si compresses the amplified stretched pulses from 13 ps down to about 20 fs. The advantage of the bulk compressor approach is the excellent transmission of the pulse energy and its simplicity without causing spatial chirp usual in CPA based on a grating compressor. Fig. 4.9 shows a calculated group delay of the stretcher, amplifier, and compressor: sign-inversed (multiplied by -1) group delay of 50-mm-long Si (black line), sign-inversed group delay of 6-mm-long MgO:LN (red line), group delay of TeO$_2$ (ordinary wave) (blue line), and group delay of TeO$_2$ (extraordinary wave) (orange line). A refractive index of Si is available in Eq. A.18 in Appendix A. Refractive indices of TeO$_2$ in the infrared region are given in Ref. [267] and in Eqs. A.14 and A.15 in Appendix A. Note that these Sellmeier equations are different from those used for the dispersion calculation in the near-infrared OPCPA stretcher. The diffracted beam by the acoustic wave in the Dazzler propagates in TeO$_2$ as an extraordinary wave. An angle between the polarization direction of the diffracted beam and the optical axis of TeO$_2$ is 51.5°. This means that the propagation direction of the diffracted beam is 38.5° away from the optical axis. This is included in the dispersion calculation of TeO$_2$ for the extraordinary wave. The sign of the group delay of Si and MgO:PPSLN is inverted to represent the dispersion to be compensated by the Dazzler. Although, in Fig. 4.9, an offset of each group delay is arbitrarily subtracted, relative difference between the group delays in TeO$_2$ (ordinary wave) and TeO$_2$ (extraordinary wave) has been kept constant. In Fig. 4.9, a range between the group delays of the ordinary (thick blue line) and extraordinary (thick orange
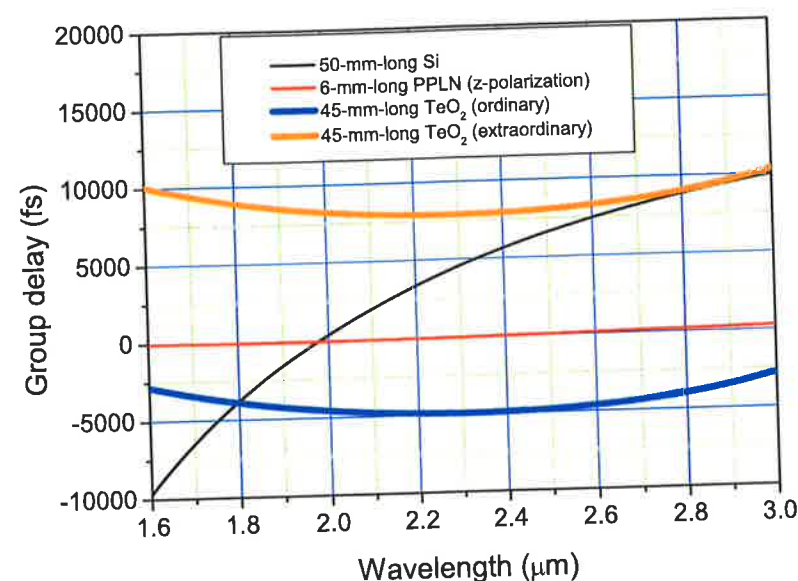
Figure 4.9: Calculated group delay of the stretcher, amplifier, and compressor for IR OPCPA. Sign-inversed group delay of 50-mm-long Si (black line), sign-inversed group delay of 6-mm-long MgO:PPSLN (red line), group delay of 45-mm-long TeO$_2$ (Dazzler crystal) for an ordinary wave (blue line), and group delay of 45-mm-long TeO$_2$ for an extraordinary wave (orange line). Note that, although, all group delays have been arbitrarily offset, difference between the group delays of TeO$_2$ (ordinary wave) and TeO$_2$ (extraordinary wave) is kept constant.

line) waves in TeO$_2$ indicates the dispersion compressible by use of the Dazzler. For example, shown in Fig. 4.9, the Dazzler can only compensate the dispersion of 50-mm-long Si (black line) in the wavelength range from 1.8 to 2.8 μm. From a different point of view, the Dazzler can stretch an input pulse to about 10 to 15 ps regardless of its spectrum. The amount of stretching given by the Dazzler is determined by the difference of the group delay between the ordinary and extraordinary waves and the length of the Dazzler.

Infrared optical parametric amplifier with the Dazzler stretcher and bulk compressor

In this section, we describe the implementation of the infrared optical parametric amplifier with the stretcher and compressor by use of an optically synchronized Nd:YLF pump amplifier chain. The schematics of the infrared OPCPA system is presented in Fig. 4.10. Output pulses from a broadband Ti:sapphire oscillator are split by a dichroic mirror, which reflects a seed pulse at 800 nm for the Ti:sapphire amplifier (Spitfire, Spectra physics) and transmits a seed pulse at 1053 nm for the Nd:YLF amplifier, respectively. We have previously described generation of the seed pulses for the infrared OPCPA based on DFG in MgO:PPSLN, the seeding scheme from the Ti:sapphire oscillator into the Nd:YLF regenerative amplifier, and the upgrade of the Nd:YLF
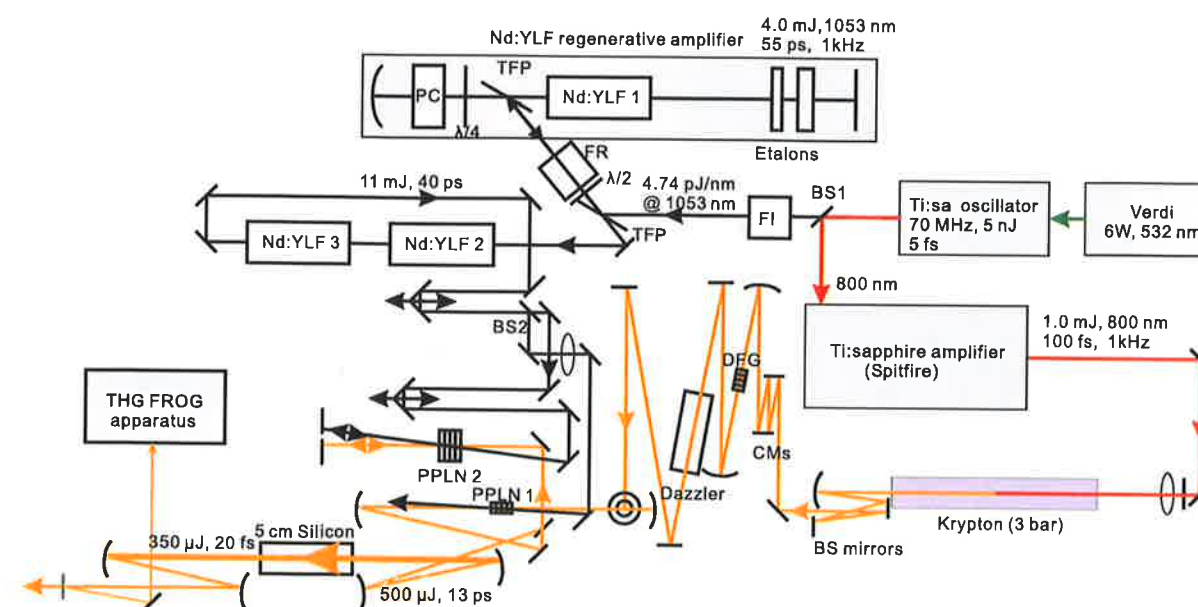
Figure 4.10: Layout of the infrared OPCPA system. BS 1: beamsplitter reflecting a seed pulse at 800 nm for the Ti:sapphire amplifier and transmitting a seed pulse at 1053 nm for the Nd:YLF amplifier; FI: Faraday isolator; TFP: thin-film polarizer; $\lambda/2$: half-wave plate; FR: Faraday rotator; $\lambda/4$: quarter-wave plate; PC: BBO Pockels cell; NdYLF 1: continuous-laser-diode gain module (Northrop Grumman Cutting Edge Optronics) with a 63-mm-long 3-mm-in-diameter a-cut Nd:YLF rod; Etalons: 0.7-mm- and 1.0-mm-thick uncoated fused silica windows; Nd:YLF 2: home-made laser-diode gain module with a 63-mm-long 3-mm-in-diameter a-cut Nd:YLF rod; Nd:YLF 3: home-made laser-diode gain module with a 120-mm-long 4-mm-in-diameter a-cut Nd:YLF rod; BS 2: beamsplitter to split the pump pulses to a first and second stages; BS mirrors: three band-stop mirrors; CMs: pair of two chirped mirrors; DFG: DF generator (MgO:PPSLN with an 11.21-μm QPM period (HC Photonics)); Dazzler: acousto-optic programmable dispersive filter (Fastlite); PPLN 1: first parametric amplifier stage using 3-mm-thick MgO:PPSLN with a 30.2-μm QPM period (HC Photonics); PPLN 2: second parametric amplifier stage using 3-mm-thick MgO:PP congruent LN (MgO:PPCLN) with a 30.6 or 30.8-μm QPM period; THG FROG: THG FROG apparatus.

amplifier chain with additional two post amplifiers in Sections 4.2, 3.3, and 4.4, respectively. The Ti:sapphire oscillator spectrum is plotted in Fig. 4.11. The spectral regions used as the seeds for the Spitfire and Nd:YLF regenerative amplifiers are indicated, respectively. The OPCPA seed pulse generated in the DFG crystal is collimated and sent to the Dazzler, which only diffracts 10% of the input pulse energy to the output pulse energy. After a periscope behind the Dazzler changes the vertical polarization of the DF to the horizontal polarization, the seed beam is focused to 180 μm in diameter (FWHM) at the first parametric crystal (MgO:PPLN) and overlapped with the pump beam. The about 300-μJ pump beam is focused to the same diameter as the seed, leading
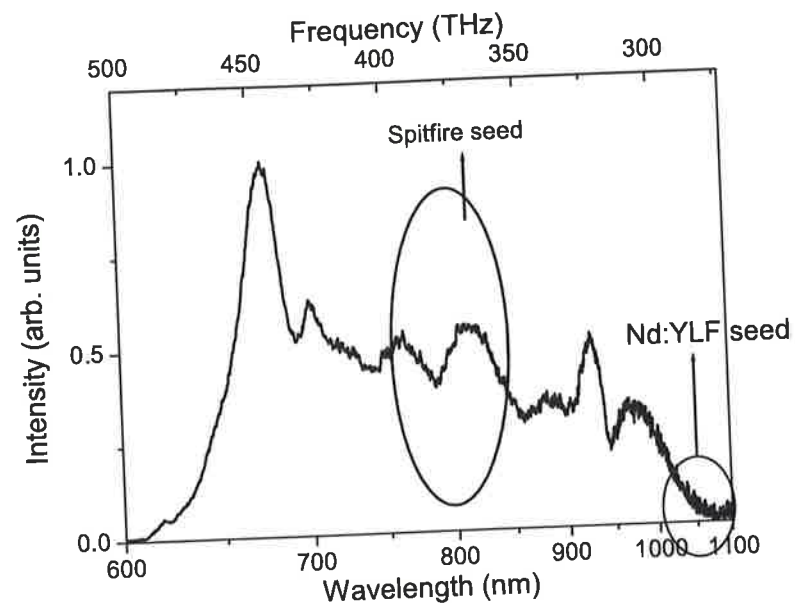
Figure 4.11: Ti:sapphire oscillator spectrum. Spectral regions used as the seeds for the Ti:sapphire amplifier and the Nd:YLF regenerative amplifier are indicated.

to the pump intensity of about 10 GW/cm^2 at the first parametric amplifier. Pulse intensity of more than 20 GW/cm^2 would results in, first, a prominent photorefractive effect [268]. The even stronger pump pulses cause the damage on the surface of the crystal. The first OPA stage employs a 3-mm-thick, 1-mm-wide, 3-mm-high MgO:PPSLN crystal (HC Photonics) with a QPM period of 30.2 μm. To maximize the gain bandwidth, we have tried several geometries between the seed and pump beams and found the external noncollinearity angle of about 3° is optimum for broadband amplification and the output pulse energy. The nonlinear crystal is heated to about 280 °C to avoid the photorefractive effect. Because of the temperature dependence of the refractive index of MgO:SLN, fine tuning of the crystal temperature is also a good tool for the control of the gain bandwidth and the output power. Although the amplified seed energy reaches up to 10 μJ without causing the damage on the surface of the parametric crystal, we have kept the pump intensity lower than the maximum intensity in order not to enhance the superfluorescence, which would be successively amplified in the second stage. Amplified beam is recollimated to 1.2 mm in diameter and sent to the second OPA stage. The pump beam from the Nd:YLF amplifier is also collimated up to the same diameter as the seed beam, resulting in the pump intensity of 10 GW/cm^2 with the pump energy of 9 mJ. The pump beam profile at the second stage before up-collimation is shown in Fig. 4.12. The good pump beam profile is sustained from the post Nd:YLF amplifiers even without the use of a relay-imaging technique. The second stage crystal is 5-mm × 5-mm aperture, 3-mm-thick MgO:PPCLN crystals with QPM periods of 30.6 or 30.8 μm. No difference in the performance of the parametric amplifier has been observed between the QPM periods of 30.6 and 30.8 μm. A noncollinearity angle of 4° between the seed and pump beams turned out to be optimum to maximize the gain bandwidth and the output energy. The
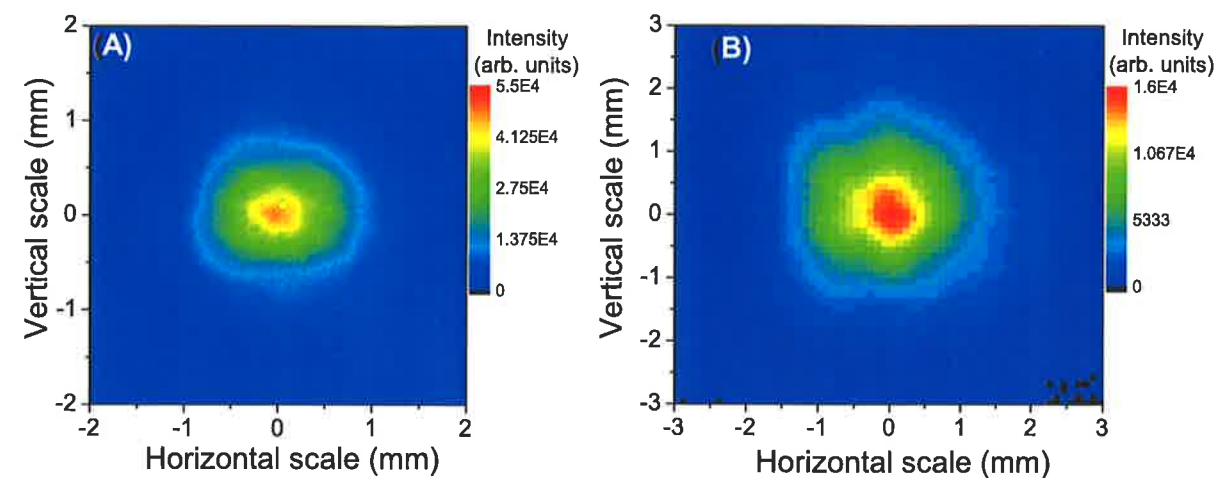
Figure 4.12: (A): Pump beam profile at the second parametric amplifier stage. (B): Amplified beam profile after the second-pass in the second parametric amplifier stage.

output energy obtained after first-pass amplification is about 200 μJ and further amplification is gained by the second-pass with the retro-reflection configuration. The 500-μJ amplified pulse is ejected from the amplifier part and sent to the beam expander in front of the Si pulse compressor.

Results of infrared parametric amplification are summarized in Fig. 4.13. Fig. 4.13 plots an amplified spectrum after the second stage (black line), an amplified spectrum after the first stage (red line), a calculated gain curve (green line), and a superfluorescence spectrum after the second stage obtained by the interception of the seed pulse (blue line). The cut-off of the amplified spectrum around 1.9 μm and 2.7 μm are attributed to the lack of the seed spectrum and the diffraction range of the Dazzler, respectively. A good beam profile of the amplified pulse after the second stage, shown in Fig. 4.12 (B), is obtained. The amplified beam is spatially expanded in order to avoid nonlinear effects in the bulk compressor and sent to the 50-mm-long anti-reflection-coated Si block. This is because of a relatively high third-order nonlinear refractive index of Si [269]. The third-order nonlinear refractive index of Si, available in Appendix E, is about hundred times higher than that of fused silica. After the compressor, the transmitted pulse energy is reduced from 500 μJ to 350 μJ because of loss of optics and the absorption of the second- and third-harmonics collinearly generated in the OPA crystal.

The infrared beam transmitting through the Si block is recollimated down and a part of the output pulse is split and sent into a THG-FROG apparatus shown in Fig. 4.14. The beam splitters are placed such that the dispersion of two arms are equally balanced to be capable of the precise measurement of the ultrashort pulses. The two infrared beams are focused onto the surface of CaF$_2$ using a gold-coated parabolic mirror with the focal distance of 50 mm. One of four third-harmonic beams emitted at the surface is selected by a diaphragm and focused by a CaF$_2$ lens into a multi-mode glass fiber connected to a visible spectrometer (Ocean Optics). The third-harmonic spectrum is recorded at each delay point and a THG FROG trace is obtained. A temporal pulse
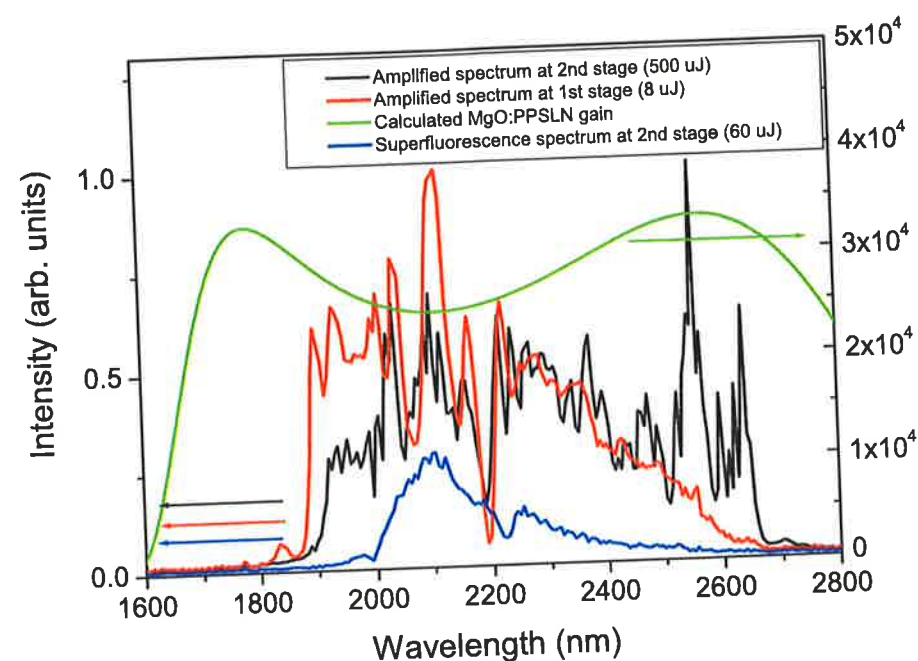
Figure 4.13: Results of infrared parametric amplification: amplified spectrum after the second stage (black line), amplified spectrum after the first stage (red line), calculated gain curve (green line), and superfluorescence spectrum obtained after the second stage by the interception of the seed pulse (blue line).
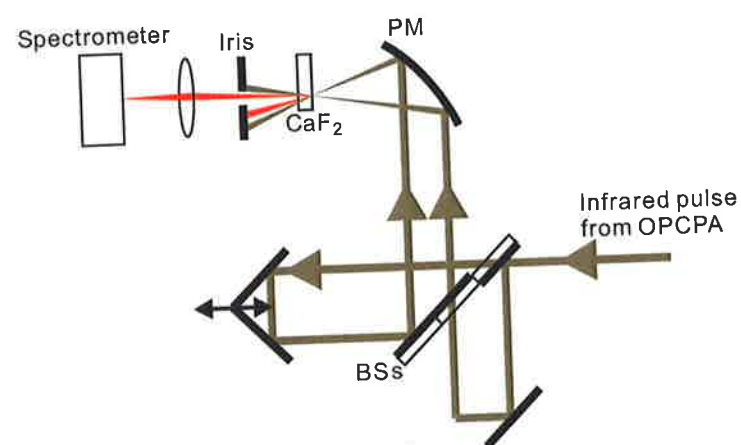

Figure 4.14: THG FROG apparatus. BSs: dielectric beamsplitters; PM: parabolic mirror (f=50 mm) coated with gold; Iris: diaphragm selecting only one of four third harmonics emitted at the surface of a CaF$_2$ plate.
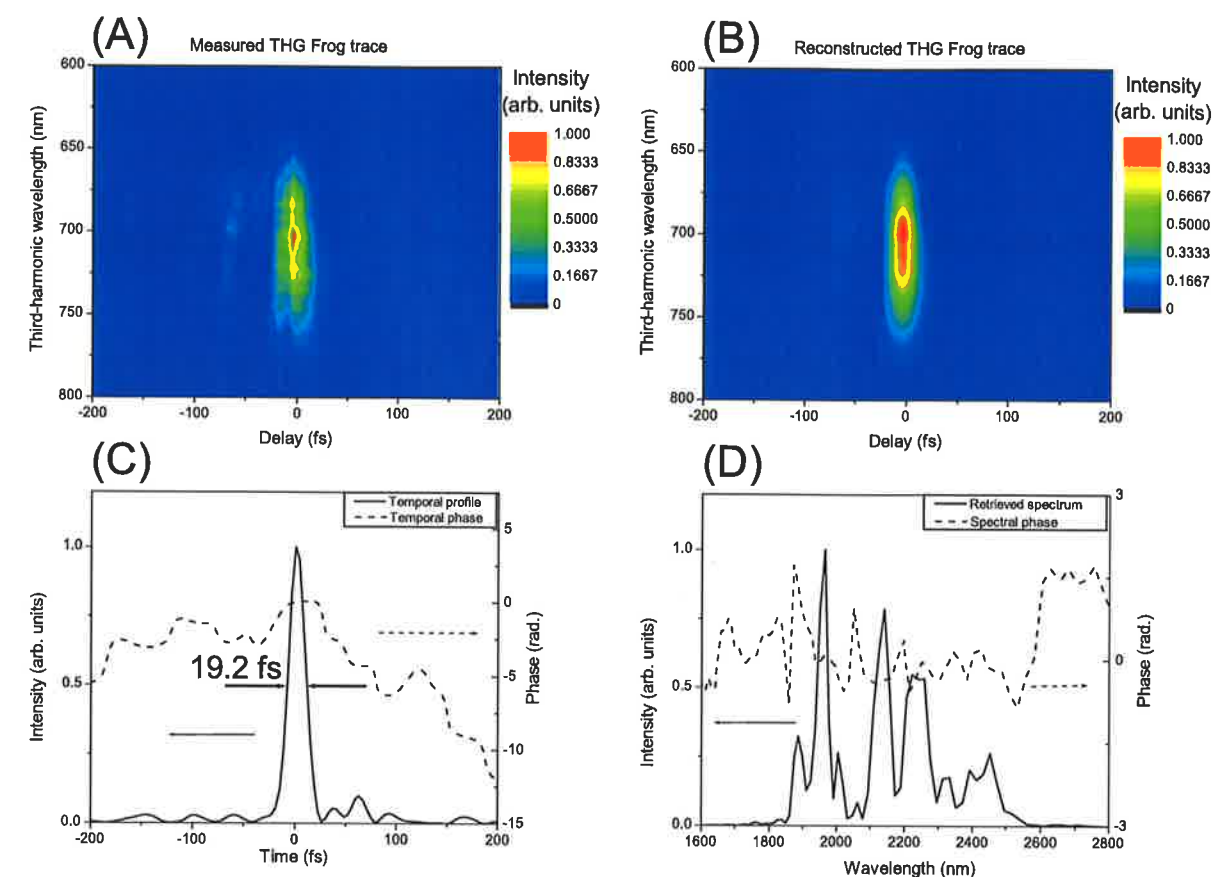
Figure 4.15: Results of few-cycle infrared pulse characterization by THG FROG. (A): measured THG FROG trace; (B): reconstructed THG FROG trace; (C): retrieved temporal pulse profile (solid line) with the duration of 19.2 fs (FWHM) and temporal phase (dashed line); (D): retrieved spectral intensity (solid line) and phase (dashed line).

shape, temporal phase, spectral intensity, and spectral phase are retrieved from the measured FROG trace. The measured residual spectral phase is fedback to the Dazzler for its correction. After several iterations, a typical FROG trace is obtained and shown in Fig. 4.15 (A). A FROG retrieve program reconstructs a FROG trace presented in Fig. 4.15 (B). From the reconstructed FROG trace, a temporal pulse profile (solid line) and a temporal phase (dashed line) are obtained and shown in Fig. 4.15 (C). A spectral intensity (solid line) and a spectral phase (dashed line) are obtained and shown in Fig. 4.15 (D). The duration of the reconstructed pulse is 19.2 fs (FWHM of the intensity). 19.2 fs corresponds to the 2.7 optical cycle at 2.1 μm. A pulse with the duration of about 16 fs is calculated by Fourier transform of the retrieved spectrum assuming a flat spectral phase.

In summary, we have built the few-cycle, high-energy infrared OPCPA system producing 350-μJ, sub-20-fs optical pulses around 2.1 μm at 1 kHz repetition rate. This system demon-

strated chirped pulse amplification in this wavelength range by use of the bulk stretcher and compressor and, as a result, produces the highest-energy ultrashort (for the pulse with the duration of less than hundred femtoseconds) laser pulses in the infrared. The CEP detection and stabilization of the output pulses from the infrared OPCPA system will be described in a next chapter by use of a novel f-to-$3f$ nonlinear interferometry. In addition, another application of high-harmonic generation in a noble gas will be described as well in the next chapter.

Chapter 5

Applications of few-cycle infrared pulses

5.1 Visible supercontinuum generation in solid-state materials and CEP detection of infrared pulses by use of an f-to-$3f$ interferometry

5.1.1 Introduction

Advance in ultrafast optics has resulted in the production of extremely ultrashort pulses whose duration corresponds to a few optical cycles of the carrier in the visible to near-infrared [270, 234]. The CEP, defined as a carrier phase of an ultrashort pulse at a peak of the pulse envelope, has become a key parameter for the few-cycle laser pulses [271]. Stabilization of the CEP of Ti:sapphire oscillator pulses was achieved independently in two groups [272, 273]. Subsequently, a CEP-preserving Ti:sapphire amplifier was constructed and its phase-locked high-energy output pulses was applied to generation of a CEP-dependent high-harmonic spectrum in a noble gas [19] and the demonstration of reproducible single attosecond pulse generation [32]. A key point in the use of few-cycle optical pulses for high-harmonic generation, single-attosecond-pulse generation, and its application to spectroscopic experiments is the stabilization and control of its CEP. In this section, we will describe experimental demonstration of visible supercontinuum generation in solid-state materials by the infrared pulses. Then, we will show detection of the CEP of the few-cycle infrared pulses based on a novel scheme, a unique f-to-$3f$ nonlinear interferometry, enabled by the spectral overlap between the visible supercontinuum and the third-harmonics (TH) of the fundamental pulses.

5.1.2 Nonlinear interferometries for CEP detection

In this subsection, we describe the experimental scheme for the detection of the CEP of laser pulses by use of nonlinear interferometries and its theoretical background. Detection and stabilization of a CEO frequency of the ultrashort pulses from a oscillator has been achieved usually by use of a f-to-$2f$ nonlinear interferometry [272, 273, 274, 275]. The CEO frequency is the

frequency of the pulse-to-pulse CEP drift. By use of this nonlinear interferometry, the CEO information can be derived from the phase information of the spectral interference between a high-frequency components of an octave-spanning spectrum obtained in a photonic crystal fiber [276] and a second harmonics of its low-frequency component. Recent advance in a CEP-detection technology has enabled another type of a nonlinear interferometry, which is a $0f$-to-f nonlinear interferometer based on the interference between the CEP-stable DF spectrum and the fundamental spectrum. [221, 222, 198]. In the case of CEP detection of a high-energy pulse, again, an octave-spanning supercontinuum generated in a sapphire plate was used for an f-to-$2f$ nonlinear interferometer [277]. In both cases, the octave spanning spectrum is necessary for detection of the CEP or CEO frequency to use the f-to-$2f$ nonlinear interferometry. Theoretical background of this f-to-$2f$ nonlinear interferometry can be derived easily below [277] and is applicable to a new f-to-$3f$ nonlinear interferometry. A Gaussian input electric field $E_1(t)$ with a phase offset between the carrier and envelope (CEP) ϕ_{cep} can be expressed in the time domain as

$$E_1(t) \propto \exp\left(-\frac{t^2}{\tau^2}\right)\exp\left\{-i\left(\omega_c t + \phi_{cep}\right)\right\}, \tag{5.1}$$

where i is the imaginary unit and τ is a half width at 1/e of the electric field amplitude. An electric field in the frequency domain $\vec{E}_1(\omega)$ can be expressed by the Fourier transform of $E_1(t)$ as

$$\tilde{E}_1(\omega) \propto \exp\left\{-\frac{\tau^2\left(\omega-\omega_c\right)^2}{4}\right\}\exp\left(-i\phi_{cep}\right), \tag{5.2}$$

$$\equiv \tilde{A}_1(\omega)\exp\left(-i\phi_{cep}\right). \tag{5.3}$$

From this equation, a second-order nonlinear polarization in the frequency domain $\tilde{P}_2(\omega)$ can be derived as

$$\tilde{P}_2(\omega) \propto \exp\left(-2i\phi_{cep}\right)\int_{\infty}^{\infty}\tilde{A}_1(\omega')\tilde{A}_1(\omega-\omega')d\omega'. \tag{5.4}$$

A second-harmonic electric field in the frequency domain $\tilde{E}_2(\omega)$ emitted by the second-order nonlinear polarization $\tilde{P}_2(\omega)$ is given by

$$\tilde{E}_2(\omega) \propto i\tilde{P}_2(\omega), \tag{5.5}$$

$$\propto \exp\left\{-i\left(2\phi_{cep}-\frac{\pi}{2}\right)\right\}\int_{\infty}^{\infty}\tilde{A}_1(\omega')\tilde{A}_1(\omega-\omega')d\omega', \tag{5.6}$$

$$\equiv \tilde{A}_2(\omega)\exp\left\{-i\left(2\phi_{cep}-\frac{\pi}{2}\right)\right\}. \tag{5.7}$$

From Eqs. 5.3 and 5.7, assuming a spectral overlap between the fundamental and second-harmonics and a relative group delay τ_d between them, the spectral intensity of the fundamental and second-harmonics exhibits a CEP-dependent spectral-interference term as

$$\tilde{I}(\omega) \propto \left[\tilde{A}_1(\omega)\exp\left(-i\phi_{cep}\right)+\tilde{A}_2(\omega)\exp\left\{-i\left(2\phi_{cep}+\omega\tau_d-\frac{\pi}{2}\right)\right\}\right]^2, \tag{5.8}$$

$$= \left|\tilde{A}_1(\omega)\right|^2+\left|\tilde{A}_2(\omega)\right|^2+2\left|\tilde{A}_1(\omega)\right|\left|\tilde{A}_2(\omega)\right|\cos\left(\phi_{cep}+\omega\tau_d-\frac{\pi}{2}\right). \tag{5.9}$$

The phase of the interference pattern is dependent on the CEP ϕ_{cep} so that CEP ϕ_{cep} shot-to-shot change can be detected by the measurement of a interference fringe pattern. The above derivation can be extended in the case of the f-to-$3f$ interferometry and a resultant formula can be derived as

$$\tilde{I}(\omega) \propto \left[\tilde{A}_1(\omega)\exp\left(-i\phi_{cep}\right)+\tilde{A}_3(\omega)\exp\left\{-i\left(3\phi_{cep}+\omega\tau_d-\frac{\pi}{2}\right)\right\}\right]^2 \tag{5.10}$$

$$= \left|\tilde{A}_1(\omega)\right|^2+\left|\tilde{A}_3(\omega)\right|^2+2\left|\tilde{A}_1(\omega)\right|\left|\tilde{A}_3(\omega)\right|\cos\left(2\phi_{cep}+\omega\tau_d-\frac{\pi}{2}\right), \tag{5.11}$$

where $\tilde{A}_3(\omega)$ is a spectral amplitude of a TH. We derived the CEP effect on the phase of the interference pattern obtained by the nonlinear interferometry. The phase shift of an interference fringe is affected by the CEP of the laser pulses two times more for the f-to-$3f$ interferometry than for the f-to-$2f$ interferometry. From these dependence, we could distinguish the order of an optical nonlinear effect from the analysis of the amount of the phase shift in the interference pattern induced by a arbitrary CEP change. Therefore we could examine an origin of a unknown nonlinear effect by this method. Later this technique will be used to determine the physical origin of the visible supercontinuum.

5.1.3   Visible supercontinuum generation in solid-state materials excited with infrared pulses

As seen above, to obtain the information about the CEP of an ultrashort pulse, an octave-spanning spectrum is necessary to utilize a nonlinear interferometry. For our case, because the few-cycle infrared pulses obtained from the infrared OPCPA system do not have an octave-spanning spectrum, we have to resort to any spectral broadening to achieve it. We have tried broadening by two ways, spectral broadening in a gas-filled hollow fiber [33] and supercontinuum generation in solid-state materials [72]. The use of supercontinuum generation in solid-state materials turned out to be the only choice for this purpose. The gas-filled hollow fiber did not produce any broadening of the infrared pulses. The generated supercontinuum, shown in Fig. 5.1 (A) and (B), has its broadened spectrum mainly in the visible and not in the infrared. Several-μJ compressed pulses were focused by a concave mirror (f=100 mm) into transparent materials (fused silica, sapphire, and undoped YAG). Fig. 5.1 (A) shows visible supercontinuum spectra obtained with 1.5-mm-thick fused silica (blue line), 2.0-mm-thick sapphire (green line), and 2.0-mm-thick undoped YAG (red line), compared to the fundamental spectrum without any sample (black line). Fig. 5.1 (B) shows the fundamental infrared pulse spectrum without any sample (black line) and the broadened spectrum with sapphire (red line). From this figure, in the infrared range around 2.1 μm, while a red wing of the fundamental spectrum was not extended so much, its blue part was slightly broadened in sapphire. However the fundamental spectrum is still not enough broadened for CEP detection. Despite the unexpected spectral range of the obtained supercontinuum, several features such as its conical emission [278, 279], its large beam divergence more than that of the fundamental [280], and its polarization identical to the fundamental pulses were convincing, to some extent, to be identified as the supercontinuum.
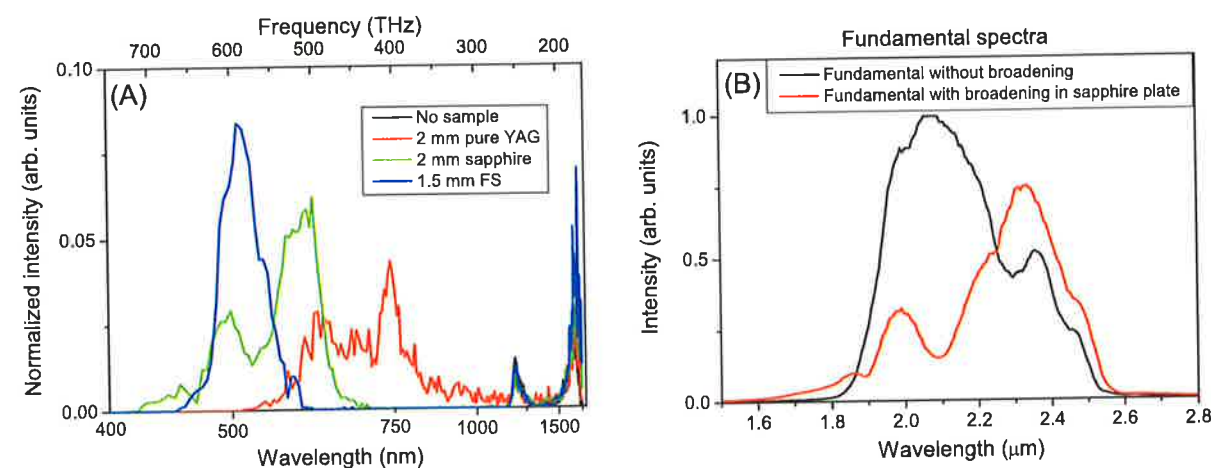
Figure 5.1: Spectral broadening of the few-cycle infrared pulse in solids: generation of supercontinuum in the visible. (A): supercontinua in the visible obtained with 1.5-mm-thick fused silica (blue line), 2.0-mm-thick sapphire (green line), and 2.0-mm-thick undoped YAG (red line) and the fundamental spectrum without any sample (black line). (B): Fundamental spectra without broadening (black line) and with broadening in sapphire (red line).

In the early days, spectral broadening of the nanosecond-picosecond pulses has been observed in liquid [281] and solid [282, 283] and main contribution to spectral broadening has been attributed to the SPM effect. Because of the availability of ultrashort laser pulses with the duration of hundred femtoseconds from 1980s, supercontinuum generation has been observed by use of femtosecond laser pulses [87]. In the case of the femtosecond pump pulse, self-steepening of the exciting pulse as well as SPM plays an important role in the spectral broadening [284]. Although the wider broadening should be expected for a sample with the higher Kerr-nonlinearity in this scenario this is not the case in the real experiment [285] and even supercontinuum in a less nonlinear medium proves to be broader [286]. A currently accepted scenario is that self-focusing and self-steepening of the ultrashort laser pulse contribute to the asymmetric broadening [287] and self-focusing is halted before the catastrophic pulse collapse due to the negative contribution to the refractive index from the plasmas created by the multiphoton ionization in the medium. Therefore the cut-off of spectral broadening becomes dependent on the band gap of a medium and the cut-off becomes more extended for a medium with the higher band gap [286, 288, 289, 280]. This tendency is clearly observed in Fig. 5.1. The supercontinuum obtained in the fused silica, which has the highest band gap among the three samples has the bluest cut-off of the supercontinuum and the undoped YAG resulted in the spectral broadening in the infrared region. So far the longest wavelength of pump pulses, which can generate a visible supercontinuum, is 1.5 μm [290]. To confirm the origin of the visible emission, where CEP detection and stabilization will be achieved by use of nonlinear interferometry, the spectral phase relation between the fundamental and supercontinuum could be derived using the above formulation of CEP dependence from the spectral phase of the interference pattern. In the next subsection, nonlinear interfer-

ometry will be achieved by spectrally overlapping the TH of the fundamental and the obtained visible supercontinuum possibly around 700 nm (an f-to-$3f$ nonlinear interferometry) and we will study its phase dependence on the CEP.

5.1.4 f-to-$3f$ nonlinear interferometer based on visible continuum and third harmonics of infrared pulses
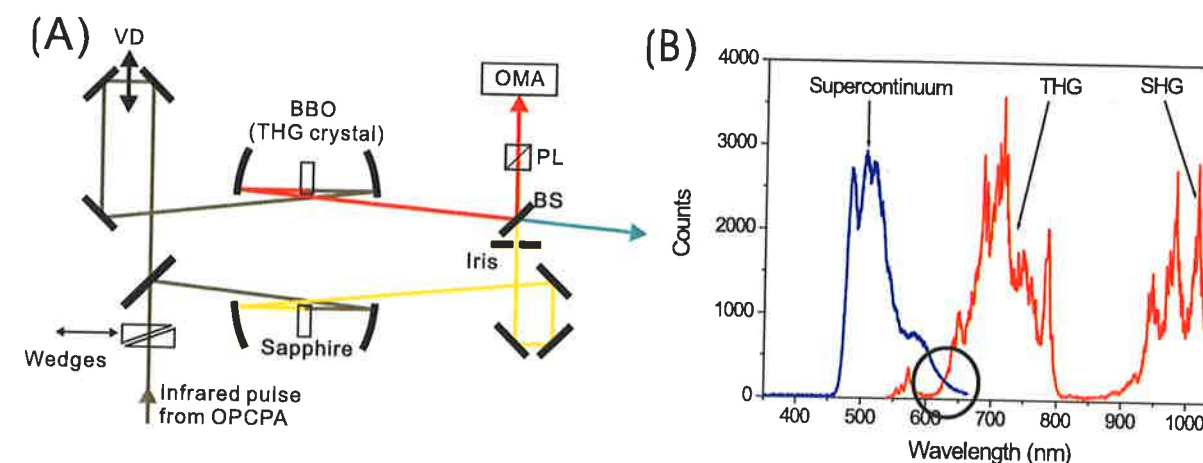

Figure 5.2: (A): Setup of the f-to-$3f$ nonlinear interferometer. VD: variable delay; Wedges: fused silica wedge pair; BBO: BBO crystal for THG; BS: beamsplitter; Iris: diaphragm for mode selection; PL: polarizer; OMA: optical multichannel analyzer (spectrometer). (B): Spectra of the TH (red line, indicated as THG) and the supercontinuum (blue line). Note that the red line has another peak, which results from the second harmonics of the infrared generated from BBO used for THG.

In this subsection, we describe the implementation of the f-to-$3f$ nonlinear interferometry by use of the TH of the infrared fundamental pulses and visible supercontinuum. Fig. 5.2 (A) shows an experimental setup for the f-to-$3f$ nonlinear interferometry. In one of two arms of the interferometer, the TH of the infrared fundamental pulse is generated in the type I ($ooo \rightarrow e$) phase-matching 1-mm-thick BBO crystal [291]. In the other arm, the supercontinuum is generated in a 2-mm-thick sapphire plate because sapphire is more robust than the undoped YAG and produces supercontinuum with a more appropriate spectral overlap with the TH than fused silica. Fig. 5.2 (B) plots the spectra of the TH (red line, indicated as THG) obtained in BBO and the supercontinuum (blue line) in sapphire. The second harmonics of the fundamental pulse, indicated as SHG in Fig. 5.2 (B), was simultaneously generated in BBO with almost the same condition as THG. We failed to spectrally overlap the SH and TH (a $2f$-to-$3f$ nonlinear interferometry) by this way because of the lack of the fundamental spectral bandwidth. The two beams are spatially overlapped by a beamsplitter and their orthogonal polarizations are mixed by use of

a cubic polarizer. The combined beam is focused into a fiber connected to an optical multichannel analyzer (spectrometer). Measured interferograms are shown in Fig. 5.3. The left graph in
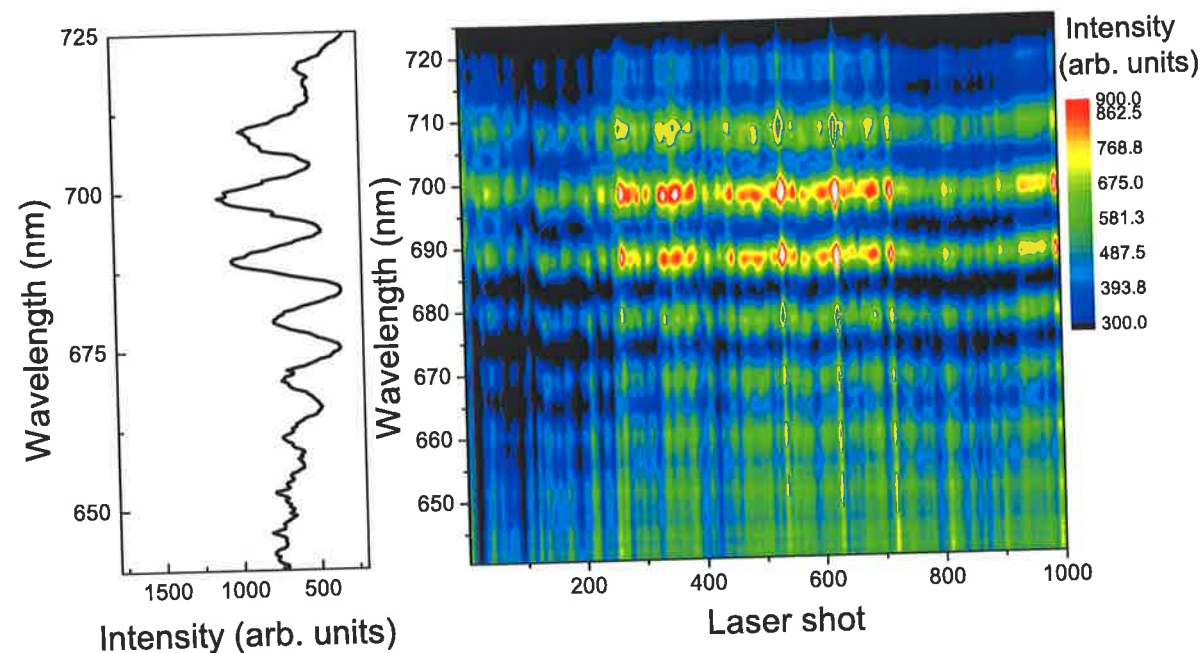

Figure 5.3: Interferogram and CEP stability measurement. Left: single-shot interferogram and Right: successively obtained interferograms.

Fig. 5.3 is a single-shot interferogram in the overlapped region and shows a clear interference fringe in the overlapped region. This interference pattern was dependent on the relative delay between the two interferometer arms and not observed when one of the two interferometer arms was blocked. The right trace is a shot-to-shot interferogram accumulated for 1 ms. This trace clearly shows that the phase of the interferogram is kept constant and indicates that the CEP is stabilized by the DFG process and preserved during parametric amplification. We have checked the phase dependence of the interferogram on the CEP. A fused silica wedge pair was inserted in front of the interferometer to shift the CEP. The difference of group and phase velocities of light is used to alter the relative phase of the carrier respect to the pulse envelope. The change of the fused silica thickness ΔL is related to the CEP $\Delta\phi_{CEP}$ shift as

$$\Delta\phi_{CEP} = \omega_c \frac{\Delta L}{v_p - v_g},\tag{5.12}$$

where ω_c is a central angular frequency of the infrared pulse and v_p and v_g are the phase velocity and group velocity, respectively. We scanned the fused silica wedge and recorded the interferogram at each insertion depth. Fig. 5.4 (A) represents the recorded interferogram with different wedge insertion depth. An x-axis represents the differential insertion depth from the different wedge insertion depth.
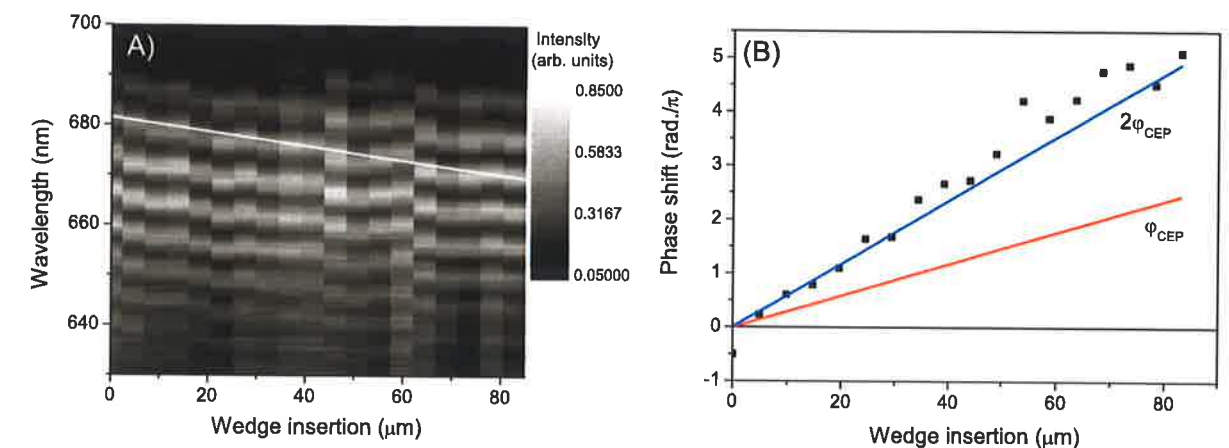
Figure 5.4: (A): Phase shift of the interference pattern by the CEP shift. (B): Phase shift dependence on the fused silica thickness and the resultant CEP. Predicted phase shift (blue line) when the phase shift of the interferogram is related to two times shift of the CEP and predicted phase shift (red line) when the phase shift of the interferogram is equal to the shift of the CEP.

first measurement point and a white line is drawn for a guide. Clearly a phase of the interference pattern shifts almost linearly with the fused silica insertion depth, indicating this interferometer is a nonlinear interferometer [253]. To the amount of the phase drift, the phase of the interference pattern is retrieved by use of the Fourier transform technique [292, 293]. An average value of intensity-weighted spectral phases at each scan point is plotted in Fig 5.4 (B). The equation 5.12 can relate the fused silica insertion depth and CEP phase drift. In Fig 5.4 (B), the interference pattern phase and the fused silica insertion depth are related as a red line for the f-to-$2f$ nonlinear interferometry, where the phase change of the interference pattern is equivalent to the change of the CEP, and as a blue line for the f-to-$3f$ nonlinear interferometry, where the phase change of the interference pattern is two times more than the change of the CEP. The measured phase data are fit on the line for the f-to-$3f$ nonlinear interferometry and a linear fit of the data gives a slope value of 2.28 ± 0.01. This is quite close to 2 and clear demonstration of the nonlinear interference fringe drift equal to $2\phi_{CEP}$. and indicates that the supercontinuum has the same CEP dependence as the fundamental because the TH carries $3 \times$ CEP and their difference should be $2 \times$ CEP. Although it is possible that this supercontinuum carries $5 \times$ CEP, however the fifth-order nonlinear effect is unlikely with such weak pulse energy and the wavelength of the supercontinuum does not corresponds to the fifth harmonics of the infrared pulse so that we exclude this possibility. Therefore the broadband visible emission from transparent media can be concluded as the supercontinuum generation carrying the same CEP as the fundamental.

In summary, we have observed and characterized the visible emission from the transparent solid-state materials. We attributed this visible emission to the supercontinuum by the ultrafast infrared optical pulse. This was confirmed by the f-to-$3f$ nonlinear interferometry and the examination of the relationship between the nonlinear interference phase shift and the CEP shift.

We have constructed the novel f-to-$3f$ nonlinear interferometer, which demonstrated the CEP stabilization by the DFG process and its preservation during the OPA process and the propagation through the stretcher and compressor.

5.2   High-harmonic generation by use of few-cycle infrared pulses

In this section, we demonstrate optical HHG of the few-cycle infrared laser pulses in a noble gas. The infrared driver laser is expected to extend the cut-off energy of the high-harmonics (HH) compared to the near-infrared driver laser based on Ti:sapphire and CPA.

After the first demonstration of third-harmonic generation [38], generation of odd-order optical harmonics in gases has been extensively investigated by use of high-peak intensity laser pulses with the relatively long nano- and picosecond duration [294, 295, 296, 297, 298]. From these experiments, a mechanism of HHG and a physical explanation of its cut-off energy have been derived and [299] and explained in detail by a three-step model [300] illustrated in Fig. 5.5. First, a bound electron in an atom is ionized either by tunneling ionization through a suppressed
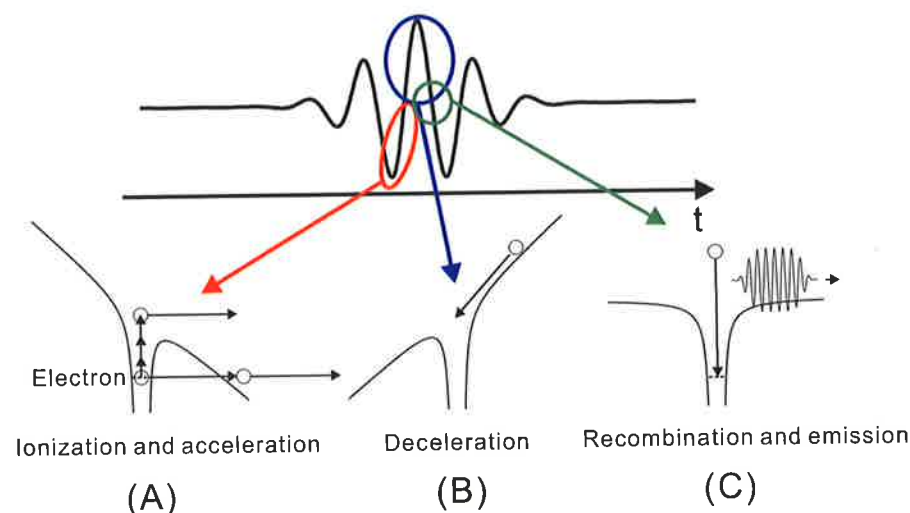

Figure 5.5: Illustration of the three-step model accounting for optical HHG. (A): bound electron ionized from an atom by tunneling ionization through the potential barrier or multiphoton ionization under a laser field and the ionized electron accelerated by the laser field. (B): The moving electron decelerated by the inversed laser field. (C): The still electron accelerated toward the parent nucleus and recombined with an emission of an extreme UV (EUV) or X-ray photon.

Coulomb barrier under the strong laser field [301] or by multiphoton ionization [302]. A dominant process between these two ionization mechanisms will be mainly determined by the laser field strength and its wavelength. Secondly, the ejected free electron is accelerated by the laser

field and, successively, decelerated by the inversed laser field after a half carrier cycle. Finally, further deceleration changes the direction of the electron motion toward the parent atom and the electron is interacted with the parent atom with certain probability and recombined with it. The recombination accompanies an emission of an EUV or soft X-ray photon, whose the energy corresponds to the sum of the kinetic energy acquired during acceleration and an atomic ionization potential energy. Therefore the emitted photon energy becomes dependent on the laser carrier period and the atomic ionization potential energy. The cut-off energy was empirically determined [299] and, later, derived using a semi-classical model [300] as

$$\hbar\omega_{\text{cut}} = I_p + 3.17 U_p \tag{5.13}$$

$$U_p = \frac{e^2 E^2}{4m\omega^2} \propto I\lambda^2, \tag{5.14}$$

where I_p is the atomic ionization potential energy, U_p is a ponderomotive or quiver energy given to the free electron by the laser field, E is the amplitude of the laser field, ω, I, and λ are an angular frequency, intensity, and wavelength of the laser pulse, and e and m is the charge and mass of the electron. In addition to this formula, a criterion, called Keldysh parameter [301], determines a dominant process for the electron ionization under the strong laser field either by the tunneling ionization through a suppressed Coulomb barrier or by the multiphoton ionization. This can be expressed as

$$\gamma = \left(\frac{I_p}{2U_p} \right)^{\frac{1}{2}}. \tag{5.15}$$

When $\gamma < 1$, the tunneling ionization becomes dominant over the multiphoton ionization [301]. Although the cut-off energy of the HH increases linearly with the laser intensity, at some point, this formula becomes inapplicable in the case of strong depletion of the electric ground-state of an atom and resultant plasmas generated in the target [303]. Several options can be found to maximize the cut-off energy with the fixed driver laser wavelength. One way is the use of shorter pump pulse, which are able to use efficiently the high peak intensity without problems of pre-ionization of a target caused by a long pulse [304]. By this approach, recent advance in ultrahigh-peak few-cycle laser pulse generation has pushed the cut-off limit to the keV range [305, 306, 307] Another way is to use an ion as a target [299, 308] because it possesses a higher ionization potential energy than a neutral atom. In addition, a novel technique using a modulated gas target is capable of quasi-phase-matching between the infrared and X-ray pulses and resulted in the keV-level HHG [309, 310]. However these demonstrations only observed the keV photon yield in the very edge of the generated HH spectrum and its spectral intensity is quite low.

The use of the infrared driver laser is more promising route to the extension of the HH cut-off, whose energy scales with the square of the driver laser wavelength indicated in Eq. 5.14. However so far HHG experiments have been exclusively investigated with a Ti:sapphire driver laser around 800 nm. A switch of the driver laser wavelength from the near-infrared to the infrared would result in the tremendous improvement in the extension of the HH photon energy. However only few theoretical and experimental works have been demonstrated so far about this topic: theoretical works on HHG cut-off extension by infrared exciting pulses [311, 312] and few

preliminary demonstrations [313, 314]. In these studies, B. Sheehy *et al.* [313] observed up to the 19th harmonics by use of 3-4 μm picosecond drive laser pulses exciting rubidium atoms. B. Shan *et al.* [314] revealed the cut-off dependence on the driving laser wavelength using argon (Ar) and xenon as targets and achieved up to 150-eV high harmonics with the Ar gas jet. Our infrared few-cycle laser source described in Chapter 4 is a quite attractive device for this application. The central wavelength of about 2.1 μm of the infrared laser pulses is 2.7 times longer than that of the Ti:sapphire laser, resulting in a 7-times higher ponderomotive energy. Simple theoretical calculations employing the single atom response without the propagation effect of the generated HH predict the extension of the cut-off up to 400 eV with an Ar target and a 2.1-μm driver laser, and above 1 keV with a neon (Ne) target [314].
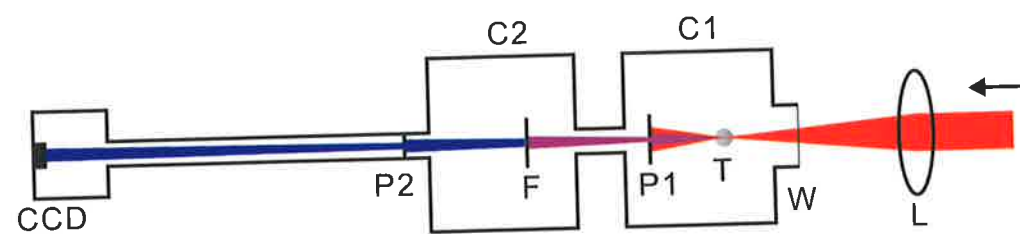

Figure 5.6: Experimental setup for HHG. L: CaF$_2$ lens with a focal distance of 100 mm; W: CaF$_2$ entrance window set at the Brewster angle; C1: HHG vacuum chamber; T: gas target (a squeezed Ni tube with holes); P1: diaphragm for alignment; C2: experimental vacuum chamber; F: 150-nm-thick zirconium (Zr) filter; P2: vacuum isolation filter between C1 and C2; CCD: back illuminated CCD, which can resolve a spectrum of the high harmonics.

The setup for the HHG experiment is shown in Fig. 5.6. The infrared laser pulses (350 μJ, 20 fs) from the infrared OPCPA system were focused with a CaF$_2$ 100-mm lens (L in Fig. 5.6) into the target. The laser beam propagates through holes made on both surfaces of a Ni tube filled with a pressurized noble gas (T in Fig. 5.6). The tube was squeezed to about 1 mm in order to avoid the phase-mismatch accumulated in the long interaction length. Measured focal spot size of the infrared pulses was about 30 μm in diameter (FWHM). The resultant intensity at the focus is about 1.1×10^{15} GW/cm^2. From these numbers and the use of an Ar as a target, Keldysh parameter γ in Eq. 5.15 becomes 0.13 , which indicates that ionization is dominated by the tunneling ionization. The ellipticity of the polarization was measured as less than 0.5% in the intensity (7% in amplitude). The ellipticity of the drive laser has been proven to decrease the high-harmonic photon yield [315]. A 150-nm-thick zirconium filter (F in Fig. 5.6) is placed behind the target to block the low harmonics and the strong fundamental light. Another pinhole (P2 in Fig. 5.6) separates vacuum conditions between the two chambers. A back-illuminated charge-coupled device (CCD) (CCD in Fig. 5.6), which is sensitive within the photon energy of from 1 eV to above 10 keV, is set up to attain the high-harmonic photon. The CCD can resolve a single photon energy by the conversion of the number of electrons generated in a pixel into the photon energy. Therefore the number of photons captured in a single pixel should be reduced to much less than one per scan in order to be sure that only less than one photon hits the single pixel. Otherwise two photons detected in a pixel per scan cannot be distinguished from a single

photon with the sum of the energies of two photons. We tried two noble gases, Ar and Ne, as targets. With Ne, no harmonics had been observed due to the weak driver laser pulses. By use of Ar with backpressure of several hundred mbar, high harmonics have been successfully obtained and its measured spectrum is shown in Fig. 5.7 (black line) (left linear scale and right logarithmic scale). The acquisition time to attain the data was about 1.5 hours. Dark counts obtained with the laser pulses and without Ar are shown in Fig. 5.7 (red line) as a comparison. Further gas pressure
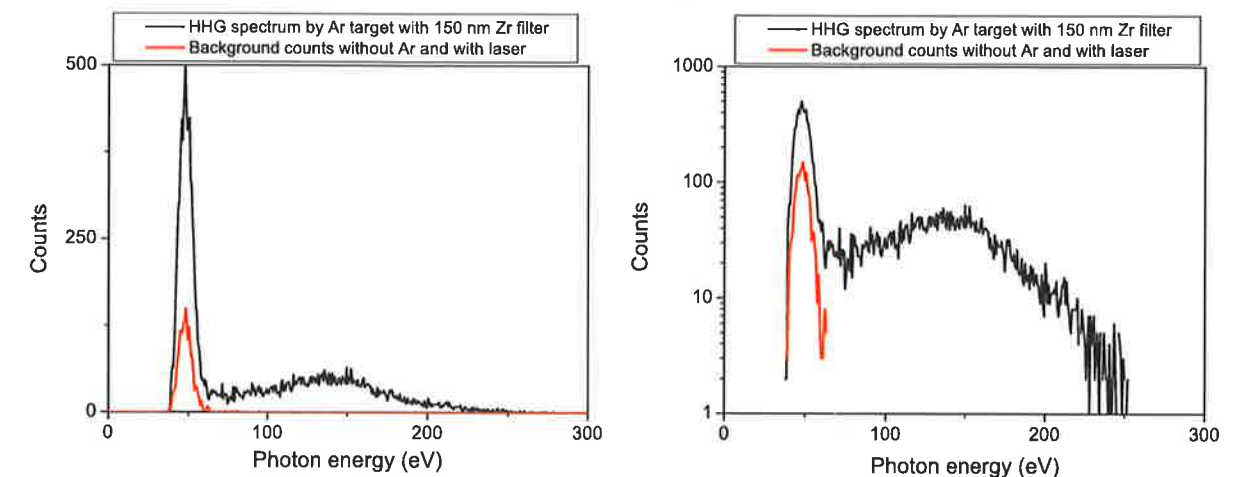

Figure 5.7: High-harmonic spectrum by use of Ar as a target excited with the few-cycle infrared laser pulses: high-harmonics spectrum with the Ar target and the driver laser (black line: linear scale in a left plot and logarithmic scale in a right plot) and background spectrum with the laser and without the Ar gas (red line). The acquisition time of the high-harmonic spectrum is about 1.5 hours.

decreased a photon yield because the vacuum pressure of 10^{-1} mbar was estimated to introduce the absorption of the generated X-ray. The experimental cut-off is about two times lower than that of the calculation based on the single atom response [314]. This effect can be explained by the propagation and phase-mismatch effects in the gas jet.

In summary we have generated the high-order harmonics from an argon gas target excited by the few-cycle infrared laser pulses. We have observed the cut-off energy of the generated harmonics around 250 eV. This is the highest photon energy achieved by the HHG mechanism in neutral Ar excited with a laser driver.

Appendix A

Refractive indices (Sellmeier equations) of crystals and optical materials

A.1   Refractive indices of birefringent crystals

Sellmeier equations used to calculate refractive indices of some optical materials are listed below. The unit of wavelength in the Sellmeier equations is μm.

- BBO (best set of Sellmeier eq., valid range UV - 2.5 μm, [80]),

$$n_o^2 = 2.7359 + \frac{0.01878}{\lambda^2 - 0.01822} - 0.01354\lambda^2 \tag{A.1}$$

$$n_e^2 = 2.3753 + \frac{0.01224}{\lambda^2 - 0.01667} - 0.01516\lambda^2 \tag{A.2}$$

- BBO (better accuracy in the infrared absorption edge, valid range UV - 3.2 μm, [316]),

$$n_o^2 = 2.7359 + \frac{0.01878}{\lambda^2 - 0.01822} - 0.01471\lambda^2 + 6.081 \times 10^{-4}\lambda^4 - 6.740 \times 10^{-5}\lambda^6 \tag{A.3}$$

$$n_e^2 = 2.3753 + \frac{0.01224}{\lambda^2 - 0.01667} - 0.01627\lambda^2 + 5.716 \times 10^{-4}\lambda^4 - 6.305 \times 10^{-5}\lambda^6 \tag{A.4}$$

- LBO (best set of Sellmeier eq., valid range 0.23 - 1.8 μm [317]),

$$n_x^2 = 2.4542 + \frac{0.01125}{\lambda^2 - 0.01135} - 0.01388\lambda^2 \tag{A.5}$$

$$n_y^2 = 2.5390 + \frac{0.01277}{\lambda^2 - 0.01189} - 0.01849\lambda^2 + 4.3025 \times 10^{-5}\lambda^4 - 2.9131 \times 10^{-5}\lambda^6 \tag{A.6}$$

$$n_z^2 = 2.5865 + \frac{0.01310}{\lambda^2 - 0.01223} - 0.01862\lambda^2 + 4.5778 \times 10^{-5}\lambda^4 - 3.2526 \times 10^{-5}\lambda^6 \tag{A.7}$$

- MgO:LiNbO$_3$ (5 mol% MgO-doped congruent LiNbO$_3$ at 294 K, valid range 0.4 - 5.0 μm, [318]),

$$n_o^2 = 1 + \frac{2.4272\lambda^2}{\lambda^2 - 0.01478} + \frac{1.4617\lambda^2}{\lambda^2 - 0.05612} + \frac{9.6536\lambda^2}{\lambda^2 - 371.216} \tag{A.8}$$

$$n_e^2 = 1 + \frac{2.2454\lambda^2}{\lambda^2 - 0.01242} + \frac{1.3005\lambda^2}{\lambda^2 - 0.05313} + \frac{6.8972\lambda^2}{\lambda^2 - 331.33} \tag{A.9}$$

- MgO:LiNbO$_3$ (temperature dependent extraordinary refractive index, T in °C, [319]),

$$Ft \equiv (T - 33.5) * (T + 564.5)$$

$$C_{\text{MgO}} \equiv 1.0270295 - 4.56346827 \times 10^{-5}T$$

$$n_e^2 = \left\{ 5.3558 + 4.6290 \times 10^{-7}Ft + \frac{0.10047 + 3.862 \times 10^{-8}Ft}{\lambda^2 - (0.20692 - 8.9 \times 10^{-9}Ft)^2} \right.$$
$$\left. + \frac{100 + 2.657 \times 10^{-5}Ft}{\lambda^2 - (11.349)^2} - 0.015334\lambda^2 \right\} / C_{\text{MgO}}^2 \tag{A.10}$$

- Stoichiometric LiTaO$_3$ (valid range 0.44 - 1.05 μm, T in K, [320]),

$$n_o^2 = 4.5281 + \frac{0.079841}{\lambda^2 - 0.047857} - 0.032690\lambda^2$$

$$n_e^2 = 4.5096 + \frac{0.082712}{\lambda^2 - 0.041306} - 0.031587\lambda^2$$

- Stoichiometric LiTaO$_3$ (temperature dependent extraordinary refractive index, valid range 0.39 - 4.1 μm, T in K, [321]),

$$n_e^2(\lambda, T) = 4.502483 + \frac{0.007294 + 3.483933 \times 10^{-8}T^2}{\lambda^2 - (0.185087 + 1.607839 \times 10^{-8}T^2)^2}$$
$$+ \frac{0.073423}{\lambda^2 - (0.199595)^2} + \frac{0.001}{\lambda^2 - (7.99724)^2} - 0.02357\lambda^2 \tag{A.11}$$

- TeO$_2$ (valid range 0.4 - 1.0 μm, [322]),

$$n_o^2 = 1.0 + \frac{2.584\lambda^2}{\lambda^2 - (0.1342)^2} + \frac{1.157\lambda^2}{\lambda^2 - (0.2638)^2} \tag{A.12}$$

$$n_e^2 = 1.0 + \frac{2.823\lambda^2}{\lambda^2 - (0.1342)^2} + \frac{1.542\lambda^2}{\lambda^2 - (0.2631)^2} \tag{A.13}$$

- TeO$_2$ (better accuracy in the infrared, valid range 0.4 - 3.5 μm, [267]),

$$n_o^2 = 1.0 + \frac{3.71789\lambda^2}{\lambda^2 - (0.19619)^2} + \frac{0.07544\lambda^2}{\lambda^2 - (4.61196)^2} \tag{A.14}$$

$$n_e^2 = 1.0 + \frac{4.33449\lambda^2}{\lambda^2 - (0.20242)^2} + \frac{0.14739\lambda^2}{\lambda^2 - (4.93667)^2} \tag{A.15}$$

A.2   Refractive indices of isotropic materials

- SF57 (from Schott, [323]),

$$n = 1.0 + \frac{1.816513871\lambda^2}{\lambda^2 - 0.0143704198} + \frac{0.428893641\lambda^2}{\lambda^2 - 0.0592801172} + \frac{1.07186278\lambda^2}{\lambda^2 - 121.419942} \tag{A.16}$$

- FS (valid from 0.210 to 3.710 μm, available in Chapter 33 of Ref. [324]),

$$n = 1.0 + \frac{0.6961663\lambda^2}{\lambda^2 - (0.0684043)^2} + \frac{0.4079426\lambda^2}{\lambda^2 - (0.1162414)^2} + \frac{0.8974794\lambda^2}{\lambda^2 - (9.896161)^2} \tag{A.17}$$

- Silicon (at room temperature, [325]),

$$n = 11.6858 + \frac{0.939816}{\lambda^2} + \frac{8.10461 \times 10^{-3} * (1.1071)^2}{\lambda^2 - (1.1071)^2} \tag{A.18}$$

- BK7 (from Schott, [326]),

$$n = 1.0 + \frac{1.03961212\lambda^2}{\lambda^2 - 0.00600069867} + \frac{0.231792344\lambda^2}{\lambda^2 - 0.0200179144} + \frac{1.01046945\lambda^2}{\lambda^2 - 103.560653} \tag{A.19}$$

Appendix B

Comparison of electronic and optical synchronizations

In Tab. B.1, characteristics of optical synchronization and electronic synchronization between the seed and pump pulses in an OPCPA system are summarized. Detailed discussions are found in Sections 2.5 and 3.2 for the electronic synchronization method and in Sections 3.3, 3.4, and 3.5 for the optical synchronization method.

	Electronic synchronization	Optical synchronization
Timing jitter (short term)	< few ps	< 1 ps
Timing drift (long term)	several ten ps	several ps
Wavelength tunability	flexible	flexible within oscillator's spectrum
Coarse timing (coarse timing adjustment required)	everyday realignment required	fixed oscillator rep. rate fixed amplifier path length (fixed round trip)
Seed energy to pump amplifier	high	low (ASE problem)
Handling	complicated	simple
Cost	two oscillators + locking electrics	ultrabroadband oscillator

Table B.1: Comparison of electronic and optical synchronization methods

Appendix C

Saturation of Nd:YLF amplifier

In this appendix, the saturation effect in a regenerative amplifier amplifier either by the average power or by an individual energy is discussed. A simple formula to calculate the accumulated effective power or energy is also derived.

In Section 3.3, the Q-switched output power of more than 3 W from a Nd:YLF regenerative amplifier was obtained. Let us compare the obtained output result with the saturation fluence and intensity of Nd:YLF at 1053 nm. The saturation fluence and intensity of Nd:YLF at 1053 nm are 0.79 J/cm^2 and 1.57 kW/cm^2, respectively. To calculate the pulse intensity in the regenerative amplifier described in Section 3.3, the amplified beam radius, defined by the half width at $1/e^2$ of the peak intensity at the Nd:YLF crystal, is determined as 0.8 mm from Fig. 3.2. From this radius, one can derive the effective mode area (2 mm^2) and, consequently, the saturation energy and power of 16 mJ and 31.6 W, respectively. In our case, the performance of the regenerative amplifier operated at 1 kHz should be limited by energy saturation and not by power saturation because the fluorescence life-time of Nd:YLF is 500 μs so that the roll-off frequency between the power and energy saturation should be 2 kHz. The output energy and power from the regenerative amplifier with the seed injected is 3.7 mJ and 3.7 W.

The effective intracavity energy and power are dependent not only on the output energy and power, but also on the initial seed energy and the gain in the amplifier. This is because the total energy and power of the pulses passing through the laser crystal in the cavity are accumulated during amplification. The following formula is suitable to calculate the optimistic (higher than real) effective energy E_{eff} and power P_{eff} in the cavity

$$E_{eff} = \sum_{i=0}^{n-1} E_{in} * g^i = \frac{g^n - 1}{g-1} E_{in} \simeq \frac{g}{g-1} E_{out}, \qquad (C.1)$$

$$P_{eff} = \sum_{i=0}^{n-1} P_{in} * g^i = \frac{g^n - 1}{g-1} P_{in} \simeq \frac{g}{g-1} P_{out}, \qquad (C.2)$$

where g, E_{in}, P_{in}, $E_{out}(\equiv E_{in} \times g^{n-1})$, and $P_{out}(\equiv P_{in} \times g^{n-1})$ are the single pass gain (not round trip gain in the regenerative amplifier), input energy into the regenerative amplifier, input power, output energy from the regenerative amplifier, and output power, respectively. In the pessimistic (less than real) case, the values could be obtained by dividing the above results by the single-pass

gain. The last approximations of the equations are verified by the total gain much higher than 1 ($g^{n-1} \gg 1$). This equation does not take into account the loss and the saturation effect in the amplifier. In our system condition with a single pass gain of 1.5 and output power of 3.7 mJ (3.7 W and 1 kHz), the effective energy in the cavity is calculated as 11.1 mJ, which is close to the Nd:YLF saturation energy of 16 mJ.
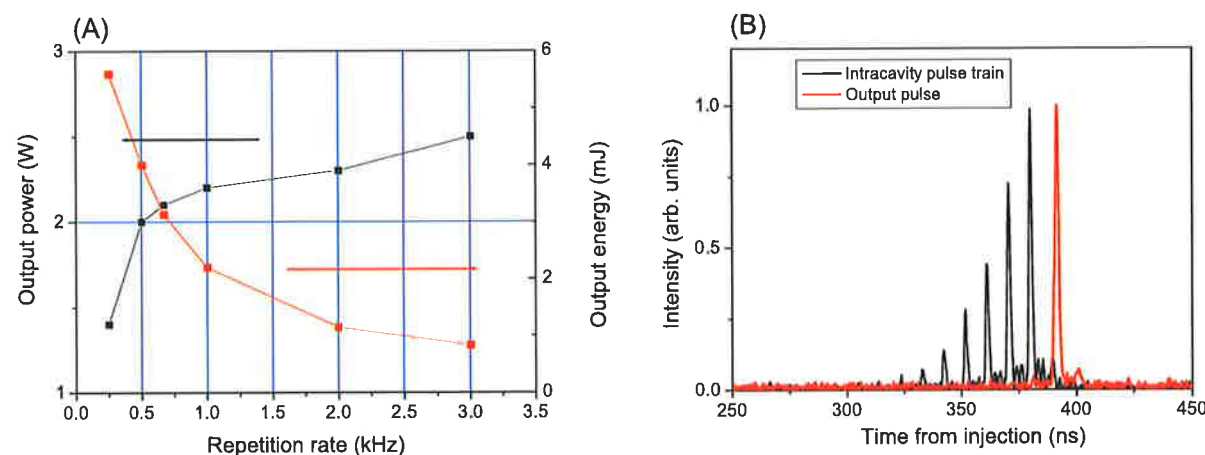

Figure C.1: Output power and energy from the Nd:YLF amplifier and intracavity pulse train and output pulse. (A): Output power (black line) and energy (red line) from the Nd:YLF amplifier with a different repetition rate. (B): Intracavity pulse train (black line) and output pulse (red line).

We have also investigated the roll-off frequency of the regenerative amplifier by changing its repetition rate. The plot in Fig. C.1 shows the output power (black line) and the output energy (red line) from the regenerative amplifier. The output power stays constant above about 750 Hz, which contradicts with the above predicted 2 kHz roll-off frequency. However, this character has been pointed out from early Nd:YLF regenerative amplifier development [210, 212]. Both experiment observed the roll-off frequency of about 750 Hz or less. This fact is also shown in Fig. C.1, where an intracavity pulse train and an output pulse of the Nd:YLF regenerative amplifier are plotted. The intracavity pulse train does not show the saturation by itself. However, when one more round trip is added, the whole intracavity pulse train is just shifted to the right and the output is not increased as would be expected by the round trip gain. Despite of the discrepancy from the simple calculation and experimental result, we conclude that the regenerative amplifier is saturated by the average power and not by the individual pulse energy.

Appendix D

Spectral filtering effect in a regenerative amplifier by use of an etalon

D.1   Introduction

In this appendix, we experimentally and theoretically analyze spectral filtering and pulse shaping of a pulse by an etalon in an amplifier (either a regenerative amplifier or a multipass amplifier).

As described in Section 3.3, the intense short strong pulses produced in an amplifier without any spectral filtering severely suffer from nonlinear effects such as self-phase modulation (SPM), self-focusing (especially small-scale self-focusing), pulse splitting, and spectral broadening. To avoid these effects and obtain a clean amplified pulse, which increases the usable energy in a pump pulse used for OPA, the pulse has to be temporally stretched either before or during amplification. In addition, a controllable stretching technique would be quite attractive. Although a pulse stretcher in front of the amplifier is frequently used in CPA, in our case, the narrow gain bandwidth of a Nd:YLF amplifier prevents the use of the chirped-pulse amplification technique. An etalon inside the amplifier cavity (a regenerative amplifier is considered here instead of a multipass amplifier) seems to be a promising candidate, which is suggested by Drs. A. Michailovas and J. Kolenda of EKSPLA Co. Ltd. in Lithuania. Another approach producing a long seed pulse for a picosecond amplifier in a near-infrared OPCPA system [136] was demonstrated by use of a 4-f system to select a narrow spectrum out of a broader oscillator pulse spectrum. The effect of the etalon can be explained both in the time and frequency domains. In the time domain, multiple reflections from the surfaces of the etalon result in pulse stretching provided that gaps between the multiple pulses are smaller than the individual pulse duration. In the frequency domain, the periodically varying transmittance of the etalon narrows the input pulse spectrum, resulting in spectral filtering and pulse stretching. In later sections, details of the effect of the etalon inside an amplifier cavity will be analyzed.

D.2 Etalon spectral filtering and gain narrowing

Usually the linear propagation of light through optics is more easily described in the frequency domain than in the time domain.
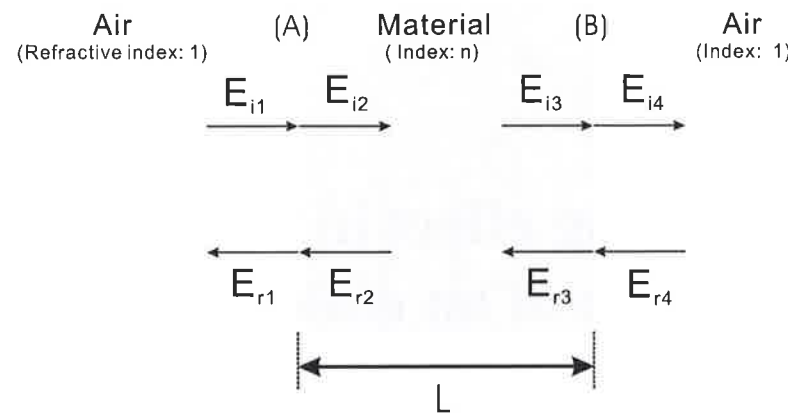

Figure D.1: Configuration and parameters for the calculation of the etalon response. E_{i1}: electric field incident on the air side of the surface (A); E_{r1}: electric field reflected on the surface (A); E_{i2}: electric field transmitting through the surface (A); E_{r2}: electric field returned from the material side of the surface (A); E_{i3}: electric field incident on the material side of the surface (B); E_{r3}: electric field reflected from the material side of the surface (B); E_{i4}: electric field transmitting through the surface (B); E_{r4}: electric field coming into the air side of the surface (B) (=0). The material thickness is L.

In order to describe the light propagation through the etalon, we use a calculation procedure written in a section "Electromagnetic Propagation in Periodic Media" in [327]. The configuration and parameters are shown in Fig. D.1. With the boundary conditions of the Maxwell equations [328, 70] and the approximation of monochromatic plane waves normally incident on the surface (A), the relationships among the electric fields are derived as

$$E_{i1} + E_{r1} = E_{i2} + E_{r2}, \tag{D.1}$$

$$ik(E_{i1} - E_{r1}) = ik_n(E_{i2} - E_{r2}), \tag{D.2}$$

$$E_{i3} = E_{i2}\exp(-ik_nL), \tag{D.3}$$

$$E_{r3} = E_{r2}\exp(ik_nL), \tag{D.4}$$

$$E_{i4} = E_{i3} + E_{r3}, \tag{D.5}$$

$$ik_n(E_{i3} - E_{r3}) = ikE_{i4}, \tag{D.6}$$

where $k\ (= \omega/c)$, $k_n\ (= n\omega/c)$, n, ω, and c represent the wave vector of the monochromatic wave in air, the wave vector in the material, the refractive index of the material, the angular frequency of the monochromatic wave, and the velocity of the light in vacuum, respectively. In a real experiment, a slight tilt of the etalon is introduced to avoid the back reflection of the input

beam into the amplifier and to match the peak of the etalon transmittance to the peak of the fluorescence spectrum of the laser medium.

After algebraic procedures, E_{i1} and E_{i4} are related as

$$E_{i1} = \left\{ \cos(k_nL) + i\frac{n+\frac{1}{n}}{2}\sin(k_nL) \right\} E_{i4}, \tag{D.7}$$

$$\Longleftrightarrow E_{i4} = \left\{ \cos(k_nL) + i\frac{n+\frac{1}{n}}{2}\sin(k_nL) \right\}^{-1} E_{i1}, \tag{D.8}$$

$$\Longleftrightarrow I_{i4} = \left\{ \cos^2(k_nL) + \frac{\left(n+\frac{1}{n}\right)^2}{4}\sin^2(k_nL) \right\}^{-1} I_{i1}, \tag{D.9}$$

where $I_{i4}\ \left(\propto |E_{i4}|^2\right)$ and $I_{i1}\ \left(\propto |E_{i1}|^2\right)$ are the intensities of the output and input waves, respectively. Consequently, formulas for transfer functions of the amplitude T_E (complex) and the intensity T_I (real) become

$$T_E = \frac{E_{i4}}{E_{i1}} = \frac{1}{\cos(k_nL) + i\frac{n+\frac{1}{n}}{2}\sin(k_nL)}, \tag{D.10}$$

$$T_I = \frac{I_{i4}}{I_{i1}} = \frac{1}{\cos^2(k_nL) + \frac{\left(n+\frac{1}{n}\right)^2}{4}\sin^2(k_nL)}, \tag{D.11}$$

respectively. Examples of the calculated single-pass transmittances of a 500-μm-thick fused silica (black line), a 1-mm-thick fused silica (red line), and a 500-μm-thick sapphire (z-cut or c-cut) (green line) and a 1.3-nm-wide simulated fluorescence spectrum of Nd:YLF (blue line) are plotted in Fig. D.2, respectively. Another spectral filtering effect in the amplifier other than the etalon effect is gain narrowing [54]. The stimulated emission cross section of the laser medium varies with wavelength and so does the amount of gain. Due to the higher gain values at the central region than at the wings, the spectrum is narrowed during amplification. The amplified-pulse spectrum becomes narrower with higher gain. Detailed description is available in many books such as "Lasers" by A.E. Siegman [54]. A calculated result is shown in Fig. D.3 for the single-pass transmittance of the 500-μm-thick fused silica (black line), the 1.3-nm-wide (FWHM) fluorescence spectrum (red line), and a 0.27-nm-wide (FWHM) output spectrum obtained after amplification of 10^{11} (green line) at the peak of the fluorescence spectrum. In Fig. D.4 (A) (in linear scale) and (B) (in logarithmic scale), a calculated spectrum (black spectrum) including gain narrowing is compared with the calculated amplified spectra including gain narrowing and spectral filtering by the 0.8-mm-thick etalon (black line) and gain narrowing and spectral filtering by the 1.0-mm-thick etalon (red line). The comparison between the spectral widths with and without the etalon clearly demonstrates the spectral narrowing effect of the etalon inside the amplifier and resultant effective stretching of the amplified pulse. From Fig. D.4 (A), it also follows that the neighboring maxima of the single-pass transmittance of the etalon with respect to the gain peak produces periodic modulation in the gain-narrowed amplified spectrum. This periodic
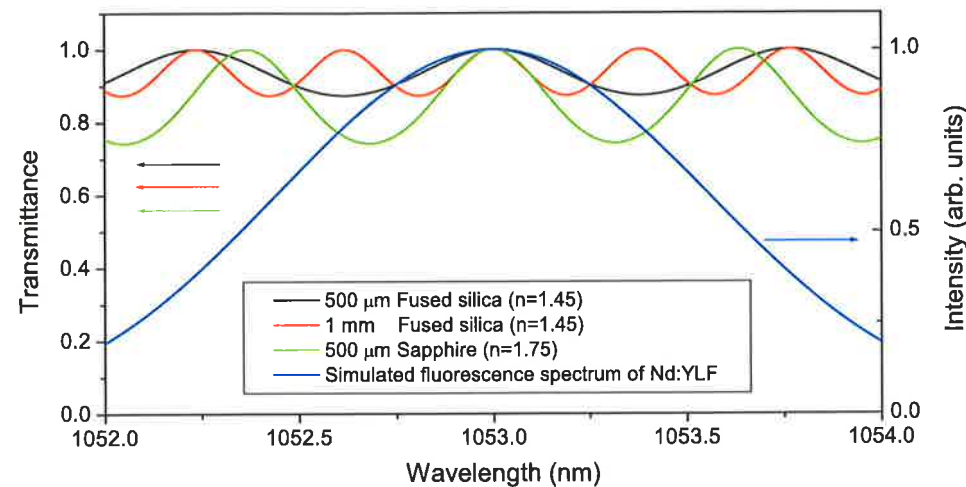
Figure D.2: Etalon transmittances and the Nd:YLF fluorescence spectrum. Transmittances: a 500-μm-thick fused silica (black line), a 1-mm-thick fused silica (red line), and a 500-μm-thick sapphire (green line). A simulated Nd:YLF fluorescence spectrum (blue line).
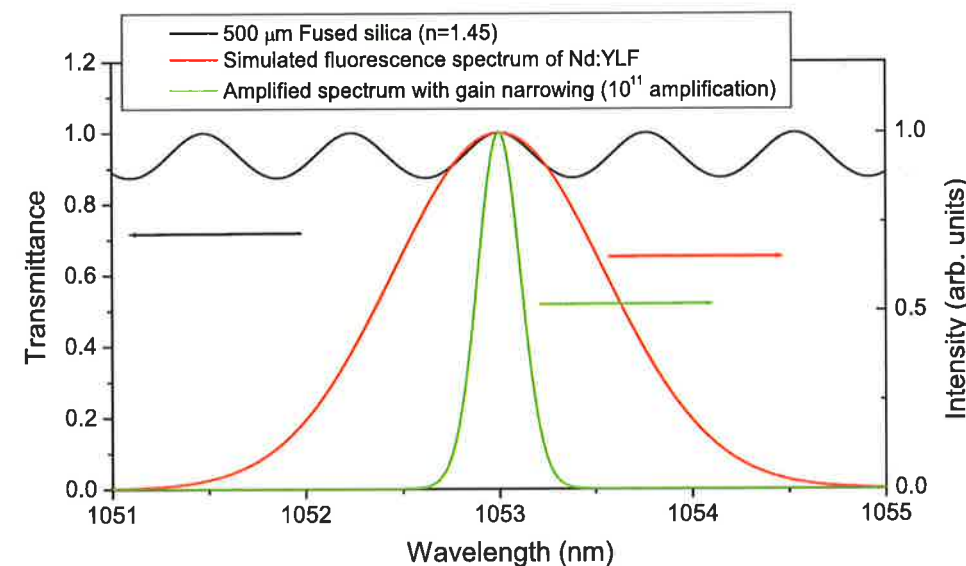

Figure D.3: Gain narrowing in the Nd:YLF amplifier: the single-pass transmittance of the 500-μm-thick fused silica (black line), the 1.3-nm-wide (FWHM) fluorescence spectrum (red line), and a 0.27-nm-wide (FWHM) output spectrum obtained after amplification of 10^{11} (green line) at the peak of the fluorescence spectrum.
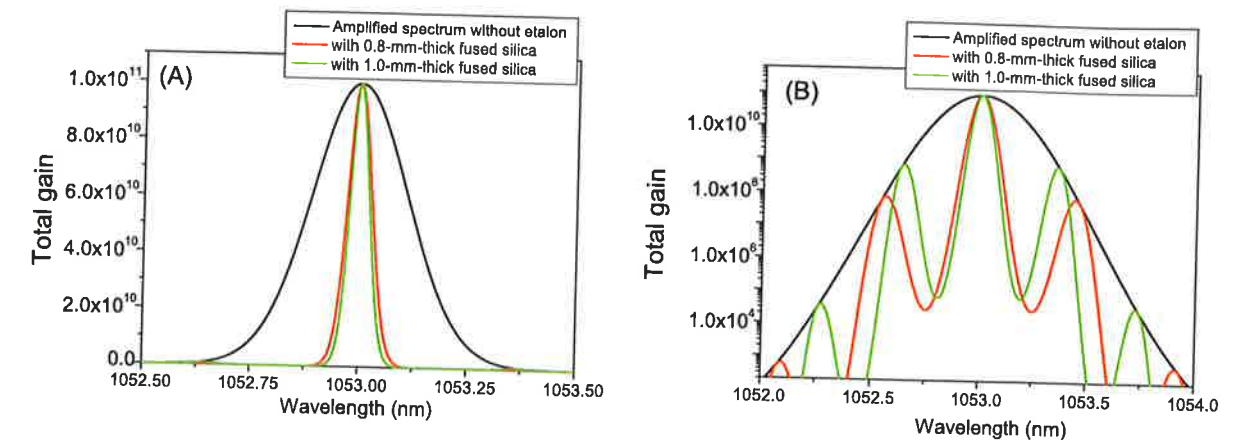
Figure D.4: Spectral filtering by the etalon and gain narrowing. Calculated amplified spectra in linear scale (A) and logarithmic scale (B) including gain narrowing (black line), gain narrowing and spectral filtering by the 0.8-mm-thick etalon (red line), and gain narrowing and spectral filtering by the 1.0-mm-thick etalon (green line).

Figure D.5: Effects of gain narrowing and etalon spectral filtering on temporal pulse profiles. (A): Calculated temporal profiles of the amplified pulses including gain narrowing and spectral filtering by the 0.8-mm-thick etalon (black line) and gain narrowing and spectral filtering by the 1.0-mm-thick etalon (red line). (B): Simulated (line) and measured (dotted line) autocorrelation traces with the 0.8-mm-thick etalon (black) and the 1.0-mm-thick etalon (red), respectively.

modulation of the spectrum causes ripples in the temporal profile of the amplified pulse. Simulated temporal pulse profiles including gain narrowing and spectral filtering by the 0.8-mm-thick etalon (black line) and gain narrowing 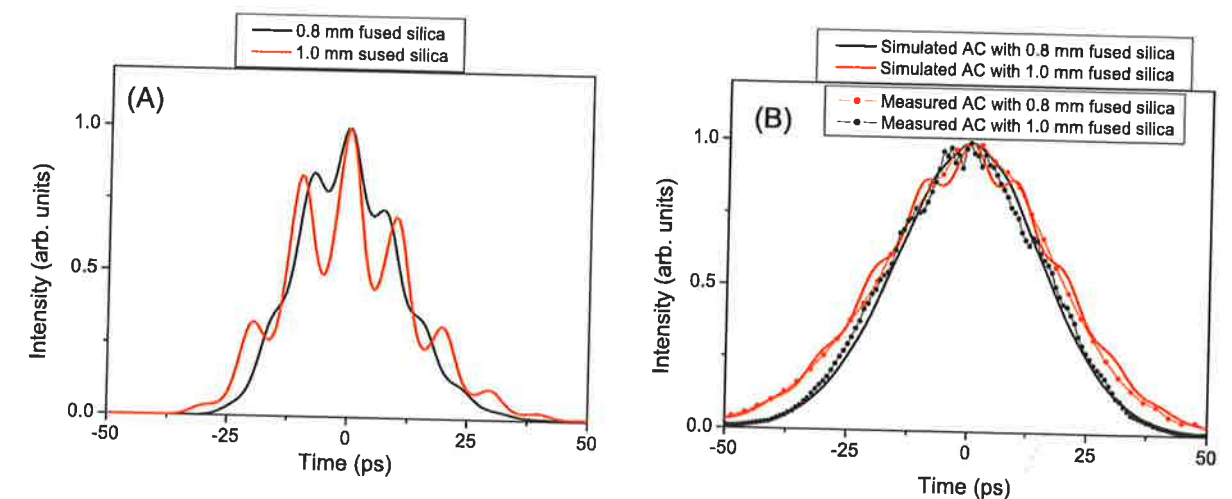and spectral filtering by the 1.0-mm-thick etalon (red line) are shown in Fig. D.5 (A). Simulated (line) and measured (dotted line) autocorrelation traces (B) with the 0.8-mm-thick etalon (black) and the 1.0-mm-thick etalon (red) are shown in Fig. D.5 (B). In Fig. D.5 (B), the good correspondence between the simulated (solid lines) and measured (dotted lines) autocorrelation traces in the both cases using the 0.8-mm-thick etalon (black) and the 1.0-mm-thick etalon (red), demonstrates the validity of our model and calculation.

In the experiment, although the calculation shows the shallow ripples in the amplified pulse with the 0.8-mm thick etalon, the degradation of the pump pulse has been hardly noticeable. However, further amplification of the pulse leads to observable effects, which are enhanced during amplification by the accumulated nonlinear effects. To extinguish completely the ripples in the temporal pulse profile, we have tried an idea to insert two different intracavity etalons, by which the oscillation of the transmittance of one etalon is cancelled out by the other. This results in a smoother amplified spectrum and a cleaner temporal pulse profile. In Fig. D.6 (A), the measured autocorrelation traces of amplified pulses with energies of 1 mJ (black line) and 17 mJ (red line) from three stage post amplifiers tried in an infrared OPCPA pump development and a simulated autocorrelation trace (green line) are shown. Enhancement of the multiple peaks found in the 17-mJ trace (Fig. D.6 (A), red line) can be explained by the self-compression of each peak caused by SPM and gain narrowing [209, 211]. In Fig. D.6 (B), the multi-etalon approach results in a measured smooth autocorrelation trace (black line), which corresponds well to the calculated autocorrelation trace (red line), and also the smooth simulated temporal pulse profile (green line). Transmittances of a 0.7-mm-thick etalon (black dashed line) and a 1.0-mm-thick etalon (red dashed line) and the amplified spectra with the 0.7-mm-thick etalon (black solid line) and the 1.0-mm-thick etalon (red solid line) are shown in Fig. D.7 (A). The transmittances of the 0.7-mm and the 1.0-mm-thick etalons show a unique oscillatory structure with different periods. The effect of the multi-etalon approach is demonstrated in Fig. D.7 (B): the single-pass transmittance (black dashed line) and the amplified spectrum (black solid line) with the 0.7-mm and 1.0-mm-thick etalons. As a result, each amplified spectrum has its own periodically modulated structure with the same period as in their transmittance curve. By using two etalons of different thicknesses, the oscillation of the transmittance of one etalon cancels the other and, totally, the transmittance of the two etalons has the only single peak at the center, resulting in a clean amplified spectrum without any side peak above the level of 10^{-7} of the peak intensity.

D.3   Summary

The simple formula for the transmittance of an etalon has been derived, compared, and verified with experiments. The simulation results of the amplified pulse spectrum including the gain narrowing effect and etalon spectral filtering have helped the experimental implementation. Experimental problems due to multiple pulses caused by the nonlinear effects have been solved by adopting the two-etalon approach. The application of this technique, however, is limited by physical dimensions (thickness of the etalon), the amount of gain narrowing caused by a laser
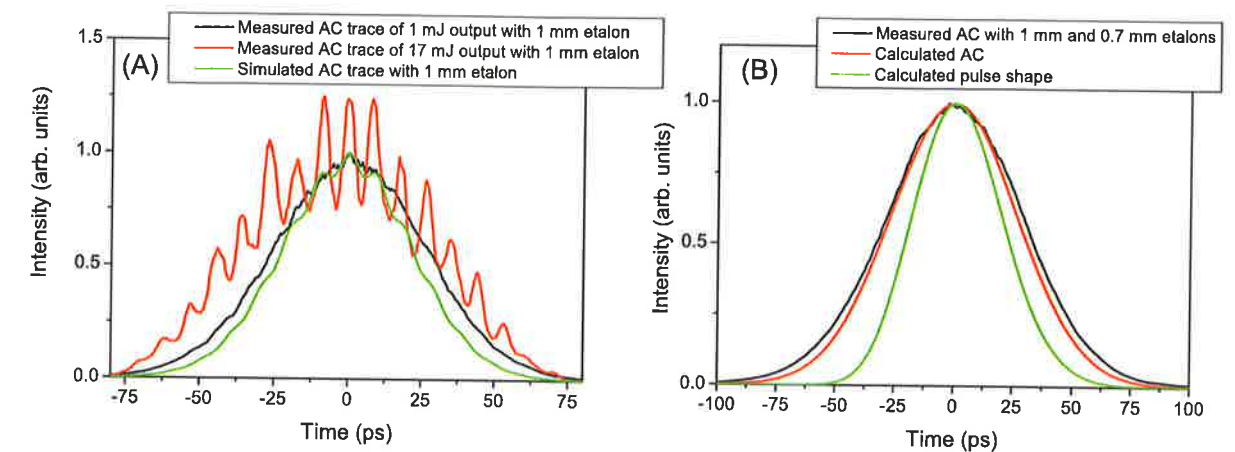
Figure D.6: (A): Measured autocorrelation traces of 1-mJ output pulses (black line) and 17-mJ output pulses (red line) and an autocorrelation trace of a calculated pulse (green line) by use of the 1-mm-thick fused silica. (B): Measured (black line) and simulated (red line) autocorrelation traces when the 0.7-mm- and 1.0-mm-thick fused silicas are used and a simulated temporal pulse profile (green line).

Figure D.7: (A): Calculated transmittance (black dashed line) and amplified spectrum (black solid line) with the 0.7-mm-thick etalon and calculated transmittance (red dashed line) and amplified spectrum (red solid line) with the 1.0-mm-thick etalon. (B): Calculated transmittance (dashed line) and amplified spectrum (solid line) with the 0.7-mm and 1.0-mm-thick etalons.

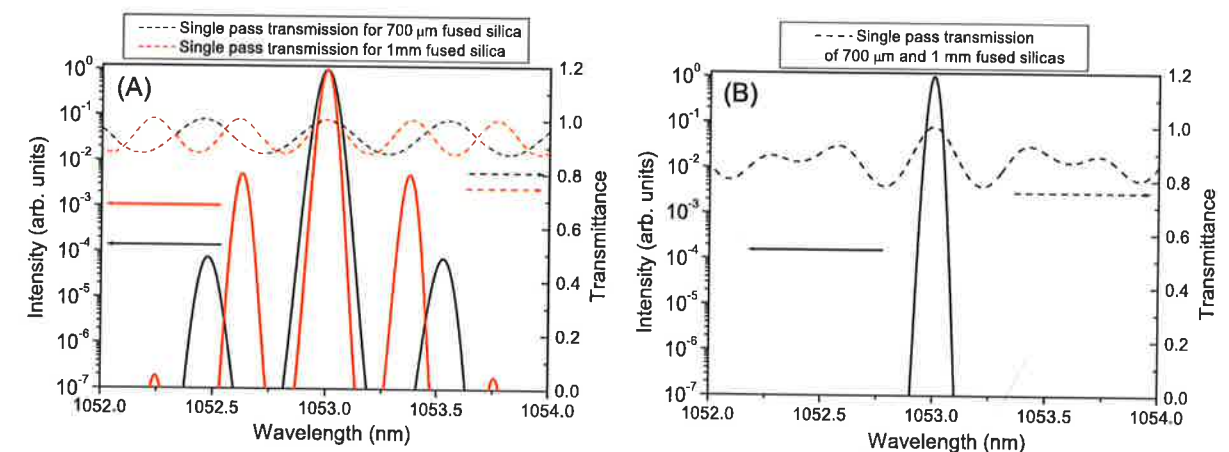medium, and the possible number of intracavity etalons, which introduce small amounts of loss. Although the peak value of transmittance of the etalon is 100%, the energy in the other parts of the spectrum is reduced by the reflection from the etalon which introduces loss. The tilt of the etalon is used to adjust the effective thickness of the crystal and to avoid the back reflection into the amplifier. So far, the use of a 2-mm and a 4-mm-thick etalon inside a Nd:YAG regenerative amplifier allowed us to obtain 2-mJ, 100-ps pulses using the optical seeding by the photonic crystal fiber. Subsequent amplification in a Nd:YAG post amplifier chain produced 1.5 J pulses with a smooth temporal profile. The pulse duration from 10 to 200 ps seems to be an applicable range in the case of Nd^{3+} doped-crystals. If a long pulse with the duration of more than 200 ps is needed, many etalons have to be placed in the cavity and a stronger seed energy is required.

Appendix E

Nonlinear refractive indices of optical materials

Nonlinear refractive indices of materials frequently used in laser science are listed in Tab. E.1.

Material	Nonlinear refractive index [cm^2/W] (multiply by 10^{-4} by a unit [m^2/W])	Reference and note
Fused silica	3.6×10^{-16} at 351 nm	[329]
Fused silica	3.0×10^{-16} at 527 nm	[329]
Fused silica	2.74×10^{-16} at 1053 nm	[329]
SF57	4.1×10^{-15}	[330]
Silicon	4.5×10^{-14}	[269]
GaAs	1.59×10^{-13}	[269]
YAG (Nd^{3+} doped)	6.2×10^{-16}	[331]
YAG (Nd^{3+} doped)	8.1×10^{-16}	[332]
YLF (Nd^{3+} doped)	1.73×10^{-16}	0.6×10^{-13} [esu] [333]
YLF (Nd^{3+} doped)	1.43×10^{-16}	[334]
BBO	5.0×10^{-16}	[335], [336]
BBO	7.4×10^{-16} at 1064 nm	[337]
BBO	8.0×10^{-16} at 532 nm	[337]
KTP	2.4×10^{-15}	[335]
KDP	2.3×10^{-16} (o) @ 1053 nm	LLE review Vol. 74 p 125
KDP	2.5×10^{-16} (e) @ 1053 nm	LLE review Vol. 74 p 125

Table E.1: Nonlinear refractive indices of frequently used material

Appendix F

Thermal expansion coefficients of materials

Thermal expansion coefficients of several materials frequently used in laser science are listed in Table F.1.

A scientific grade optical table (RS4000TM series) from New Port, is made of 400 series ferromagnetic stainless steel, which expands by 10×10^{-6} with 1 K increase in temperature.

Material	Thermal expansion coefficient
Carbon steel	10×10^{-6}/K
400 series ferromagnetic stainless steel	10×10^{-6}/K
Super invar at 20 °C	-0.2×10^{-6}/K (0 at 50 °C)
300 series non-ferromagnetic stainless steel	16.6×10^{-6}/K
6061 aluminum	23×10^{-6}/K

Table F.1: Thermal expansion coefficients of some common materials

Bibliography

[1] T. H. Maiman, "Stimulated Optical Radiation in Ruby," *Nature*, vol. 187, pp. 493–494, 1960.

[2] R. L. Fork, C. H. Brito Cruz, P. C. Becker, and C. V. Shank, "Compression of optical pulses to six femtoseconds by using cubic phase compensation," *Opt. Lett.*, vol. 12, pp. 483–485, 1987.

[3] B. F. Gächter and J. A. Koningstein, "Zero phonon transitions and interacting Jahn-Teller phonon energies from the fluorescence spectrum of of α-Al_2O_3:Ti^{3+}," *J. Chem. Phys.*, vol. 60, pp. 2003–2006, 1974.

[4] G. F. Albrecht, J. M. Eggleston, and J. J. Ewing, "Measurements of Ti^{3+}:Al_2O_3 as a lasing material," *Opt. Commun.*, vol. 52, pp. 401–404, 1985.

[5] P. F. Moulton, "Spectroscopic and laser characteristics of Ti:Al_2O_3," *J. Opt. Soc. Am. B*, vol. 3, pp. 125–133, 1986.

[6] R. A. Fisher and W. K. Bischel, "Pulse compression for more efficient operation of solid-state laser amplifier chains," *Appl. Phys. Lett.*, vol. 11, pp. 468–470, 1974.

[7] D. Strickland and G. Mourou, "Compression of amplified chirped optical pulses," *Opt. Commun.*, vol. 56, pp. 219–221, 1985.

[8] P. Maine, D. Strickland, P. Bado, M. Pessot, and G. Mourou, "Generation of Ultrahigh Peak Power Pulses by Chirped Pulse Amplification," *IEEE J. Quantum Electron.*, vol. 24, pp. 398–403, 1988.

[9] B. Kohler, V. V. Yakovlev, J. Che, J. L. Krause, M. Messina, and K. R. Wilson, "Quantum Control of Wave Packet Evolution with Tailored Femtosecond Pulses," *Phys. Rev. Lett.*, vol. 74, pp. 3360–3363, 1995.

[10] D. Meshullach and Y. Silberberg, "Coherent quantum control of multiphoton transitions by shaped ultrashort optical pulses," *Phys. Rev. A*, vol. 60, pp. 1287–1292, 1999.

[11] V. V. Yakovlev, C. J. Bardeen, J. Che, J. Cao, and K. R. Wilson, "Chirped pulse enhancement of multiphoton absorption in molecular iodine," *J. Chem. Phys.*, vol. 108, pp. 2309–2313, 1998.

[12] E. Constant, H. Stapelfeldt, and P. B. Corkum, "Observation of Enhanced Ionization of Molecular Ions in Intense Laser Fields," *Phys. Rev. Lett.*, vol. 76, pp. 4140–4143, 1996.

[13] A. H. Zewail ed., *Femtochemistry*. Singapore: World Scientific, 1994.

[14] P. B. Corkum, "Attosecond pulses at last," *Nature*, vol. 403, pp. 845–846, 2000.

[15] N. A. Papadogiannis, B. Witzel, C. Kalpouzos, and D. Charalambidis, "Observation of Attosecond Light Localization in High Order Harmonic Generation," *Phys. Rev. Lett.*, vol. 83, pp. 4289–4292, 1999.

[16] P. M. Paul, E. S. Toma, P. Breger, G. Mullot, F. Augé, P. Balcou, H. G. Muller, and P. Agostini, "Observation of a Train of Attosecond Pulses from High Harmonic Genration," *Science*, vol. 292, pp. 1689–1692, 2001.

[17] M. Hentschel, R. Kienberger, C. Spielmann, G. A. Reider, N. Milosevic, T. Brabec, P. Corkum, U. Heinzmann, M. Drescher, and F. Krausz, "Attosecond metrology," *Nature*, vol. 414, pp. 509–513, 2001.

[18] M. Drescher, M. Hentschel, R. Kienberger, M. Uiberacker, V. Yakovlev, A. Scrinzi, T. Westerwalbesloh, U. Kleineberg, U. Heinzmann, and F. Krausz, "Time-resolved atomic inner-shell spectroscopy," *Nature*, vol. 419, pp. 803–807, 2002.

[19] A. Baltuška, T. Udem, M. Uiberacker, M. Hentschel, E. Goulielmakis, C. Gohle, R. Holzwarth, V. S. Yakovlev, A. Scrinzi, T. W. Hänsch, and F. Krausz, "Attosecond control of electronic processes by intense light fields," *Nature*, vol. 421, pp. 611–615, 2003.

[20] F. Krausz, "From femtochemistry to attophysics," *Phys. World*, vol. 14, pp. 41–46, 2001.

[21] P. Agostini and L. F. DiMauro, "The physics of attosecond light pulses," *Rep. Prog. Phys.*, vol. 67, pp. 813–855, 2004.

[22] A. Dubietis, G. Jonušauskas, and A. Piskarskas, "Powerful femtosecond pulse generation by chirped and stretched pulse parametric amplification in BBO crystal," *Opt. Commun.*, vol. 88, pp. 437–440, 1992.

[23] I. N. Ross, P. Matousek, M. Towrie, A. J. Langley, and J. L. Collier, "The prospects for ultrashort pulse duration and ultrahigh intensity using optical parametric chirped pulse amplifiers," *Opt. Commun.*, vol. 144, pp. 125–133, 1997.

[24] R. Butkus, R. Danielius, A. Dubietis, A. Piskarskas, and A. Stabinis, "Progress in chirped pulse optical parametric amplifiers," *Appl. Phys. B*, vol. 79, pp. 693–700, 2004.

[25] A. Dubietis, R. Butkus, and A. P. Piskarskas, "Trends in Chirped Pulse Optical Parametric Amplification," *IEEE J. Sel. Top. Quantum Electron.*, vol. 12, pp. 163–172, 2006.

[26] N. Ishii, L. Turi, V. S. Yakovlev, T. Fuji, F. Krausz, A. Baltuška, R. Butkus, G. Veitas, V. Smilgevičius, R. Danielius, and A. Piskarskas, "Multimillijoule chirped parametric amplification of few-cycle pulses," *Opt. Lett.*, vol. 30, pp. 567–569, 2005.

[27] N. Ishii, C. Y. Teisset, T. Fuji, S. Köhler, K. Schmid, L. Veisz, A. Baltuška, and F. Krausz, "Seeding of an Eleven Femtosecond Optical Parametric Chirped Pulse Amplifier and its Nd^{3+} Picosecond Pump Laser From a Single Broadband Ti:Sapphire Oscillator," *IEEE J. Sel. Top. Quantum Electron.*, vol. 12, pp. 173–180, 2006.

[28] R. A. Fisher and W. K. Bischel, "Pulse Compression for More Efficient Operation of Solid-State Laser Amplifier Chains II," *IEEE J. Quantum Electron.*, vol. 11, pp. 46–52, 1975.

[29] C. C. Wang and G. W. Racette, "Measurement of parametric gain accompanying optical difference frequency generation," *Appl. Phys. Lett.*, vol. 6, pp. 169–171, 1965.

[30] A. Piskarskas, A. Stabinis, and A. Yankauskas, "Phase phenomena in parametric amplifiers and generators of ultrashort light pulses," *Sov. Phys. Usp.*, vol. 29, pp. 869–879, 1986.

[31] S. Backus, C. G. Durfee III, M. M. Murnane, and H. Kapteyn, "High power ultrafast lasers," *Rev. Sci. Instrum.*, vol. 69, pp. 1207–1223, 1998.

[32] R. Kienberger, E. Goulielmakis, M. Uiberacker, A. Baltuska, V. Yakovlev, F. Bammer, A. Scrinzi, T. Westerwalbesloh, U. Kleineberg, U. Heinzmann, M. Drescher, and F. Krausz, "Atomic transient recorder," *Nature*, vol. 427, pp. 817–821, 2004.

[33] M. Nisoli, S. De Silvestri, and O. Svelto, "Generation of high energy 10 fs pulses by a new pulse compression technique," *Appl. Phys. Lett.*, vol. 68, pp. 2793–2795, 1996.

[34] R. Szipöcs, K. Ferencz, C. Spielmann, and F. Krausz, "Chirped multilayer coatings for broadband dispersion control in femtosecond lasers," *Opt. Lett.*, vol. 19, pp. 201–203, 1994.

[35] P. Agostini and L. F. DiMauro, "The physics of attosecond light pulses," *Rep. Prog. Phys.*, vol. 67, pp. 813–855, 2004.

[36] A. Scrinzi, M. Y. Ivanov, R. Kienberger, and D. M. Villeneuve, "Attosecond physics," *J. Phys. B: At. Mol. Opt. Phys.*, vol. 39, pp. R1–R37, 2006.

[37] P. A. Franken, A. E. Hill, W. Peters, and G. Weinreich, "Generation of optical harmonics," *Phys. Rev. Lett.*, vol. 7, pp. 118–119, 1961.

[38] R. W. Terhune, P. D. Maker, and C. M. Savage, "Observation of saturation effects in optical harmonic generation," *Appl. Phys. Lett.*, vol. 2, pp. 54–55, 1963.

[39] J. F. Ward and G. H. C. New, "Optical Third Harmonic Generation in Gases by a Focused Laser Beam," *Phys. Rev.*, vol. 185, pp. 57–72, 1969.

[40] S. E. Harris, M. K. Oshman, and R. L. Byer, "Observation of Tunable Optical Parametric Fluorescence," *Phys. Rev. Lett.*, vol. 18, pp. 732–734, 1967.

[41] L. A. W. Gloster, I. T. McKinnie, and T. A. King, "Noncollinear phase matching in a type I barium borate optical parametric oscillator," *Opt. Commun.*, vol. 112, pp. 328–332, 1994.

[42] T. J. Driscoll, G. M. Gale, and F. Hache, "Ti:sapphire second-harmonic-pumped visible range femtosecond optical parametric oscillator," *Opt. Commun.*, vol. 110, pp. 638–644, 1994.

[43] S. Takeuchi and T. Kobayashi, "Broadband near-infrared pulse generation in $KTiOPO_4$," *J. Appl. Phys.*, vol. 75, pp. 2757–2760, 1994.

[44] T. Wilhelm, J. Piel, and E. Riedle, "Sub-20-fs pulses tunable across the visible from a blue-pumped single-pass noncollinear parametric converter," *Opt. Lett.*, vol. 22, pp. 1494–1496, 1997.

[45] G. Cerullo, M. Nisoli, and S. De Silvestri, "Generation of 11 fs pulses tunable across the visible by optical parametric amplification," *Appl. Phys. Lett.*, vol. 71, pp. 3616–3618, 1997.

[46] A. Shirakawa and T. Kobayashi, "Noncollinearly phase-matched femtosecond optical parametric amplification with 2000 cm^{-1} bandwidth," *Appl. Phys. Lett.*, vol. 72, pp. 147–149, 1998.

[47] C. Chen, B. Wu, A. Jiang, and G. You, "NA," *Sci. Sin. Ser. B*, vol. 28, pp. 235–NA, 1985.

[48] D. Magde, R. Scarlet, and H. Mahr, "Noncollinear Parametric Scattering of Visible Light," *Appl. Phys. Lett.*, vol. 11, pp. 381–383, 1967.

[49] R. G. Smith, J. G. Skinner, J. E. Geusic, and W. G. Nilsen, "Observations of Noncollinear Phase Matching in Optical Parametric Noise Emission," *Appl. Phys. Lett.*, vol. 12, pp. 97–100, 1968.

[50] J. Falk and J. E. Murray, "Single-cavity nonlinear optical parametric oscillation," *Appl. Phys. Lett.*, vol. 14, pp. 245–247, 1969.

[51] G. Cerullo and S. De Silvestri, "Ultrafast optical parametric amplifiers," *Rev. Sci. Instrum.*, vol. 1-18, pp. 831–838, 2003.

[52] M. D. Perry, T. Ditmire, and B. C. Stuart, "Self-phase modulation in chirped-pulse amplification," *Opt. Lett.*, vol. 19, pp. 2149–2151, 1994.

[53] D. A. Kleinman, "Theory of Optical Parametric Noise," *Phys. Rev.*, vol. 174, pp. 1027–1041, 1968.

[54] A. E. Siegman, *Lasers*. Mill Valley, California: University Science, 1986.

[55] J. A. Armstrong, N. Bloembergen, J. Ducuing, and P. S. Pershan, "Interactions between Light Waves in a Nonlinear Dielectric," *Phys. Rev.*, vol. 127, pp. 1918–1939, 1962.

[56] R. A. Baumgartner and R. L. Byer, "Optical Parametric Amplification," *IEEE J. Quantum Electron.*, vol. 15, pp. 432–444, 1979.

[57] R. S. Craxton, "High Efficiency Frequency Tripling Schemes for High-Power Nd:Glass Lasers," *IEEE J. Quantum Electron.*, vol. 17, pp. 1771–1782, 1981.

[58] R. López-Martens, S. Founier, C. Le Blanc, E. Baubeau, and F. Salin, "Parametric Amplification and Self-Compression of Ultrashort Tunable Pulses," *IEEE J. Sel. Top. Quantum Electron.*, vol. 4, pp. 230–237, 1998.

[59] S. K. Zhang, M. Fujita, M. Yamanaka, M. Nakatsuka, Y. Izawa, and C. Yamanaka, "Study of the stability of optical parametric amplification," *Opt. Commun.*, vol. 184, pp. 451–455, 2000.

[60] N. Bloembergen, *Nonlinear optics*. New York: W.A. Benhamin Inc, 1965.

[61] Y. R. Shen, *The Principles of Nonlinear Optics*. New York: John Wiley & Sons, 1984.

[62] A. Yariv, *Quantum Electronics 3rd Ed.* New York: John Wiley & Sons, 1988.

[63] R. L. Sutherland, *Handbook of Nonlinear Optics*. New York: Marcel Dekker, Inc., 1996.

[64] W. H. Glenn, "Parametric Amplification of Ultrashort Laser Pulses," *Appl. Phys. Lett.*, vol. 11, pp. 333–335, 1967.

[65] S. A. Akhmanov, A. S. Chirkin, K. N. Drabovich, A. I. Kovrigin, R. V. Khokhlov, and A. P. Sukhorukov, "Nonstationary Nonlinear Optical Effects and Ultrashort Light Pulse Formation," *IEEE J. Quantum Electron.*, vol. 4, pp. 598–605, 1968.

[66] J. A. Armstrong, S. S. Jha, and N. S. Shiren, "Some Effects of Group-Velocity Dispersion on Parametric Interactions," *IEEE J. Quantum Electron.*, vol. 6, pp. 123–129, 1970.

[67] M. F. Becker, Y. C. Kim, S. R. Gautam, and E. J. Powers, "Three-Wave Nonlinear Optical Interactions in Dispersive Media," *IEEE J. Quantum Electron.*, vol. 18, pp. 113–123, 1982.

[68] G. Arisholm, "General numerical methods for simulating second-order nonlinear interactions in birefringent media," *J. Opt. Soc. Am. B*, vol. 14, pp. 2543–2549, 1997.

[69] W. Koechner, *Solid-State Laser Engineering 5th Ed.* New York: Springer-Verlag, 1999.

[70] M. Born and E. Wolf, *Principles of optics 7th Ed.* Cambridge: Cambridge University Press, 1999.

[71] I. N. Ross, P. Matousek, G. H. C. New, and K. Osvay, "Analysis and optimization of optical parametric chirped pulse amplification," *J. Opt. Soc. Am. B*, vol. 19, pp. 2945–2956, 2002.

[72] R. R. Alfano, *The Supercontinuum Laser Source*. New York: Springer, 2005.

[73] J. C. Diels and W. Rudolph, *Ultrashort Laser Pulse Phenomena*. California: Academic Press, 1996.

[74] R. Y. Chiao, E. Garmire, and C. H. Townes, "Slef-Trapping of Optical Beams," *Phys. Rev. Lett.*, vol. 13, pp. 479–482, 1964.

[75] P. L. Kelley, "Self-Focusing of Optical Beams," *Phys. Rev. Lett.*, vol. 15, pp. 1005–1008, 1965.

[76] G. P. Agrawal, *Nonlinear Fiber Optics 3rd Ed.* New York: Academic Press, 2001.

[77] R. W. Boyd, *Nonlinear Optics*. New York: Academic Press, 1991.

[78] I. A. Begishev, A. A. Gulamov, E. A. Erofeev, É. A. Ibragimov, S. R. Kamalov, T. Usmanov, and A. D. Khadzhaev, "Highly efficient parametric amplification of optical beams. I. Optimization of the profiles of interacting waves in parametric amplification," *Sov. J. Quantum Electron.*, vol. 20, pp. 1100–1103, 1990.

[79] I. A. Begishev, A. A. Gulamov, E. A. Erofeev, É. A. Ibragimov, S. R. Kamalov, T. Usmanov, and A. D. Khadzhaev, "Highly efficient parametric amplification of optical beams. II. Parametric interaction of waves with conformal profiles," *Sov. J. Quantum Electron.*, vol. 20, pp. 1104–1106, 1990.

[80] K. Kato, "Second-Harmonic Generation to 2048 Å in β-BaB$_2$O$_4$," *IEEE J. Quantum Electron.*, vol. 22, pp. 1013–1014, 1986.

[81] D. Eimerl, L. Davis, S. Velsko, E. K. Graham, and A. Zalkin, "Optical, mechanical, and thermal properties of barium borate," *J. Appl. Phys.*, vol. 62, pp. 1968–1983, 1987.

[82] G. M. Gale, M. Cavallari, T. J. Driscoll, and F. Hache, "Sub-20-fs tunable pulses in the visible from an 82-MHz optical parametric oscillator," *Opt. Lett.*, vol. 20, pp. 1562–1564, 1995.

[83] A. L. Oien, I. T. Mckinnie, P. Jain, N. A. Russel, D. M. Warrington, and L. A. W. Gloster, "Efficient, low-threshold collinear and noncollinear β-barium borate optical parametric oscillators," *Opt. Lett.*, vol. 22, pp. 859–861, 1997.

[84] G. Cerullo, M. Nisoli, S. Stagira, and S. De Silvestri, "Sub-8-fs pulses from an ultra-broadband optical parametric amplifier in the visible," *Opt. Lett.*, vol. 23, pp. 1283–1285, 1998.

[85] A. Shirakawa, I. Sakane, M. Takasaka, and T. Kobayashi, "Sub-5-fs visible pulse generation by pulse-front-matched noncollinear optical parametric amplification," *Appl. Phys. Lett.*, vol. 74, pp. 2268–2270, 1998.

[86] J. Piel, M. Beutter, and E. Riedle, "20−50-fs pulses tunable across the near infrared from a blue-pumped noncollinear parametric amplifier," *Opt. Lett.*, vol. 25, pp. 180–182, 2000.

[87] R. L. Fork, C. V. Shank, C. Hirlimann, R. Yen, and W. J. Tomlinson, "Femtosecond white-light continuum pulses," *Opt. Lett.*, vol. 8, pp. 1–3, 1983.

[88] V. V. Yakovlev, B. Kohler, and K. R. Wilson, "Broadly tunable 30-fs pulses produced by optical parametric amplification," *Opt. Lett.*, vol. 19, pp. 2000–2002, 1994.

[89] M. K. Reed, M. K. Steiner-Shepard, M. S. Armas, and D. K. Negus, "Microjoule-energy ultrafast optical parametric amplifiers," *J. Opt. Soc. Am. B*, vol. 12, pp. 2229–2236, 1995.

[90] D. Zeidler, T. Hornung, D. Proch, and M. Motzkus, "Adaptive compression of tunable pulses from a non-collinear-type OPA to below 16 fs by feedback-controlled pulse shaping," *Appl. Phys. B*, vol. 70, pp. S125–S131, 2000.

[91] G. Cerullo, M. Nisoli, S. Stagira, S. De Silvestri, G. Tempea, F. Krausz, and K. Ferencz, "Mirror-dispersion-controlled OPA: a compact tool for sub-10-fs spectroscopy in the visible," *Appl. Phys. B*, vol. 70, pp. S253–S259, 2000.

[92] M. R. Armstrong, P. Plachta, E. A. Ponomarev, and R. J. D. Miller, "Versatile 7-fs optical parametric pulse generation and compression by use of adaptive optics," *Opt. Lett.*, vol. 26, pp. 1152–1154, 2001.

[93] P. Baum, S. Lochbrunner, L. Gallmann, G. Steinmeyer, U. Keller, and E. Riedle, "Real-time characterization and optimal phase control of tunable visible pulses with a flexible compressor," *Appl. Phys. B*, vol. 74, pp. S219–S224, 2002.

[94] A. Baltuška, T. Fuji, and T. Kobayashi, "Visible pulse compression to 4 fs by optical parametric amplification and programmable dispersion control," *Opt. Lett.*, vol. 27, pp. 306–308, 2002.

[95] R. L. Byer and S. E. Harris, "Power and Bandwidth of Spontaneous Parametric Emission," *Phys. Rev.*, vol. 168, pp. 1064–1068, 1968.

[96] R. Danielius, A. Piskarskas, A. Stabinis, G. P. Banfi, P. Di Trapani, and R. Righini, "Traveling-wave parametric generation of widely tunable, highly coherent femtosecond light pulses," *J. Opt. Soc. Am. B*, vol. 10, pp. 2222–2232, 1993.

[97] A. Shirakawa, *Sub-5-fs pulse generation by noncollinear optical parametric amplification and its application to the study of geometrical relaxation in polydiacetylenes*. Ph.D. dissertation, University of Tokyo, 1998.

[98] J. Wang, M. H. Dunn, and C. F. Rae, "Polychromatic optical parametric generation by simultaneous phase matching over a large spectral bandwidth," *Opt. Lett.*, vol. 22, pp. 763–765, 1997.

[99] V. G. Dmitriev, G. G. Gurzadyan, and D. N. Nikogosyan, *Handbook of Nonlinear Optical Crystals 2nd Ed.* Berlin: Springer-Verlag, 1999.

[100] I. Jovanovic, B. J. Comaskey, and D. M. Pennington, "Angular effects and beam quality in optical parametric amplification," *J. Appl. Phys.*, vol. 90, pp. 4328–4337, 2001.

[101] R. C. Eckardt, H. Masuda, Y. X. Fan, and R. L. Byer, "Absolute and relative nonlinear optical coefficients of KDP, KD*P, BaB_2O_4, $LiIO_3$, $MgO:LiNbO_3$, and KTP measured by phase-matched second-harmonic generation," *IEEE J. Quantum Electron.*, vol. 26, pp. 922–933, 1990.

[102] X. Yang, Z. Xu, Y. Leng, H. Lu, L. Lin, Z. Zhang, R. Li, W. Zhang, D. Yin, and B. Tang, "Multiterawatt laser system based on optical parametric chirped pulse amplification," *Opt. Lett.*, vol. 27, pp. 1135–1137, 2002.

[103] C. P. Hauri, P. Schlup, G. Arisholm, J. Biegert, and U. Keller, "Phase-preserving chirped-pulse optical parametric amplification to 17.3 fs directly from a Ti:sapphire oscillator," *Opt. Lett.*, vol. 29, pp. 1369–1371, 2004.

[104] J. Limpert, C. Aguergaray, S. Montant, I. Manek-Hönninger, S. Petit, D. Descamps, E. Cormier, and F. Salin, "Ultra-broad bandwidth parametric amplification at degeneracy," *Opt. Express*, vol. 13, pp. 7386–7392, 2005.

[105] B. Zhao, X. Liang, Y. Leng, Y. Jiang, C. Wang, H. Lu, J. Du, Z. Xu, and D. Shen, "Degenerated optical parametric chirped-pulse amplification with cesium lithium borate," *Appl. Opt.*, vol. 45, pp. 565–568, 2006.

[106] Y. Leng and X. Liang and B. Zhao and C. Wang and Y. Jiang and X. Yang and H. Lu and L. Lin and Z. Zhang and R. Li and Z. Xu, "Development of High-Power OPCPA Laser at 1064 and 780 nm," *IEEE J. Sel. Top. Quantum Electron.*, vol. 12, pp. 187–193, 2006.

[107] H. Takada, M. Kakehata, and K. Torizuka, "Large-ratio stretch and recompression of sub-10-fs pulse utilizing dispersion managed devices and a spatial light modulator," *Appl. Phys. B*, vol. 74, pp. s253–s257, 2002.

[108] F. Tavella, K. Schmid, N. Ishii, A. Marcinkevičius, L. Veisz, and F. Krausz, "High-dynamic range pulse-contrast measurements of a broadband optical parametric chirped-pulse amplifier," *Appl. Phys. B*, vol. 81, pp. 753–756, 2005.

[109] J. L. Collier, C. Hernandez-Gomez, I. N. Ross, P. Matousek, C. N. Danson, and J. Walczak, "Evaluation of an ultrabroadband high-gain amplification technique for chirped pulse amplification facilities," *Appl. Opt.*, vol. 38, pp. 7486–7493, 1999.

[110] I. Jovanovic, C. G. Brown, C. A. Ebbers, C. P. J. Barty, N. Forget, and C. Le Blanc, "Generation of high-contrast millijoule pulses by optical parametric chirped-pulse amplification in periodically poled $KTiOPO_4$," *Opt. Lett.*, vol. 30, pp. 1036–1038, 2005.

[111] K. Kondo, H. Maeda, Y. Hama, S. Morita, A. Zoubir, R. Kodama, K. A. Tanaka, Y. Kitagawa, and Y. Izawa, "Control of amplified optical parametric fluorescence for hybrid chirped-pulse amplification," *J. Opt. Soc. Am. B*, vol. 23, pp. 231–235, 2006.

[112] N. Forget, A. Cotel, E. Brambrink, P. Audebert, C. Le Blanc, A. Jullien, O. Albert, and G. Chériaux, "Pump-noise transfer in optical parametric chirped-pulse amplification," *Opt. Lett.*, vol. 30, pp. 2921–2923, 2005.

[113] I. Jovanovic and C. P. J. Barty and C. Haefner and B. Wattellier, "Optical switching and contrast enhancement in intense laser systems by cascaded optical parametric amplification," *Opt. Lett.*, vol. 31, pp. 787–789, 2006.

[114] A. Cotel, A. Jullien, N. Forget, O. Albert, G. Chériaux, and C. L. Blanc, "Nonlinear temporal pulse cleaning of a 1-μm optical parametric chirped-pulse amplification system," *Appl. Phys. B*, vol. 83, pp. 7–10, 2006.

[115] A. Galvanauskas, A. Hariharan, D. Harter, M. A. Arbore, and M. M. Fejer, "High-energy femtosecond pulse amplification in a quasi-phase-matched parametric amplifier," *Opt. Lett.*, vol. 23, pp. 210–212, 1998.

[116] I. N. Ross, J. L. Collier, P. Matousek, C. N. Danson, D. Neely, R. M. Allott, D. A. Pepler, C. Hernandez-Gomez, and K. Osvay, "Generation of terawatt pulses by use of optical parametric chirped pulse amplification," *Appl. Opt.*, vol. 39, pp. 2422–2427, 2000.

[117] I. Jovanovic, B. J. Comaskey, C. A. Ebbers, R. A. Bonner, D. M. Pennington, and E. C. Morse, "Optical parametric chirped-pulse amplifier as an alternative to Ti:sapphire regenerative amplifiers," *Appl. Opt.*, vol. 41, pp. 2923–2929, 2002.

[118] H. Yoshida, E. Ishii, R. Kodama, H. Fujita, Y. Kitagawa, Y. Izawa, and T. Yamanaka, "High-power and high-contrast optical parametric chirped pulse amplification in β-BaB_2O_4 crystal," *Opt. Lett.*, vol. 28, pp. 257–259, 2003.

[119] L. J. Waxer, V. Bagnoud, I. A. Begishev, M. J. Guardalben, J. Puth, and J. D. Zuegel, "High-conversion-efficiency optical parametric chirped-pulse amplification system using spatiotemporally shaped pump pulses," *Opt. Lett.*, vol. 28, pp. 1245–1247, 2003.

[120] C. N. Danson, P. A. Brummitt, R. J. Clarke, J. L. Collier, B. Fell, A. J. Frackiewicz, S. Hancock, S. Hawkes, C. Hernandez-Gomez, P. Holligan, M. H. R. Hutchinson, A. Kidd, W. J. Lester, I. O. Musgrave, D. Neely, D. R. Neville, P. A. Norreys, D. A. Pepler, C. J. Reason, W. Shaikh, T. B. Winstone, R. W. W. Wyatt, and B. E. Wyborn, "Vulcan Petawatt—an ultra-high-intensity interaction facility," *Nucl. Fusion*, vol. 44, pp. S239–S246, 2004.

[121] V. V. Lozhkarev, S. G. Garanin, R. R. Gerke, V. N. Ginzburg, E. V. Katin, A. V. Kirsanov, G. A. Luchinin, A. N. Mal'shakov, M. A. Mart'yanov, O. V. Palashov, A. K. Poteomkin, N. N. Rukavishnikov, A. M. Sergeev, S. A. Sukharev, G. I. Freĭdman, E. A. Khazanov, A. V. Charukhchev, A. A. Shaĭkin, and I. V. Yakovlev, "100-TW Femtosecond Laser Based on Parametric Amplification," *JETP. Lett.*, vol. 82, pp. 178–180, 2005.

[122] H. Kiriyama, N. Inoue, Y. Akahane, and K. Yamakawa, "Prepulse-free, multi-terawatt, sub-30-fs laser system," *Opt. Express*, vol. 14, pp. 438–445, 2006.

[123] O. Chekhlov, J. L. Collier, I. N. Ross, P. Bates, M. Notley, W. Shaikh, C. N. Danson, D. Neely, P. Matousek, and S. Hancock, "Recent Progress Towards a Petawatt Power Using Optical Parametric Chirped Pulse Amplification," in *Conference on Lasers and Electro-Optics/Quantum Electronics and Laser Science and Photonic Applications, Systems and Technologies*, (Baltimore, Maryland, USA), Optical Society of America, 2005.

[124] V. V. Lozhkarev, G. I. Freidman, V. N. Ginzburg, E. V. Katin, E. A. Khazanov, A. V. Kirsanov, G. A. Luchinin, A. N. Mal'shakov, M. A. Martyanov, O. V. Palashov, A. K. Poteomkin, A. M. Sergeev, A. A. Shaykin, I. V. Yakovlev, S. G. Garanin, S. A. Sukharev, N. N. Rukavishnikov, A. V. Charukhchev, R. R. Gerke, and V. E. Yashin, "200TW 45 fs laser based on optical parametric chirped pulse amplification," *Opt. Express*, vol. 14, pp. 446–454, 2006.

[125] Y. Kitagawa, H. Fujita, R. Kodama, H. Yoshida, S. Matsuo, T. Jitsuno, T. Kawasaki, H. Kitamura, T. Kanabe, S. Sakabe, K. Shigemori, N. Miyanaga, and Y. Izawa, "Prepulse-Free Petawatt Laser for a Fast Ignitor," *IEEE J. Quantum Electron.*, vol. 40, pp. 281–293, 2004.

[126] M. D. Perry, D. Pennington, B. C. Stuart, G. Tietbohl, J. A. Britten, C. Brown, S. Herman, B. Golick, M. Kartz, J. Miller, H. T. Powell, M. Vergino, and V. Yanovsky, "Petawatt laser pulses," *Opt. Lett.*, vol. 24, pp. 160–162, 1999.

[127] B. C. Stuart, S. Herman, and M. D. Perry, "Chirped-Pulse Amplification in Ti:Sapphire Beyond 1 μm," *IEEE J. Quantum Electron.*, vol. 31, pp. 528–538, 1995.

[128] I. Jovanovic, C. A. Ebbers, and C. P. J. Barty, "Hybrid chirped-pulse amplification," *Opt. Lett.*, vol. 27, pp. 1622–1624, 2002.

[129] I. Jovanovic, J. R. Schmidt, and C. A. Ebbers, "Optical parametric chirped-pulse amplification in periodically poled KTiOPO₄ at 1053 nm," *Appl. Phys. Lett.*, vol. 83, pp. 4125–4127, 2003.

[130] F. Rotermund, C. J. Yoon, V. Petrov, F. Noack, S. Kurimura, N. Yu, and K. Kitamura, "Application of periodically poled stoichiometric LiTaO₃ for efficient optical parametric chirped pulse amplification at 1 kHz," *Opt. Express*, vol. 12, pp. 6421–6427, 2004.

[131] M. J. W. Rodwell, K. J. Weingarten, D. M. Bloom, T. Baer, and B. H. Kolner, "Reduction of timing fluctuations in a mode-locked Nd:YAG laser by electronic feedback," *Opt. Lett.*, vol. 11, pp. 638–640, 1986.

[132] M. J. W. Rodwell, D. M. Bloom, and K. J. Weingarten, "Subpicosecond Laser Timing Stabilization," *IEEE J. Quantum Electron.*, vol. 25, pp. 817–827, 1989.

[133] S. B. Darack and D. R. Dykaar, "Timing-jitter stabilization of a colliding-pulse mode-locked laser by active control of the cavity length," *Opt. Lett.*, vol. 16, pp. 1677–1679, 1991.

[134] D. E. Spence, J. M. Dudley, K. Lamb, W. E. Sleat, and W. Sibbett, "Nearly quantum-limited timing jitter in a self-mode-locked Ti:sapphire laser," *Opt. Lett.*, vol. 19, pp. 481–483, 1994.

[135] D. J. Jones, E. O. Potma, J. Cheng, B. Burfeindt, Y. Pang, J. Ye, and X. S. Xie, "Synchronization of two passively mode-locked, picosecond lasers within 20 fs for coherent anti-Stokes Raman scattering microscopy," *Rev. Sci. Instrum.*, vol. 73, pp. 2843–2848, 2002.

[136] R. T. Zinkstok, S. Witte, W. Hogervorst, and K. S. E. Eikema, "High-power parametric amplification of 11.8-fs laser pulses with carrier-envelope phase control," *Opt. Lett.*, vol. 30, pp. 78–80, 2005.

[137] J. V. Rudd, R. J. Law, T. S. Luk, and S. M. Cameron, "High-power optical parametric chirped-pulse amplifier system with a 1.55 μm signal and a 1.064 μm pump," *Opt. Lett.*, vol. 30, pp. 1843–1845, 2005.

[138] D. Kraemer, R. Hua, M. L. Cowan, K. Franjic, and R. J. D. Miller, "Ultrafast noncollinear optical parametric chirped pulse amplification in KTiOPO₄," *Opt. Lett.*, vol. 31, pp. 981–983, 2006.

[139] T. Franz, *Active Pump Laser Synchronization for Parametric Pulse Amplification.* Dipl. thesis, Vienna University of Technology, 2004.

[140] J. T. Hunt, J. A. Glaze, W. W. Simmons, and P. A. Renard, "Suppression of self-focusing through low-pass spatial filtering and relay imaging," *Appl. Opt.*, vol. 17, pp. 2053–2057, 1978.

[141] R. Danielius, A. Piskarskas, P. D. Trapani, A. Andreoni, C. Solcia, and P. Foggi, "Matching of group velocities by spatial walk-off in collinear three-wave interaction with tilted pulses," *Opt. Lett.*, vol. 21, pp. 973–975, 1996.

[142] V. Krylov, O. Ollikainen, J. Gallus, U. Wild, A. Rebane, and A. Kalintsev, "Efficient noncollinear parametric amplification of weak femtosecond pulses in the visible and near-infrared spectral range," *Opt. Lett.*, vol. 23, pp. 100–102, 1998.

[143] C. Iaconis and I. A. Walmsley, "Spectral phase interferometry for direct electric-field reconstruction of ultrashort optical pulses," *Opt. Lett.*, vol. 23, pp. 792–794, 1998.

[144] C. Iaconis and I. A. Walmsley, "Self-Referencing Spectral Interferometry for Measuring Ultrashort Optical Pulses," *IEEE J. Quantum Electron.*, vol. 35, pp. 501–509, 1999.

[145] E. B. Treacy, "Optical Pulse Compression With Diffraction Gratings," *IEEE J. Quantum Electron.*, vol. 5, pp. 454–458, 1969.

[146] O. E. Martinez, "3000 Times Grating Compressor with Positive Group Velocity Dispersion: Application to Fiber Compensation in 1.3-1.6μm Region," *IEEE J. Quantum Electron.*, vol. 23, pp. 59–64, 1987.

[147] B. E. Lemoff and C. P. J. Barty, "Quintic-phase-limited, spatially uniform expansion and recompression of ultrashort optical pulses," *Opt. Lett.*, vol. 18, pp. 1651–1653, 1993.

[148] D. Du, J. Squier, S. Kane, G. Korn, G. Mourou, C. Bogusch, and C. T. Cotton, "Terawatt Ti:sapphire laser with a spherical reflective-optics pulse expander," *Opt. Lett.*, vol. 20, pp. 2114–2116, 1995.

[149] A. Öffner, "U.S. Patent 3,748,015: Unit power imaging catoptric anastigmat," 1971.

[150] A. Suzuki, "Complete analysis of a two-mirror unit magnification system. Part 1," *Appl. Opt.*, vol. 22, pp. 3943–3949, 1983.

[151] A. Suzuki, "Complete analysis of a two-mirror unit magnification system. Part 2," *Appl. Opt.*, vol. 22, pp. 3950–3956, 1983.

[152] G. Chériaux, P. Rousseau, F. Salin, J. P. Chambaret, B. Walker, and L. Dimauro, "Aberration-free stretcher design for ultrashort-pulse amplification," *Opt. Lett.*, vol. 21, pp. 414–416, 1996.

[153] V. Bagnoud and F. Salin, "Influence of optical quality on chirped-pulse amplification: characterization of a 150-nm-bandwidth stretcher," *J. Opt. Soc. Am. B*, vol. 16, pp. 188–193, 1999.

[154] A. M. Weiner, "Femtosecond optical pulse shaping and processing," *Prog. Quant. Electr.*, vol. 19, pp. 161–237, 1995.

[155] E. Zeek, R. Bartels, M. M. Murnane, H. Kapteyn, S. Backus, and G. Vdovin, "Adaptive pulse compression for transform-limited 15-fs high-energy pulse generation," *Opt. Lett.*, vol. 25, pp. 587–589, 2000.

[156] G. Chériaux, O. Albert, V. Wänman, J. P. Chambaret, C. Félix, and G. Mourou, "Temporal control of amplified femtosecond pulses with a deformable mirror in a stretcher," *Opt. Lett.*, vol. 26, pp. 169–171, 2001.

[157] D. M. Gaudiosi, A. L. Lytle, P. Kohl, M. M. Murnane, H. C. Kapteyn, and S. Backus, "11-W average power Ti:sapphire amplifier system using downchirped pulse amplification," *Opt. Lett.*, vol. 29, pp. 2665–2667, 2004.

[158] M. P. Kalashnikov, K. Osvay, I. M. Lachko, H. Schönnagel, and W. Sandner, "Broadband Amplification of 800-nm Pulses With a Combination of Negatively and Positively Chirped Pulse Amplification," *IEEE J. Sel. Top. Quantum Electron.*, vol. 12, pp. 194–200, 2006.

[159] P. Tournois, "Acousto-optic programmable dispersive filter for adaptive compensation of group delay time dispersion in laser systems," *Opt. Comm.*, vol. 140, pp. 245–249, 1997.

[160] D. Kaplan and P. Tourinois, "Theory and performance of the acousto optic programmable dispersive filter used for femtosecond laser pulse shaping," *J. Phys. IV France*, vol. 12, pp. Pr5–69/75, 2002.

[161] F. Verluise, V. Laude, Z. Cheng, C. Spielmann, and P. Tournois, "Amplitude and phase control of ultrashort pulses by use of an acousto-optic programmable dispersive filter: pulse compression and shaping," *Opt. Lett.*, vol. 25, pp. 575–577, 2000.

[162] C. Dorrer, B. de Beauvoir, C. Le Blanc, S. Ranc, J. P. Rousseau, P. Rousseau, J. P. Chambaret, and F. Salin, "Single-shot real-time characterization of chirped-pulse amplification system by spectral phase interferometry for direct electric-field reconstruction," *Opt. Lett.*, vol. 24, pp. 1644–1646, 1999.

[163] W. Kornelis, J. Biegert, J. W. G. Tisch, M. Nisoli, G. Sansone, C. Vozzi, S. D. Silvestri, and U. Keller, "Single-shot kilohertz characterization of ultrashort pulses by spectral phase interferometry for direct electric-field reconstruction," *Opt. Lett.*, vol. 28, pp. 281–283, 2003.

[164] W. Kornelis, M. Bruck, F. W. Helbing, C. P. Hauri, A. Heinrich, J. Biegert, and U. Keller, "Single-shot dynamics of pulses from a gas-filled hollow fiber," *Appl. Phys. B*, vol. 79, pp. 1033–1039, 2004.

[165] F. Tavella and A. Marcinkevičius, "100 mJ, 10 fs (10 TW) pulse generation by use of the near-infrared OPCPA.," Private communication, 2006.

[166] H. Tsuchida, "Pulse timing stabilization of a mode-locked Cr:LiSAF laser," *Opt. Lett.*, vol. 24, pp. 1641–1643, 1999.

[167] K. Finsterbusch, R. Urschel, and H. Zacharias, "Tunable, high-power, narrow-band picosecond IR radiation by optical parametric amplification in KTP," *Appl. Phys. B*, vol. 74, pp. 319–322, 2002.

[168] H. Zeng, J. Wu, H. Xu, K. Wu, and E. Wu, "Generation of accurately synchronized pump source for optical parametric chirped pulse amplification," *Appl. Phys. B*, vol. 79, pp. 837–839, 2004.

[169] C. Y. Teisset, N. Ishii, T. Fuji, T. Metzger, S. Köhler, R. Holzwarth, A. Baltuška, A. M. Zheltikov, and F. Krausz, "Soliton-based pump-seed synchronization for few-cycle OPCPA," *Opt. Express*, vol. 13, pp. 6550–6557, 2005.

[170] F. M. Mitschke and L. F. Mollenauer, "Discovery of the soliton self-frequency shift," *Opt. Lett.*, vol. 11, pp. 659–661, 1986.

[171] P. Russell, "Photonic Crystal Fibers," *Science*, vol. 299, pp. 358–362, 2003.

[172] E. E. Serebryannikov, A. M. Zheltikov, N. Ishii, C. Teisset, S. Köhler, T. Fuji, T. Metzger, F. Krausz, and A. Baltuška, "Soliton self-frequency shift of 6-fs pulses in photonic-crystal fibers," *Appl. Phys. B*, vol. 81, pp. 585–588, 2005.

[173] D. A. Akimov, T. Siebert, A. M. Zheltikov, and W. Kiefer, "A double-pass optical parametric amplifier seeded by a blue-shifted output of a photonic-crystal fiber," *Appl. Phys. B*, vol. 83, pp. 185–187, 2006.

[174] P. Albers, E. Stark, and G. Huber, "Continuous-wave laser operation and quantum efficiency of titanium-doped sapphire," *J. Opt. Soc. Am. B*, vol. 3, pp. 134–139, 1986.

[175] J. Goodberlet, J. Wang, J. G. Fujimoto, and P. A. Schulz, "Femtosecond passively mode-locked Ti:Al$_2$O$_3$ laser with a nonlinear external cavity," *Opt. Lett.*, vol. 14, pp. 1125–1127, 1989.

[176] D. E. Spence, P. N. Kean, and W. Sibbett, "60-fsec pulse generation from a self-mode-locked Ti:sapphire laser," *Opt. Lett.*, vol. 16, pp. 42–44, 1991.

[177] U. Keller, G. W. Hoof, W. H. Knox, and J. E. Cunningham, "Femtosecond pulses from a continuously self-starting passively mode-locked Ti:sapphire laser," *Opt. Lett.*, vol. 16, pp. 1022–1024, 1991.

[178] G. Gabetta, D. Huang, J. Jacobson, M. Ramaswamy, E. P. Ippen, and J. G. Fujimoto, "Femtosecond pulse generation in Ti:Al$_2$O$_3$ using a microdot mirror mode locker," *Opt. Lett.*, vol. 16, pp. 1756–1758, 1991.

[179] F. Krausz, C. Spielmann, T. Brabec, E. Wintner, and A. J. Schmidt, "Generation of 33-fs optical pulses from a solid-state laser," *Opt. Lett.*, vol. 17, pp. 204–206, 1992.

[180] M. T. Asaki, C. Huang, D. Garvey, J. Zhou, H. C. Kapteyn, and M. M. Murnane, "Generation of 11-fs pulses from a self-mode-locked Ti:sapphire laser," *Opt. Lett.*, vol. 18, pp. 977–979, 1993.

[181] R. L. Fork, O. E. Martinez, and J. P. Gordon, "Negative dispersion using pairs of prisms," *Opt. Lett.*, vol. 9, pp. 150–152, 1984.

[182] J. P. Gordon and R. L. Fork, "Optical resonator with negative dispersion," *Opt. Lett.*, vol. 9, pp. 153–155, 1984.

[183] J. D. Kafka and T. Baer, "Prism-pair dispersion delay lines in optical pulse compression," *Opt. Lett.*, vol. 12, pp. 401–403, 1987.

[184] F. Krausz, T. Brabec, and C. Spielmann, "Self-starting passive mode locking," *Opt. Lett.*, vol. 16, pp. 235–237, 1991.

[185] F. Salin, J. Squier, and M. Piché, "Mode locking of Ti:Al$_2$O$_3$ lasers and self-focusing: a Gaussian approximation," *Opt. Lett.*, vol. 16, pp. 1674–1676, 1991.

[186] S. Chen and J. Wang, "Self-starting issues of passive self-focusing mode locking," *Opt. Lett.*, vol. 16, pp. 1689–1691, 1991.

[187] T. Brabec, C. Spielmann, P. F. Curley, and F. Krausz, "Kerr lens mode locking," *Opt. Lett.*, vol. 17, pp. 1292–1294, 1992.

[188] V. Magni, G. Cerullo, and S. D. Silvestri, "*ABCD* matrix analysis of propagation of Gaussian beams through Kerr media," *Opt. Commun.*, vol. 96, pp. 348–355, 1993.

[189] A. Stingl, C. Spielmann, F. Krausz, and R. Szipöcs, "Generation of 11-fs pulses from a Ti:sapphire laser without the use of prisms," *Opt. Lett.*, vol. 19, pp. 204–206, 1994.

[190] A. Stingl, M. Lenzner, C. Spielmann, F. Krausz, and R. Szipöcs, "Sub-10-fs mirror-dispersion-controlled Ti:sapphire laser," *Opt. Lett.*, vol. 20, pp. 602–604, 1995.

[191] A. Kasper and K. J. Witte, "10-fs pulse generation from a unidirectional kerr-lens mode-locked ti:sapphire ring laser," *Opt. Lett.*, vol. 21, pp. 360–362, 1996.

[192] L. Xu, C. Spielmann, F. Krausz, and R. Szipöcs, "Ultrabroadband ring oscillator for sub-10-fs pulse generation," *Opt. Lett.*, vol. 21, pp. 1259–1261, 1996.

[193] U. Morgner, F. X. Kärtner, S. H. Cho, Y. Chen, H. A. Haus, J. G. Fujimoto, E. P. Ippen, V. Scheuer, G. Angelow, and T. Tschudi, "Sub-two-cycle pulses from a Kerr-lens mode-locked Ti:sapphire laser," *Opt. Lett.*, vol. 24, pp. 411–413, 1999.

[194] R. Ell, U. Morgner, F. X. Kärtner, J. G. Fujimoto, E. P. Ippen, V. Scheuer, G. Angelow, T. Tschudi, M. J. Lederer, A. Boiko, and B. Luther-Davies, "Generation of 5-fs pulses and octave-spanning spectra directly from a Ti:sapphire laser," *Opt. Lett.*, vol. 26, pp. 373–375, 2001.

[195] T. M. Fortier, D. J. Jones, and S. T. Cundiff, "Phase stabilization of an octave-spanning Ti:sapphire laser," *Opt. Lett.*, vol. 28, pp. 2198–2200, 2003.

[196] T. Fuji, A. Unterhuber, V. S. Yakovlev, G. Tempea, A. Stingl, F. Krausz, and W. Drexler, "Generation of smooth ultra-broadband spectra directly from a prism-less Ti:sapphire laser," *Appl. Phys. B*, vol. 77, pp. 125–128, 2003.

[197] L. Matos, D. Kleppner, O. Kuzucu, T. R. Schibli, J. Kim, E. Ippen, and F. Kärtner, "Direct frequency comb generation from an octave-spanning, prismless Ti:sapphire laser," *Opt. Lett.*, vol. 29, pp. 1683–1685, 2004.

[198] T. Fuji, J. Rauschenberger, A. Apolonski, V. S. Yakovlev, G. Tempea, T. Udem, C. Gohle, T. Hänsch, W. Lehnert, M. Scherer, and F. Krausz, "Monolithic carrier-envelope phase-stabilization scheme," *Opt. Lett.*, vol. 30, pp. 332–334, 2005.

[199] O. D. Muecke, R. Ell, A. Winter, J. Kim, J. R. Birge, L. Matos, and F. Kärtner, "Self-Referenced 200 MHz Octave-Spanning Ti:Sapphire Laser with 50 Attosecond Carrier-Envelope Phase Jitter," *Opt. Express*, vol. 13, pp. 5163–5169, 2005.

[200] J. E. Murray, "Pulsed Gain and Thermal Lensing of Nd:LiYF$_4$," *IEEE J. Quantum Electron.*, vol. 19, pp. 488–491, 1983.

[201] H. Vanherzeele, "Thermal lensing measurement and compensation in a continuous-wave mode-locked Nd:YLF laser," *Opt. Lett.*, vol. 13, pp. 369–371, 1988.

[202] P. J. Hardman, W. A. Clarkson, G. J. Friel, M. Pollnau, and D. C. Hanna, "Energy-Transfer Upconversion and Thermal Lensing in High-Power End-Pumped Nd:YLF Laser Crystals," *IEEE J. Quantum Electron.*, vol. 35, pp. 647–655, 1999.

[203] A. L. Harmer, A. Linz, and D. R. Gabbe, "Fluorescence of Nd^{3+} in Lithium Yttrium Fluoride," *J. Phys. Chem. Solids*, vol. 30, pp. 1483–1491, 1969.

[204] T. Kushida, H. M. Marcos, and J. E. Geusis, "Laser Transition Cross Section and Fluorescence Branching Ratio for Nd^{3+} in Yttrium Aluminum Garnet," *Phys. Rev.*, vol. 167, pp. 289–291, 1968.

[205] J. D. Zuegel and W. Seka, "Direct measurements of $^4I_{11/2}$ Terminal-Level Lifetime in Nd:YLF," *IEEE J. Quantum Electron.*, vol. 31, pp. 1742–1746, 1995.

[206] C. Bibeau, S. A. Payne, and H. T. Powell, "Direct measurements of the terminal laser level lifetime in neodymium-doped crystals and glasses," *J. Opt. Soc. Am. B*, vol. 12, pp. 1981–1992, 1995.

[207] Y. Guyot, H. Manaa, J. Y. Rivoire, R. Moncorgé, N. Garnier, E. Descroix, M. Bon, and P. Laporte, "Excited-state-absorption and upconversion studies of Nd^{3+}-doped single crystals Y$_3$Al$_5$O$_{12}$, YLiF$_4$, and LaMgAl$_{11}$O$_{19}$," *Phys. Rev. B*, vol. 51, pp. 784–799, 1995.

[208] V. Bagnoud, M. J. Guardalben, J. Puth, J. D. Zuegel, T. Mooney, and P. Dumas, "High-energy, high-average-power laser with Nd:YLF rod corrected by magnetorheological finishing," *Appl. Opt.*, vol. 44, pp. 282–288, 2005.

[209] D. F. Voss and L. S. Goldberg, "Simultaneous amplification and compression of continuous-wave mode-locked Nd:YAG laser pulses," *Opt. Lett.*, vol. 11, pp. 210–212, 1986.

[210] P. Bado, M. Bouvier, and J. S. Coe, "Nd:YLF mode-locked oscillator and regenerative amplifier," *Opt. Lett.*, vol. 12, pp. 319–321, 1987.

[211] J. S. Coe, P. Maine, and P. Bado, "Regenerative amplification of picosecond pulses in Nd:YLF: gain narrowing and gain saturation," *J. Opt. Soc. Am. B*, vol. 5, pp. 2560–2563, 1988.

[212] M. Saeed, D. Kim, and L. F. DiMauro, "Optimization and characterization of a high repetition rate, high intensity Nd:YLF regenerative amplifier," *Appl. Opt.*, vol. 29, pp. 1752–1757, 1990.

[213] G. Albrecht, A. Antonetti, and G. Mourou, "Temporal shape analysis of Nd^{3+}:YAG active passive mode-locked pulses," *Opt. Commun.*, vol. 40, pp. 59–62, 1981.

[214] S. Luan, M. H. Hutchinson, R. A. Smith, and F. Zhou, "High dynamic range third-order correlation measurement of picosecond laser pulse shapes," *Meas. Sci. Techno.*, vol. 4, pp. 1426–1429, 1993.

[215] D. Meshulach, Y. Barad, and Y. Silberberg, "Measurement of ultrashort optical pulses by third-harmonic generation," *J. Opt. Soc. Am. B*, vol. 14, pp. 2122–2125, 1997.

[216] L. M. Frantz and J. S. Nodvik, "Theory of Pulse Propagation in a Laser Amplifier," *J. Appl. Phys.*, vol. 34, pp. 2346–2349, 1963.

[217] G. Dikchyus, R. Danelyus, V. Kabelka, A. Piskarskas, and T. Tomkyavichyus, "Parametric amplification and generation of ultrashort light pulses for spectroscopic applications," *Sov. J. Quantum Electron.*, vol. 6, pp. 425–428, 1976.

[218] T. Miura, K. Kobayashi, K. Takasago, Z. Zhang, K. Torizuka, and F. Kannari, "Timing jitter in a kilohertz regenerative amplifier of a femtosecond-pulse Ti:Al$_2$O$_3$ laser," *Opt. Lett.*, vol. 25, pp. 1795–1797, 2000.

[219] T. Miura, K. Takasago, K. Kobayashi, Z. Zhang, K. Torizuka, and F. Kannari, "Reduction of Timing Jitter with Active Control in a kHz Regenerative Amplifier of Femtosecond Pulse Ti:Al$_2$O$_3$ Laser," *Jpn. J. Appl. Phys.*, vol. 40, pp. 1260–1266, 2001.

[220] F. Tavella and A. Marcinkevičius, "A 1.5 J picosecond amplifier system seeded with photonic crystal fiber output pulses," private communication, 2006.

[221] M. Zimmermann, C. Gohle, R. Holzwarth, T. Udem, and T. W. Hänsch, "Optical clock-work with an offset-free difference-frequency comb: accuracy of sum- and difference-frequency generation," *Opt. Lett.*, vol. 29, pp. 310–312, 2004.

[222] T. Fuji, A. Apolonski, and F. Krausz, "Self-stabilization of carrier-envelope offset phase by use of difference-frequency generation," *Opt. Lett.*, vol. 29, pp. 632–634, 2004.

[223] C. Manzoni, G. Cerullo, and S. De Silvestri, "Ultrabroadband self-phase-stabilized pulses by difference-frequency generation," *Opt. Lett.*, vol. 29, pp. 2668–2670, 2004.

[224] K. H. Yang, P. L. Richards, and Y. R. Shen, "Generation of Far-Infrared Radiation by Picosecond Light Pulses in LiNbO$_3$," *Appl. Phys. Lett.*, vol. 19, pp. 320–323, 1971.

[225] E. Sorokin, S. Naumov, and I. T. Sorokina, "Ultrabroadband infrared solid-state lasers," *IEEE J. Sel. Top. Quantum Electron.*, vol. 11, pp. 690–712, 2005.

[226] Q. Fu, G. Mak, and H. M. van Driel, "High-power, 62-fs infrared optical parametric oscillator synchronously pumped by a 76-MHz Ti:sapphire laser," *Opt. Lett.*, vol. 17, pp. 1006–1008, 1992.

[227] W. S. Pelouch, P. E. Powers, and C. L. Tang, "Ti:sapphire-pumped, high-repetition-rate femtosecond optical parametric oscillator," *Opt. Lett.*, vol. 17, pp. 1070–1072, 1992.

[228] M. H. Dunn and M. Ebrahimzadeh, "Parametric Generation of Tunable Light from Continuous-Wave to Femtosecond Pulses," *Science*, vol. 286, pp. 1513–1517, 1999.

[229] D. H. Auston, K. P. Cheung, and P. R. Smith, "Picosecond photoconducting Herztian dipoles," *Appl. Phys. Lett.*, vol. 45, pp. 284–286, 1984.

[230] B. B. Hu, X. C. Zhang, and D. H. Auston, "Free-space radiation from electro-optic crystals," *Appl. Phys. Lett.*, vol. 56, pp. 506–508, 1990.

[231] A. Rice, J. Jin, X. F. Ma, and X. C. Zhang, "Terahertz optical rectification from ¡110¿ zinc-blende crystals," *Appl. Phys. Lett.*, vol. 64, pp. 1324–1326, 1993.

[232] A. Bonvalet, M. Joffre, J. L. Martin, and A. Migus, "Generation of ultrabroadband femtosecond pulses in the mid-infrared by optical rectification of 15 fs light pulses at 100 MHz repetition rate," *Appl. Phys. Lett.*, vol. 67, pp. 2907–2909, 1995.

[233] A. Baltuška, T. Fuji, and T. Kobayashi, "Controlling the carrier-envelope phase of ultrashort light pulses with optical parametric amplifiers," *Phys. Rev. Lett.*, vol. 88, p. 133901, 2002.

[234] T. Brabec and F. Krausz, "Intense few-cycle laser fields: Frontiers of nonlinear optics," *Rev. Mod. Phys.*, vol. 72, pp. 545–591, 2000.

[235] T. Fuji, N. Ishii, C. Y. Teisset, X. Gu, T. Metzger, A. Baltuška, N. Forget, D. Kaplan, A. Galvanauskas, and F. Krausz, "Parametric amplification of few-cycle carrier-envelope phase-stable pulses at 2.1 μm," *Opt. Lett.*, vol. 31, pp. 1103–1105, 2006.

[236] A. Braun, G. Korn, X. Liu, D. Du, J. Squier, and G. Mourou, "Self-channeling of high-peak-power femtosecond laser pulses in air," *Opt. Lett.*, vol. 20, pp. 73–75, 1995.

[237] A. Brodeur, C. Y. Chien, F. A. Ilkov, S. L. Chin, O. G. Kosareva, and V. P. Kandidov, "Moving focus in the propagation of ultrashort laser pulses in air," *Opt. Lett.*, vol. 22, pp. 304–306, 1997.

[238] H. R. Lange, G. Grillon, J. F. Ripoche, M. A. Franco, B. Lamouroux, B. S. Prade, A. Mysyrowicz, E. T. J. Nibbering, and A. Chiron, "Anomalous long-range propagation of femtosecond laser pulses through air: moving focus or pulse self-guiding ?," *Opt. Lett.*, vol. 23, pp. 120–122, 1998.

[239] C. P. Hauri, W. Kornelis, F. W. Helbing, A. Heinrich, A. Couairon, A. Mysyrowicz, J. Biegert, and U. Keller, "Generation of intense, carrier-envelope phase-locked few-cycle laser pulses through filamentation," *Appl. Phys. B*, vol. 79, pp. 673–677, 2004.

[240] A. Suda, M. Hatayama, and K. N. ans K. Midorikawa, "Generation of sub-10-fs, 5-mJ-optical pulses using a hollow fiber with a pressure gradient," *Appl. Phys. Lett.*, vol. 86, p. 111116, 2005.

[241] A. Couairon, M. Franco, A. Mysyrowicz, J. Biegert, and U. Keller, "Pulse self-compression to the single-cycle limit by filamentation in a gas with a pressure gradient," *Opt. Lett.*, vol. 30, pp. 2657–2659, 2005.

[242] G. Stibenz, N. Zhavoronkov, and G. Steinmeyer, "Self-compression of millijoule pulses to 7.8 fs duration in a white-light filament," *Opt. Lett.*, vol. 31, pp. 274–276, 2006.

[243] J. R. Morris and Y. R. Shen, "Theory of far-infrared generation by optical mixing," *Phys. Rev. A*, vol. 15, pp. 1143–1156, 1977.

[244] R. A. Kaindl, F. Eickemeyer, M. Woerner, and T. Elsaesser, "Broadband phase-matched difference frequency mixing of femtosecond pulses in GaSe: Experiment and theory," *Appl. Phys. Lett.*, vol. 75, pp. 1060–1062, 1999.

[245] G. Gallot and D. Grischkowsky, "Electro-optic detection of terahertz radiation," *J. Opt. Soc. Am. B*, vol. 16, pp. 1204–1212, 1999.

[246] R. Trebino, K. W. DeLong, D. N. Fittinghoff, J. N. Sweetser, M. A. Krumbügel, and B. A. Richman, "Measuring ultrashort laser pulses in the time-frequency domain using frequency-resolved optical gating," *Rev. Sci. Instrum.*, vol. 68, pp. 3277–3295, 1997.

[247] V. Petrov and F. Noack, "Mid-infrared femtosecond optical parametric amplification in potassium niobate," *Opt. Lett.*, vol. 21, pp. 1576–1578, 1996.

[248] F. Rotermund, V. Petrov, and F. Noack, "Femtosecond noncollinear parametric amplification in the mid-infrared," *Opt. Commun.*, vol. 169, pp. 183–188, 1999.

[249] F. Rotermund, V. Petrov, F. Noack, M. Wittmann, and G. Korn, "Laser-diode-seeded operation of a femtosecond optical parametric amplifier with MgO:LiNbO$_3$ and generation of 5-cycle pulses near 3 μm," *J. Opt. Soc. Am. B*, vol. 16, pp. 1539–1544, 1999.

[250] S. Cussat-Blanc, A. Ivanov, D. Lupinski, and E. Freysz, "KTiOPO$_4$, KTiOAsO$_4$, and KNbO$_3$ crystals for mid-infrared femtosecond optical parametric amplifiers: analysis and comparison," *Appl. Phys. B*, vol. 70, pp. S247–S252, 2000.

[251] N. Demirdöven, M. Khalil, O. Golonzka, and A. Tokmakoff, "Dispersion compensation with optical materials for compression of intense sub-100-fs mid-infrared pulses," *Opt. Lett.*, vol. 27, pp. 433–435, 2002.

[252] J. A. Gruetzmacher and N. F. Scherer, "Few-cycle mid-infrared pulse generation, characterization, and coherent propagation in optically dense media," *Rev. Sci. Instrum.*, vol. 73, pp. 2227–2236, 2002.

[253] C. Manzoni, C. Vozzi, E. Benedetti, G. Sansone, S. Stagira, O. Svelto, S. De Silvestri, M. Nisoli, and G. Cerullo, "Generation of high-energy self-phase-stabilized pulses by difference-frequency generation followed by optical parametric amplification," *Opt. Lett.*, vol. 31, pp. 963–965, 2006.

[254] M. Yamada, N. Nada, M. Saitoh, and K. Watanabe, "First-order quasi-phase matched $LiNbO_3$ waveguide periodically poled by applying an external field for efficient blue second-harmonic generation," *Appl. Phys. Lett.*, vol. 62, pp. 435–436, 1993.

[255] M. M. Fejer, G. A. Magel, D. H. Jundt, and R. L. Byer, "Quasi-phase-matched second harmonic generation: tuning and tolerances," *IEEE J. Quantum Electron.*, vol. 28, pp. 2631–2654, 1992.

[256] L. E. Myers, G. D. Miller, R. C. Eckardt, M. M. Fejer, R. L. Byer, and W. R. Bosenberg, "Quasi-phase-matched 1.064-μm-pumped optical parametric oscillator in bulk periodically poled $LiNbO_3$," *Opt. Lett.*, vol. 20, pp. 52–54, 1995.

[257] K. Kitamura, Y. Furukawa, K. Niwa, V. Gopalan, and T. E. Mitchell, "Crystal growth and low coercive field 180° domain switching characteristics of stoichiometric $LiTaO_3$," *Appl. Phys. Lett.*, vol. 73, pp. 3073–3075, 1998.

[258] T. Hatanaka, K. Nakamura, T. Taniuchi, H. Ito, Y. Furukawa, and K. Kitamura, "Quasi-phase-matched optical parametric oscillation with periodically poled stoichiometric $LiTaO_3$," *Opt. Lett.*, vol. 25, pp. 651–653, 2000.

[259] H. Ishizuki, I. Shoji, and T. Taira, "Periodical poling characteristics of congruent $MgO:LiNbO_3$ crystals at elevated temperature," *Appl. Phys. Lett.*, vol. 82, pp. 4062–4064, 2003.

[260] G. Marcus, A. Zigler, D. Eger, A. Bruner, and A. Englander, "Generation of a high-energy ultrawideband chirped source in periodically poled $LiTaO_3$," *J. Opt. Soc. Am. B*, vol. 22, pp. 620–622, 2005.

[261] A. Fragemann, V. Pasiskevicius, and F. Laurell, "Broadband nondegenerate optical parametric amplification in the mid infrared with periodically poled $ktiopo_4$," *Opt. Lett.*, vol. 30, pp. 2296–2298, 2005.

[262] I. Shoji, T. Kondo, A. Kitamoto, M. Shirane, and R. Ito, "Absolute scale of second-order nonlinear-optical coefficients," *J. Opt. Soc. Am. B*, vol. 14, pp. 2268–2294, 1997.

[263] N. E. Yu, S. Kurimura, Y. Nomura, M. Nakamura, K. Kitamura, Y. Takada, J. Sakuma, and T. Sumiyoshi, "Efficient optical parametric oscillation based on periodically poled 1.0 mol % MgO-doped stoichiometric $LiTaO_3$," *Appl. Phys. Lett.*, vol. 85, pp. 5134–5136, 2004.

[264] H. Ishizuki and T. Taira, "High-energy quasi-phase-matched optical parametric oscillation in a periodically poled $MgO:LiNbO_3$ device with a 5 mm x 5 mm aperture," *Opt. Lett.*, vol. 30, pp. 2918–2920, 2005.

[265] G. D. Goodno, Z. Guo, R. J. D. Miller, I. J. Miller, J. W. Montgomery, S. R. Adhav, and R. S. Adhav, "Investigation of β-BaB_2O_4 as a Q switch for high power applications," *Appl. Phys. Lett.*, vol. 66, pp. 1575–1577, 1995.

[266] T. Tsang, M. A. Krumbügel, K. W. DeLong, D. N. Fittinghoff, and R. Trebino, "Frequency-resolved optical-gating measurements of ultrashort pulses using surface third-harmonic generation," *Opt. Lett.*, vol. 21, pp. 1381–1383, 1996.

[267] G. Georgiev, D. A. Glenar, and J. J. Hillman, "Spectral characterization of acousto-optic filters used in imaging spectroscopy," *Appl. Opt.*, vol. 41, pp. 209–217, 2002.

[268] P. Yeh, *Introduction to Photorefractive Nonlinear Optics*. New York: John Wiley & Sons, 1993.

[269] M. Dinu, F. Quochi, and H. Garcia, "Third-order nonlinearities in Silicon at telecom wavelengths," *Appl. Phys. Lett.*, vol. 82, pp. 2954–2956, 2003.

[270] G. Steinmeyer, D. H. Sutter, L. Gallmann, N. Matuschek, and U. Keller, "Frontiers in Ultrashort Pulse Generation: Pushing the limits in Linear and Nonlinear Optics," *Science*, vol. 286, pp. 1507–1512, 1999.

[271] L. Xu, C. Spielmann, A. Poppe, T. Brabec, and F. Krausz, "Route to phase control of ultrashort light pulses," *Opt. Lett.*, vol. 21, pp. 2008–2010, 1996.

[272] D. J. Jones, S. A. Diddams, J. K. Ranka, A. Stentz, R. S. Windeler, J. L. Hall, and S. T. Cundiff, "Carrier-Envelope Phase Control of Femtosecond Mode-Locked Lasers and Direct Optical Frequency Synthesis," *Science*, vol. 288, pp. 635–639, 2000.

[273] A. Apolonski, A. Poppe, G. Tempea, C. Spielmann, T. Udem, R. Holzwarth, T. W. Hänsch, and F. Krausz, "Controlling the Phase Evolution of Few-Cycle Light Pulses," *Phys. Rev. Lett.*, vol. 85, pp. 740–743, 2000.

[274] A. Poppe, R. Holzwarth, A. Apolonski, G. Tempea, C. Spielmann, T. W. Hänsch, and F. Krausz, "Few-cycle optical waveform synthesis," *Appl. Phys. B*, vol. 72, pp. 373–376, 2001.

[275] F. W. Helbing, G. Steinmeyer, J. Stenger, H. R. Telle, and U. Keller, "Carrier-envelope-offset dynamics and stabilization of femtosecond pulses," *Appl. Phys. B*, vol. 74, pp. S35–S42, 2002.

[276] J. C. Knight, T. A. Birks, P. S. J. Russell, and D. M. Atkin, "All-silica single-mode optical fiber with photonic crystal cladding," *Opt. Lett.*, vol. 21, pp. 1547–1549, 1996.

[277] M. Kakehata, H. Takada, Y. Kobayashi, K. Torizuka, Y. Fujihira, T. Homma, and H. Takahashi, "Single-shot measurement of carrier-envelope phase changes by spectral interferometry," *Opt. Lett.*, vol. 26, pp. 1436–1438, 2001.

[278] Q. Xing, K. M. Yoo, and R. R. Alfano, "Conical emission by four-photon parametric generation by using femtosecond laser pulses," *Appl. Opt.*, vol. 32, pp. 2087–2089, 1993.

[279] A. Brodeur, F. A. Ilkov, and S. L. Chin, "Beam filamentation and the white light continuum divergence," *Opt. Commun.*, vol. 129, pp. 193–198, 1996.

[280] M. Kolesik, G. Katona, J. V. Moloney, and E. M. Wright, "Physical Factors Limiting the Spectral Extent and Band Gap Dependence of Supercontinuum Generation," *Phys. Rev. Lett.*, vol. 91, p. 043905, 2003.

[281] F. Shimizu, "Frequency Broadening in Liquid by a Short Light Pulse," *Phys. Rev. Lett.*, vol. 19, pp. 1097–1100, 1967.

[282] R. R. Alfano and S. L. Shapiro, "Observation of Self-Phase Modulation and Small-Scale Filaments in Crystals and Glasses," *Phys. Rev. Lett.*, vol. 24, pp. 592–594, 1970.

[283] P. B.Corkum, P. P. Ho, R. R. Alfano, and J. T. Manassah, "Generation of infrared supercontinuum covering 3-14 μm in dielectrics and semiconductors," *Opt. Lett.*, vol. 10, pp. 624–626, 1985.

[284] G. Yang and Y. R. Shen, "Spectral broadening of ultrashort pulses in a nonlinear medium," *Opt. Lett.*, vol. 9, pp. 510–512, 1984.

[285] G. S. He, G. C. Xu, Y. Cui, and P. N. Prasad, "Difference of spectral superbroadening behavior in Kerr-type and non-Kerr-type liquids pumped with ultrashort laser pulses," *Appl. Opt.*, vol. 32, pp. 4507–4512, 1993.

[286] A. Brodeur and S. L. Chin, "Band-Gap Dependence of the Ultrafast White-Light Continuum," *Phys. Rev. Lett.*, vol. 80, pp. 4406–4409, 1998.

[287] A. L. Gaeta, "Catastrophic Collapse of Ultrashort Pulses," *Phys. Rev. Lett.*, vol. 84, pp. 3582–3584, 2000.

[288] A. Brodeur and S. L. Chin, "Ultrafast white-light continuum generation and self-focusing in transparent condensed media," *J. Opt. Soc. Am. B*, vol. 16, pp. 637–650, 1999.

[289] C. Nagura, A. Suda, H. Kawano, M. Obara, and K. Midorikawa, "Generation and characterization of ultrafast white-light continuum in condensed media," *Appl. Opt.*, vol. 41, pp. 3735–3742, 2002.

[290] A. Saliminia, S. L. Chin, and R. Vallée, "Ultra-broad and coherent white light generation in silica glass by focused femtosecond pulses at 1.5 μm," *Opt. Express*, vol. 13, pp. 5731–5738, 2005.

[291] P. S. Banks, M. D. Feit, and M. D. Perry, "High-intensity third-harmonic generation in beta barium borate through second-order and third-order susceptibilities," *Opt. Lett.*, vol. 24, pp. 4–6, 1999.

[292] L. Lepetit, G. Chériaux, and M. Joffre, "Linear techniques of phase measurement by femtosecond spectral interferometry for applications in spectroscopy," *J. Opt. Soc. Am. B*, vol. 12, pp. 2467–2474, 1995.

[293] A. W. Albrecht, J. D. Hybl, S. M. G. Faeder, and D. M. Jonas, "Experimental distinction between phase shifts and time delays: Implications for femtosecond spectroscopy and coherent control of chemical reactions," *J. Chem. PHys.*, vol. 111, pp. 10934–10956, 1999.

[294] J. F. Reintjes, *Nonlinear Optical Parametric Processes in Liquids and Gases*. Orland: Academic Press, 1984.

[295] B. W. Shore and P. L. Knight, "Enhancement of high optical harmonics by excess-photon ionisation," *J. Phys. B: At. Mol. Phys.*, vol. 20, pp. 413–423, 1987.

[296] A. McPherson, G. Gibson, H. Jara, U. Johann, T. S. Luk, I. A. McIntyre, K. Boyer, and C. K. Rhodes, "Studies of multiphoton production of vacuum-ultraviolet radiation in the rare gases," *J. Opt. Soc. Am. B*, vol. 4, pp. 595–601, 1987.

[297] M. Ferray, A. L'Huillier, X. F. Li, L. A. Lompré, G. Mainfray, and C. Manus, "Multiple-harmonic conversion of 1064 nm radiation in rare gases," *J. Phys. B: At. Mol. Opt. Phys.*, vol. 21, pp. L31–L35, 1988.

[298] P. Balcou, C. Cornaggia, A. S. L. Gomes, L. A. Lompré, and A. L'Huillier, "Optimizing high-order harmonic generation in strong fields," *J. Phys. B: At. Mol. Opt. Phys.*, vol. 25, pp. 4467–4485, 1992.

[299] J. L. Krause, K. J. Schafer, and K. C. Kulander, "High-Order Harmonic Generation from Atoms and Ions in the High Intensity Regime," *Phys. Rev. Lett*, vol. 68, pp. 3535–3538, 1992.

[300] P. B. Corkum, "Plasma Perspective on Strong-Field Multiphoton Ionization," *Phys. Rev. Lett.*, vol. 71, pp. 1994–1997, 1993.

[301] L. V. Keldysh, "Ionization in the field of a strong electromagnetic wave," *Sov. Phys. JETP*, vol. 20, pp. 1307–1314, 1965.

[302] S. L. Chin and P. Lambropoulos, *Multiphoton Ionization of Atoms*. New York: Academic Press, 1984.

[303] A. L'Huillier and Ph. Balcou and S. Candel and K. J. Schafer and K. C. Kulander, "Calculations of high-order harmonic-generation processes in xenon at 1064 nm," *Phys. Rev. A*, vol. 46, pp. 2778–2790, 1992.

[304] J. Zhou, J. Peatross, M. M. Murnane, and H. C. Kapteyn, "Enhanced High-Harmonic Generation Using 25 fs Laser Pulses," *Phys. Rev. Lett.*, vol. 80, pp. 3236–3239, 1998.

[305] C. Spielmann, N. H. Burnett, S. Sartania, R. Koppitsch, and M. Schnürer and C. Kan and M. Lenzner and P. Wobrauschek and F. Krausz, "Generation of Coherent X-rays in the Water Window Using 5-Femtosecond Laser Pulses," *Science*, vol. 278, pp. 661–664, 1997.

[306] M. Schnürer, C. Spielmann, P. Wobrauschek, C. Streli, N. H. Burnett, C. Kan, K. Ferencz, R. Koppitsch, Z. Cheng, T. Brabec, and F. Krausz, "Coherent 0.5-keV X-Ray Emission from Helium Driven by a Sub-10-fs Laser," *Phys. Rev. Lett.*, vol. 80, pp. 3236–3239, 1998.

[307] E. Seres, J. Seres, F. Krausz, and C. Spielmann, "Generation of Coherent Soft X-Ray Radiation Extending Far Beyond the Titanium *L* Edge," *Phys. Rev. Lett.*, vol. 92, p. 163002, 2004.

[308] D. M. Gaudiosi, B. Reagan, T. Popmintchev, M. Grisham, M. Berrill, O. Cohen, B. C. Walker, M. M. Murnane, H. C. Kapteyn, and J. J. Rocca, "High-Order Harmonic Generation from Ions in a Capillary Discharge," *Phys. Rev. Lett.*, vol. 96, p. 203001, 2006.

[309] A. Rundquist, C. G. Durfee III, Z. Chang, C. Herne, S. Backus, M. M. Murnane, and H. C. Kapteyn, "Phase-matched Generation of Coherent Soft X-Rays," *Science*, vol. 280, pp. 1412–1415, 1998.

[310] E. A. Gibson, A. Paul, N. Wagner, R. Tobey, D. Gaudiosi, S. Backus, I. P. Christov, A. Aquila, E. M. Gullikson, D. T. Attwood, M. M. Murnane, and H. C. Kapteyn, "Coherent Soft X-ray Generation in the Water Window with Quasi-Phase Matching," *Science*, vol. 320, pp. 95–98, 2003.

[311] M. Lewenstein, P. Balcou, M. Y. Ivanov, A. L'Huillier, and P. B. Corkum, "Theory of high-harmonic generation by low-frequency laser fields," *Phys. Rev. A*, vol. 49, pp. 2117–2132, 1994.

[312] A. Gordon and F. X. Kärtner, "Scaling of keV HHG photon yield with drive wavelength," *Opt. Express*, vol. 13, pp. 2941–2947, 2005.

[313] B. Sheehy, J. D. D. Martin, L. F. DiMauro, P. Agostini, K. J. Schafer, M. B. Gaarde, and K. C. Kulander, "High Harmonic Generation at Long Wavelengths," *Phys. Rev. Lett.*, vol. 83, pp. 5270–5273, 1999.

[314] B. Shan and Z. Chang, "Dramatic extension of the high-order harmonic cutoff by using a long-wavelength driving field," *Phys. Rev. A*, vol. 65, p. 011804, 2001.

[315] N. H. Burnett, C. Kan, and P. B. Corkum, "Ellipticity and polarization effects in harmonic generation in ionizing neon," *Phys. Rev. A*, vol. 21, pp. R3418–R3421, 1995.

[316] D. Zhang, Y. Kong, and J. Zhang, "Optical parametric properties of 532-nm-pumped beta-barium-borate near the infrared absorption edge," *Opt. Commun.*, vol. 184, pp. 485–491, 2000.

[317] K. Kato, "Temperature-tuned 90° phase-matching properties of LiB_3O_5," *IEEE J. Quantum Electron.*, vol. 30, pp. 2950–2952, 1994.

[318] D. E. Zelmon, D. L. Small, and D. Jundt, "Infrared corrected Sellmeier coefficients for congruently grown lithium niobate and 5 mol% magnesium oxide-doped lithium niobate," *J. Opt. Soc. Am. B*, vol. 14, pp. 3319–3322, 1997.

[319] HC Photonics, "Temperature dependent extraordinary refractive index of MgO:LN," Private communication, 2004.

[320] M. Nakamura, S. Higuchi, S. Takekawa, K. Terabe, Y. Furukawa, and K. Kitamura, "Refractive Indices in Undoped and MgO-Doped Near-Stoichiometric $LiTaO_3$ Crystals," *Jpn. J. Appl. Phys.*, vol. 41, pp. L465–L467, 2002.

[321] A. Bruner, D. Eger, M. B. Oron, P. Blau, M. Katz, and S. Ruschin, "Temperature-dependent Sellmeier equation for the refractive index of stoichiometric lithium tantalate," *Opt. Lett.*, vol. 28, pp. 194–196, 2003.

[322] N. Uchida, "Optical Properties of Single-Crystal Paratellurite (TeO_2)," *Phys. Rev. B*, vol. 4, pp. 3736–3745, 1971.

[323] Schott AG, "Refractive index of SF57 glass," available at http://www.schott.com/.

[324] M. Bass ed., *Handbook of Optics*. New York: McGraw Hill, 1995.

[325] D. F. Edwards, Silicon (Si), *in Handbook of Optical Constans of Solids,* E. D. Palik (Ed.). New York: Academic Press Inc., 1985.

[326] Schott AG, "Refractive index of BK7 glass," available at http://www.schott.com/.

[327] A. Yariv and P. Yeh, *Optical Waves in Crystals*. New York: John Wiley & Sons, 1984.

[328] J. D. Jackson, *Classical Electrodynamics, 3rd Ed.* New York: John Wiley & Sons, 1998.

[329] D. Milam, "Review and assessment of measured values of the nonlinear refractive-index coefficient of fused silica," *Appl. Opt.*, vol. 37, pp. 546–550, 1998.

[330] S. R. Friberg and P. W. Smith, "Nonlinear Optical-Glasses for Ultrafast Optical Switches," *IEEE J. Quantum Electron.*, vol. 23, pp. 2089–2094, 1989.

[331] R. Adair, L. L. Chase, and S. A. Payne, "Nonlinear refractive index of optical crystals," *Phys. Rev. B*, vol. 39, pp. 3337–3350, 1989.

[332] W. L. Smith, J. H. Bechtel, and N. Bloembergen, "Dielectric-breakdown threshold and nonlinear-refractive-index measurements with picosecond laser pulses," *Phys. Rev. B*, vol. 12, pp. 706–714, 1975.

[333] Y. Chang and Y. Kuo, "Optical Performance of Ho:YLF Q-switched Tm:YAG Laser System," *SPIE Proc.*, vol. 4914, pp. 510–521, 2002.

[334] U. Keller, "Ultrafast All-Solid-State Laser Technology," *Appl. Phys. B*, vol. 58, pp. 347–363, 1994.

[335] F. Hache, A. Zéboulon, G. Gallot, and G. M. Gale, "Cascaded second-order effects in the femtosecond regime in β-barium borate: self-compression in a visible femtosecond optical parametric oscillator," *Opt. Lett.*, vol. 20, pp. 1556–1558, 1995.

[336] R. Danielius, P. Di Trapani, A. Dubietis, A. Piskarskas, D. Podenas, and G. P. Banfi, "Self-diffraction through cascaded second-order frequency-mixing effects in β-barium borate," *Opt. Lett.*, vol. 18, pp. 574–576, 1993.

[337] R. A. Ganeev, "Nonlinear refraction and nonlinear absorption of various media," *J. Opt. A: Pure Appl. Opt.*, vol. 7, pp. 717–733, 2005.

Acknowledgments

research Center in Lithuania and invaluable discussions about the experiments. Especially thanks to R. Butkus for his kindness during my stay in Vilnius and the careful reading of my thesis.

I would like to acknowledge E. E. Serebryannikov and Prof. A. M. Zheltikov for their theoretical simulation about the photonic crystal fiber experiments and their suggestion and discussion about the optical seeding experiment by use of a photonic crystal fiber.

I wish to thank B. Schmidt, R. Holzwarth, and Prof. T. W. Hänsch for the lease of the Ti:sapphire amplifier used in the infrared OPCPA system.

Prof. A. Galvanauskas is gratefully acknowledged for his contribution and discussion about the infrared OPCPA and Yb:fiber amplifier construction.

I am grateful to R. Hartmann for his help with the infrared-pulse-driven high-harmonics generation experiment by use of the back-illuminated CCD.

The collaborative experiment with N. Forget and D. Kaplan was a great time for me and their helps with the Dazzler implementation are gratefully acknowledged.

I would like to thank to Mses D. Egger, B. Schütz, and M. Wild for their administrative help and support during my stay in Vienna and Garching.

Last but not least, I am grateful to my parents, sister and, especially, my wife, who has kindly lived with me during the stay abroad.

Curriculum Vitae

Nobuhisa Ishii

Current address:
Max Planck Institute for Quantum Optics
Hans-Kopfermann-Strasse 1, D-85748 Garching, Germany.
E-mail: nobuhisa.ishii@mpq.mpg.de
Phone: +49 89 32905-611 (Office)
Phone: +49 89 32905-767 (Lab.)
Fax: +49 89 32905-649

Personal data:
Date of birth: 25. Feb. 1979.
Place of birth: Tokyo, Japan.
Nationality: Japan.

Education:
06.2004 - present,
Ph.D. student at Max-Planck-Institut für Quantenoptik, Garching, Germany, and Ludwig-Maximilians-Universität, Garching, Germany.
"Development of optical parametric chirped pulse amplifiers and their applications,"
Supervisor: Prof. Ferenc Krausz.
(2 semesters enrollment at the LMU in Winter of 2004-05 and Summer of 2005)

04.2003 - 05.2004,
Ph.D. student at the Photonics Institute of Vienna University of Technology, Vienna, Austria.
"Development of optical parametric chirped pulse amplifiers and their applications,"
Supervisor: Prof. Ferenc Krausz.

04.2001 - 03.2003,
Master of Science from the Department of Physics, Faculty of Science, University of Tokyo, Tokyo, Japan.
"Ultrafast spectroscopy of a Polydiacetylene,"

Supervisor: Prof. Takayoshi Kobayashi.

04.1997 - 03.2001,
Bachelor of Science from the Department of Physics, Faculty of Science, University of Tokyo,
Tokyo, Japan.

Research expertise and fields:
Ultrafast laser physics and technology
Ultrafast and nonlinear spectroscopy
Ultrafast optics, nonlinear optics, and linear optics
Development of ultrafast and high-power lasers

Publications:
12 publications in peer-reviewed scientific journals
5 conference proceedings
1 patent (pending)

Multimillijoule chirped parametric amplification of few-cycle pulses

N. Ishii, L. Turi, V. S. Yakovlev, T. Fuji, F. Krausz,* and A. Baltuška

*Institut für Photonik, Technische Universität Wien, Gusshausstrasse 27/387, A-1040 Vienna, Austria, and
Max-Planck-Institut für Quantenoptik, Hans-Kopfermann-Strasse 1, D-85748 Garching, Germany*

R. Butkus, G. Veitas,† V. Smilgevičius, R. Danielius, and A. Piskarskas

Laser Research Center, Vilnius University, Saulėtekio Avenue 10, LT-10223 Vilnius, Lithuania

The concept of optical parametric chirped-pulse amplification is applied to attain pulses with energies up to 8 mJ and a bandwidth of more than 100 THz. Stretched broadband seed pulses from a Ti:sapphire oscillator are amplified in a multistage noncollinear type I phase-matched β-barium borate parametric amplifier by use of an independent picosecond laser with lock-to-clock repetition rate synchronization. Partial compression of amplified pulses is demonstrated down to a 10-fs duration with a down-chirped pulse stretcher and a nearly lossless compressor comprising bulk material and positive-dispersion chirped mirrors. © 2005 Optical Society of America

OCIS codes: 140.7090, 190.4970, 320.5520.

Typical processes in laser-driven strong-field physics[1] are confined to one or a few optical oscillations and therefore require appropriately short laser pulses of the highest possible peak power. The proven way to obtain intense few-cycle laser fields relies on external bandwidth broadening of amplified pulses in gas-filled capillaries[2,3]—a method that involves heavy energy losses and is not easily scalable in the multimillijoule regime. In contrast with laser media, the gain bandwidth of some noncollinearly phase-matched nonlinear optical crystals, especially β-barium borate (BBO),[4] is directly suitable for amplification of two-cycle visible pulses without subsequent spectral broadening.[5-7] Since the nonlinear optical crystal does not provide inversion storage, efficient broadband amplification with a narrowband pump pulse becomes possible only if the seed pulse is stretched to match the pump duration. Such optical parametric chirped-pulse amplification (OPCPA) was originally proposed and demonstrated by Dubietis et al.[8] and has since found broad recognition as a promising scheme for designing ultrahigh-peak-power laser systems.[9-11] To date, high-energy subpicosecond parametric systems[12-15] and few-cycle 100-μJ-level OPCPA[16,17] have been reported. In this Letter we demonstrate a terawatt-class 10-fs scheme that, in our opinion, presents a feasible alternative to a similar-level amplifier based on a Ti:sapphire laser.

The schematic of our OPCPA setup is presented in Fig. 1(a). Similarly to Refs. 16 and 17, the employed seed source is a nanojoule broadband Ti:sapphire seed oscillator. The repetition rates of the femtosecond seed laser and an actively mode-locked 60-ps Nd:YVO$_4$ oscillator are synchronized with an external rf clock. The pulses from the picosecond oscillator are amplified to 100 mJ at a 20-Hz repetition rate in a Nd:YAG amplifier (EKSPA Ltd.) and frequency doubled to produce a 50-mJ, 532-nm pump for OPCPA.

Our parametric amplifier consists of two 4-mm-thick antireflection-coated type I BBO crystals. The inter-nal noncollinearity angle between the pump and the seed beams is set at approximately 2.3° to provide the broadest gain bandwidth. Although we can achieve a factor of 10^6 gain in a single-stage parametric amplifier, the multistage, multipass arrangement shown in
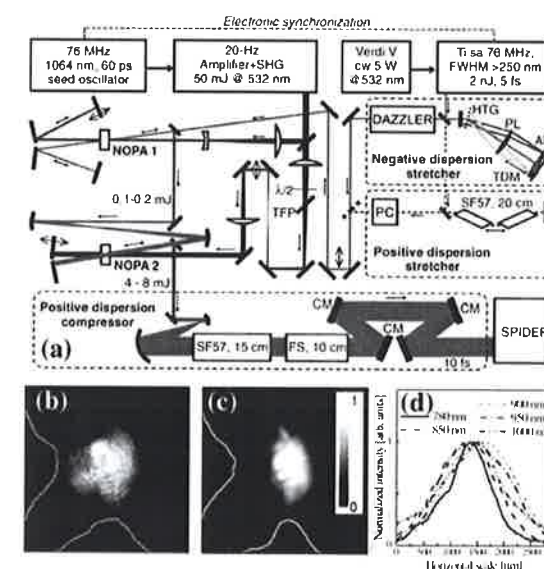

Fig. 1. Two-stage, four-pass chirped-pulse parametric amplifier: (a) layout of the optical setup, (b) relay-imaged pump beam profile at the second-stage crystal, (c) beam profile of the signal beam amplified to 5 mJ, (d) horizontal cross section of the signal beam at several wavelengths. HTG, holographic transmission diffraction grating; PL, parabolic lens; AP, micromachined aspheric plate; TDM, thermally activated mirror; PC, Pockels cell; $\lambda/2$, 532-nm half-wave plate; TFP, thin-film polarizer; SF57, block of Schott SF57 glass; FS, block of synthetic fused silica; CM, positive-dispersion chirped mirror; SHG, second-harmonic generation; Ti:sa, Ti:sapphire laser. SPIDER, spectral phase interferometry for direct electric field reconstruction.

© 2005 Optical Society of America

Fig. 1(a) is used for its pulse contrast and bandwidth. In this scheme, by using a weaker pump, we reduce the gain in a single stage below 10^4. On the one hand, this measure suppresses the competition between the external seed and the internal parametric superfluorescence generated in the presence of a strong pump, and, on the other hand, it prevents amplification of the seed replica that is caused by a small double retro-reflection from the crystal surfaces.

The BBO length was chosen as a compromise between the gain bandwidth and the amplification factor. In the first noncollinear optical parametric amplifier [NOPA 1; Fig. 1(a)] the collimated pump and signal beams are retroreflected onto the nonlinear optical crystal by flat mirrors located ~25 cm behind the crystal that filters, to some degree, the parametric superfluorescence acquired in the first pass. In contrast with NOPA 1, the reflectors in NOPA 2 are located only 7 cm behind the crystal and are slightly tilted horizontally to change both the phase matching and the noncollinearity angles for the second pass. This angular detuning in NOPA 2, in combination with an independent alignment of NOPA 1, allows us to reshape the gain bandwidth[18,19] and reduce the cumulative bandwidth narrowing through the amplifier. Another important aspect of an optical parametric amplifier is the potential angular chirp of a broadband signal wave whereby a thick noncollinearly phase-matched crystal plays the role of a dispersive monochromator.[20] To characterize this distortion, we monitored the beam profile of the signal amplified to 5 mJ [Fig. 1(c)] and frequency resolved the beam profile behind NOPA 2. As can be seen from the frequency-dependent cross sections in the pump–signal intersection plane, the high-gain amplification causes significant modulation of the output beam but does not lead to a clearly observable mode displacement characteristic of angular chirp. This result ascertains the usability of the chosen crystal length for a broadband noncollinear amplification under the condition of seed collimation, which overrides the selection of output direction imposed by phase matching.

The pump-to-signal energy conversion efficiency of NOPA 1 and NOPA 2, both optimized for the broadest bandwidth, is summarized in Fig. 2. Theoretically, the most efficient performance of OPCPA requires the pump pulse to have roughly top-hat spatial and temporal profiles. Nonetheless, even without adequate temporal (a nearly Gaussian pump pulse intensity profile) and spatial [Fig. 1(b)] shaping, the peak pump-to-signal conversion efficiency in NOPA 2 reaches 27% [Figs. 2(b)]. As can be seen in Figs. 2(a) and 2(b), the pump spot sizes were chosen to permit gain saturation and to improve signal pulse stability. However, deep saturation, observed for the pump energy around 30 mJ, was found to be detrimental because it dramatically enhances the uncompressible background of the signal pulse consisting of amplified superfluorescence. The safe operating conditions in terms of superfluorescence suppression and pulse stability correspond to approximately 5 mJ in the signal pulse, at which the rms intensity fluctuation of

the signal pulse is approximately 2.9%, whereas the pump rms fluctuation is nearly 1.5%.

To match the pump pulse duration, the seed pulse was chirped with two alternative stretchers: positive-dispersion bulk material and a negative-dispersion $4f$ dispersion line, both presented in Fig. 1(a). Amplification results obtained with bulk chirping are summarized in Fig. 3. The advantages of this stretching technique are its simplicity, excellent transmitted beam quality, and high throughput for the entire bandwidth of the seed. The solid curve in Fig. 3 shows the spectrum of the signal wave amplified to 8 mJ, which compares well with the overlap between the seed spectrum (dotted curve) and the theoretically calculated gain bandwidth (dashed curve).

Lacking an appropriate high-throughput pulse compressor for the bulk stretcher, we designed a matched pair consisting of a down-chirping stretcher and an up-chirping compressor.[21] In our stretcher [Fig. 1(a)] the beam is dispersed by a holographic 900-line/mm transmission grating (Wasatch Photonics) and passed through an $f \approx 80$ mm parabolic quartz lens. In the Fourier plane of this lens we introduced a micromachined quartz plate for higher-order
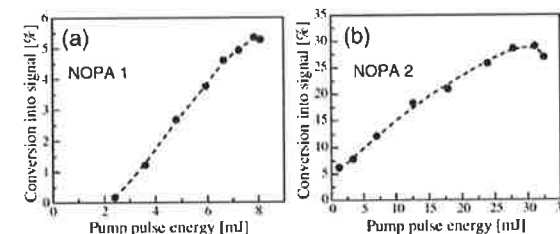

Fig. 2. Energy conversion efficiency into the signal wave. (a) First amplifier stage in a double pass. The pump and the seed beam diameters are ~0.5 and ~0.4 mm FWHM, respectively. (b) Second amplifier stage in a double pass. The pump and the seed beam diameters are ~2.5 and ~3.2 mm FWHM, respectively. Dashed curves are guides to the eye.
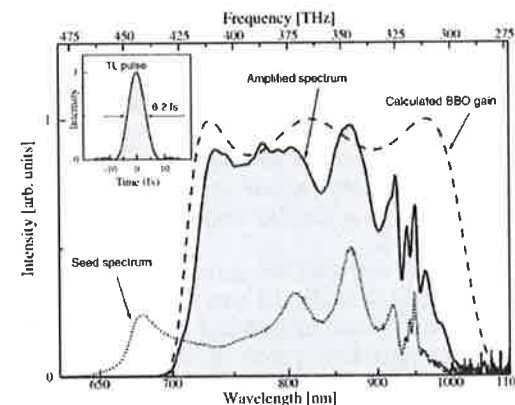

Fig. 3. Parametric amplification of a positively chirped seed pulse. The dotted curve and the shaded contour show the spectra of the seed pulse (2 nJ) and the amplified pulse (8 mJ) spectra, respectively. The dashed curve depicts the calculated gain of a 4-mm type I BBO. The inset shows a pulse profile calculated assuming an ideal compression of the amplified pulse. TL, transform-limited.
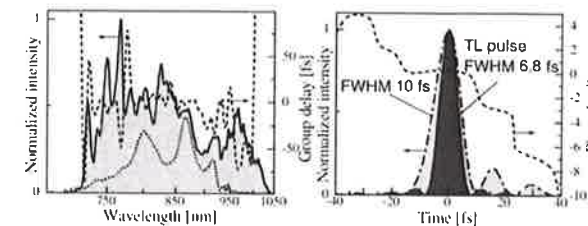
Fig. 4. Results of amplification and recompression of a negatively chirped seed pulse. (a) Seed spectrum behind the grating stretcher (dotted curve), amplified pulse spectrum (shaded contour), and residual group delay (dashed curve). (b) Recompressed 5-mJ pulse (dashed–dotted curve) and temporal phase (dashed curve). The dark contour shows the intensity profile assuming ideal pulse compression.

dispersion correction and a thermally activated deformable mirror (OKO Technologies) for wave-front correction. In total, the beam propagates through the grating four times, which significantly reshapes the transmitted seed spectrum [Fig. 4(a), dotted curve]. To provide the target pulse duration of 50 ps at the NOPAs, the stretcher precompensates the positive dispersion of the programmable acousto-optic filter (DAZZLER, Fastlite) containing a 45-mm-long TeO_2 crystal. After amplification, the beam is expanded to a FWHM diameter of ~3 cm and is sent through a compressor consisting of 15 cm of SF57 glass (Schott), followed by 10 cm of Suprasil synthetic quartz (Heraeus) and a set of three custom-made positive-dispersion dielectric chirped mirrors. This stepwise compression is used to reduce pulse self-action inside the bulk material, and the B-integral value for a fully compressed 5-mJ pulse is estimated to be below 1.3. The measured losses in the compressor are below 4%. The amplified bandwidth in the case of the grating-based stretcher [Fig. 4(a), solid curve] is somewhat narrower in comparison with the bulk stretcher and potentially supports ~7-fs pulses. By use of the feedback from a SPIDER measurement of spectral phase, the dispersion of the DAZZLER is tuned to recompress the amplified pulses to ~10 fs [Fig. 4(b)]. We expect to achieve a better pulse compression after upgrading the DAZZLER synchronization and the single-shot SPIDER setup.

In summary, we have designed multistage OPCPA for broadband multimillijoule pulse amplification around 800 nm and employed a unique pulse stretching and compression scheme. Because of the absence of thermal load on the nonlinear optical crystal, the demonstrated concept is scalable both in energy and repetition rate.

References

1. T. Brabec and F. Krausz, Rev. Mod. Phys. **72**, 545 (2000).
2. M. Nisoli, S. Stagira, S. D. Silvestri, O. Svelto, S. Sartania, Z. Cheng, M. Lenzner, C. Spielmann, and F. Krausz, Appl. Phys. B **65**, 189 (1997).
3. S. Sartania, Z. Cheng, M. Lenzner, G. Tempea, C. Spielmann, F. Krausz, and K. Ferencz, Opt. Lett. **22**, 1562 (1997).
4. G. M. Gale, M. Cavallari, T. J. Driscoll, and F. Hache, Opt. Lett. **20**, 1562 (1995).
5. A. Shirakawa, I. Sakane, M. Takasaka, and T. Kobayashi, Appl. Phys. Lett. **74**, 2268 (1999).
6. G. Cerullo, M. Nisoli, S. Stagira, and S. De Silvestri, Opt. Lett. **23**, 1283 (1998).
7. A. Baltuška, T. Fuji, and T. Kobayashi, Opt. Lett. **27**, 306 (2002).
8. A. Dubietis, G. Jonušaskas, and A. Piskarskas, Opt. Commun. **88**, 437 (1992).
9. I. N. Ross, P. Matousek, M. Towrie, A. J. Langley, and J. L. Collier, Opt. Commun. **144**, 125 (1997).
10. A. Galvanauskas, A. Hariharan, D. Harter, M. A. Arbore, and M. M. Fejer, Opt. Lett. **23**, 210 (1998).
11. I. N. Ross, P. Matousek, G. H. New, and K. Osvay, J. Opt. Soc. Am. B **19**, 2331 (2002).
12. X. Yang, Z. Xu, Y. Leng, H. Lu, L. Lin, Z. Zhang, R. Li, W. Zhang, D. Yin, and B. Tang, Opt. Lett. **27**, 1135 (2002).
13. I. Jovanovic, C. A. Ebbers, and C. P. J. Barty, Opt. Lett. **27**, 1622 (2002).
14. L. J. Waxer, V. Bagnoud, I. A. Begishev, M. J. Guardalben, J. Puth, and J. D. Zuegel, Opt. Lett. **28**, 1245 (2003).
15. N. F. Andreev, V. I. Bespalov, V. I. Bredikhin, S. G. Garanin, V. N. Ginzburg, K. L. Dvorkin, E. V. Katin, A. I. Korytin, V. V. Lozhkarev, O. V. Palashov, N. N. Rukavishnikov, A. M. Sergeev, S. A. Sukharev, G. I. Freĭdman, E. A. Khazanov, and I. V. Yakovlev, JETP Lett. **79**, 144 (2004).
16. C. P. Hauri, P. Schlup, G. Arisholm, J. Biegert, and U. Keller, Opt. Lett. **29**, 1369 (2004).
17. R. T. Zinkstok, S. Witte, W. Hogervorst, and K. S. E. Eikema, Opt. Lett. **30**, 78 (2005).
18. T. Sosnowski, P. B. Stephens, and T. B. Norris, Opt. Lett. **21**, 140 (1996).
19. E. Žeromskis, A. Dubietis, G. Tamošauskas, and A. Piskarskas, Opt. Commun. **203**, 435 (2002).
20. P. O'Shea, M. Kimmel, X. Gu, and R. Trebino, Opt. Lett. **26**, 932 (2001).
21. D. M. Gaudiosi, A. L. Lytle, D. Kohl, M. M. Murnane, H. C. Kapteyn, and S. Backus, Opt. Lett. **29**, 2665 (2004).